

Universidade de São Paulo
Instituto de Astronomia, Geofísica e Ciências Atmosféricas
Departamento de Astronomia

Fabio Cafardo

**Exploring Sagittarius A* in gamma-rays
with Fermi LAT Telescope**

São Paulo

2021

Fabio Cafardo

Exploring Sagittarius A* in gamma-rays with Fermi LAT Telescope

Thesis presented to the Astronomy department of The Institute of Astronomy, Geophysics and Atmospheric Sciences at the University of São Paulo as partial requisite to obtain the PhD in Sciences title.

Concentration Area: Astronomy

Advisor: Prof. Dr. Rodrigo Nemmen

Versão Corrigida. O original encontra-se disponível na Unidade.

São Paulo

2021

to _____

[insert your name here]

Acknowledgements

I have been helped by so many people my entire life. I take this moment to acknowledge how profoundly grateful I am.

To Julia, without whom this would be utterly impossible. Thank you very much for everything. Don't fret: fortunately, there is much more to come.

To my family for the support you gave me trough all my life.

To Flavia, who allowed for this adventure to start.

To all my friends, old and new, for the good moments. If you consider yourself a friend of mine, thank you!

To my advisor, Prof. Rodrigo, and the Black Hole Group: Prof. Roderik, Roberta, Raniere, Gustavo, Ivan, Artur, Maria Lucia, Douglas and Lucas. It was a pleasure working with you.

To all my teachers and professors, who helped to shape me into who I am.

To the *Fermi*-LAT Collaboration for providing an environment in which I could learn and get to know wonderful people.

To the people of São Paulo and Brazil for their sacrifice in funding the University of São Paulo, IAG and CNPq (who financed part of this PhD under grant number 142320/2016-1).

And to anyone that would like to see their name in this page. If you think you deserve my acknowledgment, here, take this one.

“An epigraph does more than set the tone for a poem—it raises the stakes before the poem even begins.”

Heather Bowlan

“Eu não quero aprender mais nada, nunca mais, na minha vida.”

@FalhamosBilu

“What?”

Richard M. Nixon

“The universe is a big place, perhaps the biggest.”

Kilgore Trout

Resumo

Sagitário A* — o buraco negro supermassivo no centro de nossa galáxia — já foi identificado na maior parte do espectro eletromagnético, de rádio a raios X. Em raios gama, se observa emissão difusa ao redor de Sagitário A* e uma fonte pontual foi detectada coincidindo com a posição do buraco negro supermassivo, mas ainda não há uma associação definitiva entre eles. Neste trabalho, usamos ~ 11 anos de observações da fonte pontual 4FGL J1745.6–2859 pelo *Fermi* Large Area Telescope para realizar análises detalhadas em quatro bandas de energia. Nossa meta é elucidar a origem da emissão de raios gama do centro da galáxia e investigar sua possível associação com o buraco negro supermassivo. Nós identificamos que os centróides das emissões se aproximam de Sagitário A* em energias mais altas e que eles estão associados espacialmente à distribuição de gás no centro da galáxia. Supondo que a fonte pontual de raios gama encontra-se no centro da galáxia, estimamos sua luminosidade em 2.61×10^{36} erg s $^{-1}$ no intervalo de energia entre 100 MeV e 500 GeV. Este valor é consistente com a luminosidade bolométrica de Sagitário A*. Com base nas propriedades da fonte pontual, vários potenciais candidatos para esta emissão foram descartados, favorecendo uma interpretação em que os raios cósmicos são acelerados por — ou próximos de — Sagitário A*. Também elaboramos curvas de luz, com resolução temporal de 15 dias, em busca de variabilidade no fluxo de raios gama de 4FGL J1745.6–2859. Ao contrário do observado em comprimentos de onda mais longos, nós detectamos que a distribuição do seu fluxo de raios gama é compatível com uma Gaussiana, representativa de um processo aleatório normal, um indicativo de que o mecanismo de emissão de raios gama é distinto do regime de menores energias. Finalmente, a distribuição espectral de energia de 4FGL J1745.6–2859 apresenta um “*pion-decay bump*”, característica de emissão de raios gama com origem hadrônica. Sua distribuição espectral

de energia é, também, compatível com vários modelos hadrônicos para a emissão de raios gama de Sagitário A*. Nossos resultados indicam que a fonte pontual no centro da galáxia corresponde à contrapartida em raios gama de Sagitário A* em energias da ordem de GeV. As características desta emissão — sua coincidência espacial com reservatórios de gás, sua “energética”, a falta de variabilidade e sua distribuição espectral de energia — sugerem que processos hadrônicos estejam por trás de sua origem.

Abstract

Sagittarius A* (Sgr A*)—the supermassive black hole (SMBH) in the center of our galaxy—has been identified in most of the electromagnetic spectrum, from radio to X-rays. Diffuse gamma-ray emission has been observed around Sgr A* and a gamma-ray point source has been detected coinciding with the SMBH’s position, although there is still no definitive association between the two. In this work, we have used ~ 11 years of *Fermi* Large Area Telescope (LAT) observations of the point source 4FGL J1745.6–2859 and performed a detailed analysis across four energy bands. Our goal is to elucidate the nature of the gamma-ray emission at the Galactic Center (GC) and whether it is associated with the SMBH. We find that the centroids of the emission approach Sgr A*’s location as the energy increases and they are spatially associated with gas-rich regions in the GC. Assuming that the gamma-ray point source is located at the GC, we estimate a luminosity of 2.61×10^{36} erg s $^{-1}$ in the 100 MeV to 500 GeV energy range. This is consistent with Sgr A*’s bolometric luminosity. Based on the point source properties, we ruled out several potential candidates for its nature and favor a cosmic ray origin accelerated by—or in the vicinity of—the SMBH. We also created light curves (LCs), with time bins as short as 15 days, in search of variability in the 4FGL J1745.6–2859 gamma-ray flux. In contrast with Sgr A*’s flaring behavior in longer wavelengths, we detect that its gamma-ray flux distribution is compatible with a Gaussian, representative of a normal random process, hinting that the gamma-ray emission mechanism differs substantially from the low-energy regime. Finally, 4FGL J1745.6–2859’s spectral energy distribution (SED) shows a “pion-decay bump” characteristic of gamma-ray hadronic emission. Its SED is also compatible with several hadronic models for Sgr A*’s gamma-ray emission. Our results indicate that the point source at the GC is indeed the gamma-ray counterpart of Sgr A* in the GeV

range. The characteristics of this emission—its spatial coincidence with gas reservoirs, energetics, lack of variability and SED—suggest that hadronic processes are likely behind its origin.

List of Figures

1.1	Multiwavelength observations of the inner few parsecs of the Galaxy	32
1.2	Cartoonistic depiction of the inner two parsecs of the Galaxy	33
1.3	The <i>Fermi</i> gamma-ray sky	34
1.4	The S-star cluster	38
1.5	Twenty six years observations of S2 star orbiting Sgr A*	39
1.6	Sgr A*'s broad band spectrum	46
1.7	Two bright X-rays flares from Sgr A* fit with a hotspot model	48
1.8	The <i>Fermi</i> Bubbles	52
1.9	Sensitivity of different gamma-ray detectors	55
1.10	Earth's atmospheric opacity	59
1.11	The <i>Fermi</i> Gamma-ray Space Telescope	60
1.12	The <i>Fermi</i> -LAT instrument and its constituents	63
1.13	<i>Fermi</i> -LAT's effective area as function of energy and incidence angle	67
1.14	<i>Fermi</i> -LAT's PSF as function of energy and incidence angle	69
1.15	<i>Fermi</i> -LAT's systematic uncertainty on the effective area	70
1.16	<i>Fermi</i> -LAT's PSF systematic uncertainty	71
1.17	Spatial distribution and classification of 4FGL sources	74
1.18	Central source's spectral model in 4FGL	78
2.1	Energy bands used in the analysis	84
2.2	Residuals distribution examples for the low energy model	100
2.3	Residuals map of the Universal Model	102
2.4	Residuals maps in the four tighter energy bands	103
2.5	<i>TS</i> map of the Universal Model	105

2.6	<i>TS</i> maps of the four tighter energy bands	106
2.7	<i>TS</i> map of the Universal Model after removing the central source	107
2.8	<i>TS</i> maps of the four energy bands after removing the central source	108
2.9	15 days energy flux LC of 4FGL J1747.2–2957	115
2.10	Statistical uncertainties distribution of 4FGL J1747.2–2957 15 days energy flux LC	116
2.11	Relative dispersion distribution of 4FGL J1747.2–2957 15 days energy flux LC	117
2.12	15 days bins LCs of 4FGL J1745.6–2859	119
3.1	Best-fit spectral models	126
3.2	Central source position as a function of energy	128
3.3	Distance between the central source and Sgr A* as a function of energy	129
3.4	UL on the spatial extension of the central source as a function of energy	130
3.5	Distributions of the error radii in the different <i>Fermi</i> Catalogues	131
3.6	15 days LCs of 4FGL J1745.6–2859 <i>versus</i> average flux	132
3.7	15 days LCs of 4FGL J1745.6–2859 <i>versus</i> 5 bins rolling average flux	133
3.8	The flux distribution of the 15 days bins LCs	135
3.9	15 days LCs of 4FGL J1745.6–2859 fitted with linear functions	136
3.10	90 days LCs of 4FGL J1745.6–2859 <i>versus</i> average flux in the 300 MeV–3 GeV energy band	137
3.11	90 days LCs of 4FGL J1745.6–2859 <i>versus</i> average flux in the 3–10 GeV energy band	138
3.12	180 days LCs of 4FGL J1745.6–2859 <i>versus</i> average flux in the 10–500 GeV energy band	139
3.13	90 days LCs of 4FGL J1745.6–2859 <i>versus</i> 5 bins rolling average flux in the 300 MeV–3 GeV energy band	140
3.14	90 days LCs of 4FGL J1745.6–2859 <i>versus</i> 5 bins rolling average flux in the 3–10 GeV energy band	141
3.15	180 days LCs of 4FGL J1745.6–2859 <i>versus</i> 5 bins rolling average flux in the 10–500 GeV energy band	142
3.16	Linear fit to the 90 days bins LCs in the 300 MeV–3 GeV energy band	143

3.17	Linear fit to the 90 days bins LCs in the 3–10 GeV energy band	144
3.18	Linear fit to the 180 days bins LCs in the 10–500 GeV energy band	145
3.19	The resulting SED for the Universal Model	147
4.1	Source position and gas distribution in the GC	151
4.2	The 4FGL blazars energy flux distribution	156
4.3	Trap et al. (2011) observations of a NIR and flare from Sgr A*	160
4.4	15 days energy flux LC of 4FGL J1745.6–2859 <i>versus</i> remarkable events	162
4.5	15 days photon flux LC of 4FGL J1745.6–2859 <i>versus</i> remarkable events	163
4.6	A simple model for the different energy bands emission	164
4.7	The combination of the narrower energy bands energy flux LCs	165
4.8	The combination of the narrower energy bands photon flux LCs	166
4.9	4FGL J1745.6–2859 SED compared with different models for Sgr A*’s emission	168
D.1	Examples of discontinuous models not used in this work	232
E.1	Residual maps for previous analyses for the 3 highest bands	234
E.2	TS maps with the source for previous analyses for the 3 highest bands	235
E.3	TS maps without the source for previous analyses for the 3 highest bands	236
G.1	<i>Event types</i> tests for the 60–300 MeV interval: central source’s position	242
H.1	Residuals distribution for the Universal Model offspring	246
I.1	15 days photon flux LC of 4FGL J1747.2-2957	248
I.2	Statistical uncertainties distribution of 4FGL J1747.2-2957 15 days photon flux LC	249
I.3	Relative dispersion distribution of 4FGL J1747.2-2957 15 days photon flux LC	250
J.1	45 days energy flux LC of 4FGL J1747.2-2957 in the 100 MeV–500 GeV energy range	252
J.2	Statistical uncertainties distribution of 4FGL J1747.2-2957 45 days energy flux LC in the 100 MeV–500 GeV energy range	252

J.3	Relative dispersion distribution of 4FGL J1747.2-2957 45 days energy flux LC in the 100 MeV–500 GeV energy range	253
J.4	45 days photon flux LC of 4FGL J1747.2-2957 in the 100 MeV–500 GeV energy range	253
J.5	Statistical uncertainties distribution of 4FGL J1747.2-2957 45 days photon flux LC in the 100 MeV–500 GeV energy range	254
J.6	Relative dispersion distribution of 4FGL J1747.2-2957 45 days photon flux LC in the 100 MeV–500 GeV energy range	254
J.7	90 days energy flux LC of 4FGL J1747.2-2957 in the 300 MeV–3 GeV energy range	255
J.8	Statistical uncertainties distribution of 4FGL J1747.2-2957 90 days energy flux LC in the 300 MeV–3 GeV energy range	256
J.9	Relative dispersion distribution of 4FGL J1747.2-2957 90 days energy flux LC in the 300 MeV–3 GeV energy range	256
J.10	90 days photon flux LC of 4FGL J1747.2-2957 in the 300 MeV–3 GeV energy range	257
J.11	Statistical uncertainties distribution of 4FGL J1747.2-2957 90 days photon flux LC in the 300 MeV–3 GeV energy range	257
J.12	Relative dispersion distribution of 4FGL J1747.2-2957 90 days photon flux LC in the 300 MeV–3 GeV energy range	258
J.13	90 days energy flux LC of 4FGL J1747.2-2957 in the 3–10 GeV energy range	259
J.14	Statistical uncertainties distribution of 4FGL J1747.2-2957 90 days energy flux LC in the 3–10 GeV energy range	259
J.15	Relative dispersion distribution of 4FGL J1747.2-2957 90 days energy flux LC in the 3–10 GeV energy range	260
J.16	90 days photon flux LC of 4FGL J1747.2-2957 in the 3–10 GeV energy range	260
J.17	Statistical uncertainties distribution of 4FGL J1747.2-2957 90 days photon flux LC in the 3–10 GeV energy range	261
J.18	Relative dispersion distribution of 4FGL J1747.2-2957 90 days photon flux LC in the 3–10 GeV energy range	261
K.1	45 days LCs of 4FGL J1745.6–2859 <i>versus</i> average flux	264

K.2	45 days LCs of 4FGL J1745.6–2859 <i>versus</i> 5 bins rolling average flux . . .	265
K.3	The flux distribution of the 45 days bins LCs	266
K.4	45 days LCs of 4FGL J1745.6–2859 fitted with a linear function	268
L.1	Central point position as a function of energy	270
M.1	<i>TS</i> for the 15 days LC of 4FGL J1745.6–2859 (100 MeV–500 GeV energy band)	271
M.2	<i>TS</i> for the 90 days LC of 4FGL J1745.6–2859 (300 MeV–3 GeV energy band)	272
M.3	<i>TS</i> for the 90 days LC of 4FGL J1745.6–2859 (3–10 GeV energy band) . .	272
M.4	<i>TS</i> for the 180 days LC of 4FGL J1745.6–2859 (10–500 GeV energy band)	273
M.5	<i>TS</i> for the 45 days LC of 4FGL J1745.6–2859 (100 MeV–500 GeV energy band)	273

List of Tables

1.1	Accretion rate as a function of distance from Sgr A*	42
1.2	Central source positions in <i>Fermi</i> -LAT's catalogs	77
2.1	Systematic uncertainties of the light curves used in this work	117
3.1	Central source gamma-ray flux	127
3.2	Results of the Shapiro-Wilk and the D'Agostino's K^2 normality tests for the 15 days LCs	134
3.3	Results of the Anderson-Darling normality test for the 15 days LCs	134
3.4	Results of a linear fit to the 15 days bins LCs data	136
3.5	Results of linear fits to the for the narrower energy bands LCs	145
C.1	New sources found in the 100 MeV to 500 GeV energy range.	230
E.1	Central source gamma-ray flux in previous analyses	237
F.1	New sources found in the 60 to 300 MeV energy range.	239
G.1	<i>Event types</i> tests for the 60–300 MeV interval: central source's flux	243
K.1	Results of the Shapiro-Wilk and the D'Agostino's K^2 normality tests for the 45 days LCs	267
K.2	Results of the Anderson-Darling normality test for the 45 days LCs	267
K.3	Results of a linear fit to the 45 days bins LCs data	268

Abbreviations

- 1FGL: First *Fermi*-LAT Catalog
- 1FLE: First *Fermi* Low Energy Catalog
- 2D: Two-dimensional
- 2FGL: Second *Fermi*-LAT Catalog
- 3D: Three-dimensional
- 3FGL: Third *Fermi*-LAT Catalog
- 4FGL: Fourth *Fermi*-LAT Catalog
- 4FGL-DR2: *Fermi*-LAT 10-year Catalog
- AIC: Akaike Information Criterion
- AGN: Active Galactic Nuclei
- BH: Black Hole
- CND: Circum-Nuclear Disk
- CR: Cosmic Rays
- CTA: Cherenkov Telescope Array
- DM: Dark Matter
- EAS: Extensive Air Showers

- EHT: Event Horizon Telescope
- ELT: Extremely Large Telescope
- GC: Galactic Center
- Gamma-ray Bursts: GRB
- GRMHD: General Relativistic Magneto Hydrodynamics
- GW: Gravitational Waves
- H.E.S.S.: High Energy Stereoscopic System
- IACT: Imaging Air Cherenkov Technique
- IC: Inverse Compton
- IRFs: Instrument Response Functions
- ISCO: Innermost Stable Circular Orbit
- LAT: Large Area Telescope
- LC: Light Curve
- GTI: Good Time Intervals
- MCMC: Markov chain Monte Carlo
- NIR: Near Infrared
- N_{Pred} : Predicted Number of Counts
- PWN: Pulsar Wind Nebulae
- PSF: Point Spread Function
- RIAF: Radiatively Inefficient Accretion Flow
- RoI: Region of Interest
- Sgr A*: Sagittarius A*

- SED: Spectral Energy Distribution
- SMBH: Supermassive Black Hole
- SNR: Supernova Remnants
- SSC: Synchrotron Self Compton
- UL: Upper Limit
- VLT: Very Large Telescope
- WIMP: Weakly Interacting Massive Particle

Contents

1. Introduction	29
1.1 The motivations and goals of this thesis	29
1.2 The Galactic Center	30
1.2.1 The Galactic Center in gamma-rays	34
1.3 Sagittarius A*	35
1.3.1 A historical perspective	36
1.3.2 The Galactic Center black hole	37
1.3.2.1 Basic facts about Sgr A*	40
1.3.3 Multiwavelength emission	42
1.3.3.1 Sagittarius A* in gamma-rays	43
1.3.3.2 The two states of Sagittarius A*	45
1.3.3.3 Variability and flares	47
1.3.3.4 Hints of past activity of Sagittarius A* emission	51
1.3.4 Models for Sagittarius A* emission	52
1.4 Other gamma-ray telescopes	54
1.4.1 Space-based instruments	55
1.4.2 Ground-based Cherenkov telescopes	56
1.4.2.1 The Imaging Air Cherenkov Technique	57
1.4.2.2 The Extensive Air Showers Technique	58
1.5 Fermi Gamma-ray Space Telescope	58
1.5.1 The <i>Fermi</i> Large Area Telescope	61
1.5.2 <i>Fermi</i> -LAT data products	64
1.5.3 <i>Fermi</i> -LAT performance	66

1.5.4	Caveats and systematics	68
1.5.4.1	Effective area	68
1.5.4.2	PSF	70
1.5.5	The 4FGL Catalog	71
1.5.5.1	The diffuse models	75
1.5.5.2	The 4FGL J1745.6–2859 source	77
1.6	The production of astrophysical gamma-rays	78
1.6.1	Leptonic emission	79
1.6.2	Hadronic emission	79
1.6.3	Dark matter self annihilation	80
1.7	Publication resulting from this work	80
2.	<i>Data and Methods</i>	83
2.1	Data	83
2.1.1	Data selection: Universal Model	85
2.1.2	Data selection: low energy custom model	86
2.1.3	Energy boundaries	87
2.2	Maximum likelihood modeling	87
2.2.1	The likelihood function	88
2.2.1.1	Likelihood model fitting with Fermitools	90
2.2.1.2	Model selection	91
2.3	Defining models with the Fermitools	92
2.3.1	Universal Model	93
2.3.2	Custom model (60–300 MeV)	97
2.3.3	Evaluating the quality of the fitting process	99
2.4	Assessing the source position	109
2.4.1	Identifying the source position with the Fermitools	109
2.4.2	Systematic uncertainties	111
2.5	Variability of the GC	112
2.5.1	Creating a light curve	112
2.5.2	Systematic uncertainties	114
2.5.3	Searching for variability in the LCs	118

2.6	Spectral Energy Distribution	122
3.	<i>Results</i>	125
3.1	Spectral model	125
3.2	Position in different energy bands	127
3.3	Light curves	131
3.3.1	15 days bins, Universal Model	132
3.3.2	Separate energy intervals	137
3.4	SED	146
4.	<i>Discussion</i>	149
4.1	Energetics and centroid	149
4.1.1	Nature of emission	151
4.2	On the temporal flux evolution	157
4.2.1	The 15 days bins LC	157
4.2.2	The LCs created for the narrower energy bands	163
4.3	SED and emission models	167
5.	<i>Conclusions</i>	171
5.1	The evidence points to Sagittarius A*	171
5.2	Future perspectives	173
	<i>Bibliography</i>	177
	<i>Appendix</i>	201
A.	<i>Article: Fermi LAT observations of Sagittarius A*: I - Imaging Analysis</i>	203
B.	<i>Additional Publications</i>	223
C.	<i>New sources found in the analysis between 100 MeV and 500 GeV</i>	229
D.	<i>Examples of discontinuous models</i>	231
E.	<i>Comparing the results obtained through the minimal fitting method to a more standard approach</i>	233

<i>F. New sources found in the analysis between 60 and 300 MeV</i>	<i>239</i>
<i>G. Comparing different event type selection for the low energy model</i>	<i>241</i>
<i>H. Residuals distribution for the Universal Model offspring</i>	<i>245</i>
<i>I. Estimating the systematic uncertainties in the 15 days photon flux LC</i>	<i>247</i>
<i>J. Estimating the systematic uncertainties in the LCs</i>	<i>251</i>
<i>J.1 Systematic uncertainties in the 45 days LC</i>	<i>251</i>
<i>J.1.1 Energy flux</i>	<i>252</i>
<i>J.1.2 Photon flux</i>	<i>253</i>
<i>J.2 Systematic uncertainties in the 90 days, 300 MeV–3 GeV LC</i>	<i>255</i>
<i>J.2.1 Energy flux</i>	<i>255</i>
<i>J.2.2 Photon flux</i>	<i>257</i>
<i>J.3 Systematic uncertainties in the 90 days, 3–10 GeV LC</i>	<i>258</i>
<i>J.3.1 Energy flux</i>	<i>259</i>
<i>J.3.2 Photon flux</i>	<i>260</i>
<i>K. The 45 days bins LC created based on the Universal Model (100 MeV–500 GeV)</i>	<i>263</i>
<i>L. The 95% confidence level central point position as a function of energy</i>	<i>269</i>
<i>M. The TS of the LCs</i>	<i>271</i>

Introduction

In 1915, Albert Einstein published the theory of general relativity, forever changing the way we understand gravity. Only a few months later, Karl Schwarzschild found a solution to the Einstein field equations that would characterize a black hole (BH) as a region of space from which nothing can escape. The 1960's and 1970's are brimful of theoretical works that developed and solidified the concept of BHs in the science literature and, also, in the zeitgeist.

More recently, the interest in these objects was propelled by extraordinary observational results, such as the confirmation of the presence of a SMBH in the center of Our Galaxy, Sgr A*, inferred from stellar orbits; the detection of gravitational waves from the merger of two black holes in 2015; and the first image of a BH silhouette captured by the Event Horizon Telescope (EHT) in 2019. Two of these exceptional results were rightfully awarded with Nobel prizes: in 2017, Rainer Weiss, Kip S. Thorne and Barry C. Barish shared the Nobel Prize in Physics for the detection of gravitational waves and in 2020, Andrea Ghez and Reinhard Genzel were awarded the Nobel Prize in Physics for the showing that Sgr A* contains a SMBH.

This thesis is the result of over 4 years of work to provide our small contribution to the scientific effort of understanding these alluring objects.

1.1 The motivations and goals of this thesis

Sgr A* is an interesting laboratory to investigate the behavior and environment of SMBHs in the center of galaxies. Although it has been observed in most of the electro-

magnetic spectrum, there is still no definitive association between the gamma-ray emission from the Galactic Center (GC) and Sgr A*.

The *Fermi*-LAT source 4FGL J1745.6–2859 is coincident with Sgr A* position and hence an appealing subject to our research of Sgr A* gamma-ray emission. We focused our work in this source, using ~ 11 years observations with *Fermi*-LAT in the 60 MeV to 500 GeV energy range, with the aim of elucidating the physical nature of the high energy processes associated with the source and investigating the relation of the gamma-ray emission with Sgr A*. Therefore, we characterized its image, position and extension; studied its flux variability, searching for flaring events; and measured the SED.

1.2 The Galactic Center

The GC is an extraordinary laboratory to investigate the physical processes happening in the vicinity of a SMBH. Since it is at least 5 orders of magnitude closer than the nearest quasar the GC is subject to high-resolution observations, with much more detail than possible in any other galaxy nucleus.

It is believed that every sufficiently massive galaxy harbors a SMBH in its center (Lynden-Bell, 1969; Kormendy and Richstone, 1995; Miyoshi et al., 1995; Heckman and Best, 2014). Including the Milky Way, these objects dominate the dynamics and hence much of the physical processes, occurring in the innermost regions of the nuclei. In this thesis, we focus on the GC’s SMBH, Sgr A*, behavior in gamma-rays with *Fermi*-LAT observations. But, before we delve in Sgr A* (described in Section 1.3), we will present a brief review of the GC picture. The focus is on the central few parsecs of the Galaxy, which contain a dense star cluster, several gaseous components and the SMBH.

The central 1.5 pc is a mostly ionized, low density “cavity”. It is pervaded by Sagittarius A West (also referred as the mini-spiral), a region of H II composed of filaments with the appearance of a three-arm spiral, from the point of view of the Earth (Lo and Claussen, 1983; Christopher et al., 2005); and a concentration of extremely hot gas, detected in X-rays (Baganoff et al., 2001, 2003; Munro et al., 2004). At ~ 1.5 pc from the GC there is a sharp transition between the central cavity and the circumnuclear disk (CND). The CND has a ~ 1.5 –4 pc radius and is comprised of orbiting dense molecular clouds and warm

dust (Becklin et al., 1982; Guesten et al., 1987; Jackson et al., 1993; Christopher et al., 2005; Armillotta et al., 2019). In Figure 1.1, adapted from Genzel et al. (2010), we show multiwavelength observations of the central 3 pc of our Galaxy. The structures mentioned are highlighted in the right panels, along with other features.

Not only gas inhabits the CND. A dense star cluster is also found in the inner parts of the Galaxy. The stellar density inside this cluster increases inward, from a scale of tens of parsecs to within the GC (Becklin and Neugebauer, 1968; Genzel et al., 1994; Do et al., 2013; Calderon et al., 2020). Many of these are young massive stars (Genzel et al., 1996; Blum et al., 1997; Paumard et al., 2003, 2006; Tanner et al., 2006). In the inner 1" of the Galaxy, there is a concentration of mainly B stars: the S-star cluster, discussed in more details in Section 1.3.2 (see, also, Figure 1.4) (Schödel et al., 2009; Habibi et al., 2017). The nuclear star cluster is one of the highest concentrations of massive young stars in the Galaxy. The presence of such young stars in the extreme environment so close to a SMBH offers a challenge for the current understanding of star formation and the dynamics close to a SMBH.

Inside its sphere of influence—a region around a SMBH in which its gravitational potential dominates (see Section 1.3.2.1), in the case of Sgr A* it is delimited by a radius of 2–3 pc (Genzel et al., 2010; Eckart et al., 2017)—Sgr A* dominates the mass distribution. Additional contribution arises from stars, stellar remnants (stellar mass BHs and neutron stars) (Freitag et al., 2006; Ghez et al., 2008; Gillessen et al., 2009; Gillessen et al., 2009), gas (Christopher et al., 2005) and dark matter (Navarro et al., 1997; Vasiliev and Zelnikov, 2008) though the later two components do not contribute significantly. Figure 1.2, obtained from Murchikova et al. (2019), shows a cartoonistic depiction of the region inside the CND. Other than the structures already described in this Section, they show the orbits of the S2 star and the G2 object (both described in Section 1.3.2); a 10^4 K ionized gas disk within $2 \times 10^4 R_S$ detected by the authors using the 1.3mm recombination line $H30\alpha$ (that they interpret in terms of a rotating disk of mass 10^{-4} to $10^{-5} M_\odot$), the clockwise stellar system (a concentration of stars, inside the nuclear star cluster, arranged in a Keplerian disk around Sgr A* Genzel et al. 2000) and the Keplerian fall-off radius (the radius of 0.3 pc at which the point mass of Sgr A* visibly dominates the velocity dispersion of the stars in the surrounding cluster and the contribution of an extended component, related to the stars in the nuclear star cluster, is negligible, Schödel et al. 2009).

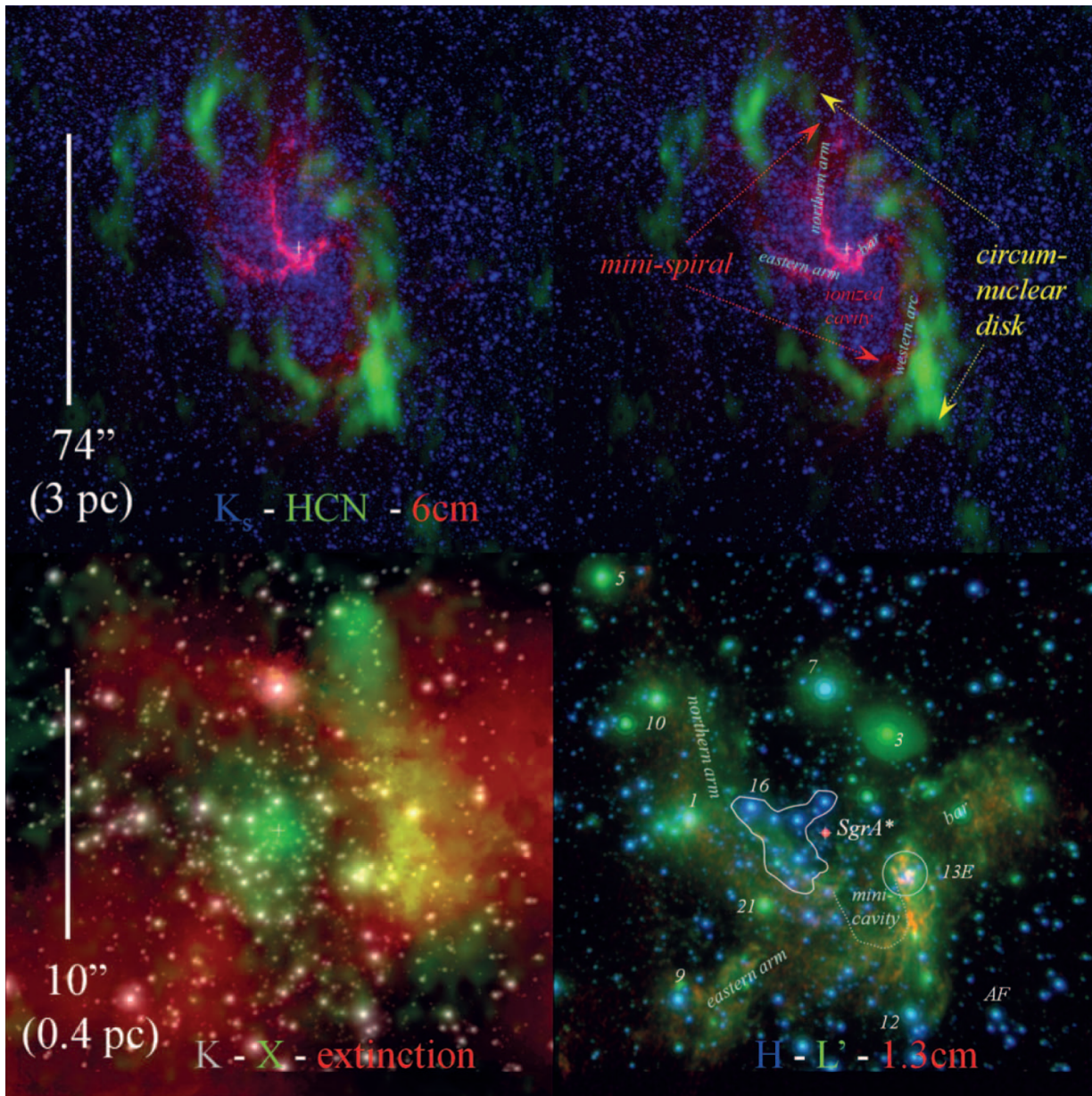


Figure 1.1: The central few parsecs of the Galaxy. Top row: multiwavelength overview of the central parsecs. Top left panel: 6 cm emission (pink: Yusef-Zadeh et al. 1986; Roberts and Goss 1993), HCN 1–0 emission (green: Christopher et al. 2005), and NIR K-band (blue: Schödel et al. 2007). Top right panel: the same as the top left panel, with interstellar features marked. Bottom row: zoom into the central region. Bottom left panel: K-band (white: Genzel et al. 2003), derived dust extinction (red-yellow: Schödel et al. 2007), and x-ray emission (green: Baganoff et al. 2003). Bottom right: NIR adaptive optics H-band and L'-band (blue and green, respectively: Genzel et al. 2003), and 1.3 cm radio continuum (red: Zhao and Goss 1998), some of the interstellar features are marked. Sgr A*'s position is marked with a faint white cross in every panel. North is up and East is to the left. The galactic plane runs at a position angle of 32° southwest-northeast. The lengths in pc correspond to structures at the GC distance. Source: adapted from Genzel et al. (2010).

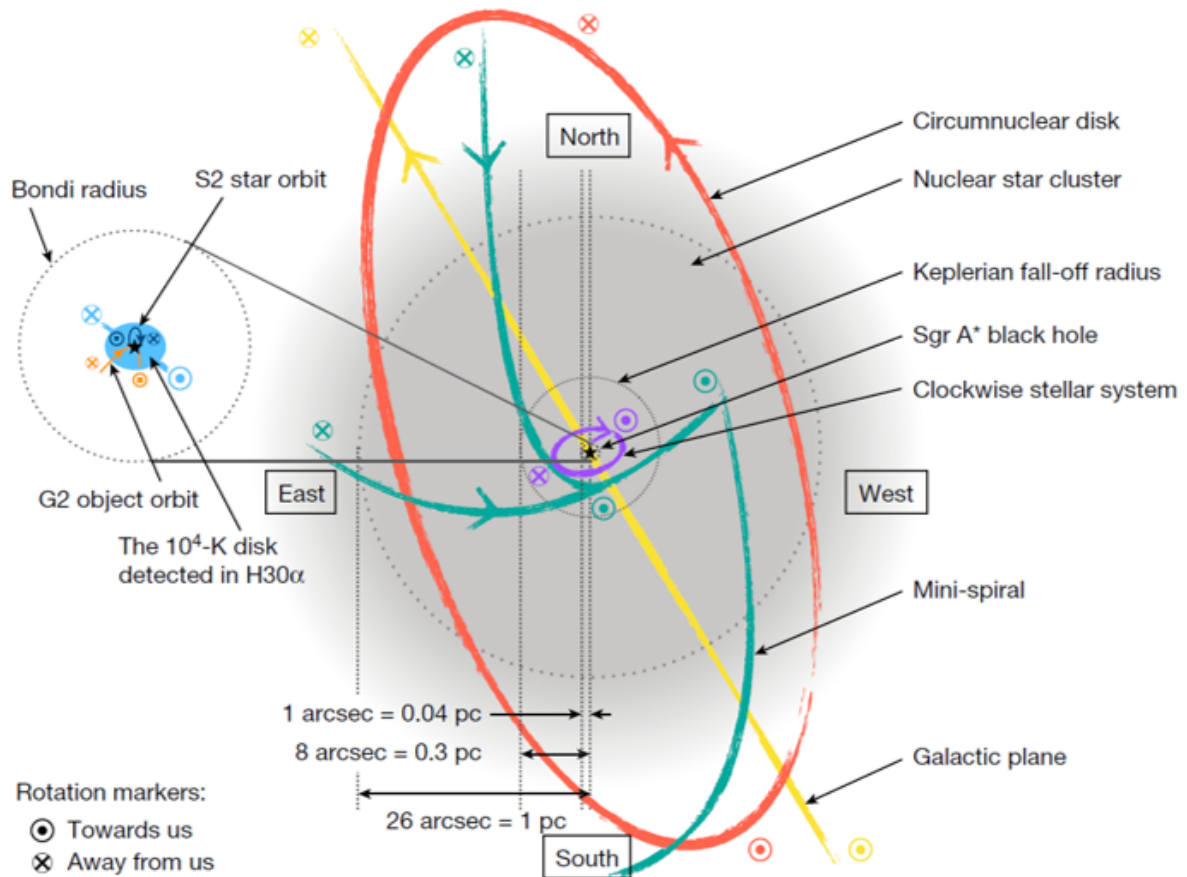


Figure 1.2: Schematic plot, to scale, of the inner two parsecs of the Galaxy. The main structures are indicated by different colors. The structures within the R_B are plotted in the zoomed-in region on the left. The direction of rotation of the structures are shown with arrows, the circled cross indicates recession from Earth, and the circled dot indicates approach to Earth. The projected distances in parsecs were calculated based on the GC distance (at this distance, $1'' \approx 0.04$ pc). Source: Murchikova et al. (2019).

Beyond the East edge of the CND, lies Sagittarius A East, a young supernova remnant. Also, the region is surrounded by several massive and dense molecular clouds with scale of 5–100 pc. (Gusten and Downes, 1980; Mezger et al., 1996).

Despite the wealthy reservoir of gas in its surroundings, Sgr A* is remarkably faint. This is the result of a combination of low efficiency converting the accreting material into radiative energy and a decrease of the accretion rate toward the SMBH (see Section 1.3.4).

1.2.1 The Galactic Center in gamma-rays

The GC is the brightest region of the gamma-ray sky. In Figure 1.3 we show 5 years of *Fermi*-LAT observations of the whole sky in energies >1 GeV. Since the image is in Galactic coordinates, the GC is located at its center. The most prominent feature is the bright band of diffuse glow along the map's center, which marks the central plane of the Galaxy. This is the result of cosmic rays (CR) collisions with the interstellar gas (more details in Sections 1.5.5.1 and 1.6). The GC is embedded in this gamma-ray component.

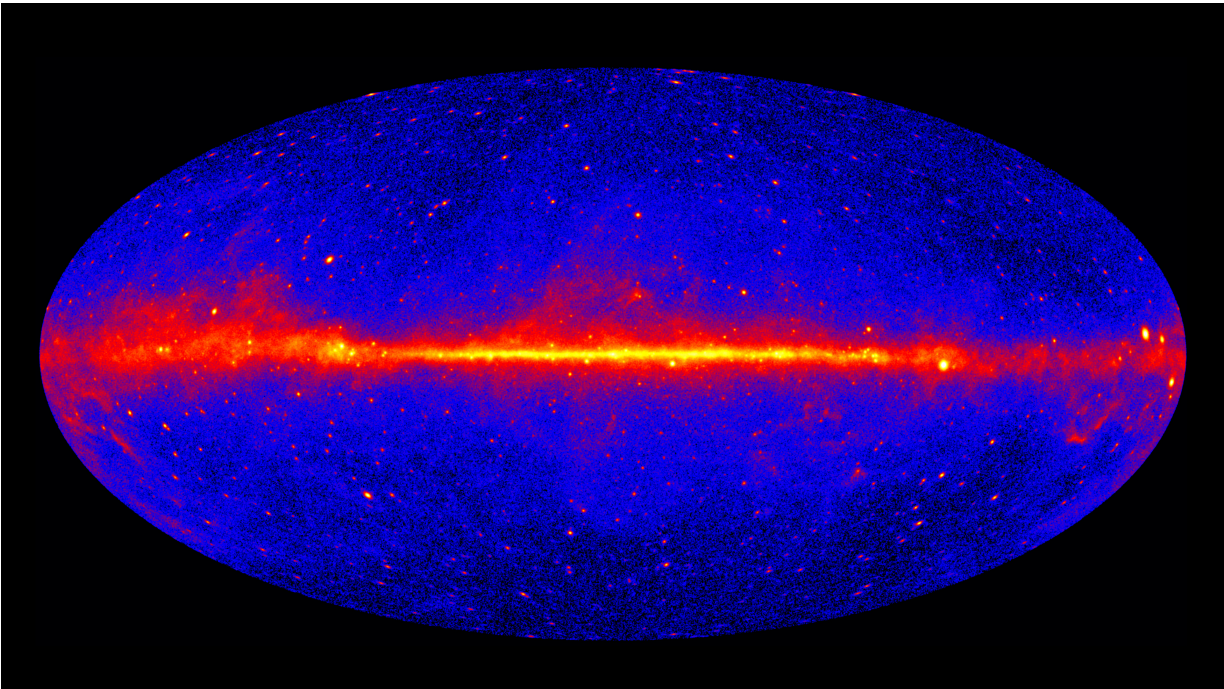


Figure 1.3: This is a *Fermi*-LAT all-sky view at energies > 1 GeV created with five years of data. For better angular resolution, the map shows only gamma rays converted at the front of the instrument's tracker (See Section 1.5). Brighter colors indicate brighter gamma-ray sources. The map is shown in galactic coordinates, centralized in the GC. Source: NASA/DOE/*Fermi* LAT Collaboration (svs.gsfc.nasa.gov/11342).

In the most recent catalog of *Fermi*-LAT sources, there are 36 cataloged sources in the inner 3° of the Galaxy, the most crowded region of the *Fermi* sky.

Even when the emission associated with the interaction of CR with the interstellar gas and the cataloged point sources are taken into account, there is an excess of diffuse gamma-ray emission in the GC that can not be explained by the current models (Goodenough and Hooper, 2009; Ajello et al., 2016; Ackermann et al., 2017). Several interpretations for this phenomenon were suggested in the literature: self-annihilating dark matter (Calore et al. 2015; Ackermann et al. 2017, but see Abazajian et al. 2020), an unresolved population of millisecond pulsars (Abazajian and Kaplinghat, 2012; Hooper and Linden, 2016), an unresolved population of young pulsars (O’Leary et al., 2015; The Fermi-LAT Collaboration et al., 2017), or a series of periods of enhanced activity from Sgr A* caused by accretion phenomena (Petrovic et al., 2014; Cholis et al., 2015). Even interpretations related to imperfections in the GC gas distribution have been suggested (Macias et al., 2018).

In even higher energies, $\gtrsim 1$ TeV, H.E.S.S. Collaboration et al. (2016) observe an extended emission centered in Sgr A* that was explained as the result of the interaction of PeV protons with the gas content in the central 10 pc of the Galaxy. They also report a centrally-peaked profile for the CR density in the GC. They propose the presence of a petaelectronvolt accelerator (‘PeVatron’) of CR in the GC to explain the observations. Later, these results were confirmed by H.E.S.S. Collaboration et al. (2018), that also describe a new point source, HESS J1746-285, in the vicinity of the GC and argue that it is produced by a pulsar wind nebula candidate. MAGIC Collaboration et al. (2020) also corroborate the centrally-peaked CR profile, although their data are only marginally compatible with the PeVatron scenario, suggesting CRs with slightly lower energies. The three works, in their spatial modeling of the GC gamma-ray sky, require the inclusion of a point source coincident with Sgr A*’s position. They also suggest a more active phase of Sgr A* in the past as the origin of the high energy CRs.

1.3 Sagittarius A*

The SMBHs that lie in the center of every sufficiently massive galaxy manifest themselves in a myriad of different and complex ways. The majority is in a quiet state, not revealing itself in any dramatic way. Others are really conspicuous and detected as Active Galactic Nuclei (AGNs, Ho 2008).

The center of our galaxy hosts the nearest SMBH with a mass of $4.02 \pm 0.20 \times 10^6 M_{\odot}$ (Boehle et al., 2016) located at a distance of 8.2 kpc (GRAVITY Collaboration et al., 2019). It is, therefore, an attractive laboratory to investigate SMBHs, even though it is in a tranquil state.

In this Section we present more details about this alluring object, Sgr A*. We start with a historical perspective about its discovery. Then, we present its current and past, characteristics.

1.3.1 A historical perspective

The history of the discovery of Sgr A* and its association with a SMBH is heartwarmingly recounted by Goss et al. (2003). They focus on the period up to 1985. The first observations of a source that would later be associated with Sgr A* were made by Balick and Brown (1974) in radio wavelengths.

The first use of the name Sgr A* to describe the GC compact radio source was by Brown (1982). In Goss et al. (2003), Bob Brown gives the following rationale for the name:

“Scratching on a yellow pad one morning I tried a lot of possible names. When I began thinking of the radio source as the ‘exciting source’ for the cluster of H_{II} regions seen in the VLA maps, the name Sgr A* occurred to me by analogy brought to mind by my PhD dissertation, which is in atomic physics and where the nomenclature for excited state atoms is He^* , or Fe^* etc.” (Goss et al., 2003)

By the end of the 1970s and beginning of 1980s, the discovery that the line of sight velocities of ionized gas increased to a few hundred km s^{-1} in the central parsec of the Galaxy (Wollman et al., 1977) suggested the presence of a mass concentration in the GC (with $2\text{--}4 \times 10^6 M_{\odot}$). This virial analysis of the gas led to the conclusion that this mass concentration might be a massive black hole plausibly associated with the compact radio source Sgr A* (Lacy et al., 1980, 1982). During the 1980s, more detailed measurements of the dynamics of gas (ionized as well as of atomic and molecular) in the GC improved the case. But, since gas is sensitive to forces other than gravity, further progress required stellar dynamics. Through the 1980s, stellar velocity dispersion measurements in the GC confirmed and refined these conclusions. Genzel et al. 2010 presents a nice review about these works in Section IV-b.

As the resolution of the observations and the quality of the dynamics tracers (diffuse gas, in the beginning, stellar velocity dispersion in the 1980s) increased, the space volume allowed for the central mass in the GC got smaller and smaller. The case for the presence of a SMBH associated with the radio source Sgr A*'s position became stronger.

The next big leap came from the detection of the first stellar proper motions. This, along with other stronger evidences of the presence of a SMBH in the center of the Milky Way, is described in Section 1.3.2.

1.3.2 The Galactic Center black hole

In this section, we review the most recent evidence for the presence of a SMBH in the center of Our Galaxy.

Using adaptive optics at near-infrared (NIR) wavelengths has allowed the identification and study of several stars orbiting Sgr A* in the inner arcsecond of Our Galaxy. These high velocity stars, referred as the the S-star cluster, have highly eccentric and inclined orbits. Their reconstructed orbital parameters can be used to infer Sgr A*'s mass and distance (Eisenhauer et al., 2005; Ghez et al., 2008; Gillessen et al., 2009; Boehle et al., 2016; GRAVITY Collaboration et al., 2019), test General Relativistic effects in the surroundings of a SMBH (Zucker et al., 2006; GRAVITY Collaboration et al., 2018b) and, also, study the mass distribution in the GC (Rubilar and Eckart, 2001; Mouawad et al., 2005).

The GRAVITY Collaboration has been monitoring stellar orbits in the GC in NIR wavelengths for more than 20 years (e.g., Eisenhauer et al. 2005; Gillessen et al. 2009; GRAVITY Collaboration et al. 2019), mainly with the SINFONI and NACO adaptive optics instruments at the ESO Very Large Telescope (VLT), and since 2016 with the GRAVITY instrument. Complete orbits of the S-star cluster members have already been observed. In Figure 1.4 we show an image of the S-star cluster from Gillessen et al. (2009) with dozens of identified members.

Among these stars, S2 is one of the brightest. It has a very short orbital period around Sgr A* of just ≈ 16 years and, hence, is a sensitive probe of the gravitational field in the GC. GRAVITY Collaboration et al. (2018b) reported results of ≈ 26 years of S2 observations. Figure 1.5, shows several detections of the star through the years. Near pericenter (at ≈ 1400 Schwarzschild radii from Sgr A*), the star has an orbital speed of ≈ 7650 km s⁻¹, such that special relativity effects were detected. The S2 data are inconsistent with pure

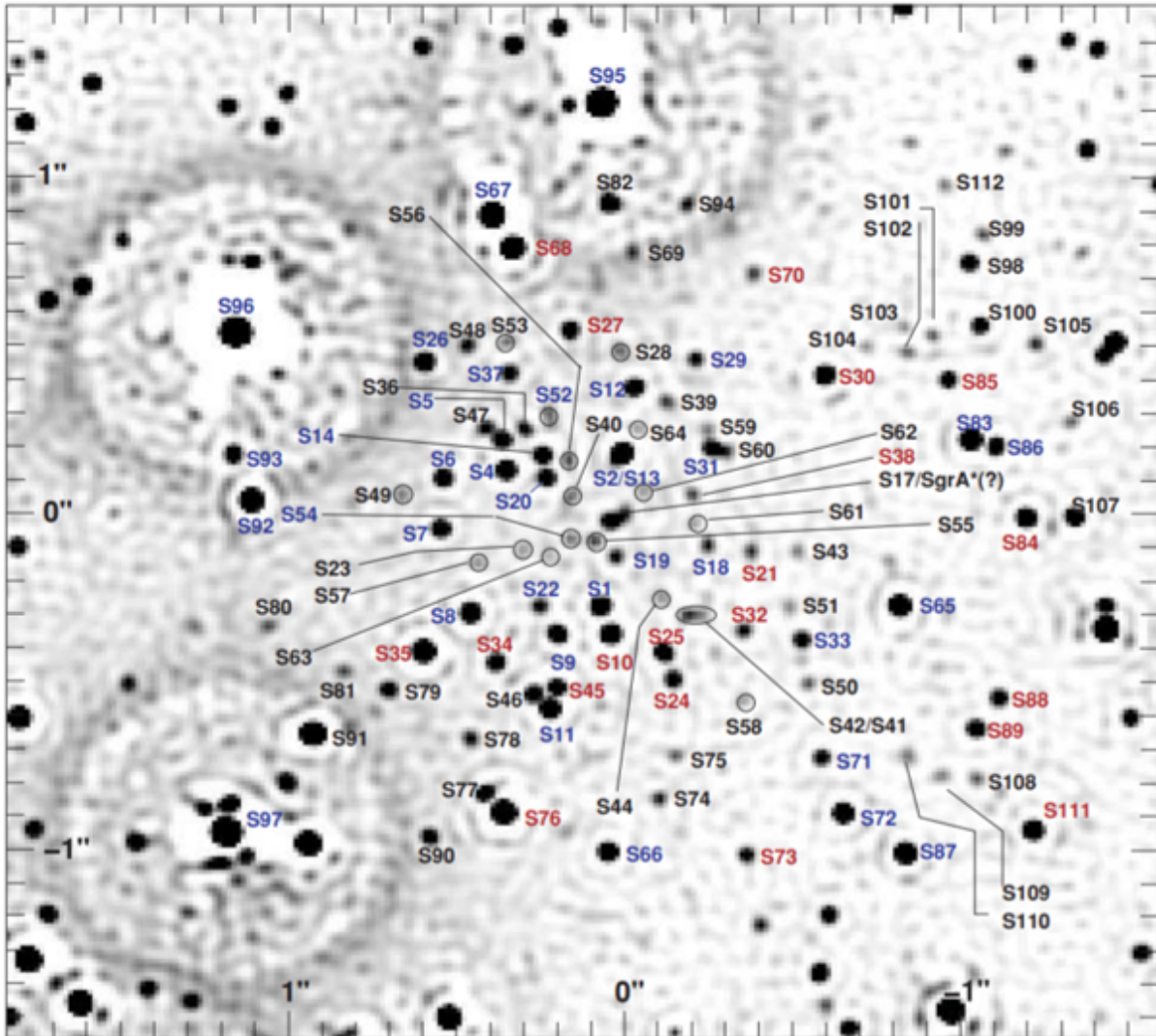


Figure 1.4: The S-star cluster. This figure is based on an image in the H band obtained using the NACO system mounted at the VLT array. Only stars that are unambiguously identified in several images have designated names, ranging from S1 to S112. Blue labels indicate early-type stars, red labels late-type stars. Stars with unknown spectral type are labeled in black. At the GC distance, this image is $\sim 0.14 \times 0.14$ pc. Source: Gillessen et al. (2009).

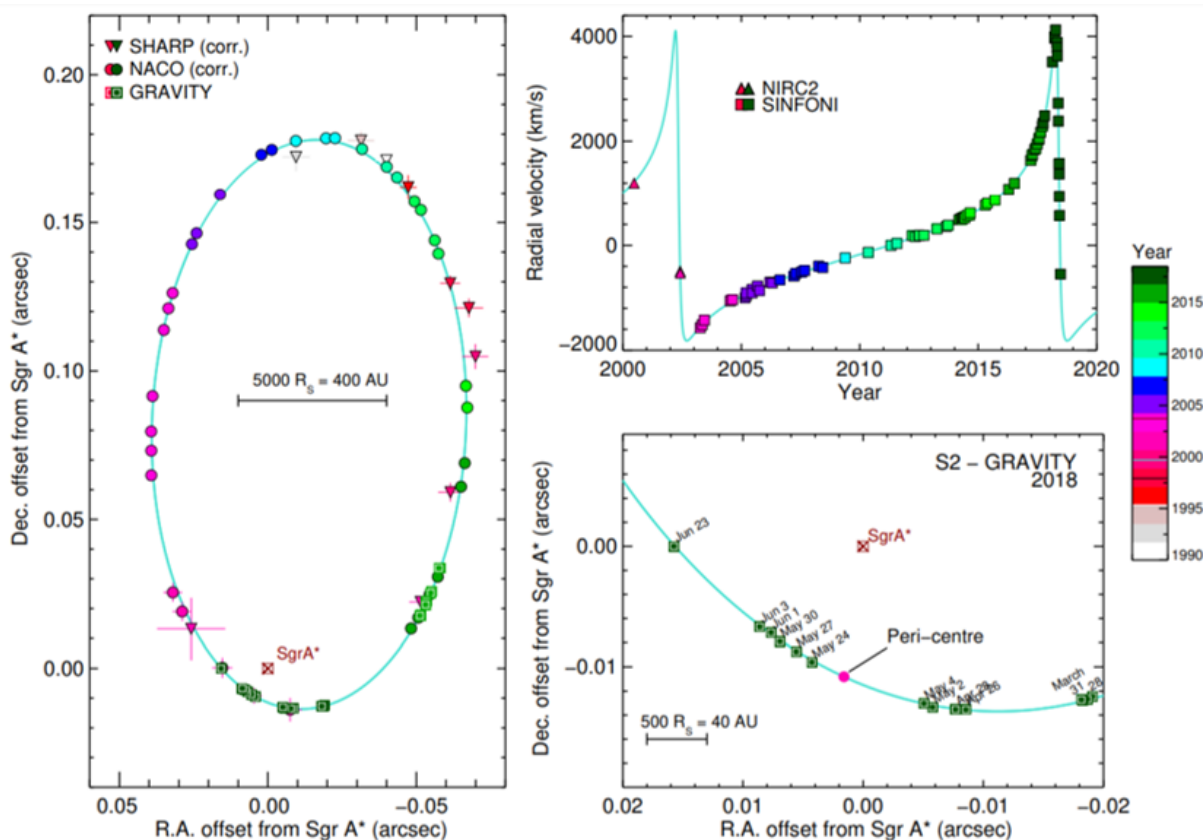


Figure 1.5: Summary of the observational results of monitoring the S2 orbit from 1992 to 2018. Left: projected orbit of the star S2 on the sky (J2000) relative to the position of the compact radio source Sgr A*. Triangles and circles denote the position measurements with different instruments, color-coded for time (color bar on the right side). The bottom right panel shows a zoom around pericenter in 2018. Top right: radial velocity of S2 as a function of time. The cyan curves show the best-fitting S2 orbit to all these data, including the effects of General Relativity. Source: GRAVITY Collaboration et al. (2018b).

Newtonian dynamics.

Recently, Peiβker et al. (2020) reported indications of a population of faint fast-moving stars even closer to Sgr A* than S2. They were detected with the SINFONI and NACO instruments in the NIR. One of these stars, S4714, has an orbital period of just ~ 12 years, an eccentricity of 0.985 and has an orbital speed of up to $\approx 24000 \text{ km s}^{-1}$ ($\approx 8\%$ of the light speed).

Gillessen et al. (2012) detected, with VLT's instruments NACO and SINFONI observations, a dense gas cloud, with approximately three times the mass of Earth, falling inside the sphere of gravitational influence of Sgr A*. The pericenter of this orbit was predicted to occur in the beginning of 2014 (Gillessen et al., 2013; Phifer et al., 2013). The GC community was eagerly expecting this close encounter, with hopes of observing a tidal disruption event in the heart of Our Galaxy and that G2's fragments could potentially

increase Sgr A*’s accretion rate (Schartmann et al., 2012; Saitoh et al., 2012) leading to bursts and outflows. Several observing campaigns were organized to witness this event. *Fermi*, for instance, changed its observing strategy during 2014 to increase its exposure of the GC¹. Unfortunately, Nature did not favor the GC enthusiasts: pericenter and post-pericenter observations showed that the G2 object, after a maximum approximation of ~ 1500 Schwarzschild radii from Sgr A*, escaped relatively unscathed. The scenario for the G2 object, thus, is more complicated than a simple gas cloud, although it was elongated by the encounter (Plewa et al., 2017).

The GRAVITY Collaboration has published several other interesting discoveries regarding the GC and Sgr A*. Among them the detection of orbital motions of “hot spots” in the accretion flow near the last stable circular orbit of Sgr A* (GRAVITY Collaboration et al., 2018a), which is the observation probing the closest distances to the event horizon. These “hot spots” move at about 30% the speed of light, exhibit continuous rotation of the polarization angle with about the same period as that of their motions and are consistent with a near face-on, circular orbit of a compact polarized “hot spot” of infrared synchrotron emission at about 6 to 10 gravitational radii of Sgr A*.

Even closer observations of Sgr A* are still anxiously anticipated. Results of the EHT observational campaign to reveal the image of the shadow of Sgr A* on the accretion flow were not revealed still, due to the much shorter dynamical timescales of Sgr A* (compared to M87*) which leads to higher flux variability and to the scattering effects caused by the interstellar medium (Event Horizon Telescope Collaboration et al., 2019).

1.3.2.1 Basic facts about Sgr A*

In this Section, we report useful data about Sgr A*. These are the values and definitions we use throughout this work, unless clearly stated:

- Mass: $M = (4.02 \pm 0.20) \times 10^6 M_{\odot}$ (Boehle et al., 2016).
- Distance: $d = 8.2$ kpc (GRAVITY Collaboration et al., 2019).
- Schwarzschild radius: $R_S \approx 1.2 \times 10^{12}$ cm = 1.2×10^7 km.

¹ fermi.gsfc.nasa.gov/ssc/observations/types/exposure/

- ISCO: the Innermost Stable Circular Orbit (ISCO) is defined as the smallest circular orbit in which a particle can stably orbit a black hole without falling through the event horizon. The ISCO defines the inner edge of the accretion disk around a black hole. For a non-rotating black, $R_{ISCO} = 3R_S$. For a black hole with Sgr A* mass, we have: $R_{ISCO} \approx 3.6 \times 10^{12} \text{ cm} = 3.6 \times 10^7 \text{ km}$ (it is smaller in the case of a rotating black hole).
- Bondi radius: defined as the radius where the gravitational energy owing to the black hole surpass some material's kinetic energy and, therefore, it is bound to the black hole, in a spherical accretion context. The Bondi radius, hence, gives an approximate idea of how far from the black hole an object (like stellar winds) is likely to be drawn in and accreted. For Sgr A*, the reported Bondi radius is: $R_B \sim 10^5 R_S$ (Genzel et al., 2010).
- Sphere of influence: the sphere of influence is a region around a SMBH in which the gravitational potential of the SMBH dominates that of the host galaxy. The radius of the sphere of influence is the Gravitational Influence Radius: $R_{inf} = \frac{GM_{BH}}{\sigma_*^2}$, where G is the Gravitational Constant, M_{BH} is the BH mass and σ_* is the the stellar velocity dispersion of the galaxy bulge. For Sgr A*: $R_{inf} \approx 2 - 3 \text{ pc}$ (Genzel et al., 2010; Eckart et al., 2017).
- Luminosity: assuming isotropical emission, $L_{bol} \sim 10^{36} \text{ erg s}^{-1}$ (from radio to X-rays, Genzel et al. 2010).
- Eddington luminosity: defined as the maximum luminosity a generic object can reach before the radiation pressure generated by the emitting material surpass the gravitational force towards the center of mass. The Eddington luminosity assumes spherical accretion, hence, is used only as an order of magnitude approximation in the case of BH. For a SMBH with Sgr A* mass: $L_{Edd} \sim 5 \times 10^{44} \text{ erg s}^{-1}$.
- Accretion rate: a characteristic of Radiatively Inefficient Accretion Flow models (used to explain Sgr A* accretion, see Section 1.3.4) is that the mass accretion rate varies with the distance to the SMBH. Genzel et al. (2010) collects several observational measurements of the accretion rate in Sgr A*. The innermost measurement (\lesssim

$10^2 R_S$) is: $10^{-9} \lesssim \dot{M} < 10^{-7} M_\odot/\text{yr}$. We included other values reported by Genzel et al. (2010) in Table 1.1.

- Eddington mass accretion rate: this value can be obtained by solving the relation $L_{Edd} = \eta_r \dot{M}_{Edd} c^2$, where η_r is the radiative efficiency of the accretion process. If we consider $\eta_r \sim 0.1$, we get: $\dot{M}_{Edd} \approx 9 \times 10^{-2} M_\odot$.

Table 1.1 - Overview of the accretion rate as a function of distance from the Galactic Center black hole.

Region	Radius	Mass accretion rate (M_\odot/yr)
Giant molecular clouds	Tens to few hundreds of parsec	10^{-2}
Circum nuclear disk	1.7–7 pc	$10^{-3} - 10^{-4}$
Central cavity, minispiral, and stellar cluster	<1.7 pc	$10^{-3} - 10^{-4}$
Stellar winds at Bondi radius	$0.05 \text{ pc} = 10^5 R_S$	A few 10^{-6}
Outer accretion zone	$10^2 - 10^3 R_S$	$< 10^{-6}$
Inner accretion zone	A few to $10^2 R_S$	A few $10^{-9} - 10^{-7}$

Source: Genzel et al. (2010)

1.3.3 Multiwavelength emission

The GC is the closest example of a galactic nucleus and hence has been the subject of observational scrutiny with hopes of understanding the environment close to the SMBH. The electromagnetic radiation from Sgr A* has been detected in several wavelengths (e.g., Genzel et al. 2010; Morris et al. 2012; Eckart et al. 2018), with the exceptions being the visible band and gamma-rays.

The obstacle to observe the GC in visible spectrum is the presence of considerable amount of dust and gas in the Galactic disk, which is in the line of sight. Seminal spectrophotometric studies show that the GC is shrouded by ~ 30 magnitudes in visible wavelengths as light travels through the interstellar medium (Becklin and Neugebauer, 1968; Becklin et al., 1978; Rieke and Lebofsky, 1985; Rieke et al., 1989).

The hindrance in observing gamma-rays is from a different nature. Gamma-ray emission has been detected coincident with the position of Sgr A*. But, given the large point-spread function (PSF) of astronomical gamma-rays detectors (as an example, in Section 1.5.3, especially Figure 1.14, we characterize *Fermi*-LAT's PSF), associating this emission to a single source is very challenging. The diffuse gamma-ray emission from the GC region was presented in Section 1.2.1 and the emission spatially coincident with Sgr A* is

comprehensively discussed in this thesis.

In this Section we discuss the observations of Sgr A* across the electromagnetic spectrum. First, we center on its potential gamma-ray emission (Section 1.3.3.1). Then, we focus on its different states (Section 1.3.3.2), its variability (Section 1.3.3.3), and finish showing evidences of past periods of activity (Section 1.3.3.4).

1.3.3.1 Sagittarius A* in gamma-rays

Gamma-ray emission (in the MeV to TeV energy range) coincident with the position of Sgr A* has been reported through the years. But no unique Sgr A* counterpart has been reported in the gamma-ray domain, given the low spatial resolution of gamma-ray telescopes. In the next paragraphs, we mention several astrophysical gamma-ray detectors. We refer the reader to Sections 1.5 and 1.4 for more technical details about *Fermi* and other gamma-ray instruments (EGRET, VERITAS, H.E.S.S. and MAGIC), respectively.

In this Section, we give a brief overview about these observations. Here, we are talking about emission potentially associated with the SMBH. In Section 1.2.1 we describe gamma-ray emission from the GC as a region, including diffuse emission and other likely point sources.

The bright EGRET source 3EG J1746-2851 is listed in the third EGRET catalog (Hartman et al., 1999) with an 95% confidence contour radius of $0^\circ.13$, is consistent with Sgr A*'s position and was considered as the gamma-ray counterpart to the GC region (Mayer-Hasselwander et al., 1998). However, an independent analysis of the EGRET data by Hooper and Dingus (2005) indicates a point source whose position is different from Sgr A* at a confidence level beyond 99.9%. Later, 3EG J1746-2851 was associated with Sgr A East, with the gamma-ray emission arising from the decay of neutral pions produced by high-energy protons, accelerated in the supernova remnant, interacting with the ambient matter (Fatuzzo and Melia, 2003).

Also, sub-TeV gamma-ray emission from the direction of the GC was detected with CANGAROO-II Imaging Atmospheric Cerenkov Telescope² (Tsuchiya et al., 2004). The centroid was consistent with Sgr A* position and compatible with a point source. Sgr A*

² The CANGAROO (Collaboration between Australia and Nippon for a Gamma-Ray Observatory in the Outback) Project operated a series of Imaging Air Cherenkov Technique gamma-ray telescopes from a previous generation (Mori, 2003).

was considered as a potential association for this emission.

Another gamma-ray detection from the GC suggesting an association with Sgr A* was performed with the Whipple 10-meter gamma-ray telescope, a predecessor of VERITAS. Kosack et al. (2004) report a possible detection of TeV gamma rays from the GC. The 95% confidence region has an angular extent of about $0.^\circ15$ and includes the position of Sgr A*. The detection is consistent with a point source and shows no evidence of variability.

Aharonian, F. et al. (2004) reported the detection of a point source of very high energy gamma-rays coincident within $1'$ with Sgr A*, obtained with H.E.S.S.. More recently, TeV emission observed by H.E.S.S. indicates the presence of PeV protons within the central 10 pc of the Galaxy (H.E.S.S. Collaboration et al., 2016). They propose that a more active phase of Sgr A* in the past could have accelerated this population of high-energy protons. H.E.S.S. Collaboration et al. (2018) reported the detection of an extended central component around Sgr A* that most likely originates from an enhancement of CRs in the inner tens of pc around the GC, thereby confirming the results presented in H.E.S.S. Collaboration et al. (2016).

Albert et al. (2006) confirmed, with MAGIC observations, the gamma-ray source at the GC. Ahnen, M. L. et al. (2017) present results of a monitoring campaign of the GC between 2012-2015. They identified a point-like gamma-ray excess whose location is spatially consistent with Sgr A* as well as SgrA East. Updated MAGIC observations of the GC also corroborates the previous observations (MAGIC Collaboration et al., 2020).

Following the H.E.S.S. Collaboration et al. 2016 TeV detections of the GC, several candidates have been proposed for this gamma-ray flux: Sgr A* itself, either from its immediate vicinity (Aharonian and Neronov, 2005a) or from a “plerion” produced by the SMBH winds (Atoyan and Dermer, 2004; Kusunose and Takahara, 2012); the interaction between the dense molecular clouds in the GC with cosmic rays accelerated by Sgr A* and/or by some other nearby source (Aharonian and Neronov, 2005b; Ballantyne et al., 2011; Chernyakova et al., 2011; Linden et al., 2012; Fatuzzo and Melia, 2012; Guo et al., 2013); the pulsar wind nebula (PWN) G359.95-0.04 (Wang et al., 2006; Hinton and Aharonian, 2007); the supernova remnant Sagittarius A East (Crocker et al., 2005) (but see Aharonian et al. 2009; Acero et al. 2010); self-annihilating dark matter particles accumulating at the GC (Hooper and Goodenough, 2011; Hooper and Linden, 2011) and an as-yet undetected pulsar (or population of pulsars) (Hooper and Linden, 2011).

Prominent gamma-ray emission from MeV to TeV energies coincident with Sgr A*’s position is observed by *Fermi*-LAT. Since the beginning of *Fermi*’s operations, a point source has been observed coinciding with the position of Sgr A*. This source was studied by Chernyakova et al. (2011) with 25 months of *Fermi* observations. They found no temporal variability at GeV energies and proposed a model in which the gamma-ray emission in the inner 10 pc of the Galaxy arises from relativistic proton interactions. Later, Malyshev et al. (2015) analyzed the same source using 74 months of data and the Second Catalogue of *Fermi* LAT Sources (Nolan et al., 2012). They also found no variability in the flux, and considered the observed spectrum as consistent with Inverse Compton (IC) scattering of high-energy electrons.

Ahnen, M. L. et al. (2017) collected several models for the MeV to TeV emission from Sgr A*. The list includes leptonic (Kusunose and Takahara, 2012), hadronic (Fatuzzo and Melia, 2012; Linden et al., 2012; Chernyakova et al., 2011) and hybrid (Guo et al., 2013) models. We call the models in this list “Fermi-era”, since they were all constructed taking into account *Fermi*-LAT’s data.

Despite all these observations, the nature of the gamma-ray emission from the direction of Sgr A* is still a matter of debate. Its spectrum and variability is so far unconstrained. And a solid association between this emission and Sgr A* is yet to be established.

1.3.3.2 The two states of Sagittarius A*

Most of the time, Sgr A* is in a steady state, emitting $\sim 10^{36}$ erg s⁻¹ (Genzel et al., 2010), between radio wavelengths and X-rays. This emission is dominated by the radio-to-sub-mm emission. On top of the steady emission, there is also a variable component in X-rays, near-infrared and also in longer wavelengths.

Given the surplus of gas reservoirs in the GC region, Sgr A* is remarkably under luminous. Its luminosity is more than 8 orders of magnitude smaller than L_{Edd} and ~ 4 orders of magnitude lower than the expected luminosity³ estimated based on the accretion rate at its Bondi radius (a few $\times 10^{-6} M_{\odot} yr^{-1}$, Baganoff et al. 2003; Xu et al. 2006). The luminosity of Sgr A* is dominated by accretion from stellar winds in its vicinity. In addition, larger accretion rates probably occur from time to time due to stochastic density

³ Calculated as $L_B = 0.1 \times \dot{M}_B c^2$, where \dot{M}_B is the Bondi accretion rate and assuming a 10% efficiency rate

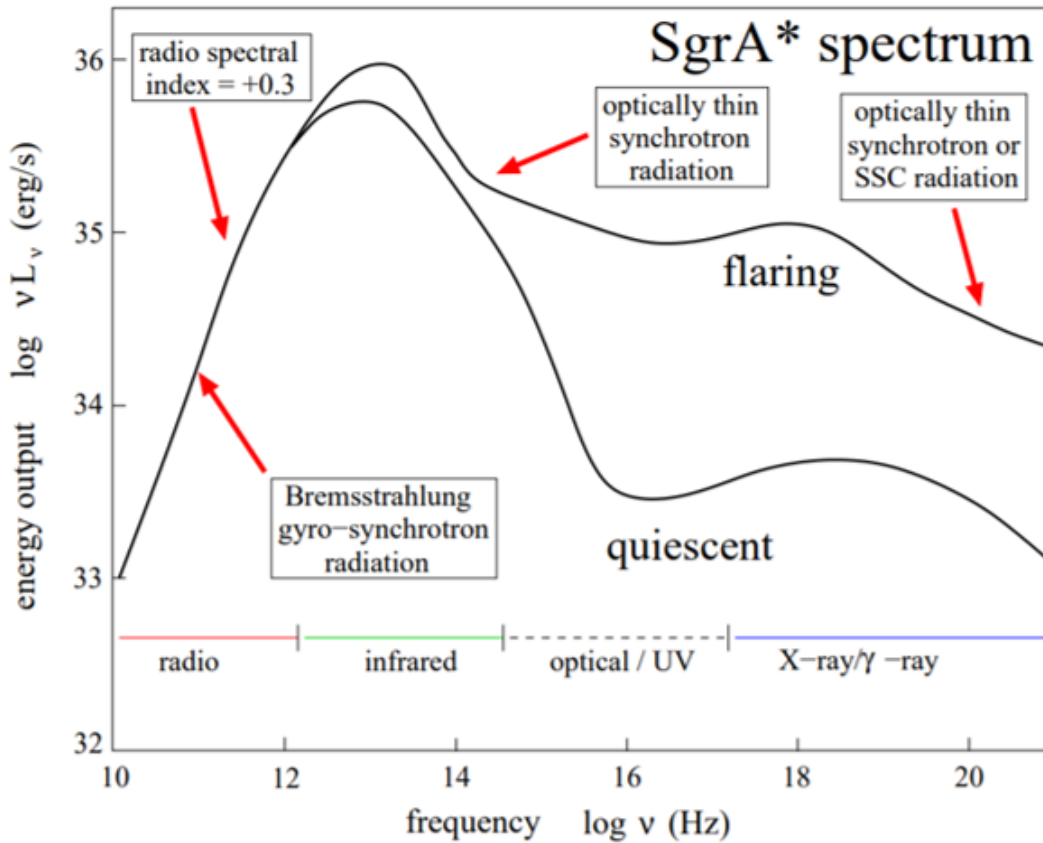


Figure 1.6: Sgr A* spectrum in quiescent and flaring states. Some of the prominent radiation mechanisms are highlighted. This plot was created based on models from Yuan et al. (2003); Narayan et al. (1998); Narayan and McClintock (2008) and using data from several works (radio from Falcke et al. 1998; Zhao et al. 2003; IR from Eckart et al. 2018 and references in there; and X-ray from Baganoff et al. 2001, 2003; Porquet et al. 2003, 2008; Neilsen et al. 2013). Source: Eckart et al. (2018); Yuan et al. (2003).

fluctuations in the accretion disk, or when large gas clouds with low angular momentum fall into the center.

Sgr A* has been detected in most of the electromagnetic spectrum (e.g., Dibi et al. 2014). In Figure 1.6 we show a sketch, created by Eckart et al. (2018) based on Yuan et al. (2003) work, of Sgr A*'s quiescent and flaring broad band spectrum. Some of the prominent radiation mechanisms are highlighted (see Section 1.3.4 for more details).

The compact radio source Sgr A*'s radio emission, discovered in the 1970s, is clearly detectable at all times and shows only moderate flux and spectral variations. The variable NIR source associated with the accretion flow around Sgr A* was unambiguously identified in the first years of this millennium (Genzel et al., 2003; Ghez et al., 2004). Twenty two years of NIR data collected from Sgr A* shows consistent brightness and variability during the whole period (Chen et al., 2019). This emission is consistent with synchrotron radiation

from a non-thermal electron population (Witzel et al., 2018). A steady and faint X-ray counterpart do Sgr A* was first reported by Baganoff et al. (2003). The quiescent emission level is likely to arise relatively far from the black hole, at the Bondi accretion radius. There, the accretion flow undergoes shocks and thermalizes, producing bremsstrahlung X-rays (Quataert et al., 2002; Xu et al., 2006).

1.3.3.3 Variability and flares

Sgr A* is highly variable in the infrared (Genzel et al., 2003; Ghez et al., 2004; Hornstein et al., 2007; Dodds-Eden et al., 2009; Witzel et al., 2012; Hora et al., 2014; Witzel et al., 2018; von Fellenberg et al., 2018; Fazio et al., 2018; Boyce et al., 2019) and X-rays (Baganoff et al., 2001; Nowak et al., 2012; Neilsen et al., 2013; Barrière et al., 2014; Neilsen et al., 2015; Ponti et al., 2015; Fazio et al., 2018; Boyce et al., 2019), which suggests a compact source. One can put an upper limit (UL) to the size of the region from which a flare originated by calculating the light crossing time since any disturbance that originated the flare must have spread through the source with speeds lower than light's. Variability has also been reported in longer wavelengths (Zhao et al., 2003; Miyazaki et al., 2004; Mauerhan et al., 2005; Macquart et al., 2006; Yusef-Zadeh et al., 2006; Marrone et al., 2008; Yusef-Zadeh et al., 2009; Plambeck et al., 2014; Brinkerink et al., 2015; Stone et al., 2016). The gamma-ray flux, though, does not seem to be variable (Chernyakova et al. 2011; Malyshev et al. 2015; Ahnen, M. L. et al. 2017 and Sections 3.3 and 4.2 of this thesis) and there is still no definitive association between this emission and Sgr A* (Section 1.3.3.1).

Typically, about one X-ray flare is generated per day with duration of a few tens of minutes Neilsen et al. (2013). The brightest observed X-rays flares are ~ 100 times above the quiescent level (e.g., Nowak et al. 2012). The NIR flares are even more frequent. X-ray flares usually follow, after a few tens of minutes, the NIR ones, but there are multiple NIR flares without X-rays counterparts (e.g., Eckart et al. 2006; Yusef-Zadeh et al. 2012; Ponti et al. 2017; but see Fazio et al. 2018). Flares are also observed in millimeter and sub-mm wavelengths (e.g., Yusef-Zadeh et al. 2006; Stone et al. 2016). They last from hours to days with amplitudes of $\sim 25\%$ of the quiescent level (Yusef-Zadeh et al., 2008; Fazio et al., 2018).

Flaring emission is an indicative that some accretion, heating, or magnetic reconnection mechanism has given rise to enhanced emission from the vicinity of the SMBH. They

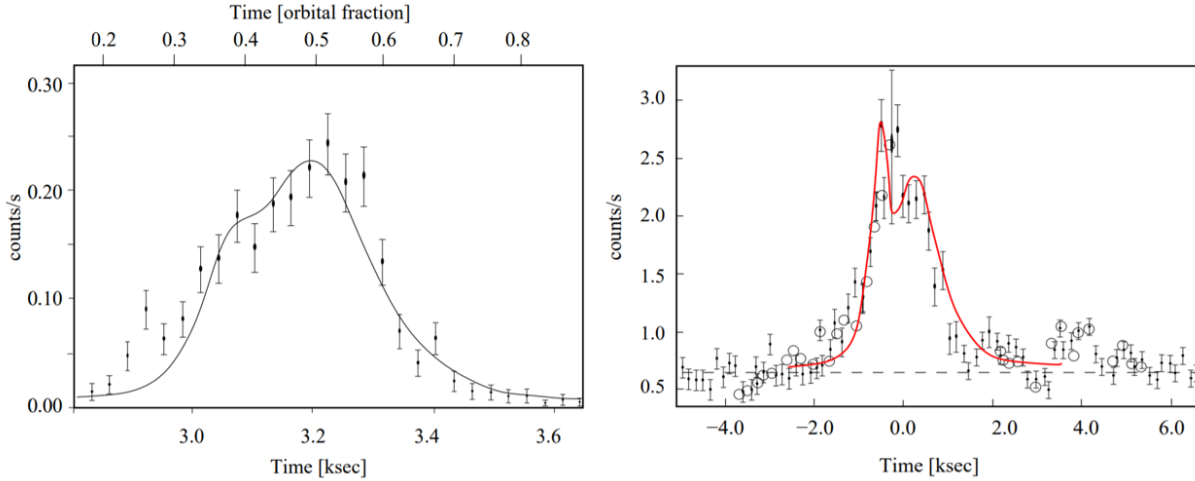


Figure 1.7: Fit of the hotspot model of Karssen et al. (2017) to two bright X-ray flares. Left: flare published by Nowak et al. (2012). Right: flare reported by Ponti et al. (2017). In these plots, the “shoulder” is due to gravitational lensing when the hotspot is behind the black hole. The peak is due to boosting when the hotspot approaches the observer after passing around the black hole. OBS: the horizontal axis in the left panel is incorrect. The scale should be of 10^4 s, as in Figure 1 of Nowak et al. (2012). Source: Eckart et al. (2018).

are, consequently, subject to relativistic effects. Based on General Relativistic Magnetohydrodynamics (GRMHD) simulations, short term variability is often explained by hotspot emission from the accretion disk which can be produced, for example, by magnetic reconnection (Meyer, L. et al., 2006a,b; Eckart et al., 2006; Broderick and Loeb, 2005, 2006; Ball et al., 2016). Close to the SMBH, the interplay of relativistic effects may influence the appearance of flare emission (Doppler boosting, gravitational redshift, light focusing, and light-travel time delays, e.g. Broderick and Loeb 2005, 2006; Eckart et al. 2006). In some bright X-ray flares these characteristic shapes may be visible (Nowak et al., 2012; Karssen et al., 2017; Ponti et al., 2017).

Figure 1.7, obtained from Eckart et al. (2018), shows the data of two bright X-ray flares fitted with a hotspot flare model from Karssen et al. (2017). In these plots, the “shoulder” is due to gravitational lensing when the hotspot is behind the black hole. The peak is due to boosting when the hotspot approaches the observer after passing around the black hole. Since bright X-ray flares are often seen (almost) synchronous with bright NIR-flares, this model is probably also applicable for NIR-flares. Also, the Karssen et al. (2017) model indicates that, at least for the bright x-ray flares, the flare duration is coupled to the dynamical time scale of the hotspot (see the top horizontal axis on the left panel of Figure 1.7).

The NIR variability can be modeled as a purely random process (Meyer et al., 2008; Do et al., 2009; Dodds-Eden et al., 2011; Witzel et al., 2012). Polarimetric observations indicate that the NIR emissions are consistent with a hotspot model (Eckart et al., 2006; Meyer, L. et al., 2006a,b, 2007; Trippe et al., 2007; Zamaninasab, M. et al., 2010).

Numerous X-ray flares have been observed since the discovery of the GC X-ray source (e.g., Baganoff et al. 2001; Porquet et al. 2003, 2008; Nowak et al. 2012; Zhang et al. 2017; Ponti et al. 2017; Boyce et al. 2019; Haggard et al. 2019). Their variability time scales, including temporal structure during the flares (see Figure 1.7), indicate that they are generated much closer to the SMBH than the quiescent emission, probably within a few tens of Schwarzschild radii. They typically last for ~ 30 min and their peak fluxes range between a few and tens of times the quiescent flux. The rate of detectable flares is of about once per day. But, this may be limited by sensitivity: weaker flares possibly go undetected and contribute to the mean detected quiescent flux.

Most studies have focused on variability in the X-ray and IR, where variations are often simultaneous, and because long time series at sub-mm and radio wavelengths are limited. Nevertheless, Sgr A*'s radio variability has been studied for several decades. They indicate that the flares time scales vary from hours to days (Bower et al., 2002; Zhao et al., 2003; Herrnstein et al., 2004; Miyazaki et al., 2004). Mauerhan et al. (2005) performed observations at a wavelength of 3 mm and characterized the variability as a red noise process with amplitudes up to 40%. Marrone et al. (2006) reported strong variability of both total intensity and polarization fraction on a time scale of hours at 880 μm .

Comparing Sgr A*'s light curves in different wavelengths can generate clues to the nature of the emission processes. Yusef-Zadeh et al. (2006) observed two frequencies simultaneously: 22 and 43 GHz. Their light curve shows show a delay of 20 to 40 min of the 22 GHz light curve, relative to 43 GHz one. They explained this with an expanding plasma model in which the plasma cools and becomes optically thin as it expands, and thus reaches an emission maximum, at progressively lower frequencies with time. Yusef-Zadeh et al. (2008) observed Sgr A* in the same frequencies and also in sub-mm and X-ray wavelengths. The X-ray flare precede the sub-mm flare by about 90 min, as the expanding plasma model would qualitatively predict, and again that the 22 GHz emission was lagging the 43 GHz emission.

There are a plethora of observations claiming delays of a few hours between NIR flares

and subsequent, associated, mm/sub-mm peaks: Eckart et al. (2006, 2008, 2009); Yusef-Zadeh et al. (2006, 2008, 2009); Meyer et al. (2008); Morris et al. (2012) (but see Fazio et al. 2018). Collectively, the delays are ~ 150 min, consistent with an expanding relativistic plasma blob model if the expansion occurs at $\sim 0.1c$ (Marrone et al., 2008; Yusef-Zadeh et al., 2009).

The expanding plasma model would predict that X-ray and near-IR emission peaks should occur simultaneously, since they are both optically thin throughout the expansion. There are observations that seem to favor this relation. It appears that every X-ray flare corresponds reasonably well in time with a well-defined and relatively bright maximum in the infrared light curve (Eckart et al., 2004, 2012; Ghez et al., 2004; Marrone et al., 2008; Dodds-Eden et al., 2009; Trap et al., 2011). The reverse is not true: only a fraction of the IR maxima correspond with an X-ray flare. Yusef-Zadeh et al. (2012) reanalyzed a body of existing data and reported of a significant time lag between the infrared maxima and the X-ray flares of a few to tens of minutes. These results are more compatible with a model in which the NIR events occur in the inner regions of the accretion flow while the X-ray flares are the result of IC scattering of the NIR photons by thermal electrons in the accretion flow, possibly at a greater radius, which causes the delay (Yusef-Zadeh et al., 2009; Wardle, 2011). Combining the mechanisms responsible to Sgr A* flares in different wavelengths is challenging and maybe distinct process are taking place.

Using the Keck telescope, Do et al. (2019) observed a flare from Sgr A* with unparalleled NIR flux, exceeding the historical peak value by a factor of two. Subsequently, the light curve exhibited a drop in the measured flux of a factor of 75 in a period of two hours. The authors suggested that the flare was a consequence of an increase in the SMBH mass accretion rate, possibly resulting from the deposition of additional gas coming from a “windy” star (e.g., S2) or the passage of the G2 object in 2014. It was argued by Ressler et al. (2018), however, that S2 should have a negligible effect on the Radiatively Inefficient Accretion Flow (see Section 1.3.4) structure. Moreover, there are no other stars from the S-star cluster that are both close to Sgr A* and more massive than S2. Thus, the framework of a “windy” star is likely flawed. In Gutiérrez et al. (2020), in which the PhD candidate is a coauthor, a completely different scenario is proposed—independent of an increase in the mass accretion rate. Analogously to a nonthermal bomb, we suggest that the flare was the result of particle acceleration to nonthermal energies, leading to an explosive event in

the innermost parts of the accretion flow. The NIR light curve is quantitatively explained by the proposed model, and testable predictions are also suggested at other wavelengths.

For the last few hundred of years, Sgr A* is in a state of very low activity, a consequence of its current extremely low accretion rate. But there are hints showing that Sgr A* was much more active in the past, as we discuss in the following Section.

1.3.3.4 Hints of past activity of Sagittarius A* emission

Although Sgr A* exhibits daily flares, it is in a very quiet phase (Section 1.3.3.2). But there is tantalizing evidence for an enhanced level of activity in the recent past of Sgr A*. Using 1.66 year of *Fermi*-LAT data Su et al. (2010) detected two large gamma-ray bubbles, extending 50° above and below the Galactic plane, with a width of about 40° in longitude (Figure 1.8). The *Fermi* Bubbles should have formed 1–3 Myr ago during a large episode of energy injection in the GC that lasted 0.1–0.5 Myr (Yang et al., 2018). The origin of the bubbles is still debated and could be due to a previous nuclear starburst or some past accretion event of the SMBH. Herold and Malyshev (2019) studied the base of the *Fermi* Bubbles with 9 years of *Fermi*-LAT observations. They reported that it is shifted to the west (negative longitudes) from the GC. If the emission at the base of the Bubbles is indeed connected to the high-latitude Bubbles, then this shift disfavors models in which they are created by Sgr A*.

Further evidence for higher levels of activity in Sgr A* comes from X-ray observations of circumnuclear clouds (Ponti et al., 2010). Concretely, X-ray observations since the 1990s show rapid variations in the 6.4 keV of Fe $K\alpha$ line propagating through molecular clouds in the inner Galactic regions. These variations are likely the result of a highly variable active phase of Sgr A* within the past few hundred years, which are echoing through the clouds. Models indicate at least two luminous outbursts (~ 100 and 400 years ago) on few-year timescales during which the luminosity of Sgr A* went up to at least 10^{39} erg s^{-1} (Ponti et al., 2010; Clavel et al., 2013). In summary, it seems that Sgr A* was 10^3 times more active within the past few centuries compared to current levels. Considering the estimated energy of these events, Sgr A* is a very promising candidate for their origin.

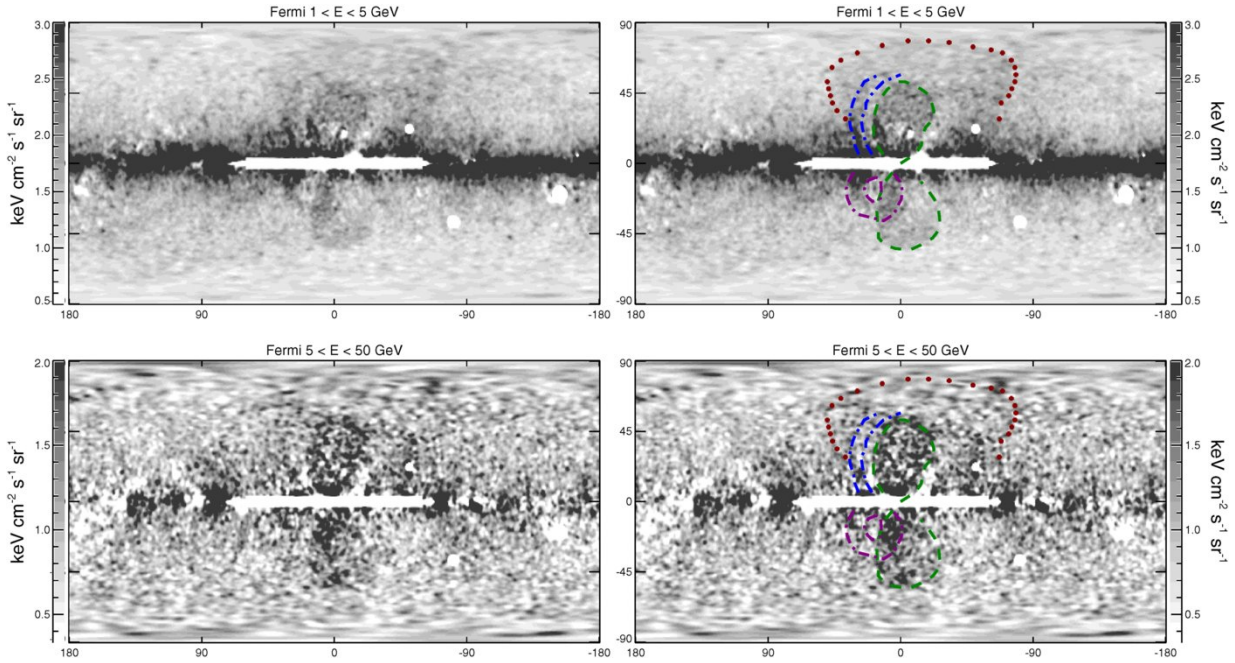


Figure 1.8: Full sky residual maps after subtracting dust and disk templates from the *Fermi*-LAT maps in two energy bins. Point sources are subtracted, and large sources, including the inner disk, have been masked. Two large bubbles are seen in both cases. Right panels: Apparent *Fermi* Bubbles features marked in color lines, overlotted on the maps displayed in the left panels. Source: Su et al. (2010).

1.3.4 Models for Sagittarius A* emission

As mentioned in Section 1.3.3.2, if gas was accreting into Sgr A* via optically thick, geometrically thin accretion disk—a model successfully used to explain accreting sources, like blazars (Koratkar and Blaes, 1999)—, its expected luminosity (based on the accreting rate at the Bondi radius) would be ~ 4 orders of magnitude higher than the observed value. This indicates that an optically thick, geometrically thin accretion disk is not compatible with Sgr A* behavior. Another argument is the lack of any any disk-like blackbody emission component in the spectrum of the SMBH (Narayan, 2002). The observational data of the quiescent state of Sgr A* (from radio to X-rays) favor models in which very little of the gravitational potential energy of the inflowing gas is radiated away: the Radiatively Inefficient Accretion Flow (RIAF). These kind of models have been the most successful in fitting Sgr A*'s spectrum.

The RIAF model describes the dynamics of rotating accretion flows in which much of the gravitational potential energy of the accreting material is not radiated away (e.g., Narayan et al. 1995; Yuan et al. 2003, 2004; Yuan and Narayan 2014) but is, instead, stored as thermal energy. For this reason, the temperatures in the accreting gas are very high.

The electron temperature depends on the processes responsible for heating them (shocks, turbulence, magnetic reconnection) and, thus, are difficult to be precisely estimated. Since collisions are unimportant in the GC environment (at such high temperatures and low gas densities, the Coulomb collision time is much longer than the gas accreting time) the electron distribution function is not expected to be thermal.

Numerical simulation of RIAFs (e.g., Stone et al. 1999; Igumenshchev and Abramowicz 1999, 2000; Igumenshchev et al. 2000; Hawley and Balbus 2002; Igumenshchev et al. 2003; Sądowski et al. 2013; Almeida and Nemmen 2020) have shown that $\dot{M} \ll \dot{M}_B$ (where \dot{M} is the actual accretion rate in the SBMH), which means that a very small fraction of the mass available at large radii is effectively accreted. The implication is that in the RIAF models, rather than just a low efficiency, a low accretion rate is also contributing to the SMBH faintness.

To allow for accretion in a RIAF context, there must be non-radiative energy loss of some kind. One way the binding energy of the accreting matter can be carried away is in the form of an outflow (‘winds’) (Quataert, 2003).

See Table 1.1 for an overview of the accretion rate towards several different radii from Sgr A*.

The relative faintness of Sgr A* has been explained through RIAF models (e.g., Narayan et al. 1995; Yuan et al. 2003, 2004). The broadband spectrum is dominated by the radio-to-sub-mm emission which is understood as synchrotron radiation from a thermal population of electrons, with temperatures between ~ 5 –20 MeV, as well as a small fraction (a few percent) of nonthermal electrons (Yuan et al., 2003). The observed polarization in the sub-mm domain argues for a low accretion rate in the inner few parsecs of $\dot{M} < 10^{-7} M_{\odot}/yr$ (Mezger and Wink, 1986; Morris and Serabyn, 1996; Marrone et al., 2006).

The Sgr A*’s X-ray emission has been separated into two components (Baganoff et al., 2001, 2003): a nearly constant component and a flaring one. The quiescent component is extended, with size of $\approx 10^5 R_S$ (the Bondi accretion radius), and is explained by thermal bremsstrahlung originating from shocks in the transition region between the ambient medium and the accretion flow (composed by material from stellar winds) (Quataert et al., 2002; Xu et al., 2006).

The flaring component is not extended and, given the duration and shape of the flares, is compatible with emission arising from the close vicinity of Sgr A*. There is evidence

that the X-ray flare emission is due to synchrotron processes (Dodds-Eden et al., 2009; Barrière et al., 2014; Ponti et al., 2017) although they have also been interpreted as IC upscattered photons by the mildly relativistic, nonthermal electrons (Yusef-Zadeh et al., 2009; Ball et al., 2016). The NIR component is associated with the accretion flow around Sgr A* (Genzel et al., 2003; Ghez et al., 2004; Chen et al., 2019) and its variable component is compatible, as is the case for the X-ray variability, with hotspot model.

1.4 Other gamma-ray telescopes

Since Earth's atmosphere is opaque to gamma-ray, astronomers have developed two kinds of instruments to make astrophysical gamma-rays observations attainable: space-based (from which *Fermi*LAT is an example) and Cherenkov telescopes. Both approaches are complementary. Astrophysical gamma-rays energy spans from ~ 100 keV to ~ 100 TeV, which comprehends 9 decades in energy, with flux rapidly decreasing towards high energies. It is necessary, thus, to have instruments with larger effective areas to detect significant flux in higher energies. Unfortunately, the cost to send instruments to space limits the size (and hence, the effective area) of gamma-ray space telescopes making them appropriate to operate only up to the ~ 100 GeV energy range, as is the case of *Fermi*-LAT. The larger effective areas necessary to operate above these energies are only attainable by ground-based instruments. They take advantage of the electromagnetic air showers formed when gamma-rays enter the atmosphere. They are the result of a cascade of secondary particles formed when a gamma-ray converts into pairs of e^- and e^+ at high altitude. These particles radiate secondary gamma-rays mostly through bremsstrahlung, which further convert into $e^- e^+$ pairs with lower energies. These particles can be detected when they reach the ground or through the Cherenkov radiation they emit. Showers formed by gamma-rays with energies $\gtrsim 30$ GeV start to become detectable.

In Figure 1.9 we reproduce the Figure 3 from de Angelis and Mallamaci (2018) in which they show the point source continuum differential sensitivity of different gamma-ray (and X-ray) instruments for a source at high Galactic latitude. It is clear how the space-based and ground-based approaches are complementary. The ground-based telescopes operate in higher energies. They are, thus, concentrated in the right hand side of the plot (i.e.,

HESS/VERITAS, HAWC, MAGIC and the upcoming CTA South). The space-based ones are in the the ~ 1 to $\sim 10^5$ MeV energy range (i.e., Fermi-LAT, EGRET, COMPTEL and the concept e-ASTROGAM). In this Section, we describe both of these techniques.

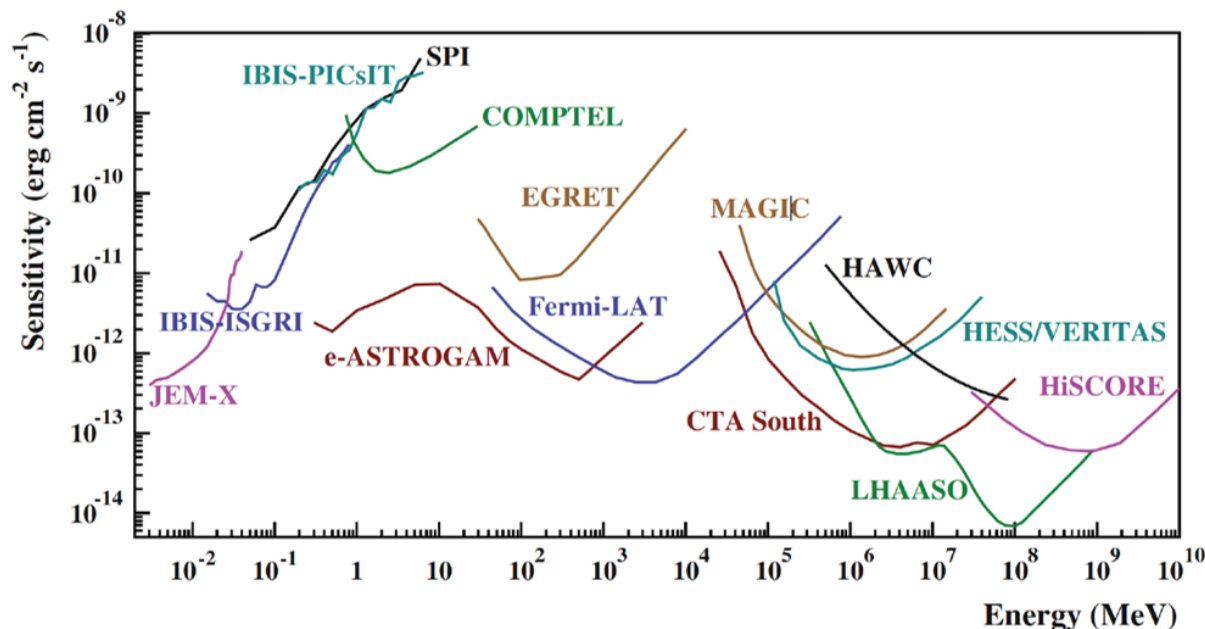


Figure 1.9: Point source continuum differential sensitivity of different X-ray and gamma-ray instruments for a source at high Galactic latitude. Source: de Angelis and Mallamaci (2018). We refer to their work for a discussion on how the the sensitivities were estimated.

1.4.1 Space-based instruments

The energy range of space-based gamma-ray telescopes vary between ~ 300 keV⁴ and ~ 500 GeV. The upper boundary is limited by flux because of the small effective area and the scarcity of high energy gamma-ray photons.

The angular resolution of these telescopes is limited by multiple scattering, which increases with the mass of the converter. At the same time, the detector efficiency is a function of mass (denser materials correspond to higher probability of interaction). So, there is a compromise between increasing the effective area and degrading the angular resolution.

The history of gamma-rays space telescopes is plentiful of examples:

- The first generation of such instruments were launched between the end of the 1960s and the beginning of the 1970s: The Third Orbiting Solar Observatory⁵ (OSO-3) in

⁴ Not considering the Gamma-ray Burst Monitor instrument on board of *Fermi*, which is sensitive to photons with energies between ~ 8 keV and ~ 40 MeV (Section 1.5)

⁵ heasarc.gsfc.nasa.gov/docs/heasarc/missions/oso3.html

1967; the second NASA Small Astronomy Satellite⁶ (SAS-2) in 1972; and the COS-B in 1975 (Swanenburg et al., 1981).

- The Compton Gamma-ray Observatory⁷ (CGRO) operated from 1991 until 2000. It was comprised of four instruments: the Burst And Transient Source Experiment (BATSE), the Oriented Scintillation Spectrometer Experiment (OSSE), the Imaging Compton Telescope (COMPTEL), and the Energetic Gamma Ray Experiment Telescope (EGRET).
- The INTErnational Gamma-Ray Astrophysics Laboratory⁸ (INTEGRAL, launched in 2002) and The Neil Gehrels Swift Observatory⁹ (launched in 2004) are monitoring the sky in lower energies (going from 100 keV to a few MeV).
- The Astro-rivelatore Gamma a Immagini LEggero¹⁰ (AGILE) was launched in 2007 and is still in operation.
- *Fermi* Gamma-ray Space Telescope initiated a new era for space-based observations in 2008. This instrument is described in further details in Section 1.5.
- The DArk Matter Particle Explore¹¹ (DAMPE) was launched in 2015. It is an instrument of the Chinese Academy of Sciences and searches for Dark Matter signatures.

Proposed MeV-GeV missions e-ASTROGAM (de Angelis et al., 2018) and AMEGO (McEnery et al., 2019) can dramatically improve the observational sensitivity in this energy band.

1.4.2 Ground-based Cherenkov telescopes

The ground-based gamma-ray telescopes come in two flavors, depending on how they detect the electromagnetic cascade originated by the interaction of the gamma-rays with the atmosphere.

⁶ heasarc.gsfc.nasa.gov/docs/sas2/sas2.html

⁷ heasarc.gsfc.nasa.gov/docs/cgro/

⁸ cosmos.esa.int/web/integral

⁹ swift.gsfc.nasa.gov

¹⁰ agile.rm.iasf.cnr.it/

¹¹ dpnc.unige.ch/dampe/

Instead of using instruments to convert the gamma-ray, they use the atmosphere, greatly increasing the effective area. This allows the detection of very high energy photons—in the GeV and TeV range. At the same time, electromagnetic showers originated by lower energy photons are not detectable, which constrains the operation of these instruments.

1.4.2.1 The Imaging Air Cherenkov Technique

The Imaging Air Cherenkov Technique (IACT) detects the Cherenkov radiation from the charged particles of the electromagnetic shower in the atmosphere. Since most of them have a speed larger than light in air, they emit Cherenkov radiation that can be detected by special telescopes on the ground. These instruments have effective area sizes comparable to that of the light pool on ground (i.e. $\sim 10^4$ m²).

By observing the air shower with several different detectors spread on the ground, it is possible to reconstruct (with the aid of computational models) the direction and energy of the original gamma-ray. The intensity and area of the image provide an estimate of the energy, while the image orientation is related to the direction. Also, the shape of the image is characteristic of the nature of the events originating them and is used to identify and reject the background from charged particles.

These instruments are installed at high altitudes to facilitate detections. For instance, from a primary photon of 100 GeV, about 10 Cherenkov photons per square meter will arrive at the ground in a mountain at 2000m above sea level (de Angelis and Mallamaci, 2018). A collection area of 100 m² is therefore sufficient to detect gamma-ray showers. Also, clear and dark nights are necessary for observations since the Cherenkov light is faint.

Among the IACTs, three deserve mention. The Very Energetic Radiation Imaging Telescope Array System¹² (VERITAS) operates since 2007 in Arizona at the Whipple Observatory. Its observational energy range is between ~ 100 GeV and ~ 30 TeV. The Major Atmospheric Gamma-ray Imaging Cherenkov Telescopes¹³ (MAGIC) operates since 2004 at the Canary Island of La Palma. The High Energy Stereoscopic System¹⁴ (H.E.S.S.) started functioning in 2004, in Namibia. Both MAGIC and H.E.S.S. can detect photons with

¹² veritas.sao.arizona.edu/

¹³ magic.mpp.mpg.de/

¹⁴ mpi-hd.mpg.de/hfm/HESS/

energies as low as 30 GeV.

The Cherenkov Telescope Array (CTA, Cherenkov Telescope Array Consortium et al. 2019) is planned to start operating in the next few years. It will consist of two IACTs arrays: one in the Southern Hemisphere, in the Atacama Desert in Chile, focused on galactic sources, including a Key Science Project concentrated in the GC; and another in the Northern Hemisphere, on the Spain's Canary Islands, with emphasis on the study of extragalactic objects. CTA will be the most important instrument to study high-energy gamma-rays in the next decade. For instance, it will allow a deep exposure of the GC in energies up to ~ 300 TeV, thereby enabling studies in spatial and spectral details which are not possible today, with arc-minute resolution at energies above *Fermi*'s operational range.

1.4.2.2 *The Extensive Air Showers Technique*

The Extensive Air Showers (EAS) observatories detect the secondary particles formed in the air showers originated by the interaction of a gamma-ray photon with the atmosphere. The shower geometry is reconstructed based on the arrival times, distribution and density of the secondary particles. Showers originated from the interaction of CR with the atmosphere can be rejected based on their geometry and muon content

The most prominent EAS is the High Altitude Water Cherenkov¹⁵ (HAWC) that is in operation at 4100 m above sea level in Mexico. It consists of 300 water-Cherenkov detectors. The secondary particles in the air showers emit Cherenkov radiation when traveling through the water in the detectors. This emission is used to reconstruct the direction and energy of the gamma-ray.

1.5 *Fermi Gamma-ray Space Telescope*

Earth's atmosphere is opaque to gamma-rays (Figure 1.10). One way to deal with this limitation is to detect them from space. Different approaches and instruments are described in Section 1.4.

The way gamma-rays interact with matter—through Compton scattering, $e^- e^+$ pair

¹⁵ hawc-observatory.org/

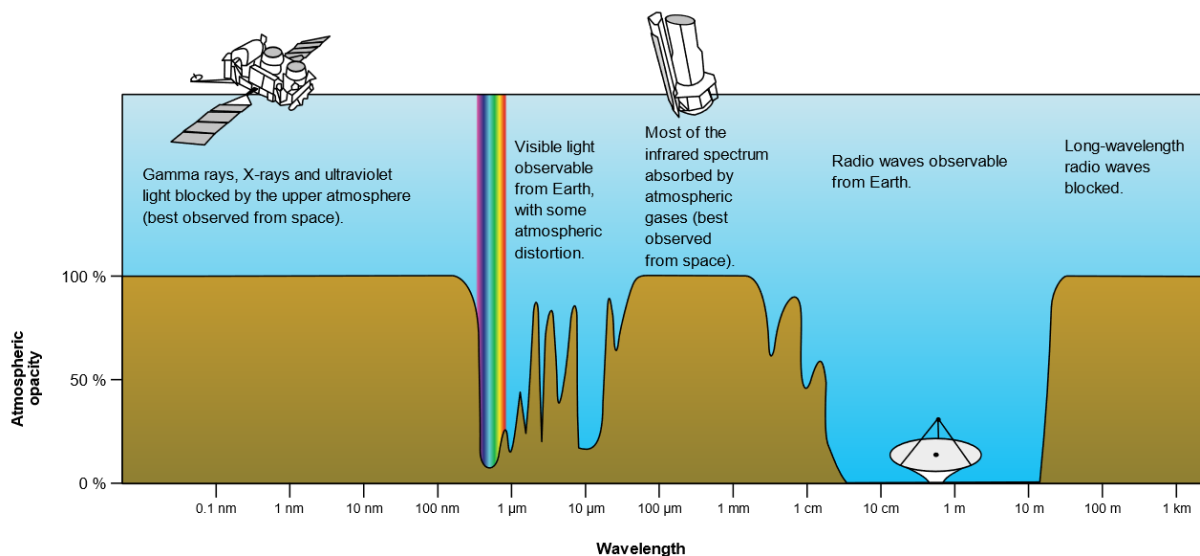


Figure 1.10: A diagram showing Earth's atmospheric opacity as a function of wavelength of the electromagnetic spectrum. Source: NASA (original); vectorized by Mysid / Public domain.

production and photoelectric effect—prevents the use of reflection or refraction to focus them. For this reason, a gamma-ray telescope uses techniques from particle accelerators to detect the byproducts of the photon interaction.

In June 11th, 2008, Fermi Gamma-ray Space Telescope (*Fermi*, Atwood et al. 2009) was launched to an orbit of ≈ 535 km above sea level. *Fermi* carries two instruments: the Gamma-ray Burst Monitor (GBM) and the Large Area Telescope (LAT, more details in Section 1.5.1). In Figure 1.11 we show a reproduction of the telescope and its instruments.

The GBM was designed to detect sudden flares of gamma-rays produced by gamma ray bursts. It observes the whole sky (that is not obstructed by Earth). It is sensitive to X-rays and gamma rays with energies between ~ 8 keV and ~ 40 MeV. After a trigger, GBM calculates preliminary position and spectral information that is transmitted to the ground. A GBM detection can also lead to an autonomous repointing of *Fermi* to expose the region to *Fermi*-LAT and proceed with more-detailed data collection. Other observatories can also use GBM's alerts to make opportunistic data collection.

In its regular operation (*survey mode*) both instruments on board *Fermi* observe the whole sky every ≈ 3 hours (equivalent to 2 complete orbits, each one with the telescope's zenith facing opposite hemispheres). This allows for two complementary approaches to gamma-ray astronomy:

- Continuous exposure of the gamma-ray sky, allowing for deeper and sharper images,



Figure 1.11: An illustration of *Fermi* in orbit. The cube on the top of the telescope is *Fermi-LAT*. The GBM is composed of the yellow instruments at the bottom. Source: NASA (original from: fermi.gsfc.nasa.gov); adapted for this thesis.

but eventually limited by the instruments resolution, even of faint sources;

- Time domain gamma-ray astronomy, enabling variability investigations into time scales going from milliseconds to years.

According to criteria defined by the *Fermi*-LAT Collaboration, *Fermi* can also operate in pointed mode observation, when the zenith of the telescope is altered to emphasis observations of selected sources or regions. This happened, for instance, during the whole 2014 year (from December 5th 2013 to December 3rd 2014) to accompany the approximation of the G2 object to Sgr A* (Section 1.3.2).

With more than 12 years of data collection, *Fermi* has been instrumental in a series of momentous discoveries. Here we describe only three (two that were considered the most important on the occasion of *Fermi*'s 10th anniversary celebration¹⁶, and one that occurred more recently):

- Fermi Bubbles: they were discussed in Section 1.3.3.4.

¹⁶ fermi.gsfc.nasa.gov/fermi10/brackets/

- Multi-messenger observations from a binary neutron star merger: up until October 16th 2017, the five published astrophysical Gravitational Waves (GW) detection by the LIGO and VIRGO Collaborations were of merging BHs, which are not expected to produce a detectable electromagnetic signal. In August 17th 2017, occurred the first GW observation which has been confirmed by non-gravitational means (Abbott et al., 2017a). *Fermi* played an important role in this detection. As the neutron stars collide, some of the debris blasts away in particle jets moving at nearly the speed of light, producing a brief burst of gamma-rays. They were also detected by GBM and INTEGRAL which helped to constrain the location of the merger and started an intense observing campaign to search for the expected emission at longer wavelengths. The aftermath of this merger was also seen by many dozens of observatories, across the electromagnetic spectrum, marking a significant breakthrough for multi-messenger astronomy (Abbott et al., 2017b).
- Neutrino detection from a flaring blazar: Both gamma rays and neutrinos can be produced from the interaction of cosmic rays (CRs) with nuclear targets, such as molecular clouds (see Section 1.6.2). Neutrinos are not deflected by magnetic fields, nor, because of their small interaction cross-section, are absorbed. On the other hand, they are extremely difficult to detect, because their cross-section are the lowest among elementary particles. Identifying neutrino sources and their association with gamma ray counterparts therefore provides unique insights into the long-standing problem of the CR origin. A potentially compelling evidence has been found on September 22nd 2017, when *Fermi*-LAT and MAGIC (described in Section 1.4) detected an enhanced gamma-ray emission from the source TXS 0506+056, positionally consistent with a ~ 300 TeV neutrino, IC170922A, detected by IceCube (The IceCube Collaboration et al., 2018). This suggests that blazars may indeed be one of the long sought sources of very-high-energy CR.

In the next Section, we focus on the main instrument used in this work, the *Fermi*-LAT.

1.5.1 The Fermi Large Area Telescope

Fermi-LAT is the main instrument on board of *Fermi*. In this Section, we briefly describe its chief characteristics, components, and functioning. For a comprehensive technical

description of *Fermi*-LAT, we refer the reader to Atwood et al. (2009).

Fermi-LAT detects gamma-rays in the energy range of ~ 10 MeV to \sim a few TeV. Its effective area and PSF depend on the photon energy (Section 1.5.3). The spacecraft orbits Earth in ~ 96 minutes. It is oriented so that *Fermi*-LAT always points towards the zenith, therefore the Earth does not block the view. On alternate orbits *Fermi* rocks to the North and South. This, together with its large field of view ($\gtrsim 2$ sr) allows for the whole sky to be surveyed in two orbits.

Since photons in the *Fermi*-LAT energy range can not be refracted or reflected, the telescope uses the same technology used in high-energy particle detectors. The gamma-rays interact with the detector through pair production. This process provides a unique signature for gamma-rays, which distinguishes them from charged CRs. It is important since the CR flux is $\sim 10^5$ times higher than the gamma-rays flux. Also, the reconstruction of the $e^- e^+$ pair trajectories throughout the instrument allows for the determination of the incident gamma-ray direction.

Fermi-LAT was constructed in a 4 x 4 array of identical towers. Each tower comprises a tracker, a calorimeter and a data acquisition module (Figure 1.12). The instrument is covered with a thin anticoincidence shield scintillator. Incoming gamma-rays pass freely through the shield, while charged cosmic rays cause a flash of light, allowing the identification of the relatively rare gamma-rays. Efficient rejection of the charged particle background is essential for *Fermi*-LAT's functioning. The anticoincidence shield rejects 99.97% of unwanted signals produced by cosmic rays that enter the telescope.

The tracker is composed of 18 layers of Silicon-strip particle tracking detectors interleaved with Tungsten converter foils. The probability of pair production in photon-matter interactions increases approximately as the square of atomic number of the nearby atom. That is the reason behind using Tungsten (atomic number 74). When a gamma-ray enters *Fermi*-LAT, it proceeds until interacting with a nucleon from the tracker producing an $e^- e^+$ pair. They proceed on, creating ions in the Silicon detectors, allowing for the track of these particles to be precisely measured and used to reconstruct the incident gamma-ray direction. The pair-conversion signature is also used to help reject the CR background.

The design of *Fermi*-LAT had to attain an equilibrium between the need for thin converters to achieve a good PSF at low energies—which would reduce the amount of scattering of the $e^- e^+$ pair inside the instrument, making for a better reconstruction of

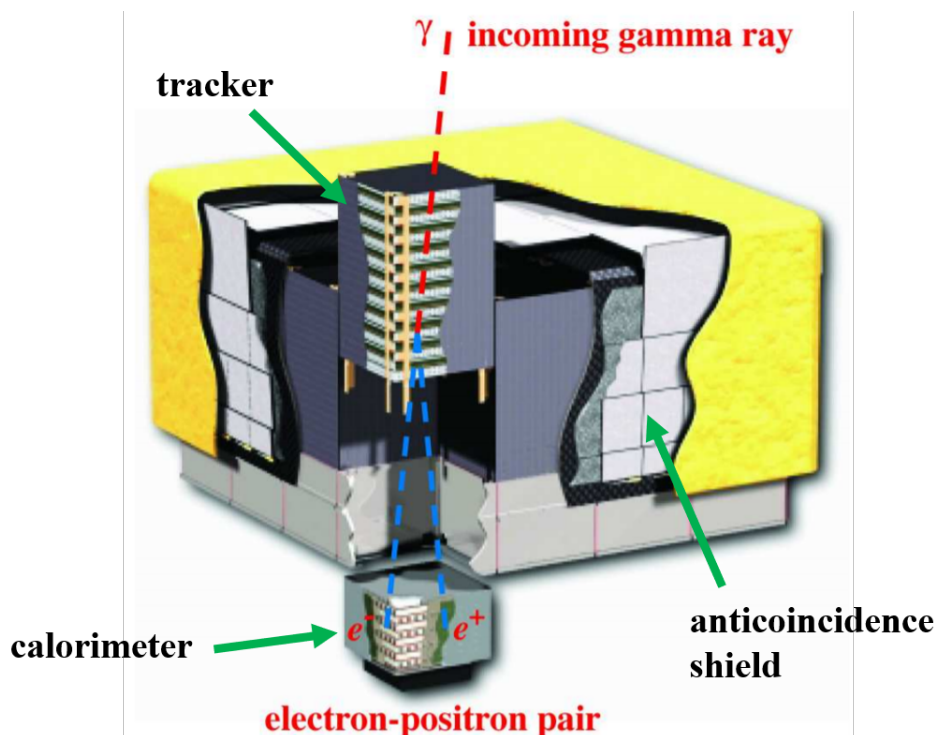


Figure 1.12: An illustration of *Fermi*-LAT instrument and its constituents. The path of an incoming gamma-ray up to conversion in the instrument is shown, as well as the track of the $e^- e^+$ pair until they reach the calorimeter. Source: original from Atwood et al. (2009); adapted for this thesis to label *Fermi*-LAT's components.

the gamma-ray direction—versus the need for thick converter foils to maximize the effective area, important at high energies—which would increase the likelihood of a conversion. The solution was to separate the tracker into two regions: “front” and “back”. The “front” region (composed of the first 12 tracking planes) has thin converters, each 0.03 radiation lengths thick, to optimize the PSF at low energies. The “back” converters (the remaining 4 layers) are ~ 6 times thicker, to maximize the effective area at the expense of the angular resolution of photons converting in this region.

After going through the tracker, the $e^- e^+$ pair is absorbed by a calorimeter made of Cesium Iodide scintillators (for a total thickness of 10 radiation lengths) which measures the total energy deposited. The material in the calorimeter produces flashes of light whose intensity is proportional to the energies of the incoming particle. The calorimeter can measure the three-dimensional profiles of showers which also helps to reject cosmic rays, since their pattern of energy deposition is different from that of gamma-rays.

The information from the three components (anticoincidence shield, tracker and calorimeter) are combined by a data acquisition system in order to identify when a likely

gamma-ray has been detected and to decide which information will be sent to the ground for further processing and distribution.

1.5.2 *Fermi-LAT data products*

Any *Fermi-LAT* data analysis starts with a list of counts that have been identified as resulting from astrophysical photons. It requires information about where the telescope was pointing and what was its observing efficiency. To accomplish this, it is necessary to use two types of data: a file with the photons information and one with the spacecraft information. All these data are available¹⁷ for the whole scientific community, together with the analysis software¹⁸ (the `Fermitools`), without embargoes. In Section 2 we describe in further details how these files and software were used for the analyses presented in this work.

The *Fermi-LAT* records individual readouts, called events, that are made available by the *Fermi-LAT* Collaboration in the form of `event files` (with `.fits` extension). They contain the reconstructed direction, the reconstructed energy, the moment in time of the detection and quality parameters for each event. There are about 3.6×10^9 events in the *Fermi-LAT* database detected from the whole sky between August 4th 2008 (the beginning of *Fermi* operation) and September 21st 2020¹⁹. When only the events with a high probability of being photons (as will be explained below) are considered, this number decreases to around 1.4×10^9 .

Fermi-LAT instrument response varies significantly with the photon incident angle (section 1.5.3). So it is necessary to know the position and orientation of *Fermi* to account for variation in the telescope exposure to the source of interest during its orbit. This information is provided in 30-second intervals by the *Fermi-LAT* Collaboration through the `spacecraft file` (also a `.fits` file). Another reason for this file is that the spacecraft is not collecting data during the whole time. No science data is taken while the telescope is under software maintenance or instrument calibration and while the observatory is transiting the South Atlantic Anomaly (a region over the South Atlantic with a high concentration of charged particles trapped by the Earth's magnetic field configuration).

¹⁷ fermi.gsfc.nasa.gov/ssc/data/access/

¹⁸ fermi.gsfc.nasa.gov/ssc/data/analysis/

¹⁹ fermi.gsfc.nasa.gov/cgi-bin/ssc/LAT/LATDataQuery.cgi

The information regarding these moments are provided in the spacecraft file.

A description of every column in the *Fermi*-LAT data files (both for the `event files` and the `spacecraft file`) is available online²⁰.

Other files, also provided by the *Fermi*-LAT Collaboration are necessary in the analyses. They include the Instrument Response Functions (IRFs), a catalog of sources (1.5.5) and diffuse emission models (1.5.5.1).

The combination of these files in an analysis is possible with the `Fermitools`. This process is described in section 2.1 in which we also explain our data selection and preparation.

The likelihood of each *Fermi*-LAT's detection to be a well-reconstructed gamma-ray is determined by algorithms developed by the *Fermi*-LAT Collaboration. These quality parameters separate the data into *event classes*. The categories are hierarchical: the higher probability photon selections are subsets of less restrictive selections. Evidently, the higher probability photon selections have narrower PSF and lower contamination of background events (detections with high likelihood of being contamination from CRs). At the same time, the choice of categories with only probability photon comes with a corresponding drop in statistics. It is, therefore, a trade off that the user has to make. The loosest selection criteria is recommended for short duration events (like gamma-ray bursts, GRBs, with timescales of a few seconds), and timing studies that benefit from increased photon statistics while tolerating a higher background fraction and broader PSF. The cleaner photon selections provide lower background contamination at the expense of lower effective areas. For most of the analysis, like the one presented in this work, an intermediate selection (*event class SOURCE*) is prescribed.

Fermi-LAT photons are also classified in different *event types*. They can be categorized according to the location where they converted in the detector (photons converted in the `front` of the equipment have better angular resolution than those converted in the `back`), or according to the quality of the reconstructed direction (the photons are divided in quartiles depending on the quality of this reconstruction), or according to the quality of the energy reconstruction (again, in quartiles). In our work, we chose to use the 75% photons with better reconstructed directions.

In addition to differences in the quality of the data, each subdivision uses a different

²⁰ fermi.gsfc.nasa.gov/ssc/data/analysis/documentation/Cicerone/Cicerone_Data/LAT_Data_Columns.html

instrument response function. We explain the impact of this choice on the performance of *Fermi*-LAT in the next Section.

1.5.3 *Fermi*-LAT performance

The performance of *Fermi*-LAT is determined by three entities: its hardware, the event reconstruction algorithms and the photon selection (referred as *event class* and *event type*, respectively). The IRFs are parametrized representations of the *Fermi*-LAT instrument performance and are factored into three terms: efficiency in terms of the detector’s effective area, resolution as given by the PSF, and energy dispersion. They are used in the analysis process to transform the data collected into meaningful results.

Since *Fermi*’s launch, the *Fermi*-LAT Collaboration periodically releases updated versions of *Fermi*’s photon dataset and analysis software. This is done to take advantage of improvements in the understanding of the LAT and its orbital environment. The current version at the time of writing is Pass 8 Release 3 version 2 (P8R3_V2, Ackermann et al. 2012a).

The plots in this section were obtained in the *Fermi*-LAT Performance webpage²¹. They were created with P8R3_V2 for different choices of *event class* and *event type*. In Figure 1.13 we show two plots, both considering only *event class SOURCE*. The one on the top shows how *Fermi*-LAT’s effective area is dependent on the photon energy for photons classified with *event types front, back* and *front + back* (indicated as “total” in the plot). The bottom panel shows the effective area as a function of incidence angle (θ) for 10 GeV photons with *event types PSF0, PSF1, PSF2, PSF3* and *PSF0+PSF1+PSF2+PSF3* (in which *PSF0* represents the 25% photons with the worst quality of their reconstructed direction, while *PSF3* represents the quartile with the best quality of their reconstructed direction).

For energies < 1 GeV and > 1 TeV the effective area decreases. For lower energies, the reason is the smaller probability of pair production in *Fermi*-LAT’s conversion foils. For the higher energies the decrease in effective area happens because the peak of the particle shower can form outside the calorimeter, making the detections not feasible.

In Figure 1.14 we show four plots with the impact of photon energy and incidence angle on *Fermi*-LAT’s PSF. All were created considering only photons with *event class*

²¹ slac.stanford.edu/exp/glast/groups/canda/lat_Performance.htm

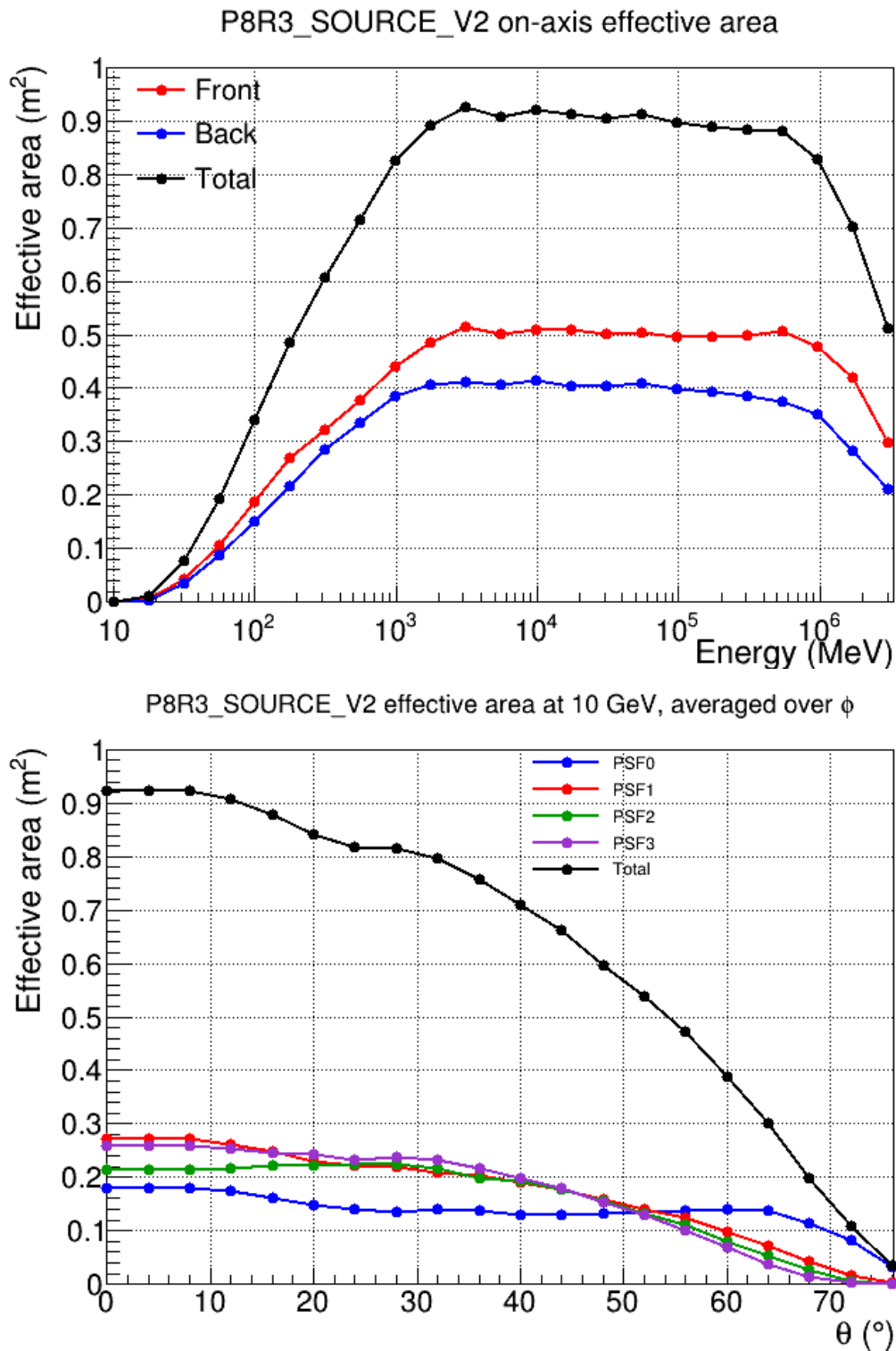


Figure 1.13: Fermi-LAT's effective area as function of energy and incidence angle for photons with *event class SOURCE*. Top panel: effective area as a function of the photon energy for *event types front* (red), *back* (blue) and *front + back* (black). Bottom panel: effective area as a function of the photon incidence angle for 10 GeV photons with: *event types PSF0* (blue), *PSF1* (red), *PSF2* (green), *PSF3* (purple) and *PSF0+PSF1+PSF2+PSF3* (black). Source: slac.stanford.edu/exp/glast/groups/canda/lat_Performance.htm.

SOURCE. The top row shows how *Fermi*-LAT's PSF depends on the photon energy for different selections of *event types*: on the left, we show the 68% and the 95% confidence level containment angle for photons classified with *event types front, back* and *front + back* and on the right the 68% confidence level containment angle for photons with *event types PSF0, PSF1, PSF2, PSF3* and *PSF0+PSF1+PSF2+PSF3*. For energies $\lesssim 100$ MeV, the uncertainty in the reconstructed direction of a single photon is $\gtrsim 5^\circ$. This large value, of course, is diminished with statistics of several photon detections. Because of the broadening of *Fermi*-LAT's PSF in lower energies, the probability of source confusion is enhanced. Also, since the Galactic diffuse emission is brighter in lower energies, this probability is intensified.

The bottom row in Figure 1.14, we show *Fermi*-LAT's 68% confidence level containment angle as a function of incidence angle (θ) for 10 GeV photons. The impact of the incident angle is mostly significant for high angles. The plots on the right column support our decision to disregard photons classified with *event types PSF0* in our analysis with the goal of obtaining better resolution on the photons reconstructed direction.

1.5.4 Caveats and systematics

The current version of *Fermi*'s photon dataset and analysis software, P8R3.V2, has a few caveats regarding the different event selections and the IRFs. The constant evaluation of all aspects of the data and analysis ensures that the `Fermitools` are constantly improved and the systematic uncertainties reduced. The *Fermi*-LAT Collaboration perform constant studies to check the precision and the consistency of the instrument simulations and the instrument response representation provided by the IRFs.

1.5.4.1 Effective area

There are differences between the efficiency of *Fermi*-LAT instrument in collecting photons (evaluated by the data) and the IRFs predictions. They are translated into systematic uncertainties on the effective area, which is defined as the product of the detector's geometrical area and its efficiency. The effective area is, then, dependent on the source position in relation to the telescope and on the photon energy. These dependencies are considered in the IRFs.

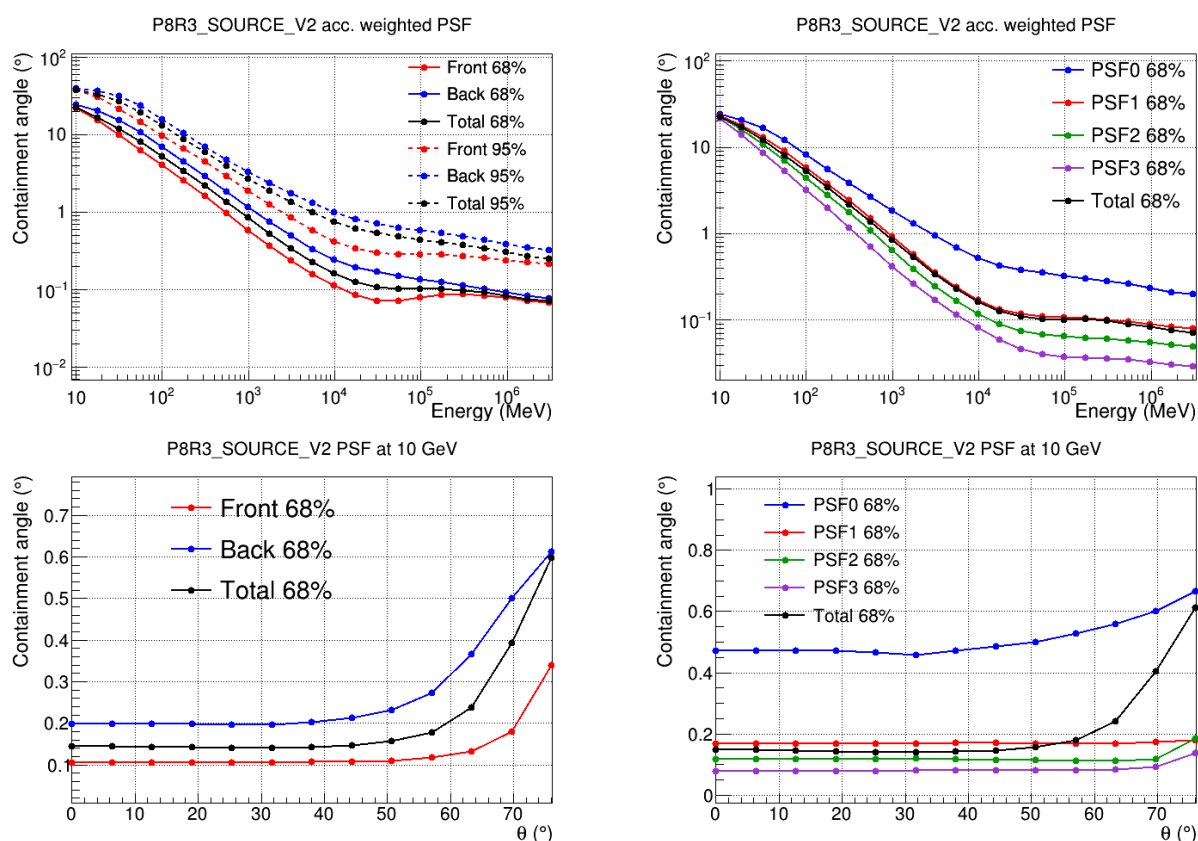


Figure 1.14: *Fermi*-LAT's PSF as function of energy and incidence angle for photons with *event class SOURCE* and different choices of *event types*. Top row, left panel: 68% and the 95% confidence level *Fermi*-LAT's PSF dependency on the photon energy for different for photons classified with *event types front* (red), *back* (blue) and *front + back* (black). Top row, right panel: 68% confidence level containment angle as a function of energy for different for photons classified with *event types PSF0* (blue), *PSF1* (red), *PSF2* (green), *PSF3* (purple) and *PSF0+PSF1+PSF2+PSF3* (black). Bottom row: 68% confidence level PSF as a function of the photon incidence angle (θ) for 10 GeV photons with the same *event types* as in the top panels. Source: slac.stanford.edu/exp/glast/groups/canda/lat_Performance.htm.

The systematic uncertainty on the effective area affects the flux. It is particular important to assess *Fermi*-LAT's when dealing with light curves (see Section 2.5.2). It is usually less than the statistical uncertainty affecting the light curves points and hence often neglected.

The plot in Figure 1.15 shows how this uncertainty varies with energy for different selection of *event types* and whether or not energy dispersion is taken into account (see Section 2.3.1 for a discussion on energy dispersion).

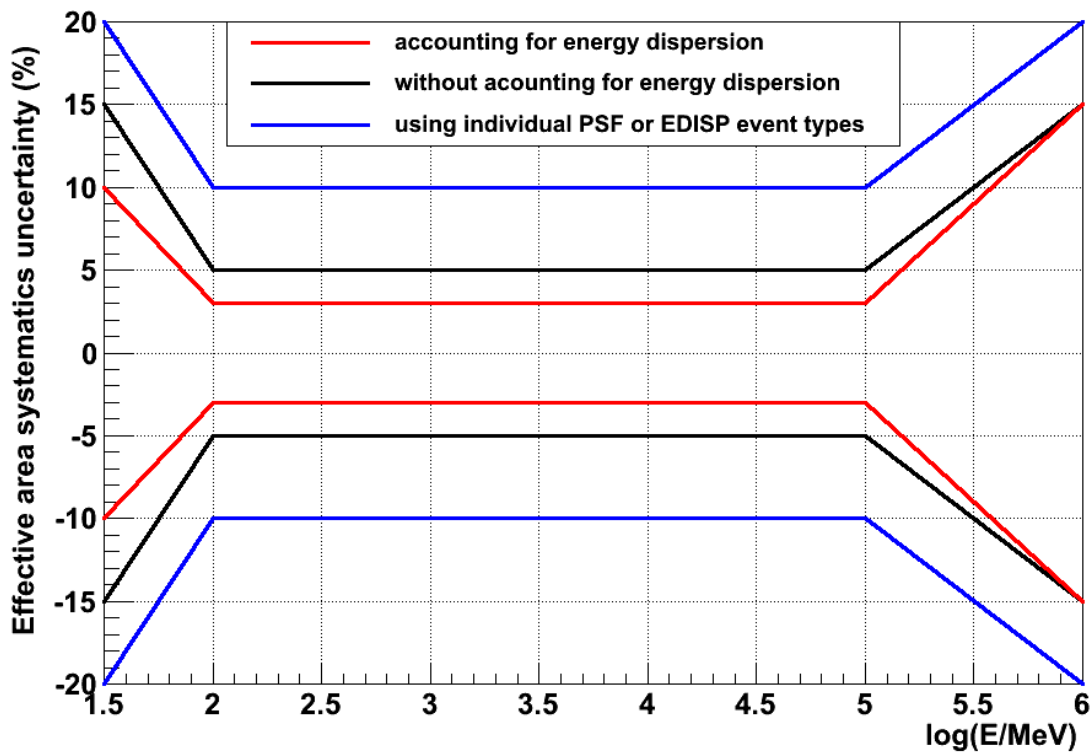


Figure 1.15: The systematic uncertainty band of the *Fermi*-LAT's effective area for three different configurations: data selection that does not include all events within an *event type* category and/or with energy dispersion disabled (blue); other data selection with energy dispersion correction disabled (black); and other data selection with with energy dispersion correction enabled (red). Source: fermi.gsfc.nasa.gov/ssc/data/analysis/LAT_caveats.html.

1.5.4.2 PSF

The systematic uncertainties in *Fermi*-LAT's PSF is quantified in terms of the uncertainty on the 68% containment radius of a point source. This is performed, for instance, with stacked, high-latitude AGNs.

The systematic uncertainty on the PSF is shown in Figure 1.16. It is $< 5\%$ in the 100 MeV to 10 GeV energy range and increases outside this energy band. Above 10 GeV the increase is driven by the limited statistics in the AGNs validation sample. This values apply to all *event class* and *event type* selections.

The impact of systematics on the PSF must be evaluated when localizing or assessing a source's extension (see Section 2.4.2).

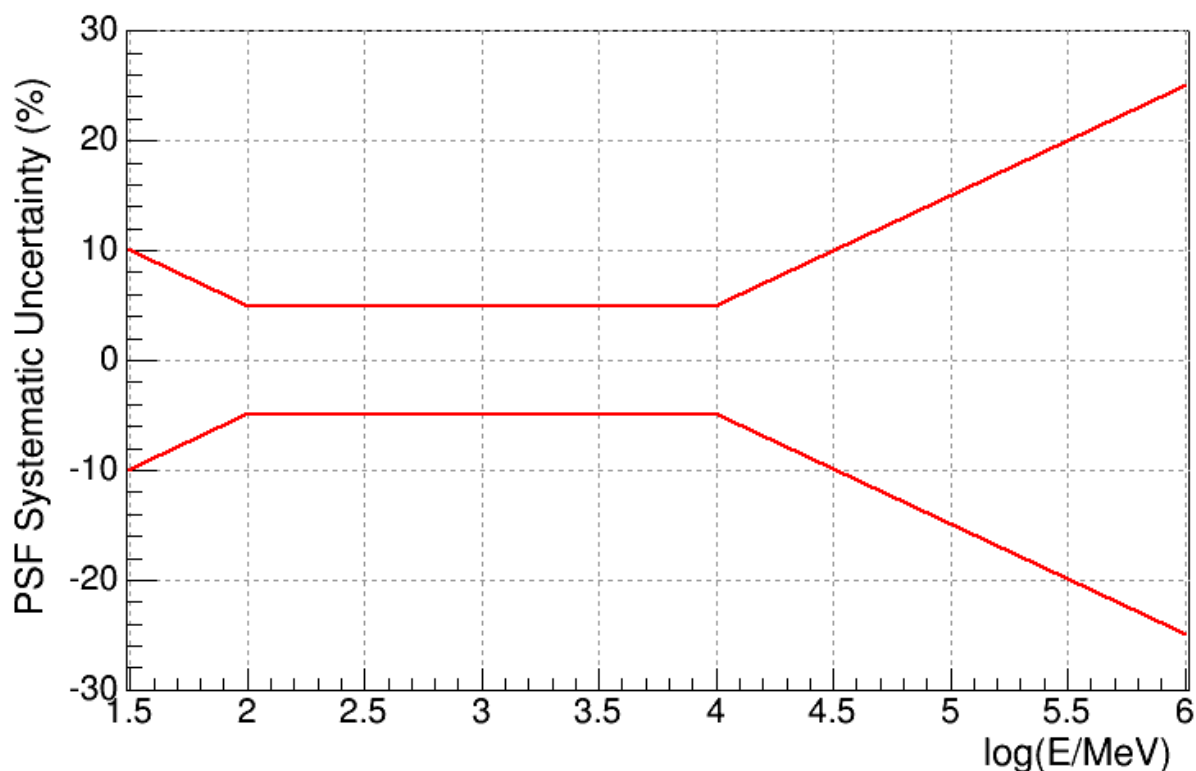


Figure 1.16: The variation of *Fermi*-LAT's PSF systematic uncertainty with energy. Source: fermi.gsfc.nasa.gov/ssc/data/analysis/LAT_caveats.html.

1.5.5 The 4FGL Catalog

As will be further detailed in Section 2.3, to work with *Fermi*-LAT data, it is necessary to create a model of the gamma-ray emitting sources in the region of the sky being studied. This is a necessity due to (i) the instrument's PSF, (ii) the dependence of *Fermi*-LAT's effective area on the photon energy and angle of incidence, (iii) the way *Fermi* operates, and (iv) the nature of the gamma-ray sky backgrounds. An essential resource to create the model is a catalog of known *Fermi* gamma-ray sources, with their position and spectral model. Since the launch of *Fermi* (in June, 2008), the *Fermi*-LAT Collaboration has been

releasing catalogs of detected sources. The first catalog (1FGL, Abdo et al. 2010) was released after 1 year of data collection. Other versions of the catalog are 2FGL (Nolan et al. 2012, with 2 years of observations), 3FGL (Acero et al. 2015, with 4 years) and the current version, 4FGL (The Fermi-LAT Collaboration, 2019), with 8 years of survey data and the 50 MeV-1 TeV range. Recently (June 2020) an incremental version (4FGL-DR2, for Data Release 2, Ballet et al. 2020) of the fourth full catalog of LAT sources, based on 10 years of survey data in the same energy range, was released.

In our work, we used the 3FGL in preliminary analyses that were later updated and expanded with 4FGL data. We did not use 4FGL-DR2 because it was released after all the gamma-ray models we created were already being used and most of the analyses completed. Therefore, in this Section we will describe the 4FGL and its contents. We will briefly mention the upgrades incorporated by the 4FGL-DR2, only to specify that using the 10 year catalog would not significantly improve our analyses and results.

The 4FGL is based on the first eight years of science data from *Fermi*-LAT in the energy range from 50 MeV to 1 TeV. It was created with the most recent version of *Fermi*-LAT data, Pass 8 release 3 Version 2 (Atwood et al., 2013) and *event class SOURCE* (in Section 2.1 we further describe what is the *event class* selection). The only difference between 4FGL and 4FGL-DR2 data selection regards the time interval covered (from 8 to 10 years).

The 4FGL includes 5064 sources (cf. Figure 1.17) which were detected above 4σ significance. The catalog provides their localization and spectral properties. Of these, 75 sources are modeled as spatially extended. A *Fermi*-LAT source is considered identified with another in different wavelength based on periodic variability for *Fermi*-LAT-detected pulsars or X-ray binaries, correlated variability at other wavelengths for AGNs, or spatial morphology related to that found in another band for extended sources. A total of 358 sources are considered as identified in 4FGL. As opposed to an identification, an association with a source in other wavelength is usually based on the spatial coincidence. This method is unsuitable when dealing with large surveys in the search of a counterpart. In this case, they use a method that retrieve some associations with relatively bright counterparts that were missed by the angular-separation-only method. The 4FGL has 3370 associated sources.

Among the identified and associated sources, more than 3130 are active galaxies of the

blazar class and 239 are pulsars. Together with the 1336 sources for which they found lower probability of counterparts at other wavelengths, 4FGL totals 5064 sources. The 4FGL-DR2 reported 723 new sources (not already in 4FGL), mostly just above the detection threshold. Since in our work we perform a search for new sources (Sections 2.3.1 and 2.3.2)—although not as thoroughly as in 4FGL-DR2—and the new 4FGL-DR2 sources are very faint, they did not impact significantly in our results.

Each source in 4FGL has a spectral model. Three different functions were used where the normalization, N_0 , was defined at a reference energy, E_0 , chosen such that the error on N_0 was minimal:

- a subexponentially cutoff power law for all sources identified or associated with a pulsar and with significantly curved spectra:

$$\frac{dN}{dE} = N_0 \left(\frac{E}{E_0} \right)^{-\Gamma} \exp(\alpha(E_0^b - E^b)) \quad (1.1)$$

where Γ is the low-energy spectral slope, α is the exponential factor and β is the exponential index

- a log-normal representation, also referred as ‘log-parabola’ in this thesis²² for the other sources with significantly curved spectra:

$$\frac{dN}{dE} = N_0 \left(\frac{E}{E_0} \right)^{-\alpha - \beta \log(E/E_0)} \quad (1.2)$$

where α is the spectral slope at E_0 and β gives the curvature of the spectrum

- a simple power-law for all sources not significantly curved:

$$\frac{dN}{dE} = N_0 \left(\frac{E}{E_0} \right)^{-\Gamma} \quad (1.3)$$

where Γ is the spectral slope.

For point source spectral models, the units of these functions are $\text{cm}^{-2} \text{s}^{-1} \text{MeV}^{-1}$.

Also, 4FGL provides a model for two gamma-ray diffuse components: one representing the Galactic emission—associated with hadronic CRs interacting with the molecular gas

²² a log-normal distribution has the shape of a parabola in log-log scales, hence it is sometimes referred as ‘log-parabola’

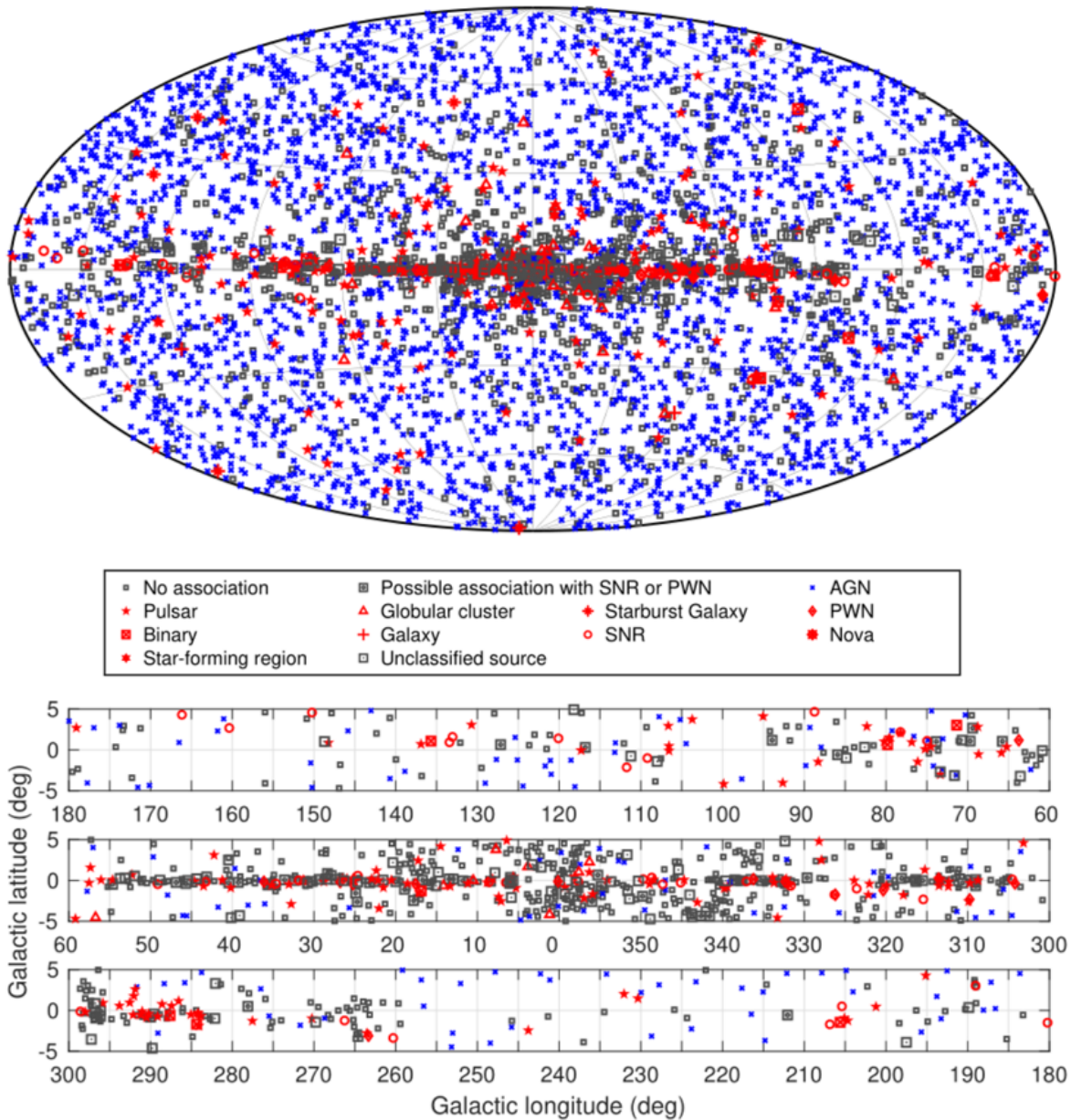


Figure 1.17: Full sky map (top) and blow-up of the Galactic plane split into three longitude bands (bottom) showing sources by source class (no distinction is made between associations and identifications). All AGN classes are plotted with the same blue symbol for simplicity. Other associations to a well-defined class are plotted in red. Unassociated sources are plotted in black. Source: The Fermi-LAT Collaboration (2019).

content of the Galaxy (Section 1.6.2)—and a isotropic one. They are discussed in Section 1.5.5.1.

1.5.5.1 The diffuse models

In addition to the point and extended sources in 4FGL, there are at least two diffuse components that must be taken into account when dealing with astrophysical gamma-rays in *Fermi*-LAT's energy range: the Galactic and the isotropic components.

The Galactic diffuse model:

As will be explained in Section 1.6.2, the interaction of hadronic CR with molecular gas emits gamma-rays. Because of the gas distribution in the Galaxy, this gamma-rays-emitting component is more prominent at low Galactic latitudes. The *Fermi*-LAT Collaboration released, with 4FGL, the most recent spatial and spectral template of this emission. The development of the model is described in more detail (including illustrations of the templates and residuals) online²³. Here, we briefly summarize the components of the model and its cataloged spectral model.

This model is based on linear combinations of templates representing components of the Galactic diffuse emission. The templates are the following:

- Gas templates (H_I and CO): This component was developed using spectral line surveys of H_I and CO (as a tracer of H_2) to derive the distribution of interstellar gas in 10 Galactocentric rings. Infrared tracers of dust column density were used to correct column densities in directions where the optical depth of HI was either over or underestimated. The model of the diffuse gamma-ray emission was then constructed by fitting the gamma-ray emissivities of the rings in several energy bands to the LAT observations.
- Dark Gas: This is the component of the cold interstellar medium that is not traced in H_I and CO emission. The existence of this component was established with intercomparison of dust thermal emission maps with H_I , CO, and gamma-ray observations (Grenier et al., 2005). They also split this component into the same 10 Galactocentric rings.

²³ fermi.gsfc.nasa.gov/ssc/data/analysis/software/aux/4fgl/Galactic_Diffuse_Emission_Model_for_the_4FGL_Catalog_Analysis.pdf

- Inverse Compton on the Interstellar Radiation Field: they used a model from Ackermann et al. (2012b) that was also subdivided in the same 10 Galactocentric rings.
- Large-scale structures: this component represents non-template diffuse gamma-ray emission, primarily Loop I and the Fermi bubbles.
- Cataloged sources: A model that considered the cataloged sources was developed with preliminary versions of 4FGL. This component was used in the Galactic diffuse model creation in order to avoid wrongly attributing cataloged sources' emission to the diffuse model.
- Unresolved Galactic sources: Galactic sources that are too faint to be detected individually undoubtedly contribute to the bright band of interstellar gamma-ray emission at low latitudes.
- Solar and Lunar emission: The Sun and Moon are effectively diffuse sources of gamma-rays when considered in long, integrated data sets. So Solar and Lunar templates were also used.

The Galactic diffuse model was created through a linear combination of these templates. A power-law (Equation 1.3) was used as the spectral model. Because of its large spatial extension, it is the brightest gamma-ray component in the models we created.

The Isotropic diffuse model:

Fermi-LAT data contains a significant background isotropic contribution from extragalactic diffuse gamma-rays, unresolved extragalactic sources, and residual cosmic-ray emission. They are included in the isotropic diffuse model. Although extragalactic unresolved sources are assumed to contribute to the model, it is not strictly a measure of the extragalactic isotropic gamma-ray emission because it includes residual charged particle background.

This model was created over 45 energy bins in the energy range of 30 MeV to 1 TeV, from the eight-year data. Emissions close to the Galactic plane ($|b| > 15^\circ$) were not considered to reduce contamination from the bright Galactic diffuse emission. The model was obtained as the residual between the data and the sum of the Galactic diffuse emission model (described above), a preliminary version of the 4FGL catalog and the solar and lunar templates.

The isotropic diffuse model is provided to the users in a series of tables with the differential flux for each energy bin. There are several versions of this model based on the different data selection used to derive them (i.e., *event class* and *event type*, see Section 1.5.1). When fitting a model with *Fermi*-LAT data, the user can allow a normalization factor to vary the contribution of the isotropic diffuse model.

1.5.5.2 The 4FGL J1745.6–2859 source

The GC is the closest example of a galactic nucleus and a compelling laboratory to investigate the physical processes responsible for accelerating particles to TeV and PeV energies. Of the several sources near the GC in 4FGL, 4FGL J1745.6–2859 is the brightest and the closest to Sgr A* at a distance of $\sim 0.01^\circ$.

Since the beginning of *Fermi*-LAT’s operations, a point source has been observed coinciding with the position of Sgr A*. This source was studied by Chernyakova et al. (2011) with 25 months of *Fermi* observations (using 1FGL). Later, Malyshev et al. (2015) analyzed the same source using 74 months of data (using 2FGL). In Table 1.2 we show the GC gamma-ray source’s position evolution through *Fermi*-LAT catalogs. We also include the distance do Sgr A* position in radio wavelengths (Reid and Brunthaler, 2004).

Table 1.2 - The position of the central source in the different *Fermi*-LAT catalogs. We also show the source’s distance do Sgr A*’s position in radio wavelengths.

Catalog version	Source name	Position ¹ (°)	Distance to Sgr A* ² (°)
1FGL	1FGL J1745.6-2900	266.419, -29.014	0.035
2FGL	2FGL J1745.6-2858	266.423, -28.979	0.030
3FGL	3FGL J1745.6-2859c	266.416, -28.995	0.013
4FGL	4FGL J1745.6-2859	266.415, -28.997	0.011
4FGL-DR2	4FGL J1745.6-2859	266.415, -28.997	0.011

¹ RA and Dec (in the J2000 epoch)

² in respect to Sgr A*’s position in radio wavelengths

It is a point source in all catalogs versions. Its spectral model has changed since the 1FGL and is now cataloged as a log-parabola (Equation 1.2) in both 4FGL and 4FGL-DR2. In Figure 1.18 we show its cataloged spectral model, used as the initial template for our models of the *Fermi*-LAT’s gamma-ray sky.

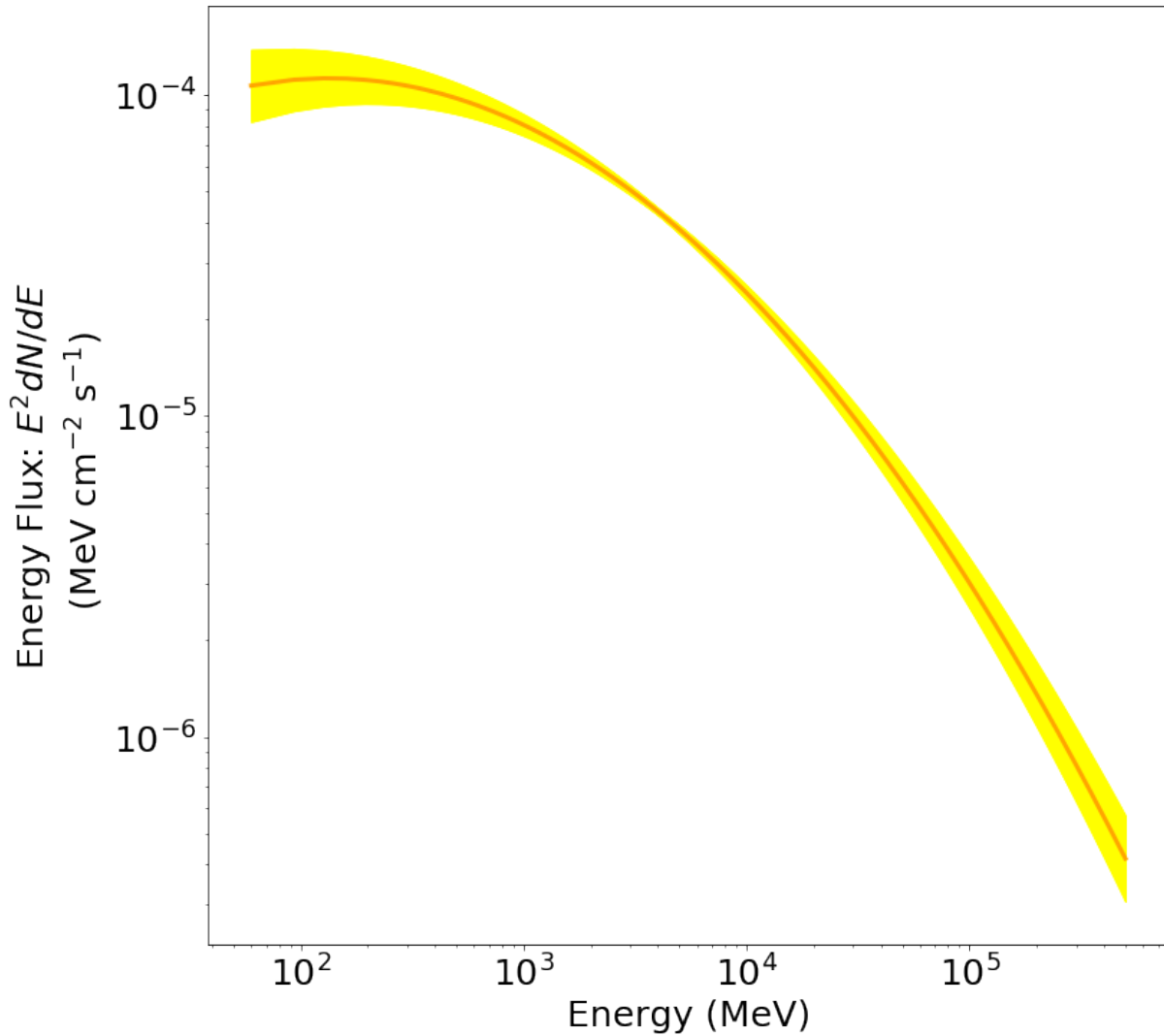


Figure 1.18: The central source’s spectral model is cataloged as a log-parabola in 4FGL. Here we show its modeled Energy Flux as a function of energy ($E^2 dN/dE$).

Other than the central source, there are ~ 200 4FGL sources in the central 10° of the Galaxy. It is the most crowded region of the *Fermi*-LAT sky and also the brightest one. Since *Fermi*-LAT’s PSF gets to a few degrees in the energy range we are working (Section 1.5.3, specially Figure 1.14), this region is greatly affected by source confusion and considerable care should be taken when modeling it.

1.6 The production of astrophysical gamma-rays

In order to understand astrophysical gamma-rays it is fundamental to understand their origin by modeling the electromagnetic emission at the source. The most usual starting

point is a population of accelerated charged particles in an environment with sufficient magnetic field. The gamma-rays from extragalactic sources are frequently associated to Active Galactic Nuclei (AGNs). Among the Galactic sources, pulsars, pulsar wind nebulae (PWN), supernova remnants (SNR) and binary systems are the most typical sources. Sgr A* is a natural candidate as a source of CR responsible for astrophysical gamma-rays. The mechanism responsible for generating gamma-rays is different depending on whether the CRs are leptons or hadrons. In this section, we describe both cases (Sections 1.6.1 and 1.6.2, respectively). Also, we briefly describe, in Section 1.6.3, an additional scenario in which the gamma-rays are the result of the decay of exotic particles (i.e., dark matter).

1.6.1 Leptonic emission

Relativistic charged particles accelerated by magnetic fields emit synchrotron radiation. Since the radiated energy is proportional to m^{-4} , where m is the particle mass, this process is much more important for leptons than for hadrons. Typically, the synchrotron photons do not reach to the gamma-ray energy range. Nevertheless, this process is important to understand leptonic gamma-ray production because leptons can also up scatter low energy photons, transferring part of their kinetic energy to the photons (IC scattering).

Both synchrotron and IC can take place in some astrophysical environments. In particular, ultra-relativistic electrons can generate photons with energies up to the X-ray band via synchrotron. These photons, then, are IC upscattered by the same population of electrons up to the gamma-ray energy band. This process is called Synchrotron Self Compton (SSC) (Dermer and Menon, 2009).

1.6.2 Hadronic emission

The interaction of accelerated hadrons with the astrophysical environment can also generate gamma-rays. The collision of a proton with a target nucleon (in a molecular cloud, for instance) initiates a hadron cascade. Almost the same number of π^+ , π^- and π^0 are produced. The π^0 decays almost immediately in two gamma-rays photons, each with close to half the energy of the π^0 . The hadronic scenario that is relevant in the context of this thesis is schematically represented by Equations 1.4 and 1.5:

$$p + p \rightarrow p + p + \pi^0 \quad (1.4)$$

$$\pi^0 \rightarrow 2\gamma \quad (1.5)$$

Each gamma-ray photon depicted in Equation 1.5 has an energy of $m_{\pi^0}c^2 = 67.5$ MeV in the rest frame of the π^0 , where m_{π^0} is the rest mass of the π^0 (of ≈ 135 MeV) and c is the light speed. The gamma-ray number spectrum, thus, is symmetric about 67.5 MeV in a log-log plot. The SED of this radiation, in the usual E^2dN/dE representation, has a distinct bell-type shape, rising steeply in energies below a few hundreds MeV (Stecker, 1971). This spectral feature is often referred as the ‘‘pion-decay bump’’ and is used to identify hadronic astrophysical gamma-ray emission.

The hadronic gamma-rays production is always accompanied by the production of neutrinos. While the π^0 decays almost immediately into two gamma-rays photons, neutrinos are generated as a result of the charged pions decay.

Hadronic gamma-ray emission is the main contribution for the diffuse gamma-ray flux associated to the Galactic disk. The gamma-ray flux with a hadronic origin is thus a function of the CR and the target gas densities. This process is also relevant in RIAFs. Since ions hardly radiate, they are heated to very high temperatures, resulting in proton-proton collisions that result in gamma-ray photons (Mahadevan et al., 1997; Oka and Manmoto, 2003; de Menezes et al., 2020).

1.6.3 Dark matter self annihilation

Gamma-rays might also be produced as the result of the decay or annihilation of exotic particles. The primary candidate, among several, for dark matter (DM) is elementary particle, in particular, weakly interacting massive particles (WIMPs). The gamma-ray flux expected as the result of these particles self-annihilation depends quadratically on the DM density along the line of sight (de Angelis and Mallamaci, 2018). This motivates searches on targets where one expects DM density enhancements, like the GC.

1.7 Publication resulting from this work

We intend to report the results of this work in two articles, both with this PhD candidate as first author:

- Fermi LAT observations of Sagittarius A*: I - Imaging Analysis
- Fermi LAT observations of Sagittarius A*: II - γ -ray SED and Variability

The first article of this list describes imaging analysis of the source 4FGL J1745.6–2859 across four energy bands from which we obtained its position as a function of energy. We also evaluated its “energetics” in the same energy bands. These results allowed us to rule out several potential candidates for the nature of the point gamma-ray flux from the GC. Our observations favor a cosmic ray origin either from protons, electrons or both, accelerated by—or in the vicinity of—the SMBH. This article was submitted in August 19th 2020 to *The Astrophysical Journal*. The PhD candidate is the first author and leader of this research with their advisor Prof. Dr. Rodrigo Nemmen as a coauthor. In Appendix A we reproduce the draft version of the article as submitted to *The Astrophysical Journal*. The work reported in this article is reproduced in this thesis (with several additional details) in Sections: 2.2, 2.4, 3.1, 3.2 and 4.1.

The second article of the list is still in preparation. In this work we plan on reporting 4FGL J1745.6–2859 SED and light curve. The goal is to constrain the physical processes responsible with the emission. Several models found in the literature for Sgr A* gamma-ray emission will be compared with the results. Also for this project, the PhD candidate will be the first author with their advisor as a coauthor. The target is to submit this article to *The Astrophysical Journal* in the second semester of 2021. Most of the analysis and results that will compose this article are already described in this thesis, in Sections 2.5, 2.6, 3.3, 3.4, 4.2 and 4.3.

In Appendix B, we report the participation of the PhD candidate in the publication of three additional articles. They are not immediately related to the subject of this thesis and are included only for the sake of completeness.

Data and Methods

In this section we discuss the data and the methods used in this work. We start describing how to create a model of the gamma-ray sky with *Fermi* observations. Then, we explain how we obtained the GC gamma-ray point source position, flux variability and SED with the `Fermitools`—a suite of data analysis software provided by the *Fermi*-LAT Collaboration—and `Fermipy` (Wood et al., 2017)—a Python package that facilitates analysis of data from *Fermi*-LAT.

2.1 Data

The *Fermi*-LAT data are available in the form of `event files` (with `.fits` extension), with the reconstructed direction and energy of the detection and quality parameters for each event. The *Fermi*-LAT instrument response varies significantly with the photon incident angle, so it is necessary to know the position and orientation of the satellite to account for variation in exposure to the source of interest during its orbit. This information is provided at 30-second intervals in the `spacecraft file`, which is also a `.fits` file.

The combination of the photon and spacecraft files is possible with the `Fermitools`.

Throughout this work we used `Fermitools` with the aid of `Fermipy` to deal with *Fermi* data and analysis.

The first step is to make cuts on the raw data based on our selection of: energy range, time range, position (RA, Dec), size of the region of interest (RoI), *event class*, *event types* and maximum zenith angle.

These cuts are performed using the tool `gtselect` available in `Fermitools`.

In the following paragraphs we explain each item of this list and our choices for them.

We start by describing our energy selection cuts.

With the goals of taking advantage of the better *Fermi*-LAT’s PSF at higher energies (section 1.5.3) and also to evaluate the impact of photon energy on the source position, we divided our analysis into four energy bands that were chosen as explained in section 2.1.3:

- 60–300 MeV
- 300 MeV–3 GeV
- 3–10 GeV
- 10–500 GeV

The three highest energy bands analysis are based in an analysis that we call “Universal Model”. It was performed with energies between 100 MeV and 500 GeV and later split in tighter energy bands. The lowest energy band used a custom model created from scratch. We explain the modeling process in Section 2.3. Figure 2.1 shows how we split the analysis in different energy bands.

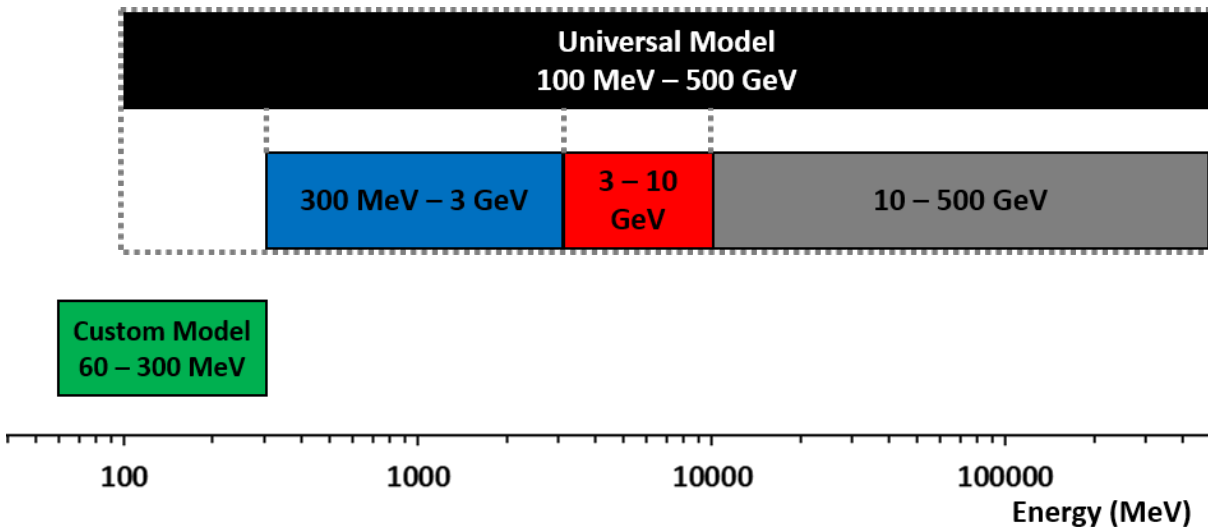


Figure 2.1: We divided our analysis in four energy bands (60–300 MeV, 300 MeV–3 GeV, 3–10 GeV and 10–500 GeV). The three highest energy bands models were created based in an analysis that considered energies between 100 MeV–500 GeV. This is our Universal Model which was also used to create LCs and a SED for 4FGL J1745.6–2859. The lowest energy band was studied with a custom model.

To work with *Fermi* data, it is necessary to create a model for the gamma-ray emitting sources in the RoI. This process will be further described in Section 2.3. Here we focus on the data selection and preparation before the modeling starts.

2.1.1 Data selection: Universal Model

For our Universal Model we worked with photons detected with energies between 100 MeV and 500 GeV. We chose events detected since the start of *Fermi*-LAT operations (in August 4th 2008, 15:43:36 UTC) until December 1st 2019, 00:00:00 UTC, adding up to ~ 11.3 years of data collection.

We considered photons detected inside a square with 20° side centered in the cataloged point source 4FGL J1745.6–2859 that is coincident with the position of Sgr A*, and rotated $\sim 58^\circ.6$ to the East in Galactic coordinates. This large area—when compared with usual astrophysical observations, specially in longer wavelengths—is necessary to account for *Fermi*'s large PSF (section 1.5.3) and the complexity of the gamma-ray sky in the direction of the GC (section 1.2.1).

Gamma-rays can also be generated by cosmic-ray interaction with the Earth's atmosphere. For this reason, the Earth limb is a strong source of background in *Fermi*-LAT's data. The maximum zenith angle selection was designed to exclude from the analysis time periods in which the Earth's limb is too close to the RoI. The 90° recommended¹ value for analysis similar to ours was adopted. This value is sufficient to provide a buffer between the RoI and the Earth's limb (that lies at a zenith angle of 113°). In the next step of the data selection process, we will use the `gtmktime` tool to remove any time period in which the RoI overlaps this buffer region.

The *Fermi*-LAT events (available through the `event files`) are classified based on their photon probability and the quality of their reconstruction (section 1.5.2). This separates the photons in different *event class*, each with its own set of instrument response function. In this work, we used the recommended¹ *event class* for the characteristics of our analysis, i.e. photons classified as *SOURCE*. *Fermi*-LAT photons are also classified in different *event types*. In this work we chose to consider only the 75% photons with better reconstructed direction (*event types PSF1, PSF2 and PSF3*). This was done in order to minimize the risk of source confusion, since the GC is a region crowded with *Fermi* sources, but without compromising the amount of photons available for the analysis.

The *Fermi*-LAT response functions are dependent of the angle between the source and the telescope axis. It changes as the satellite orbits Earth and/or its axis is moved to make

¹ fermi.gsfc.nasa.gov/ssc/data/analysis/documentation/Cicerone/Cicerone_Data_Exploration/Data_preparation.html

some specific opportunistic observation (to focus on a gamma-ray burst, for instance). Thus, the number of photons detected from a source depends on the amount of time it spends at different inclination angles during the data collection. Also, the detection of photons will depend on the accumulated time during which *Fermi*-LAT is actively taking data, the “livetime”. Using the tool `gtmktime` is a necessary step for this purpose. This tool reads the spacecraft file and creates a set of Good Time Intervals (GTI). A GTI is a time range in which the data, based on the pointing and livetime history of *Fermi*-LAT, can be considered valid: periods when the instrument was collecting data over the selected time range and the RoI was not close to Earth’s limb (based on the maximum zenith angle criteria). Only after removing the time periods when the data quality is not considered good that the exposure (effective area multiplied by livetime) of the RoI is assessed.

After all these steps, we have a list of detection events that satisfy our selection criteria available to work with. They will be now be addressed as ‘counts’.

Then, the tool `gtl1cube` computes the livetime as a function of inclination and location on the sky for a specified observation period.

It is interesting to create an exposure map with the total exposure in every position of the RoI during the analysis period. This makes the data processing faster and less computational demanding. The effective area of *Fermi*-LAT, as explained in Section 1.5.3, is a function of the incident photon energy. For this reason, the exposure map also depends on the energy. The counts produced by a source at any given position of the RoI is the integral of the source flux and the exposure map at that position. The exposure map is particularly important to account for extended sources such as *galdiff* and *isodiff*.

2.1.2 Data selection: low energy custom model

The low energy (60–300 MeV) model was created totally independent from the Universal Model. Since we generated it a few months before the Universal Model, its time range is smaller, going from August 4th 2008, 15:43:36 UTC to February 16th 2019, 00:00:00 UTC, adding up to ~ 10.8 years.

We chose to work with a larger RoI—a square with $30^\circ \times 30^\circ$ sides centered on the point source 4FGL J1745.6–2859, and with the same orientation used for the Universal Model—because *Fermi*-LAT’s PSF is larger at lower energies. Again, we used the recommended²

² fermi.gsfc.nasa.gov/ssc/data/analysis/documentation/Cicerone/Cicerone_Data_Exploration/Data_preparation.html

value of 90° for the maximum zenith angle cut.

The other data selection choices were the same as in the Universal Model, i.e. *event class SOURCE* and *event types PSF1, PSF2* and *PSF3*.

Now that the data is selected and prepared, we move on to create the models of the gamma-ray sky necessary to deal with the *Fermi* data. Before we describe the modeling process *per se* we will explain how the energy bands we are using were selected (Section 2.1.3) and, then, we will briefly describe the statistical tool used in this step (Section 2.2).

2.1.3 Energy boundaries

The choice of the energy bands we used in this work (Figure 2.1) was decided semi-empirically. We wanted bands with enough counts to obtain statistically significant results in the analyses. We used 4FGL J1745.6–2859’s spectral model (Figure 1.18) to split the total predicted number of photons between 60 MeV and 500 GeV into 4 energy bands with more or less the same number of counts. To do that, we multiplied Equation 1.2 by E (the energy) and integrated in respect with E using several different integration limits. Since Equation 1.2 gives results in terms of an area and the instrument effective area is dependent on the photon energy (Figure 1.16), we knew the results we got were approximations. After obtaining approximated results for the bands frontiers, we chose the closest round values. Then, we performed the data selection steps (Section 2.1) with the obtained energy boundaries and assessed the number of events in each energy band to check if the four of them had about the same number of counts. We had to expand and reduce some of the bands but managed to find limits that granted bands with the desired characteristics.

2.2 Maximum likelihood modeling

We use the maximum likelihood technique to find the best fit model to the data. The likelihood is the probability of obtaining the data given a specific input model. In our case, the model consists of the gamma-ray sources distribution on the sky, including their spectra and position. To fit a model, we vary these parameters until the likelihood is maximized.

An underlying hypothesis behind the likelihood fitting is that we suppose that the

model with the highest probability to explain the data is, indeed, the model closest to the reality beneath the observations. That is not necessarily true, but it represents our best understanding of the underlying reality we are trying to study.

To fit a model to *Fermi*-LAT's data, the four steps listed below are necessary. We already explained the first three. So, we will just briefly mention them here and address the reader to the Sections where they were further discussed. The fourth item of the list is the one we are interested now.

1. Data selection: This step was explained in Section 2.1. In short, we take data from a spatial region centered in the source of interest to account for nearby sources' emission (because of *Fermi*-LAT's large PSF and the complexity of the region).
2. Model selection: As mentioned, the model includes the position and spectra of the sources in the RoI. Also, it includes a model of the diffuse emission. The *Fermi*-LAT Collaboration provides a catalog with these sources and also models for the diffuse components (See Section 1.5.5).
3. Precomputing important quantities: During the model fitting the parameters are varied several times until the maximization of the likelihood. This is a computationally intensive process. To speed it up the livetime and the exposure map (presented in Section 2.1) are previously calculated.
4. Performing the fit: The actual fitting process searches for the combination of parameters that maximize the likelihood of the model explaining the data. Several parameters are fit simultaneously in an iterative fashion. The result of the fitting process is a set of best-fitting parameters and their uncertainties.

2.2.1 The likelihood function

Every count in the *Fermi*-LAT data is characterized by many different variables such as direction, energy, time of detection, part of the telescope in which it was converted, etc.. For analysis in which the number of counts is large (typically, every analysis that take into consideration extended time periods and/or sources that are not extremely faint) the time to calculate the likelihood becomes prohibitive. For this reason, before performing the fit, the data is binned according to the counts' characteristics. Given the number of

variables and the reduced number of gamma-ray photons that are detected by *Fermi*-LAT (see Section 1.5.2) when the data is binned, each bin will contain a small number of counts. The observed number of counts in each bin follows a Poisson distribution and can not be approximated by a Gaussian distribution.

For a Poisson distribution, the probability of a number of counts being detected in a given pixel is:

$$p_i = \frac{m_i^{n_i} e^{-m_i}}{n_i!} \quad (2.1)$$

where m_i is the expected number of counts predicted by the model in pixel i , and n_i is the observed counts in that pixel.

The likelihood \mathcal{L} is the product of the probabilities for every pixel:

$$\mathcal{L} = \prod_i p_i = \prod_i \frac{m_i^{n_i} e^{-m_i}}{n_i!} \quad (2.2)$$

We can factor this product into two terms:

$$\mathcal{L} = \prod_i e^{-m_i} \prod_i \frac{m_i^{n_i}}{n_i!} \quad (2.3)$$

We can calculate the first term as:

$$\prod_i e^{-m_i} = e^{-m_1} \times e^{-m_2} \times \dots \times e^{-m_i} = e^{\sum_i -m_i} = e^{-N_{pred}} \quad (2.4)$$

where N_{Pred} is the total number of counts predicted by the model. This term is independent of the data. The second term of Equation 2.3 does depend on the data (n_i). Using the result of Equation 2.4 in Equation 2.3, we get:

$$\mathcal{L} = e^{-N_{pred}} \prod_i \frac{m_i^{n_i}}{n_i!}. \quad (2.5)$$

This is the appropriate likelihood function form for a binned analysis.

We are interested in the set of parameters that maximize the likelihood, displayed in Equation 2.5. Because logarithms are strictly increasing functions, maximizing the likelihood (\mathcal{L}) is equivalent to maximizing the log-likelihood (ℓ). But for practical purposes it is usually more convenient to work with the log-likelihood function in maximum likelihood estimation. So, we take the logarithmic transformation of Equation 2.5:

$$\log \mathcal{L} = \ell = \log e^{-N_{pred}} + \log \prod_i m_i^{n_i} + \log \prod_i \frac{1}{n_i!} \quad (2.6)$$

Which gives:

$$\ell = -N_{pred} + \sum n_i \log m_i - \sum \log n_i! \quad (2.7)$$

The first term in Equation 2.7 is just the negative of the total number of counts predicted by the model. The third term is model independent and, hence, neglected. So, the log-likelihood function that is maximized is simply:

$$\ell = \sum n_i \log m_i - N_{pred} \quad (2.8)$$

The binning process destroys information because we don't have access to the precise values of the quantities describing a count. So, the smaller the bins the more accurate the likelihood.

For bin sizes infinitesimally small, which means an unbinned analysis, we get to $n_i = 1$ (or $n_i = 0$). Then, Equation 2.5 is reduced to:

$$\mathcal{L}_{unbinned} = e^{-N_{pred}} \prod_i m_i \quad (2.9)$$

where i is now the number of detected counts.

In this case, m_i is calculated using the precise values for each count (instead of an average over a bin). For this reason, the unbinned likelihood is the most accurate.

And, the log-likelihood function, that is maximized for the unbinned analysis, is:

$$\ell_{unbinned} = \log m_i - N_{pred} \quad (2.10)$$

In our work, due to the amount of data and huge number of sources in the model, we used only the binned likelihood method, described by Equations 2.5 and 2.8.

2.2.1.1 Likelihood model fitting with FermiTools

The set of parameters that maximizes the likelihood is determined by the fitting process. The maximum is found through in an iterative manner, by calculating ℓ for different sets of parameters. Then, its derivative with respect to the parameters is calculated, which

guides the choice of a new set of parameters by the algorithm that are progressively closer to the set that maximizes the function. These steps are repeated until the change in the function value between iterations is sufficiently small (or the number of iterations reaches a maximum value). During the iterations, the algorithm maps the dependence of the function on the parameters, particularly near the maximum. The uncertainties on the best fit parameters are related to this dependence and, hence, provided as a result of the fitting process.

The `Fermitools` offer five choices of algorithms, called optimizers. They vary in how rapidly they converge to the function maximum, the amount of computer memory they require, and the accuracy with which they map out the dependence of the function. `Fermipy` restrict the choice to only the most used two: `MINUIT`³ and its newer version `NEWMINUIT`. `NEWMINUIT` is a conservative optimizer that converges more slowly, but offers more accurate result and more reliable uncertainty estimates. The `MINUIT` manual suggests a maximum number of around 15 free parameters during the fitting process. This limitation was respected during our work.

This process is facilitated by the `Fermitool` `gtlike` that was used with the aid of `Fermipy`'s function `fit`. The output are the parameters values that maximized the likelihood and their uncertainties, the value of ℓ , the increase in ℓ , in respect to the previous version of the model and the Test Statistic (TS) value resulting from the fit. The TS is described in Section 2.2.1.2.

2.2.1.2 Model selection

The maximum likelihood method provides the best fit parameters and the corresponding confidence intervals. However it does not include a measurement of the quality of the fit. The only way forward is to compare different potential models and select the one with the best fit to the data. The rationale behind this model selection is an underlying assumption that a higher probability of obtaining the data from a model (which means a model with a higher \mathcal{L}) signifies that this model offers a better description of the underlying reality than an adversary model.

The quantity used to select between two potential models is the TS , defined as

³ cds.cern.ch/record/2296388/files/minuit.pdf

$$TS = -2 \log \frac{\mathcal{L}_{max,0}}{\mathcal{L}_{max,1}} \quad (2.11)$$

where $\mathcal{L}_{max,0}$ is the maximum likelihood value for the ‘null hypothesis’, and $\mathcal{L}_{max,1}$ is the maximum likelihood value for a new model that is being evaluated.

Suppose we are interested in evaluating the existence of a source that is not currently part of the model. We can evaluate this possibility using Equation 2.11. We just maximize the likelihood for a model without the additional source ($\mathcal{L}_{max,0}$) and for the model with the additional source ($\mathcal{L}_{max,1}$) and apply Equation 2.11. Thus, a larger TS indicates that the null hypothesis is incorrect, i.e., a new source is a better explanation. As a general rule, $\sqrt{TS} \approx$ significance (σ) of the preferred model against the alternative (Mattox et al., 1996). Hence, in the example, the TS would be approximately the square of the detection significance of the source in standard deviations. This is precisely the meaning of the TS values we report, for instance in Table 3.1, for a given source.

This can be used to search for additional sources in the RoI (see Section 2.3.3). We just need to input an spectral model to a putative source and calculate, in an iterative way, the TS for a model with this additional source included in every pixel of the RoI. Since Equation 2.11 is a monotonically increasing function of $\mathcal{L}_{max,1}$, maximizing TS on a grid is equivalent to maximizing the likelihood on a grid. Thus, locations in the map with TS above some threshold indicate positions where additional sources may be included.

2.3 Defining models with the Fermi tools

The analysis of *Fermi*-LAT data starts with the data selection and preparation, a process explained in section 2.1. A qualitative exploration of this data will present spatial clustering of photons, which hints for the presence of sources. But a quantitative study requires fitting models to this data. This necessity is justified by *Fermi*-LAT’s effective area being dependent on the photon energy and angle of incidence; by the way *Fermi* operates scanning the whole sky every 3 hours, which results in a single source going from unexposed to the instrument to being exposed by several different angles in a matter of tens of minutes; by the instrument large PSF; and by the nature of the gamma-ray sky backgrounds.

We have chosen the size of the RoI taking into account *Fermi*-LAT’s large PSF, specially

at lower energies. This requires that counts detected in a region around the source of interest must also be taken into account. And the sources lying in this region have to be properly modeled as well. The influence of these other sources will be attenuated as they are farther away from the source of interest, which limits the size of the RoI. The ideal size of the RoI is a trade off between a more accurate model and the amount of data to process (which leads to higher computational demand). The optimal size is a matter of experimentation and experience.

As a starting point for our modeling of *Fermi*-LAT data, we used the 4FGL catalog of *Fermi* sources created by the *Fermi*-LAT Collaboration. The catalog contains the positions and spectral models of more than 5,000 gamma-ray sources detected during the first 8 years of *Fermi* operation. The parameters of these spectral models are the variables that can be altered to improve the quality of the fitting of the model to the data. In this process new sources can also be added to the model. We also considered two diffuse components to the model: the Galactic diffuse emission model (*galdiff*) and the extragalactic isotropic diffuse emission model (*isodiff*). The fitting of the model to the data is performed with a maximum likelihood technique.

2.3.1 Universal Model

Here we describe the process for the creation of the Universal Model with counts with energies between 100 MeV and 500 GeV and its offspring: the three models with energies between 300 MeV–3 GeV, 3–10 GeV and 10–500 GeV. The data selection for this model was described in section 2.1.1

The region was modeled based on the preliminary release of 4FGL (`gll_psc_v20.fit`), the updated model of interstellar gamma-ray emission, `gll_iem_v07.fits`, and standard isotropic spectral templates selected according to the *event types* and *event class* used in this work. In the model, we included the 4FGL sources inside a square larger than the size of the RoI (with 25° side) to account for *Fermi*-LAT's PSF. We performed a binned likelihood analysis using `Fermitools` conda package version 1.2.1, `Fermipy` Python package version 0.17.4 and Pass 8 release 3 Version 2 response functions (Atwood et al., 2013). Data was binned to a pixel size of 0°.08 and into 8 logarithmically spaced bins per decade in energy (for a total of 30 energy bins).

Fermi-LAT does not measure the energy of the photons with infinite precision. *Energy*

dispersion is how the finite energy resolution of *Fermi*-LAT is called. It has been characterized by the *Fermi*-LAT Collaboration and this information is part of the instrument response functions. Turning on energy dispersion correction reduces systematic uncertainties. In this analysis, energy dispersion was disabled for the isotropic diffuse component only, as recommended by the *Fermi*-LAT Collaboration, since this component was created with data that did not take energy dispersion into account.

We performed a joint likelihood analysis with three components accounting for the isotropic emission because *event types PSF1*, *PSF2* and *PSF3* have different isotropic spectral templates.

We began the analysis using *Fermipy*'s `optimize` method. It uses an iterative strategy to perform an automatic optimization of the model by fitting every source in the RoI. According to the *Fermipy*'s developers⁴, it is generally a good practice to run this method once at the start of every analysis to ensure that all parameters are close to their global likelihood maxima.

The first step of the `optimize` tool is to simultaneously fit the normalization of the N brightest sources in the RoI that together sum up to a fraction `npred_frac` of the total predicted counts in the model. The N_{Pred} for every source is a quantity easily calculated by *fermipy* based on their spectral models. We used `npred_frac = 0.93` which, based on previous analysis with similar characteristics, corresponds to $N \lesssim 15$. The next step is to individually fit the normalizations of every other source of the RoI, skipping any one that have $N_{Pred} < npred_threshold$ (we used the *default* value of `npred_threshold = 1`). The last step is to individually fit the shape (the index) and normalization of all sources with $TS > shape_ts_threshold$, where TS is determined from the first two steps of the ROI optimization and `shape_ts_threshold = 25.0` (the *default* value).

After that we started fitting the sources in the RoI, using *Fermipy*'s `fit` tool which performs a likelihood fit of all free parameters of the model and updates the characteristics of the corresponding model components (TS , N_{Pred} , *spectral parameters*, etc.).

Since the GC region is very rich in sources (section 1.5.5.2) we used an iterative approach on the fitting of the RoI, always taking care to limit the number of free parameters to less than 15 to avoid numerical issues⁵ with MINUIT and NEWMINUIT, optimizers used

⁴ fermipy.readthedocs.io/en/latest/fitting.html

⁵ fermi.gsfc.nasa.gov/ssc/data/analysis/documentation/Cicerone/Cicerone.Likelihood/Fitting_Models.html

for maximizing the likelihood. Following the recommended procedure, we started every new round of fitting using the MINUIT optimizer until convergence for a rough likelihood maximization and then NEWMINUIT, a conservative optimizer that converges more slowly, for a more accurate result.

Several iterations were performed in order to fit the brightest sources closest to 4FGL J1745.6–2859. In all iterations, the normalization of our source of interest was allowed to vary as well as the normalization of *galdiff* and *isodiff*. The spectral models of these sources are, respectively, a log-parabola (Equation 1.2), a power-law (Equation 1.3) and a custom model (as explained in Section 1.5.5.1). The normalization of selected sources were also iteratively freed based on their proximity to the center of the RoI and their brightness in gamma-rays, obtained by the N_{Pred} in each energy interval. We performed several iterations to fit the desired sources. Only the best quality fits, with Status: 0 and Quality: 3, were considered. The “Status: 0” flag indicates that the fitting procedure converged. And the “Quality: 3” indicates that the optimizer obtained a full accurate covariance matrix.

Fits that did not converge or with lower quality were disregarded. In this case we would go back to the previous step of the fitting procedure and continue from there with a smaller quantity of free sources.

The next step was to use the Fermipy function `find_sources`. This is an iterative source-finding algorithm that uses peak detection on a TS map to find new source candidates. In section 2.3.3 we delineate better what a TS map is. But, roughly, it indicates positions in the RoI where there is a high probability of existing a source not included in the model or a modeled source whose flux is ‘under-predicted’, which is not the case in this step of our analysis since we covered that in the previous fitting rounds. We used $TS > 25$ —which translates to a significance $\gtrsim 5\sigma$ of the existence of a new source in some region of the RoI—as a threshold to include new sources. After several rounds of this procedure, 29 sources were found. A power-law with index 2 was used as their initial spectral model. This spectral model was selected because it is typically adequate for relatively faint sources, and in fact the majority of sources in 4FGL are modeled with a power-law spectrum. Finding and characterizing new sources is not a goal of this work. The aim of this source-finding step was to improve the quality of the model. Some of the newly found sources are likely spurious detection due to unmodeled background emission. After they

were found, some of them were refitted based on their distance to the central source, their brightness, or their proximity to regions with poor modeling (the evaluation of the fitting quality is detailed in section 2.3.3). The new sources are listed in Appendix C.

After every round of fitting we evaluated the quality of our fitting procedures using both:

- Residuals maps: built by subtracting modeled counts from the real data and searching for regions with significant residuals.
- TS maps: searching for the presence of an additional source component in each bin of the RoI.

In section 2.3.3 we detail how these maps were created and used to evaluate the quality of our fitting.

The normalization of sources close to excesses in those maps was allowed to vary, together with the normalization of 4FGL J1745.6–2859 and of the diffuse components, in a new round of fitting.

The last step was fitting the index of our source. The approach was the same as described above. We performed different iterations of fitting, always with the normalization and the index of 4FGL J1745.6–2859 as free parameters together with other free parameters that usually included the normalization and the index of nearby bright sources and the *galdiff* and *isodiff* diffuse models. Once again, only iterations with the best fit quality were considered. By “index” of 4FGL J1745.6–2859 we mean the α and β parameters of its *Log-Parabola* spectral model (Equation 1.2). The parameter E_0 was not freed during the fitting process.

These steps, after 86 rounds of fitting, led to the creation of the Universal Model with photons between 100 MeV and 500 GeV. Then, it was used as a initial model for the analysis in three energy bands (300 MeV–3 GeV, 3–10 GeV and 10–500 GeV). In each energy band, the only sources that were allowed to vary in a single new round of fitting were 4FGL J1745.6–2859 (normalization and index) and the *galdiff* and *isodiff* diffuse models (normalization only). We used this “minimal fitting” approach with the objective of keeping a similar model in the three energy bands. By not fitting other sources of the RoI, we made sure that their spectral models were continuous between the three highest energy bands. In Appendix D, for the sake of clarity, we show examples of discontinuous

models that we obtained in analyses in which the “minimal fitting” procedure was not used (they were not used in our work).

It is important to notice that we also created unique models, from scratch, to each of this three energy bands (300 MeV–3 GeV, 3–10 GeV and 10–500 GeV) and performed the fitting procedure reported in this section and the analysis detailed in section 2.4. The results we got with these unique models were compatible within 1σ with the ones reported in sections 3.1 and 3.2. We detail these comparisons in Appendix E.

Some results already naturally arise from the fitting procedure: we got the photon and the energy flux of 4FGL J1745.6–2859 between 100 MeV–500 GeV (the Universal Model), 300 MeV–3 GeV, 3–10 GeV and 10–500 GeV. They are reported in section 3.1.

In addition to that we will use the Universal Model to obtain 4FGL J1745.6–2859’s gamma-ray luminosity, SED and LCs in the *Fermi* energy range. Also, we used the 300 MeV–3 GeV, 3–10 GeV and 10–500 GeV models to evaluate the source position as a function of the photon energy. To improve this location study, we used a model created from scratch with photons in the 60–300 MeV energy range as well. We explain how this model was created in the next section.

2.3.2 Custom model (60–300 MeV)

Our initial desire was to create a gamma-ray sky model in the lower energy band using the Universal Model as a starting point, following the same process described in section 2.3.1. But this proved to be challenging. We couldn’t get a good quality model with the minimal fitting process nor with several additional rounds of fitting: in both cases we ended up with models whose Residuals and TS maps showed many regions with excesses above the acceptable levels (i.e., $TS < 25$ and Residuals $< |5\sigma|$). So we decided to use a specific model to the 60–300 MeV energy band.

We considered data inside a $30^\circ \times 30^\circ$ square centered on the point source 4FGL J1745.6–2859. This choice of size for the RoI permit low energy photons to be properly modeled given the large PSF. We used $0^\circ.1$ pixel size and 8 logarithmically spaced bins per decade in energy.

We modeled the region using the preliminary release of 4FGL (`gll_psc_v17.fit`), the updated model of interstellar gamma-ray emission (`gll_iem_v07.fits`), and standard isotropic spectral templates. We included in the model all 4FGL sources in a region with

35° side to account for *Fermi*-LAT’s PSF. We performed a binned likelihood analysis using `Fermitools` conda package version 1.2.1, `Fermipy` Python package version 0.17.4 and Pass 8 release 3 Version 2 response functions. Energy dispersion was disabled for the isotropic and Galactic diffuse components.

As we did for the Universal Model (section 2.3.1), we performed a joint likelihood analysis with the three components accounting for the isotropic emission.

Before starting the analysis we changed the Spectrum Type of 4FGL J1745.6–2859. It is cataloged as log-parabola in 4FGL but we adopted a power-law in this low energy model. This change is appropriate since in small energy ranges (like the ones we are using here) a log-parabola can be approximated by a power-law. We used results obtained in previous analysis using the Third Fermi LAT catalog (3FGL, Acero et al. 2015), in which the source’s spectra was modeled as a power-law, as the starting values for the parameters that were later refitted with the new data. The main reason for the change was the ease to fit power-laws, which have one less parameter compared to log-parabolas.

After that, we followed the same process described in Section 2.3.1 to fit the model until the source finding process. In this step, we encountered 14 new sources with `Fermipy`’s function `find_sources` in regions associated with $TS > 25$. But in new rounds of fitting, several of them showed a reducing in their TS to values below 25. Since *Fermi* LAT’s PSF is poorer at lower energies, we decided to exclude—one at a time—the new sources in this condition from the model to avoid them interfering in the results of our source of interest. We started excluding the farthest from the center of the RoI and refitted the model. The normalization of the sources closest to the excluded one were let free, together with the normalization of the Galactic diffuse emission model, of the isotropic spectral template and of 4FGL J1745.6–2859. We repeated this process until there were no new sources with $TS < 25$ in the model. After excluding these sources, we ended up with 5 new sources. These new sources may be spurious detections due to inaccuracies in the models. They are listed in Appendix F.

In total, 67 rounds of fitting were performed in the process of creating a gamma-ray sky model for the 60–300 MeV energy range.

We also tried the same analysis with different combinations of *event types*: *PSF2* + *PSF3* (which means the 50% photons with better PSF in the data) and *front* (that consider only the events that converted in the *Fermi*-LAT’s “front”, a part of the instrument that

provides counts with better spatial resolution, as explained in section 1.5.1). Although we were not as thorough in the fitting process with this different *event type* selection—since we were just assembling preliminary tests—as in the analysis presented here, the results we obtained with them are all compatible with the values reported here in $< 2\sigma$. More details can be found in Appendix G.

2.3.3 Evaluating the quality of the fitting process

A new round of fitting was only considered valid if the model’s likelihood increased, otherwise, it was discarded. This is implemented in *Fermitools* and *Fermipy*. But a simple increase in the likelihood was not enough to assure us that the new model was better than the previous one. For instance, some source’s flux can become under-predicted (underpredicting the gamma-ray flux detected in that region of the sky) and the likelihood can increase notwithstanding. In the case of this example, we would identify an excess in the diagnostic plots. The opposite (i.e. an ‘over-predicted’ source) would show-up in a region with negative excess in the residual maps. The maps would, then, indicate which sources models were sub-optimal or which region of the RoI demanded further modeling.

The set of diagnostic plots used in this work includes residual maps, *TS* maps (both of them briefly described in section 2.3.1) and residual histograms. In this section we explain them in length, delineate how they are created and in which way they are used to evaluate the quality of the models.

In every round of fitting the *Fermitools* (that we employ with the aid of *Fermipy*) use a maximum likelihood estimation (section 2.2) to fit a model to the available data. To do this, the software varies the selected spectral parameters of a sample of sources chosen by the user. It generates a three-dimensional (3D) distribution of counts: with two dimensions of space and a third dimension that considers the energy of the counts.

To create the spacial distribution, the positions and shapes of the sources in the model are convoluted with the instrument response (energy-dependent) functions to spatially distribute the model counts. For the point sources, only their positions are used. In the case of the extended sources, either a symmetric two-dimensional (2D) Gaussian (with a cataloged width), a symmetric 2D disk (with a cataloged radius) or an arbitrary 2D shape (with morphology defined by a template) is used as the spatial model. In the case of *isodiff*, its spatial model is a constant value in every position of the sky. And *galdiff* has also an

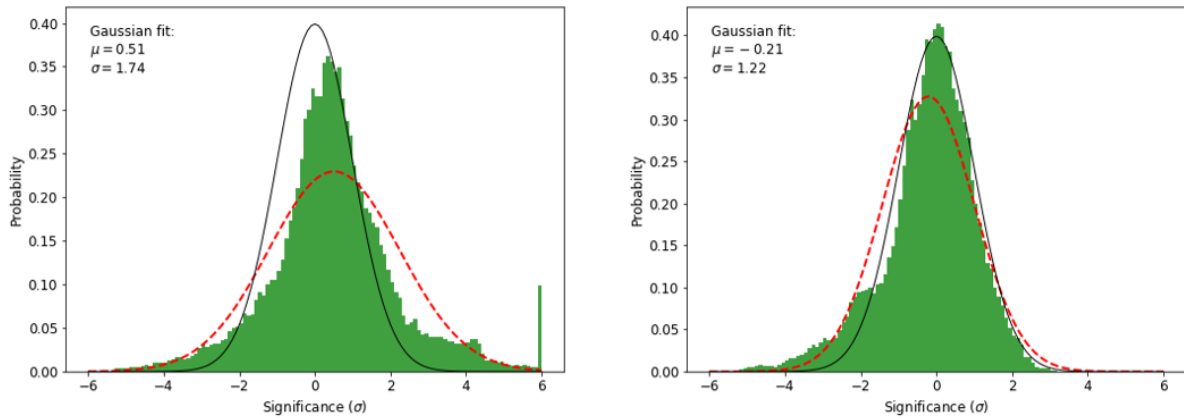


Figure 2.2: Examples with the residuals distribution for two steps in the fitting process of the 60–300 MeV model. The panel on the left is from the beginning of the fitting process and shows a concentration of pixels with very high residuals, indicative of a poor modeling. The plot on the right is the same plot after the final step of fitting. The black line is a standard normal distribution and the red dashed line is the distributions for the best-fit Gaussian to the data.

arbitrary 2D model available through a `.fits` file.

This (after the process described in Section 2.3) generates the gamma-ray model. Comparing the model with the data (the detected photon counts) is straightforward. On simple way is to evaluate the residuals, calculated by subtracting the modeled counts from the real data.

One initial diagnostic tool is to evaluate the automatic-generated plots with the residuals distribution. In the case of a good model, one expects this to be a Normal distribution with $mean = 0$ and $\sigma = 1$ (a standard normal distribution). On the left-hand side of Figure 2.2 we show one of this histograms from an initial round of the fitting process of the low energy model (right after the use of the `optimize` tool). The one on the right-hand side is the final distribution of residuals for the same model. In Appendix H we show the resulting histograms obtained after fitting the three offspring of the Universal Model (i.e., 300 MeV–3GeV, 3–10 GeV and 10–500 GeV).

In both plots of Figure 2.2, the green blocks represent the probability (in %) to find a pixel in the residual map (see Figure 2.3 as an example) with the significance indicated in the horizontal axis. This significance is calculated in units of standard deviation of the pixel value in respect to the mean value of all the pixels in the image. The black line is a standard normal distribution. The red dashed line is the distributions for the best-fit Gaussian to the data. The plot on the left, generated at the beginning of the fitting

process, shows a concentration of pixels with very high residuals ($> 6\sigma$), an indication that many counts are not attributed to modeled sources. The plot on the right was created after the last fitting: the concentration of pixels with high residuals is vanished and the best-fit Gaussian is closer to a standard normal distribution. The plots with the residuals distribution, however, were only used as a very preliminary analysis to the quality of the fit. Other diagnostic tools, described below, were always favored.

The results of our fitting steps discussed in Section 2.3 can be seen in Figures 2.3 and 2.4. These residual maps are useful to assess goodness-of-fit. The colors indicate the significance of the residuals in each pixel, calculated as the difference between the data and the model. Positive residuals indicate regions that are under-predicted whereas negative ones indicate over-predicted regions. Cyan crosses indicate the position of 4FGL sources and green crosses the position of new sources found during the analysis.

In the case of the Universal Model residual map (Figure 2.3) a few regions with negative residuals (in black) correlates with the extent of the Galactic plane. These regions are over-predicted, which means that the model predicts a higher gamma-ray flux than what was detected by *Fermi*-LAT. They are not associated with specific sources, which makes it harder to treat them. If that was the case, a simple round of fitting with the coincident source's parameter(s) freed could resolve that issue. In fact, their distribution along the Galactic plane suggests a strong association with the Galactic diffuse emission model (*galdiff*). As explained in section 1.5.5.1, the spatial distribution of this model follows observations in other wavelengths that try to map the interstellar gas distribution in the Galaxy. It is expected that the observational coverage varies for different regions. Our supposition is that the *galdiff* model is not successful in correcting for the lack of observational data in some regions. The same pattern shows up in the residual map of the 300MeV–3GeV (top right panel of Figure 2.4) but is not seen in the other panels that also originated from the Universal Model (bottom row of Figure 2.4), again, a strong suggestion that it may be originated from the *galdiff* since it is brighter in lower energies. Since the results we obtain through the *Fermi* data are based on the models, a consequence of this over-predicting would be a flux measurement higher than the reality for, at least, the 300MeV–3GeV energy band. But, as mentioned before (and detailed in the Appendix E) the results we obtained in this energy range's model and with a different one with less regions of negative residuals excess were consistent with each other. Also, as will

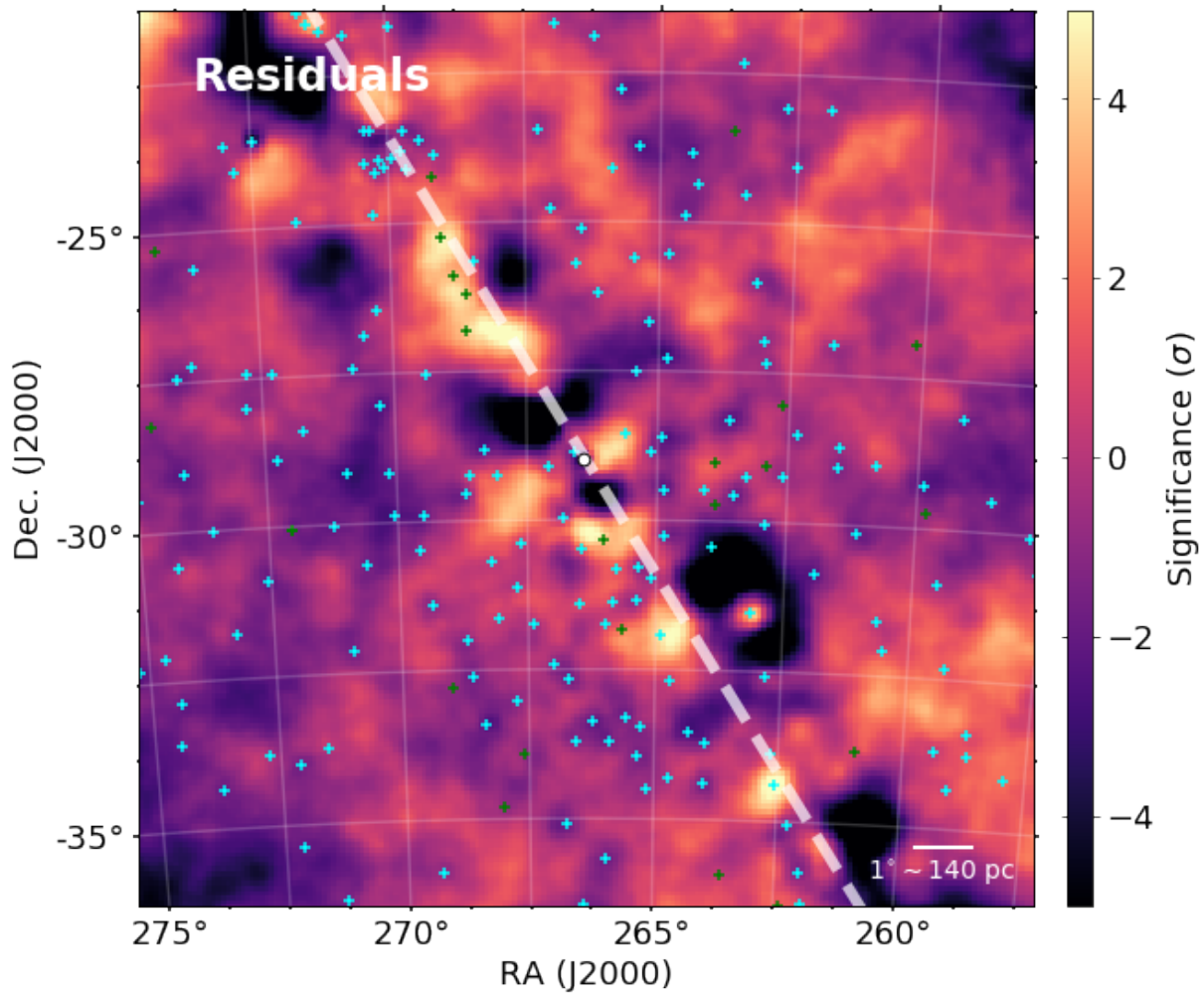


Figure 2.3: Residual map of the Universal Model created in the 100 MeV–500 GeV energy range. The colors show the significance of the residual. The point at the center of the image corresponds to the cataloged source position. 4FGL point sources are displayed as cyan crosses and new sources found during the analysis as green crosses. The white dashed line indicates the direction of the Galactic plane.

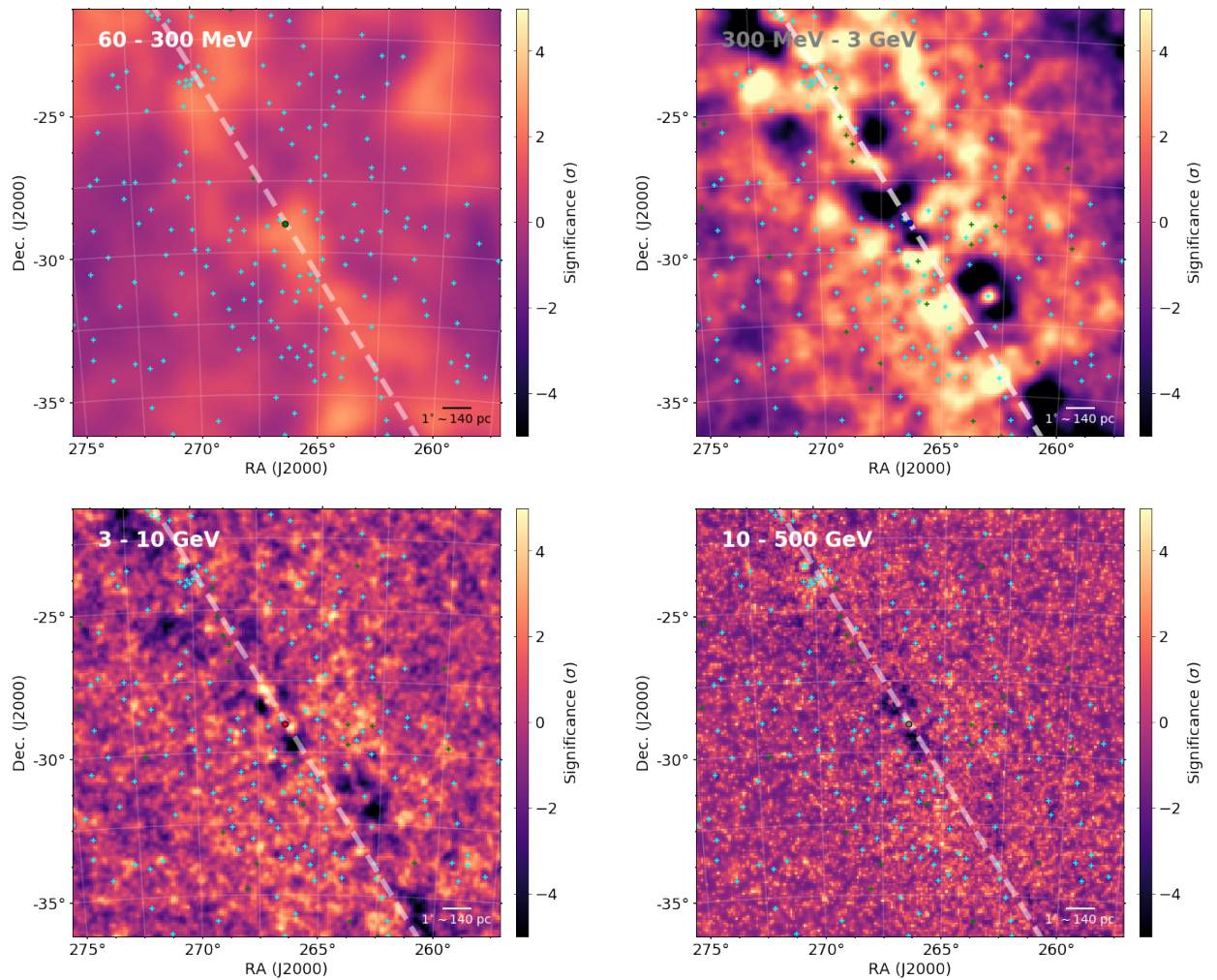


Figure 2.4: Residuals maps at the four different energy ranges. The colors show the significance of the residual. The point at the center of each panel corresponds to the source position obtained in each energy range. 4FGL point sources are displayed as cyan crosses and new sources found during the analysis as green crosses. The white dashed lines indicate the direction of the Galactic plane.

be evident in Section 3.1, the spectral model for the source in the 300MeV–3GeV energy band is coincident with the one reported in 4FGL.

Another diagnostic plot that we generated to evaluate the quality of our fitting are the TS Maps. They are constructed with the `Fermipy`'s `tmap` tool. This tool moves a putative point source (with a power-law spectral model with a spectral index of -2) through the RoI and performs a maximum likelihood fit at each point. The TS is a function of the maximum likelihood of a model with an additional source at a specified location (the putative source in this case) versus a model without it (section 2.2). The TS values computed for the presence of the putative source in each pixel devise the TS Maps. They are presented in Figures 2.5 and 2.6. The former regards the results for the Universal Model and the latter contemplate the results for the four tighter energy bands. In these maps, the colors indicates the TS value at a given position. 4FGL J1745.6–2859 position (obtained with the method described in section 2.4) in each energy range is marked by a colored circle in the center of the images. The crosses follow the same pattern as in Figure 2.4.

The central point source itself is not visible in the maps since it is included in the models. For both the Universal Model (Figure 2.5) and for the 60–300 MeV energy band (Figure 2.6, upper left panel) there is no region with $TS \geq 25$ (i.e. no emission with significance $> 5\sigma$). This shows that the presence of an additional source not already included in the models is unlikely. But in the maps of the high energy (> 300 MeV) models this is not true. These models were created with minimal fitting based on the Universal Model (Section 2.3.1) which led to regions that could be better modeled if its sources were refitted and new sources were added to the models. Nevertheless, as we mentioned before, results we got for these energy models are compatible with the ones obtained through models created specifically to each energy band and that had no region with $TS > 25$ (as presented in the Appendix E).

We also created different versions of the TS Maps. In this case, before using the `Fermipy`'s `tmap` tool, we removed 4FGL J1745.6–2859 from the model (and performed no additional fit). One expects, in this case, to observe TS excess in the region around the position of the source. The goal here is twofold: first as a sanity check to confirm that the source is really there and to search for deviations from a circular region, characteristic of a point source.

The results of this process are shown in Figures 2.7 and 2.8 for the Universal Model

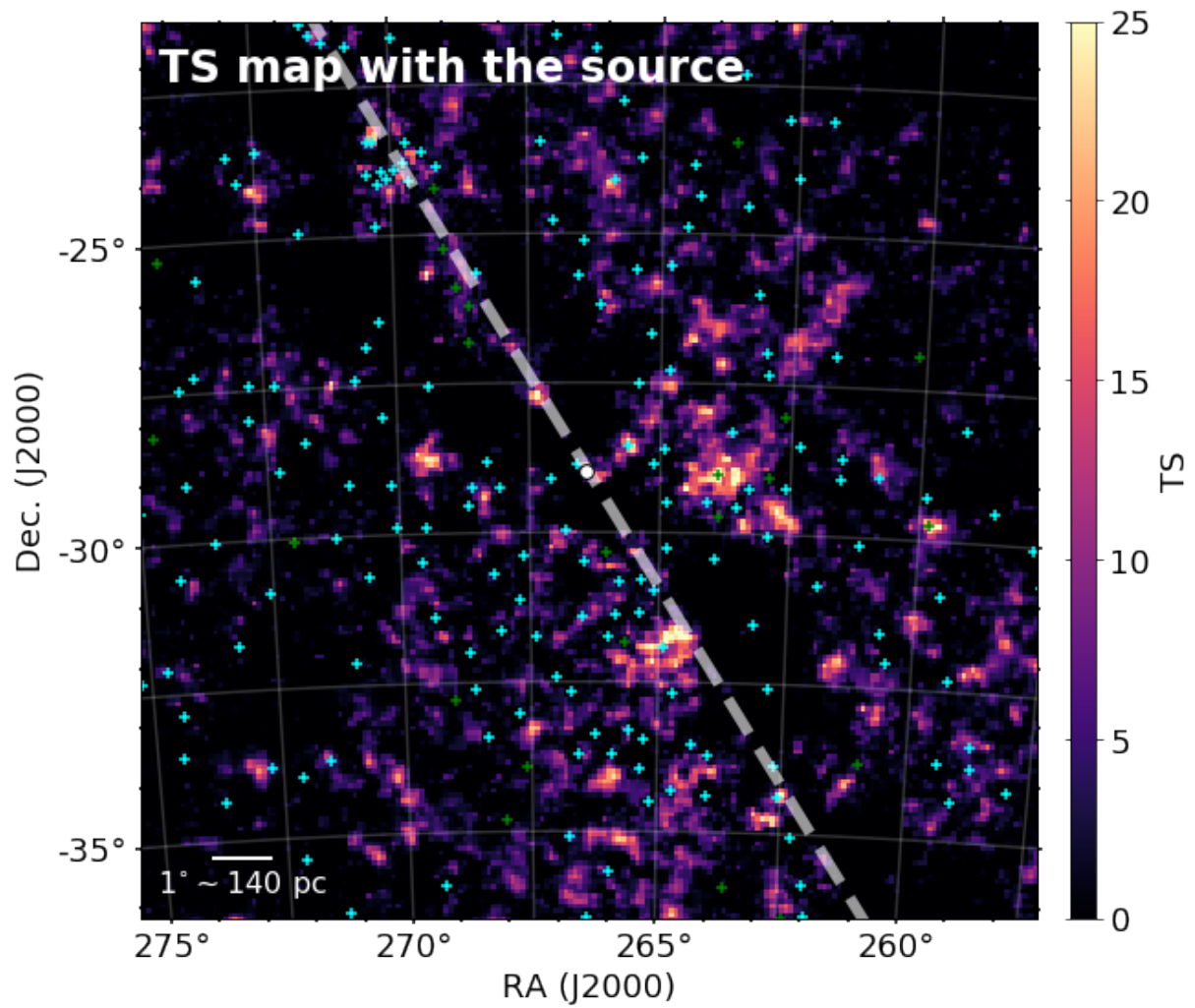


Figure 2.5: *TS* map of the Universal Model created in the 100 MeV–500 GeV energy range. The central point source is not prominent in this map since it is part of the model. The circle at the center of the image corresponds to the central point source cataloged position. 4FGL point sources are displayed as cyan crosses and new sources found during the analysis as green crosses. The white dashed lines indicate the direction of the Galactic plane.

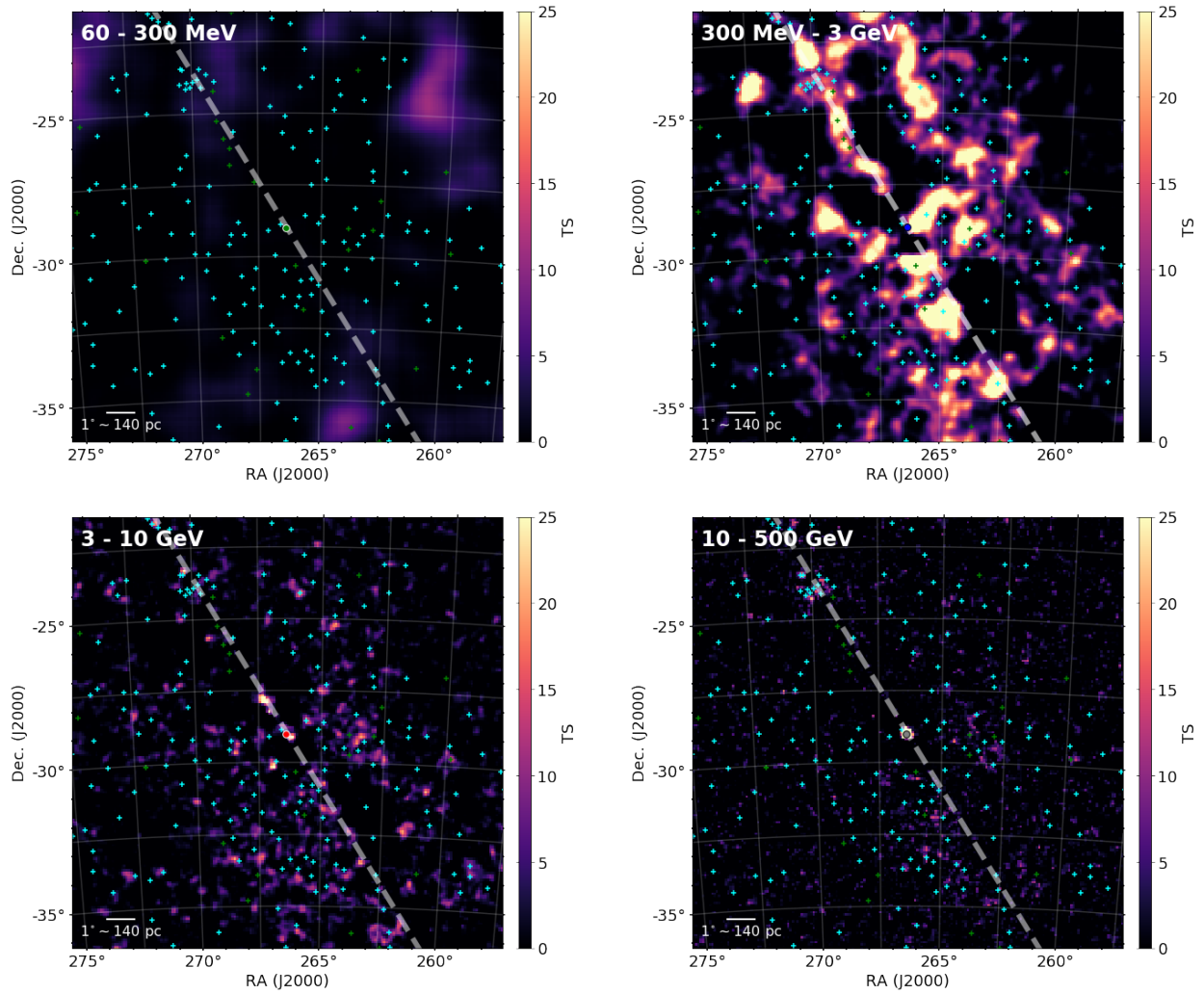


Figure 2.6: *TS* maps of the RoI at four different energy ranges. The circles at the center of the panels correspond to the central point source position obtained in each energy range. 4FGL point sources are displayed as cyan crosses and new sources found during the analysis as green crosses. The white dashed lines indicate the direction of the Galactic plane.

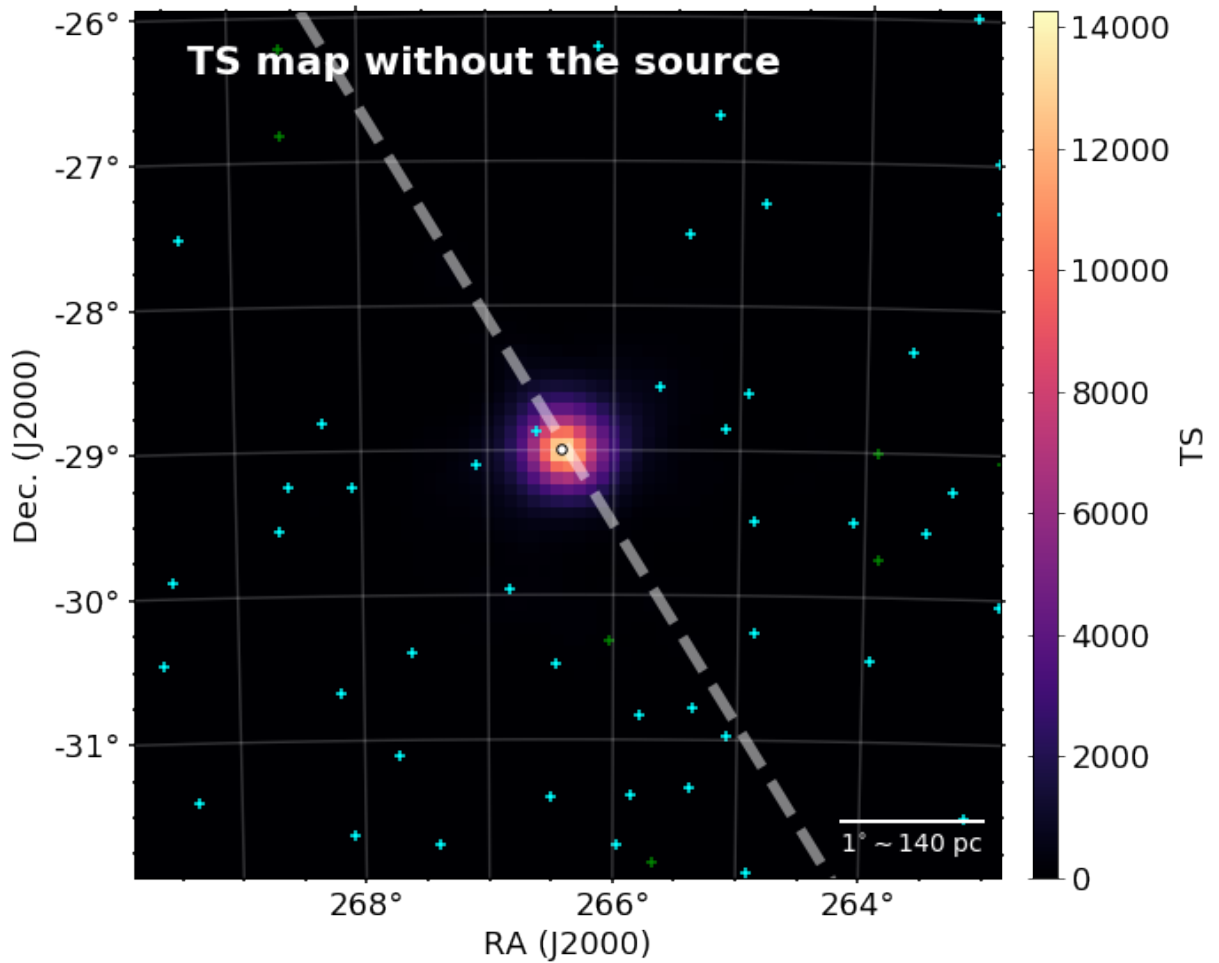


Figure 2.7: TS map of the inner $8^\circ \times 8^\circ$ of the RoI created for the Universal Model created in the 100 MeV–500 GeV energy range without 4FGL J1745.6–2859. The point at the center of the image corresponds to the source position in the catalog. The other 4FGL point sources are shown as cyan crosses and new sources found during the analysis are shown as green crosses. The white dashed lines indicate the direction of the Galactic plane.

and the ones created with tighter energy bands, respectively. They show the TS maps of the inner $8^\circ \times 8^\circ$ of the RoI, evidencing that 4FGL J1745.6–2859 is detected with very high significance in the whole energy range used in this work. The colors and crosses have the same meaning as in the previous Figures. TS excesses are observed in both images and are always coincident with 4FGL J1745.6–2859’s position. The size of the emitting region seems to decrease with energy but this is an outcome of the improvement of *Fermi* LAT’s PSF with energy as mentioned in Section 1.5.3. Although we didn’t perform a quantitative test, no clear deviations from a circle can be observed in these images. Further quantitative investigation on the point source hypothesis will be presented in section 2.4.

The maps shown in this sections are for the final version of each model. But, they

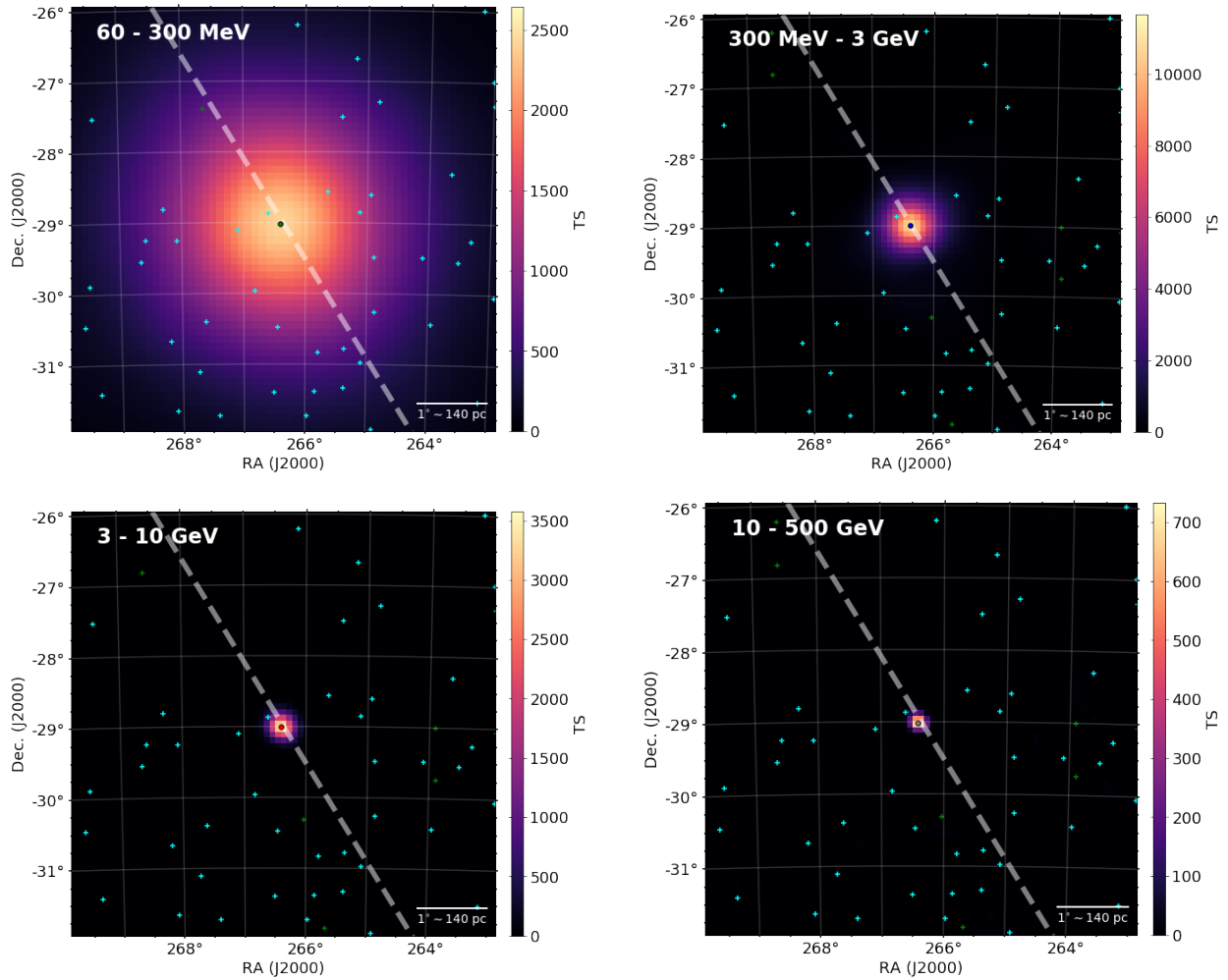


Figure 2.8: TS maps of the inner $8^\circ \times 8^\circ$ of the RoI evidencing the contribution of the central point source. They were constructed after excluding 4FGL J1745.6–2859 from the models, as explained in the text. The point at the center of each panel corresponds to the source position obtained in each energy range. The other 4FGL point sources are shown as cyan crosses and new sources found during the analysis are shown as green crosses. The white dashed lines indicate the direction of the Galactic plane.

were generated and evaluated at every fitting step of the analysis in order to identify sources and/or regions in the RoI that demanded further fitting. This was made by the identification of excesses in the images. In this case, at least the normalization of a source (or several sources) near or coincident with the excess was allowed to vary in a future round of fitting.

With the models created and evaluated, we can move on to the next steps of the analysis. In them, we assess the source position in the four energy bands we studied, its variability in time and its SED.

2.4 Assessing the source position

One of the goals of our work was to identify if 4FGL J1745.6–2859’s position changes with photon energy, this was the main reason behind the division of the analysis into four different energy bands. To identify the source’s position and calculate the likelihood of it being spatially extended, we used `Fermipy`’s `extension` method. In addition to finding the location of the point source, it computes the likelihood of the source being extended with respect to it being pointlike and calculates the extension that maximizes the model likelihood.

2.4.1 Identifying the source position with the `Fermitools`

In this step of our work, we followed exactly the same process for the four tighter energy bands (60–300 MeV, 300 MeV–3 GeV, 3–10 GeV and 10–500 GeV). We used `Fermipy`’s `extension` method. This tool finds the location of the point source, computes the likelihood of the source being extended with respect to it being pointlike and, also, gives the best fit-model for the extension.

To localize the point-like source, the tool first scan the TS map around the cataloged source position. Basically, it investigates maps very similar with the ones presented in Figures 2.7 and 2.8 with the difference that instead of using a power-law spectral model with a spectral index of -2 as the putative source, it uses the spectral model obtained in the last round of fitting. The spectral parameters of every source source in RoI are kept fixed in their current values. This creates a first estimate of its position. The size of

the search region was a circle with radius $0^\circ.5$ centered in the original position of 4FGL J1745.6–2859. Then, in a second iteration, the tool refines the source localization by performing a scan of the likelihood surface in a box centered on the best-fit position found in the previous iteration. The size of this box circumscribe the 99% positional uncertainty contour obtained before. In this second round, the free spectral parameters of every source in the RoI are re-fit. If a peak is found in the likelihood surface and the positional fit succeeds the tool updates the position of the source in the model to the new best-fit position. In this step of the analysis, other than keeping every spectral parameter in the RoI fixed, we tried to let free several different combinations of the normalization and index of the following sources: 4FGL J1745.6–2859, *galdiff*, *isodiff* and the four brightest sources closer than $2^\circ.0$ from the central source. The fitting was not successful in most of these analyses. Of the few of them that returned meaningful results, all of them were compatible in 1σ with each other. We chose, then, to report (in Section 3.2) the one with the highest likelihood value which was the one with every parameter fixed. The model with the background sources fixed were the ones with the highest likelihood in the four energy bands studied.

With this method, we got the position (RA, Dec) of the point source in each of these energy bands and also the statistical uncertainty. In section 2.4.2 we explain how we estimated the systematic uncertainty of this measurement.

Apart from computing its position in the four energy bands, we also tried to estimate if it was compatible with an extended source. This is also part of `Fermipy`'s `extension` method. The method computes a likelihood ratio between a hypothesis of the source being point-like and a best-fit model for extension. To obtain the best-fit extension model, `extension` varies the source width (the 68% containment radius of the point source model) and finds the extension that maximizes the model likelihood. We used a 2D Gaussian as the spatial model for the source. We tried to free the same combinations of spectral parameters in the RoI as we did in the localization of the point-like source (described above). When the `extension` method works flawlessly, it returns the TS of the extension (a measure of the likelihood between the extended versus the point-like hypothesis); the best fit and an UL for the extended source radius; and the location (RA and Dec) of the extended source center. We couldn't get good results in the vast majority of the tries in all energy bands. The most probable culprit for this is the strong source confusion. As we mentioned in

Section 1.5.5.2, the GC is the most crowded region of the *Fermi* sky. The closest source to 4FGL J1745.6–2859 is only $0^\circ.21$ away and there are 21 sources closer than $2^\circ.0$ from 4FGL J1745.6–2859, for instance. Because of that, we decided to report only the 95% confidence level UL of the extension (in Section 3.2). We took care to select the highest meaningful UL obtained in each energy band (presented in Figure 3.4).

2.4.2 Systematic uncertainties

To calculate the total error Δ_{tot} , on the location of the point source we followed the approach used by The Fermi-LAT Collaboration (2019) for the creation of the 4FGL Catalog:

$$\Delta_{tot}^2 = (f_{rel}\Delta_{stat})^2 + \Delta_{abs}^2, \quad (2.12)$$

where f_{rel} is the systematic factor, Δ_{stat} is the statistical error and Δ_{abs} is *Fermi*-LAT’s absolute precision (obtained by the *Fermi*-LAT Collaboration by comparing the location of the brightest cataloged sources with associations with their true positions in the sky obtained in other wavelengths).

For Δ_{abs} , we used the value of $0.^\circ0068$ (The Fermi-LAT Collaboration, 2019) in the two energy bands below 3 GeV and $0.^\circ0075$ (Ajello et al., 2017) for higher energies bands (both values at the 95% confidence level). For f_{rel} we used 1.1 for the three lowest energy bands and 1.2 for the 10–500 GeV band. These values are estimated by the *Fermi*-LAT Collaboration with validation studies performed with the Vela pulsar and stacked high-latitude AGNs which are less subject to contamination from the diffuse Galactic emission. Its value is of ~ 1.05 in the 100 MeV–10GeV and increases for lower and higher energies, as shown in Figure 1.16. We decided to use more conservative values since the source we are studying lies in the most densely packed region of the gamma-ray sky. The Δ_{stat} were the 68% positional uncertainty obtained during the analysis.

The uncertainties we report in Table 3.1 and Figures 3.2 and 3.3 correspond to the value of Δ_{tot} computed above.

2.5 Variability of the GC

Fermi covers the whole sky every three hours since August 2008 therefore its data are specially suitable to investigate temporal behavior of a gamma-ray source. In this section we explain how, using `Fermipy`'s method `lightcurve`, we created LCs for 4FGL J1745.6–2859. We used the Universal Model as a baseline. In a nutshell, this process is very similar to the fitting we used to create the Universal Model. But, now, we also separate the data in time bins.

Additionally in this section we present the methods we used to search for periodicity and variability in the LCs.

2.5.1 Creating a light curve

We start with the Universal Model and use the method `lightcurve` from `Fermipy`. This method fits a source, just like we described in Section 2.3, but now in a sequence of time bins. The tool returns several quantities in each time bin: flux, spectral parameters, TS , among others.

Since the creation of LCs is a very time consuming process, we used the SLAC National Accelerator Laboratory computer cluster, operated by Stanford University (as a member of the *Fermi*-LAT Collaboration, we have access to this resource). Even using the cluster, the creation of the LC takes a long period of time. The amount of data generated during the creation of a LC is huge: it is about the same volume of data created in the fitting process (of a few tens of GB) multiplied by the number of time bins. Because of storage limitation in the cluster, we had to split the LC in several smaller jobs. The creation of the ~ 11.3 years LC with 45 days bins (91 bins in total) took almost a month (in real time) to be generated.

It is possible to free other sources of the RoI so their spectral parameters can also vary during the fitting. It is important to avoid the contamination from other nearby sources variability in the LC of the source of interest. In order to save time, we investigated every source closer than 5° from the center of the RoI in the 4FGL (total: 105 sources). The catalog offers a measurement of the probability of each source being steady (`variability_index`). We started by selecting all the sources with a value of `variability_index` consistent with a variable source (the sample reduced to 85 sour-

ces). Then, we eliminated the sources with average flux smaller than 10% of 4FGL J1745.6–2859’s average flux. We finished with only 4 sources that are: a) close to 4FGL J1745.6–2859; b) variable; and c) with flux above 10% of 4FGL J1745.6–2859’s. All of this sources are identified in the 4FGL as either a pulsar, a pulsar wind nebula or a globular cluster (whose gamma-ray emission is associate with mili-second pulsar; de Menezes et al. 2019). These sources are not expected to be variable in the time ranges we are working with. The diffuse sources (*galdiff* and *isodiff*) are also not variable. For this reason, we decided to let free only the spectral parameters of our source of interest during the creation of the LCs.

First, we created a LC with 45 days bins. Then, since we did not find any period of significant variability, we decided to create a LC with 15 days bins (which took more than 2 months of processing). Smaller time bins gives resolution for the LC. At the same time, the number of photon available for the fitting decreases, reducing the statistical significance of the detections.

The output of the `lightcurve` method is the source’s photon and energy flux. It also gives the TS of the source in each time bin. Using it, we can evaluate if the source was detected in specifics time bins and, if it was not, proceed accordingly reporting not the (energy or photon) flux but an UL. As a threshold for the detection significance in the time bins, we used $TS > 16 \approx 4\sigma$.

Additionally, we created three other LCs, using the three models created from the Universal Model in the 300 MeV–3 GeV, 3–10 GeV and 10–500 GeV energy bands. Since the amount of counts in these models are significantly smaller than in the Universal Model ($\sim 1/3$ of the counts), we had to work with larger time bins in order to obtain points with good significance. We decided for these sizes empirically, testing LCs with different times bins (> 45 days) and checking the source’s TS . We ended with 90 days bins for the energy bands 300 MeV–3 GeV and 3–10 GeV, and 180 days bins for the remaining band.

We did not create LCs for the lowest energy band used in this work (60–300 MeV). The main reason is that the tighter energy bands LCs were created with the goal of searching for “echoes” in the gamma-ray flux. As will be clear in Figures 3.2 and 3.3, the centroids of the emission in the 3 highest energy bands are displaced from the position of Sgr A* in reverse order of energy. We were interested in searching for some signal of variability in the inner centroid being reproduced in the outer centroids after the light crossing time

between these regions. Figure 3.2 shows that this analysis was not possible for the 60–300 MeV energy band because its position has larger uncertainty and it is spatially consistent with the emission in the 3 higher energy bands.

With the LCs created, we proceeded looking for periods of variability of the source. We describe how we performed this search in Section 2.5.3.

2.5.2 Systematic uncertainties

In this section we estimate the contribution of systematic uncertainties in the LC. They arise from the (incompletely corrected-for) variation of the acceptance as a function of time, which impacts the flux measurements. This is governed by the systematic uncertainty on the effective area. This is between 3% and $\sim 20\%$ (Figure 1.15), depending on the analysis conditions.

In order to refine the estimate of the systematic uncertainty, we can quantify the apparent flux variation of bright and steady sources such as pulsars. This method was developed by Dr. Benoit Lott (Centre d'Études Nucléaires de Bordeaux Gradignan, Université de Bordeaux) to the *Fermi*-LAT Collaboration.

The standard deviation of the apparent flux distribution is the quadratic sum of the statistical and systematic uncertainties. So we can simply subtract the statistical uncertainty from the ones obtained through the `lightcurve` method to get to the systematic uncertainty.

Dr. Lott made the estimation in 2008 using the first ~ 2.5 months of data from the Vela pulsar, which is a very bright gamma-ray source. The method starts with the creation of a LC for Vela with the flux normalized to 1. Then, they find the mean value of the distribution of the uncertainties in the LC (i.e., the mean value of the error bar in the LC). They got $\sigma_{mean} = 0.13$. Finally, they make the distribution of relative dispersion:

$$Rel. \ dispersion = \frac{F_i - F_{mean}}{\sigma_i} \quad (2.13)$$

The expected distribution for the relative dispersion, supposing that the error bars are purely statistical, is a Gaussian distribution with unity width. The standard deviation of this distribution was found to be 1.23. Then, they simply estimate the systematic variation as: $0.13 \times \sqrt{1.23^2 - 1^2} = 0.093$, which translates to 9.3% systematic uncertainty. Other

members of the *Fermi*-LAT Collaboration, using different methods, arrived at the same value.

We follow Dr. Lott’s method but using a different pulsar. We chose to use the 4FGL J1747.2–2957 source. This is identified as a pulsar (PSR J1747-2958) ~ 5 kpc away from Earth (Hales et al., 2009) that lies only $1^\circ.03$ from the center of the RoI. It is important to select a source close (in the plane of the sky) to the center of the RoI to assure that it is also subject to the same confusing environment as 4FGL J1745.6–2859. Also, since it is a source in the RoI, we could use exactly the same analysis used in the Universal Model, which made the comparison between the LCs possible. We started by simply running a LC focused in this source as we had done to 4FGL J1745.6–2859 (in Section 2.5.1). In Figure 2.9 we show the 15 days bins energy flux LC with the average flux normalized to 1.

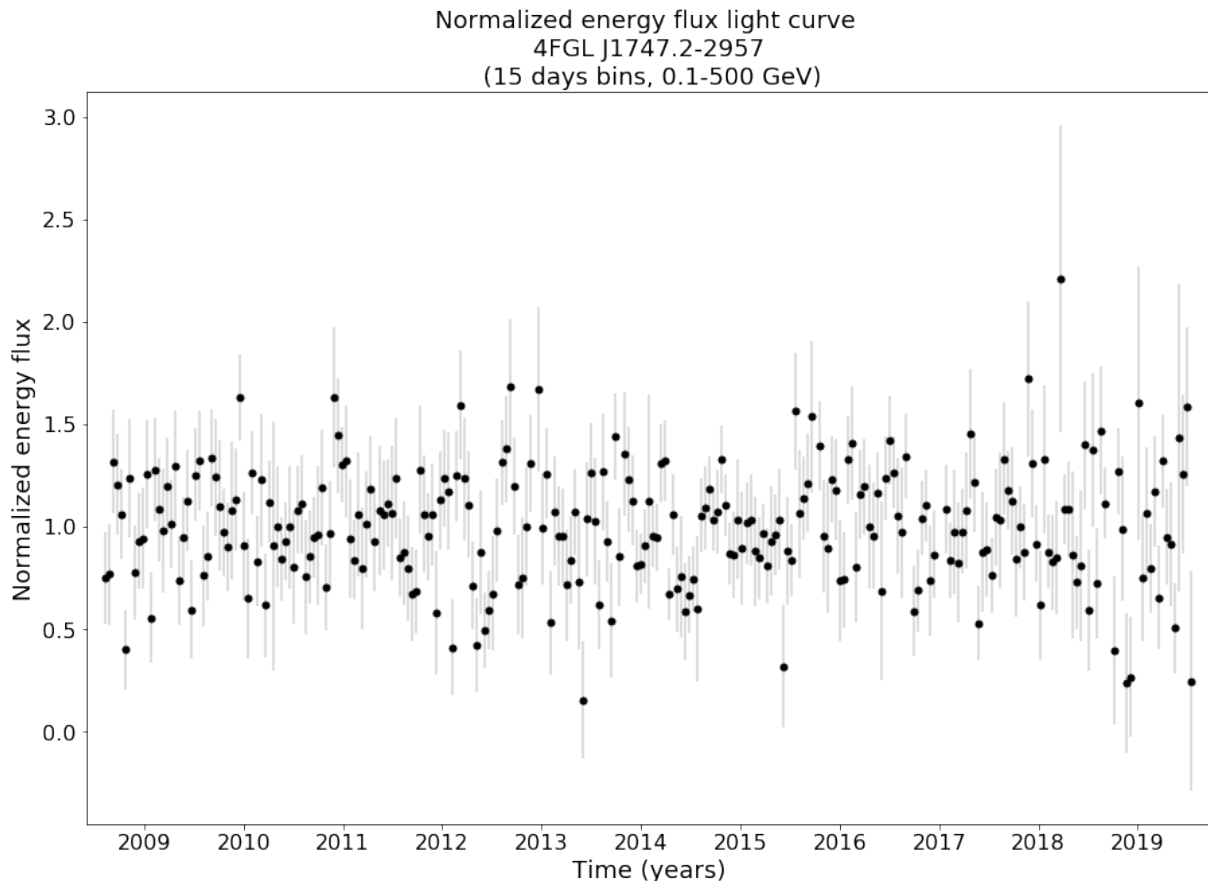


Figure 2.9: 15 days average normalized energy flux LC of 4FGL J1747.2–2957 (pulsar PSR J1747-2958). This is a presumably steady sources and its flux variability is used to estimate the systematic uncertainty in the data. This LC was created following the exact same data selection and methods used to create 4FGL J1745.6–2859 LC.

Then, we prepared the LC’s uncertainties distribution, shown in Figure 2.10. We are

interested in the average value of this distribution: 0.258.

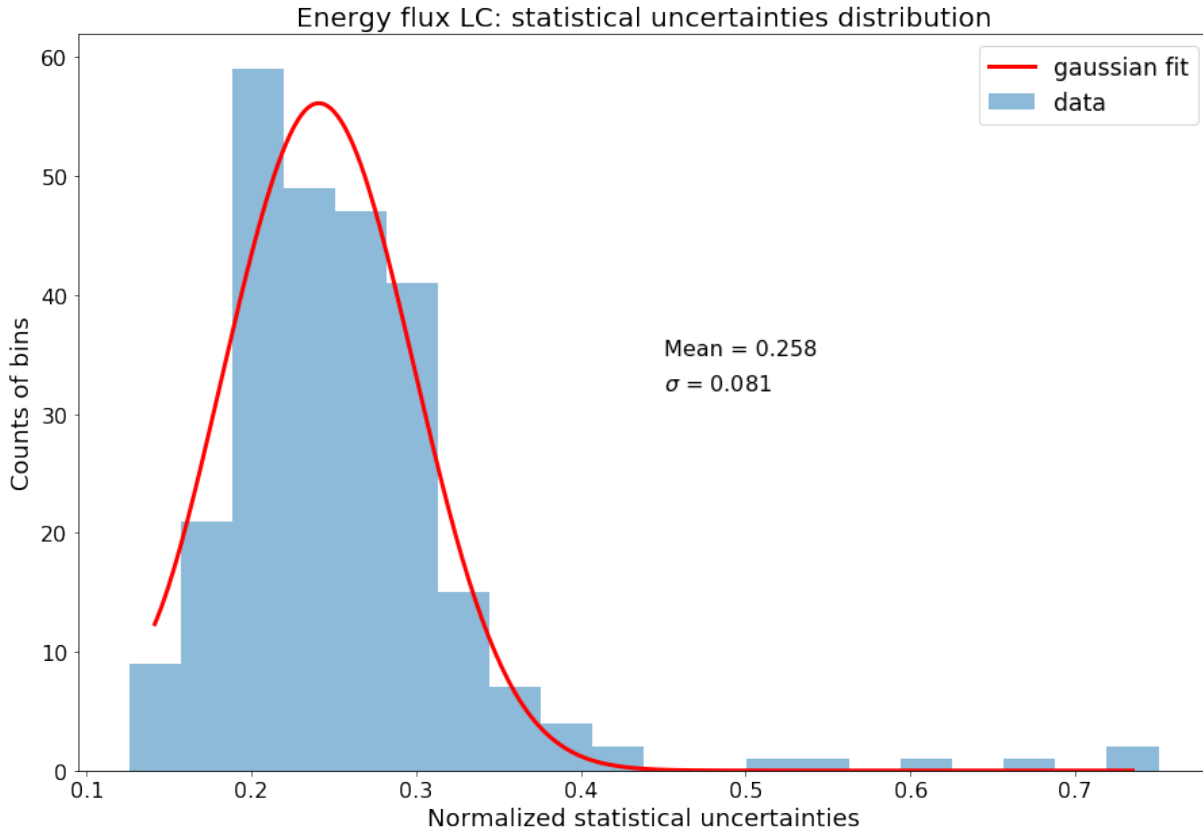


Figure 2.10: Histogram of the statistical uncertainties of the 15 days average normalized energy flux LC of 4FGL J1747.2–2957 (Figure 2.9). The dotted red line is a normal distribution with the same mean and standard deviation of the statistical uncertainties (the values are shown in the Figure).

The next step was to prepare the distribution of the relative dispersion. The value of the relative dispersion was calculated as in Equation 2.13. In Figure 2.11 we show the distribution of these values. The standard deviation of this distribution is 1.109. This leads to a systematic uncertainty of $0.258 \times \sqrt{1.109^2 - 1^2} = 0.124$, or 12.4%.

We followed this same procedure with the photon flux LC of 4FGL J1747.2–2957 and obtained a systematic uncertainty of 9.8% (the plots are available in Appendix I). These results indicate that the statistical uncertainty dominates the error bars in the LCs.

We also evaluated, using the same process described above, the systematic uncertainties of the other LCs we created, except for the 10–500 GeV energy band. In this particular case, we could not apply this method because the pulsar we used as a “standard candle” for the analysis (4FGL J1747.2–2957) is very weak in this energy band and hence it was not detected in the LC (the source has $TS \lesssim 5$ in every time bin of its 180 days LC). For this energy band we estimate the systematic uncertainty to be $< 20\%$. This is based on

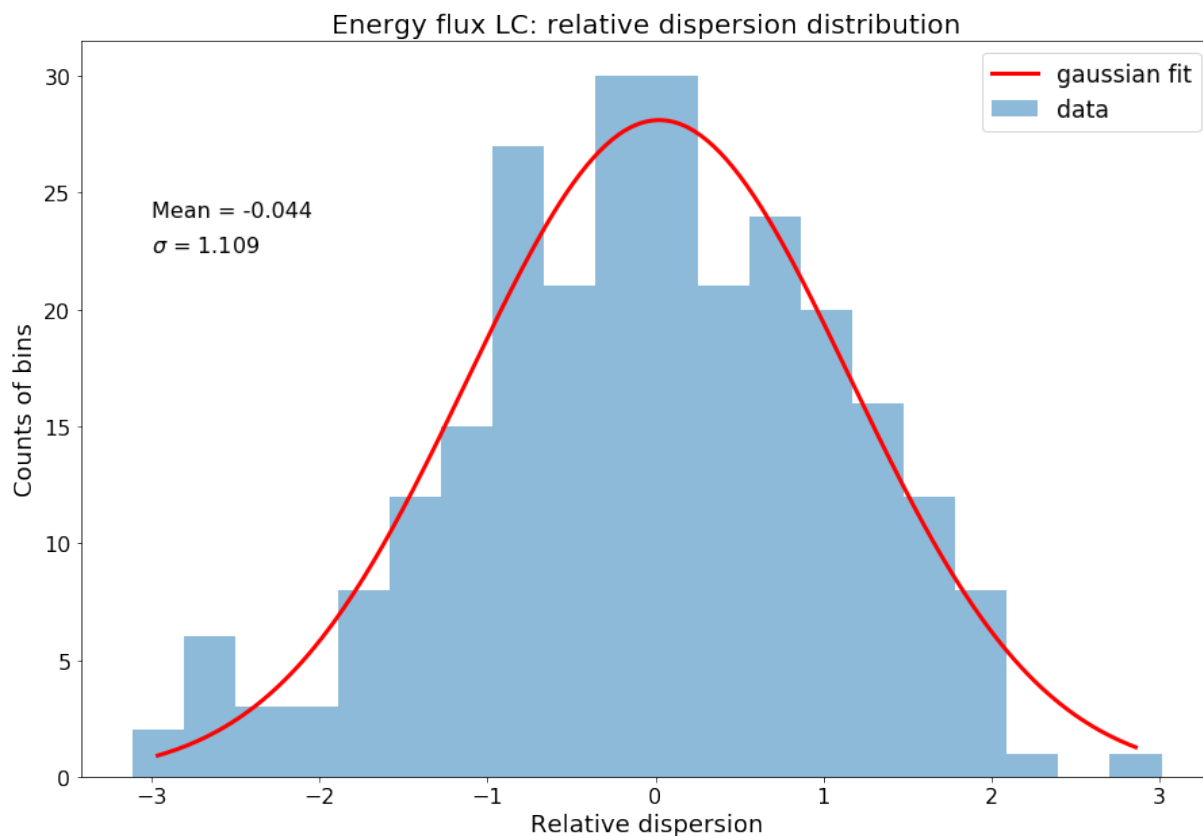


Figure 2.11: Histogram of the relative dispersion distribution of the 15 days average normalized energy flux LC of 4FGL J1747.2–2957 (Figure 2.9) calculated following Equation 2.13. The mean and standard deviation of this distribution are also shown in the Figure.

two arguments. First, the plot in Figure 1.15 indicates that 20% is an upper limit for this uncertainty. Also, the estimated systematic uncertainties of the two other energy bands are much smaller than $< 20\%$, and *Fermi*-LAT’s effective area uncertainty decreases with the size of the time bin (180 days in this case, the largest used in this work). The values we obtained for all LCs reported in this work are listed in Table 2.1. In Appendix J we show the plots equivalent to Figures 2.9, 2.10 and 2.11 for the other LCs. We also report the relevant statistics to obtain the systematic uncertainties in each case.

Table 2.1 - The estimated systematic uncertainties of the LCs used in this work.

Energy band (GeV)	Bin size (days)	Systematic uncertainty (%)	
		energy flux	photon flux
0.1 – 500	15	12.4	9.8
0.1 – 500	45	9.8	9.0
0.3 – 3	90	6.0	6.4
3 – 10	90	9.0	7.0
10 – 500	180	< 20	< 20

2.5.3 Searching for variability in the LCs

Following the methods previously outlined, we now have these photon and energy flux LCs for the GC:

- with 45 days bins created based on the Universal Model (energy range: 100 MeV–500 GeV);
- with 15 days bins created based on the Universal Model;
- with 90 days bins in the 300 MeV–3 GeV energy band;
- with 90 days bins in the 3–10 GeV energy band; and
- with 180 days bins in the 10–500 GeV energy band.

As examples of the results we obtained, we show the 15 days bins energy and photon flux LCs in the upper and bottom panels of Figure 2.12, respectively (the other LCs are shown in Section 3.3). They are used to demonstrate the methods we employed to search for variability in the LCs. The error bars correspond to the 68% confidence level uncertainty. For the time bins in which the TS of the source is < 16 , we show the 95% confidence level UL.

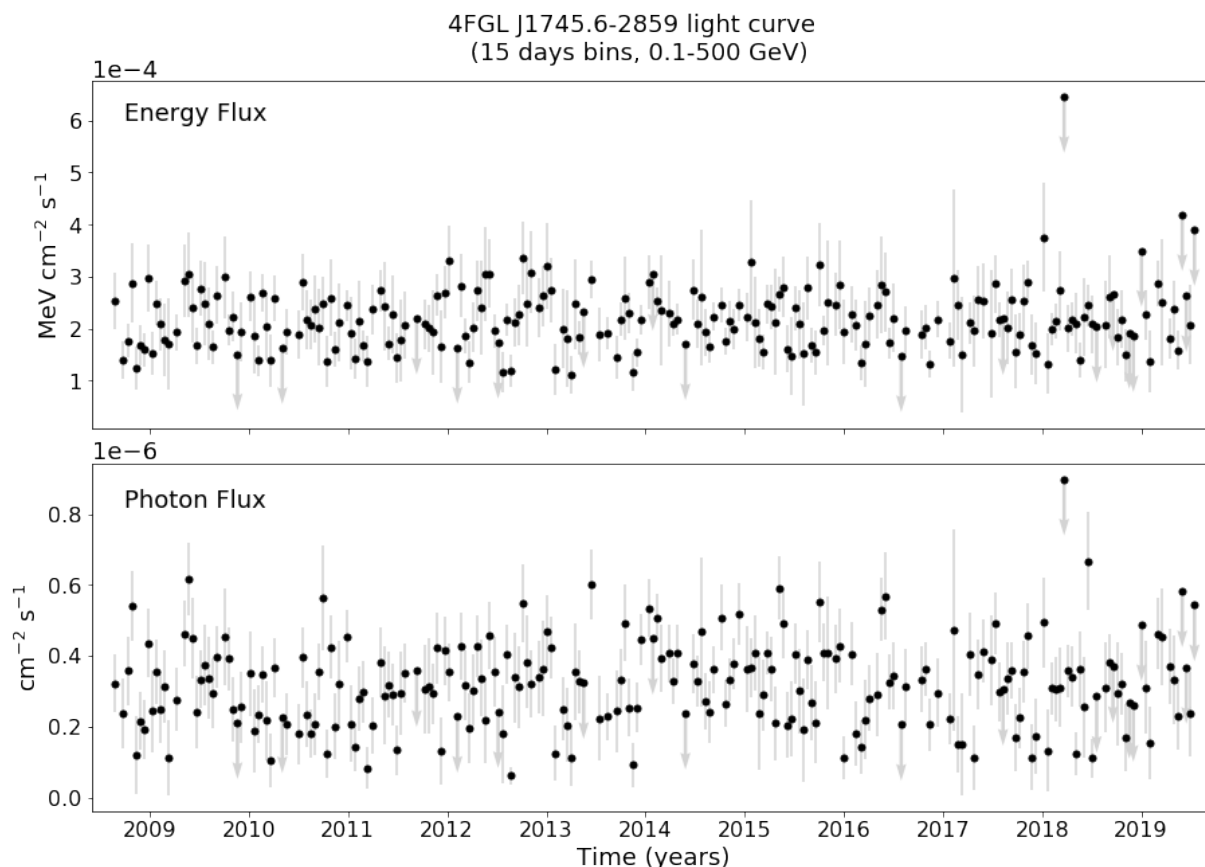


Figure 2.12: 15 days bins LCs of 4FGL J1745.6–2859 in the 100 MeV–500 GeV energy band. In the upper panel we show the energy flux and in the bottom panel we show the photon flux LC. The error bars correspond to the 68% confidence level uncertainty. For the time bins in which the TS of the source is < 16 , we show the 95% confidence level UL.

A visual inspection of both panels of Figure 2.12 (and the others shown in Section 3.3) suggests no significant time variability. We tested this hypothesis using several different approaches that we described below in order of growing level of complexity. In the analysis below, we focus on the 15 days bins LCs created for the 100 MeV–500 GeV energy band. Since the 15 days bins LCs have much better time resolution than the 45 days bins, we disregard the later along this thesis. If the reader is interested in the 45 days bins LCs, they are addressed to Appendix K. Some of the plots regarding the other LCs are shown in Section 3.3, when appropriate.

First, we calculated the mean flux during the whole period covered by the LCs (~ 11.3 years) to compare with the flux in each bin. This is shown in Figure 3.6 at Section 3.3. The flux observed in most of the time bins is compatible with the average flux, what is an indication that the source is in a quiescent state most of the time. This does not rule out the hypothesis of variability, of course. We decided to use the rolling average of the flux to

look for bins that with fluxes significant higher (or lower) than the neighboring bins. We calculated the rolling average flux in groups of 5 bins consecutive bin (= 75 days in total). The rolling average values were plotted on the date corresponding to the central of the 5 bins in Figure 3.7 (Section 3.3).

These comparisons with the average fluxes are only preliminary examination of the data. They did not show any sign of variability, though. We moved on to more detailed and statistically supported methods.

We can check if the variability in the LCs arises from a random process by observing its probability density function. It can be estimated by fitting a model function to histograms of the observed flux (and its logarithm). We used a Gaussian distribution, representative of a normal random process. Also, there are evidence suggesting that the gamma-ray fluxes in blazars, intrinsically variable sources, are preferentially log-normally distributed (Sinha, A. et al., 2016; Shah et al., 2018). Log-normal flux variability is not unusual for accreting galactic sources (such as X-ray binaries, Uttley and McHardy 2001) and it has been linked to the underlying accretion process. We tested, therefore, whether the flux distributions are distributed normally or log-normally.

To inspect if 4FGL J1745.6–2859 flux variation in time is normally (representative of a random process) or log-normally (compatible with a the flux distribution of a flaring source) distributed we performed 3 different tests to quantify whether the data follow a Gaussian distribution. The results of theses tests are in Section 3.3 (Tables 3.2 and 3.3). The first is the Shapiro-Wilk test (Shapiro and Wilk, 1965), that quantifies how likely it is that the data was drawn from a Gaussian distribution. The second is the D’Agostino’s K^2 test (D’Agostino, 1971; D’Agostino and Pearson, 1973), a goodness-of-fit measure of departure from normality. This test is based on transformations of the sample kurtosis (that quantifies how much of the distribution is in the tails) and skewness (a quantification of how much a distribution is asymmetric). Finally, the Anderson–Darling test (Stephens, 1974) evaluates whether a data sample comes from one of among many known data samples (in our case, a Gaussian distribution). We used the open-source Python library SciPy (Virtanen et al., 2020) functions `scipy.stats.shapiro`, `scipy.stats.normaltest`, and `scipy.stats.anderson` to do the testings. To perform the tests, we assumed that our data followed a Gaussian distribution (or a log-normal distribution for the logarithm of the photon flux), which means that this was the null hypothesis (H_0) we were trying to

reject.

For the Shapiro-Wilk and the D’Agostino’s K^2 tests we used the p-value (p) obtained to decide whether we reject H_0 or not. The p-value is interpreted as the probability of obtaining test results at least as extreme as the results actually observed, under the assumption that the null hypothesis is correct. We chose 5% ($\alpha = 0.05$) as a threshold. If a test resulted in an $p > \alpha$ we would consider it a fail to reject H_0 , hence the distribution was considered compatible with a Gaussian (or log-normal, when appropriate) distribution. Otherwise, we would consider the distribution not Gaussian (or not log-normal).

Each of these `SciPy` tests also returns a test statistic, a quantity that can be interpreted in the context of the test via comparing it to critical values from the distribution of the test statistic relevant to each test. For the Anderson–Darling test we compared the statistic with a list of critical values returned by the function, which allows a more thorough interpretation of the result. A test with *statistic* > *critical value* results in a rejection of H_0 .

Finally, we tested if the source flux displayed a global trend during the ~ 11.3 years observation. To do this, we simply fitted a linear function to the observed data following the Markov chain Monte Carlo (MCMC) method presented by Hogg et al. (2010) with the aid of the `emcee` Python implementation (Foreman-Mackey et al., 2013). During the fitting process, the error bars of our data were taken into account.

To assess if the LCs have a global trend in time, we are interested in the angular component of the linear fit, which gives the slope of the function and, hence, shows if the source’s flux increased, decreased or kept constant in the observed period. Angular components close to (or compatible with) zero indicate that there is no measurable global trend in the data. In Section 3.3 we show the results of these fittings.

All these tests and analyses were performed for the 15 and 45 days LCs created in the 100 MeV–500 GeV energy range. For the other LCs (the ones with 90 days bins in the 300 MeV–3 GeV and in the 3–10 GeV energy bands and the one with 180 days bins in the 10–500 GeV energy band) we did not accomplish the Gaussian fit. The reason is the lack of statistics caused by the larger time bins and consequently small number of time bins.

2.6 Spectral Energy Distribution

In this section we explain how to use *Fermi* data in order to create the SED of a source. Again, the process is very similar to the one used to create the Universal Model. But, now, we separate the data in energy bins channels. Each channel will give rise to one point in the SED. We used the Universal Model as the baseline. When the Universal Model was created (Section 2.3.1) we turned on the energy dispersion correction to reduce the systematic uncertainties in the measurements.

We used `Fermipy`'s `sed` method. It performs independent fits for the flux normalization of a source in bins of energy. The source's original spectral model (the one obtained after fitting the Universal Model) is used as prior. The normalization in each bin is fit using a power-law spectral parametrization with an index that can be fixed or allowed to vary over the energy range according to the local slope of the original spectral model. We explored both possibilities.

We chose to split the energy band (100 MeV–500 GeV) in 8 bins per decade of energy, which accounts for 30 bins in the SED. Since *Fermi*-LAT's energy resolution varies with energy, it is important to choose an energy binning that is fine enough to capture this energy dependence and, at the same time, that is wide enough to have sufficient counts to get statistically significant results. Previous versions of this analysis indicate that using more than 8 bins per decade leads to many points with low significance. This empirical test is corroborated by the *Fermi*-LAT Collaboration's suggestion⁶ of using between 8 and 10 energy bins per decade.

During the SED creation, we can chose to also free other sources in the RoI. We tried different combination of free parameters, going from zero to a total of 5 free (normalization only) background sources. The background sources allowed to vary were selected among the brightest ones in the central 4° of the RoI plus *galdiff* and *isodiff*.

We created a total of 7 SEDs with different selection of free parameters. To chose which one to report, we used the Akaike Information Criterion (AIC) (Akaike, 1974). Given a collection of models (in our case, the resulting SEDs are models, as explained in Section 2.2) for a set of data (the observed counts), this method estimates the quality of each model, relative to each of the other models. Thus, AIC provides a means for model selection.

⁶ fermi.gsfc.nasa.gov/ssc/data/analysis/documentation/Pass8_edisp_usage.html

This allows us to select the best SED. The best-fit model according to AIC is the one that explains the greatest amount of variation using the fewest possible independent variables. AIC can be calculated as:

$$AIC = 2K - 2\log(\mathcal{L}) \quad (2.14)$$

where K is the number of independent variables in the model and $\log \mathcal{L}$ is its log-likelihood. Models with lower AIC are considered better.

We calculated the AIC for the 7 models. The best model according to this criteria had the following free parameters: normalization and the index of 4FGL J1745.6–2859, the normalization of 3 point sources (4FGL J1747.2–2957, 4FGL J1742.5–2833 and 4FGL J1745.8–3028e) and the normalization of the diffuse components (*galdiff* and *isodiff*).

During the SED creation, the data is split into energy bins. The TS of the source of interest (see Section 2.2.1.2) is calculated for every bin (similarly as in the LCs creation). We decided to report the 95% confidence level UL for the energy bins in which the source was detected with $TS < 5$ (which corresponds to $\lesssim 2.2\sigma$). For the other energy bins, we report the energy flux ($E^2 dN/dE$, see Equations 1.1 to 1.3) and the 1σ uncertainty.

The resulting SED is reported in Section 3.4.

Results

In this section we present the results obtained with our work for the gamma-ray properties of the GC. We start with 4FGL J1745.6–2859’s spectral models. Then we report its gamma-ray fluxes in four different energy bands. After that, we move on to the updated position of the source in the same bands. Finally, we describe the variability of the source and its SED.

3.1 Spectral model

In our work, we subdivided the analysis into four energy ranges. In Figure 3.1 we compare the results of these four models with the log-parabola spectral model adopted in the 4FGL Catalog for 4FGL J1745.6–2859. We can see there is a considerable discrepancy between the low energy custom model (60–300 MeV) and the Universal Model. This is the result of the different modelling for the 60–300 MeV band, as discussed in Section 2. Only part of this difference can be explained by the addition in the 60–300 MeV model of a new source which is not included in 4FGL but listed as PS J1750.6-2723 in Appendix F, at a distance smaller than 2° from 4FGL J1745.6–2859. This difference means that the gamma-ray flux for this energy band might be underestimated. It is important to notice that the GC is among the most complicated regions in the sky to study with *Fermi* LAT data: in addition to the high density of sources, the region is also engulfed by the Galactic diffuse emission. These issues become more severe in lower energies due to the large PSF.

The central source was detected in the four energy ranges used in the analysis with TS varying from ~ 300 to ~ 10000 , corresponding to detections with significance above

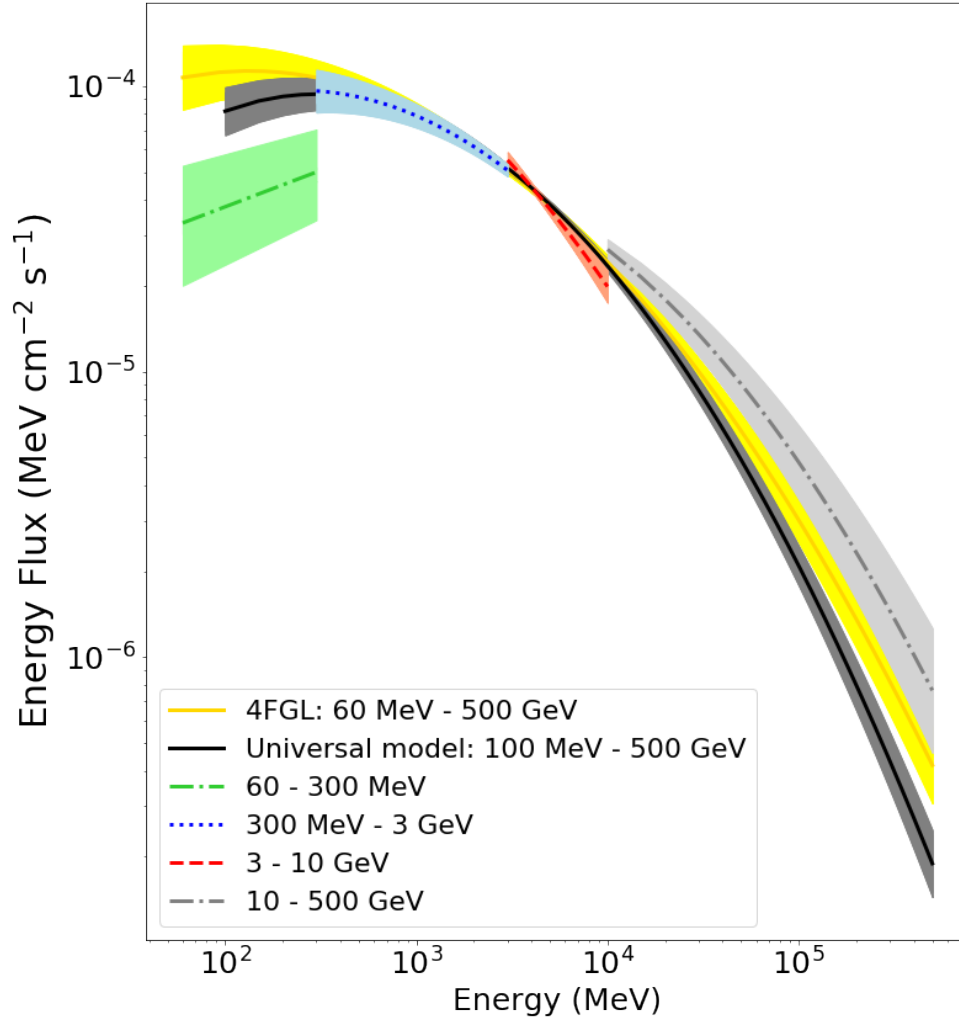


Figure 3.1: Comparison of the best-fit spectral models for 4FGL J1745.6–2859. The black line shows the Universal Model created in the 100 MeV–500 GeV energy range. It was later used as basis to create models in three different energy bands: 300 MeV–3 GeV (blue), 3–10 GeV (red) and 10–500 GeV (gray). They were created with log-parabolas templates. A power-law model was used in the 60–300 MeV energy range (green). The log-parabola spectral model used by the 4FGL Catalog for this source is also shown (yellow).

background ranging from $\sim 17 \sigma$ to $\sim 100 \sigma$. Its photon and energy flux were also measured and the results are shown in Table 3.1. We also report the results of the Universal Model (100 MeV–500 GeV).

Table 3.1 - Results from likelihood modeling of the central point source. The last line presents the results for the universal model. The photon and energy flux uncertainties include only statistical errors.

Energy range (GeV)	TS ¹	Photon flux (cm ⁻² s ⁻¹)	Energy flux (erg cm ⁻² s ⁻¹)	Centroid ² (°)	Positional Uncertainty ³ statistical (°)	total (°)	Extension UL ⁴ (°)
0.06 – 0.3	2246	$(5.17 \pm 0.16) \times 10^{-7}$	$(1.06 \pm 0.03) \times 10^{-10}$	266.407, -29.013	0.045	0.050	0.2404
0.3 – 3	10522	$(1.49 \pm 0.17) \times 10^{-7}$	$(1.99 \pm 0.20) \times 10^{-10}$	266.394, -28.997	0.005	0.009	0.1141
3 – 10	3618	$(8.94 \pm 0.22) \times 10^{-9}$	$(6.69 \pm 0.17) \times 10^{-11}$	266.406, -29.003	0.005	0.009	0.0785
10 – 500	321	$(1.23 \pm 0.11) \times 10^{-9}$	$(3.45 \pm 0.35) \times 10^{-11}$	266.415, -29.010	0.005	0.010	0.0478
0.1 – 500	14724	$(2.83 \pm 0.08) \times 10^{-7}$	$(3.26 \pm 0.05) \times 10^{-10}$				

¹ $\sqrt{TS} \approx$ detection significance of the source in each energy range

² RA and Dec. corresponding to the emission centroid in degrees

³ 68% positional uncertainty

⁴ 95% confidence level

Assuming a distance to 4FGL J1745.6–2859 of 8.2 kpc (GRAVITY Collaboration et al., 2019) and isotropic emission, the energy flux of $(3.26 \pm 0.05) \times 10^{-10}$ erg cm⁻² s⁻¹ measured in the 100 MeV to 500 GeV energy range corresponds to a gamma-ray luminosity of $(2.61 \pm 0.05) \times 10^{36}$ erg s⁻¹. This luminosity is comparable to the observed radio-to-X-ray luminosity of Sgr A* $\sim 10^{36}$ erg s⁻¹ (Genzel et al., 2010). The implications of this similarity will be discussed in Section 4.

3.2 Position in different energy bands

We used `Fermipy`'s `extension` tool to constrain the point source location in each energy range. Figure 3.2 shows the dependence of the source location on energy, together with the radio position of Sgr A* as measured by the Very Long Baseline Array (Petrov et al., 2011) and locations of other potential gamma-ray emitters in the GC. For a version of this plot with the 95% confidence level positional uncertainty, see Appendix L.

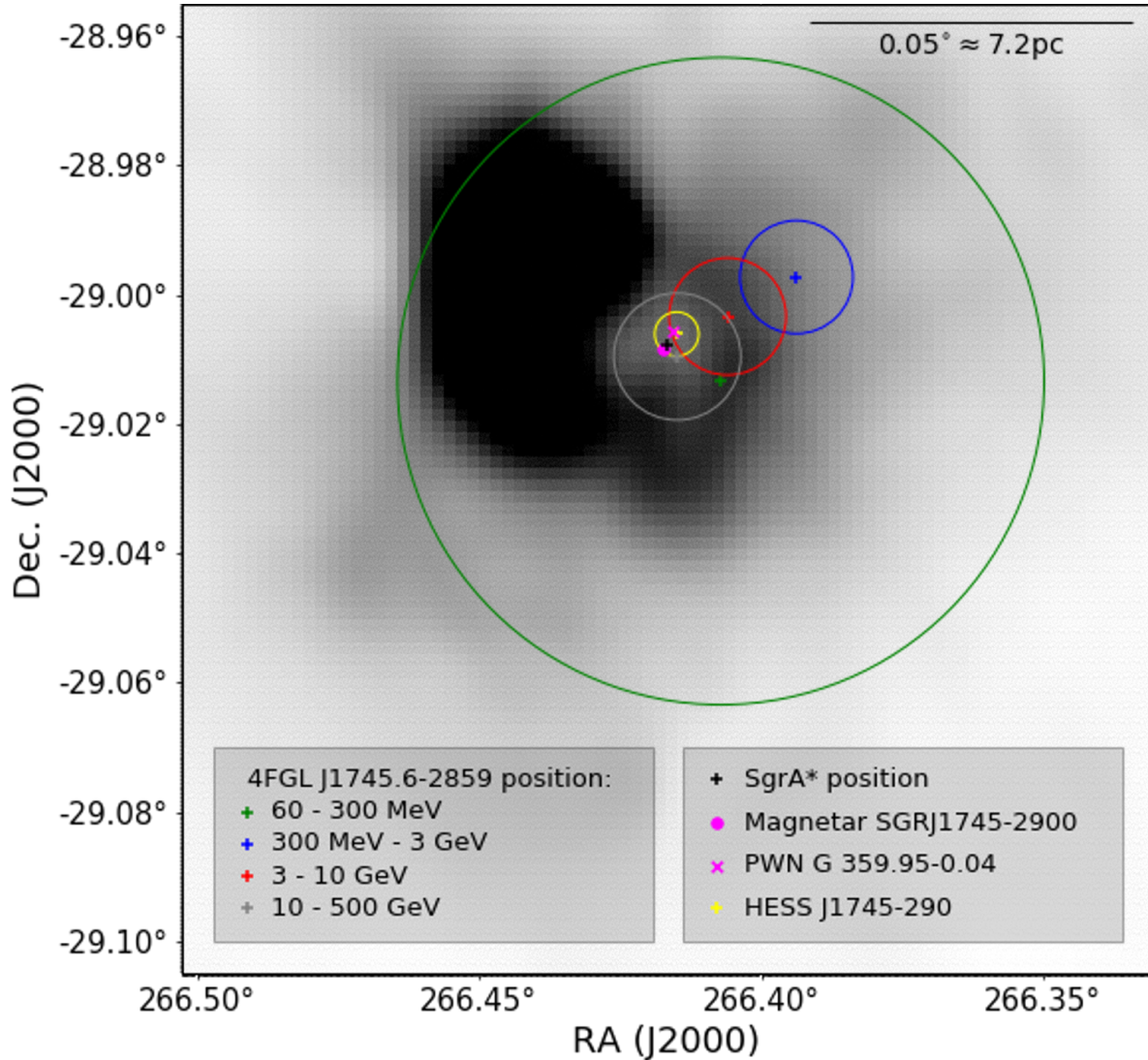


Figure 3.2: The position of the central source as a function of the energy range used in the analysis: green (60–300 MeV), blue (300 MeV–3 GeV), red (3–10 GeV) and gray (10–500 GeV). The circles represent the 68% positional uncertainty. The radio position of Sgr A* is indicated by the black cross. The positions of other gamma-ray-emitters in the GC are also indicated. The gray scale represents the 90 cm radio flux density map of Sagittarius A East (LaRosa et al., 2000), with darker color meaning brighter emission.

In Figure 3.2 we can see that the position uncertainty of the source in the lowest energy range is the largest. This is the result of a combination of factors: the broadening of *Fermi* LAT’s PSF at lower energies, the energy dependence of the instrument’s field of view and effective area, the central source’s spectrum and the impact of the Galactic diffuse emission which is more prominent at lower energies.

The position of the source is consistent within 1σ with Sgr A* in the energy ranges 60–300 MeV and 10–500 GeV. The gamma-centroid recedes from Sgr A* as the energy decrea-

ses. This is also seen in Figure 3.3, which shows the distance between 4FGL J1745.6–2859 and Sgr A* as a function of energy.

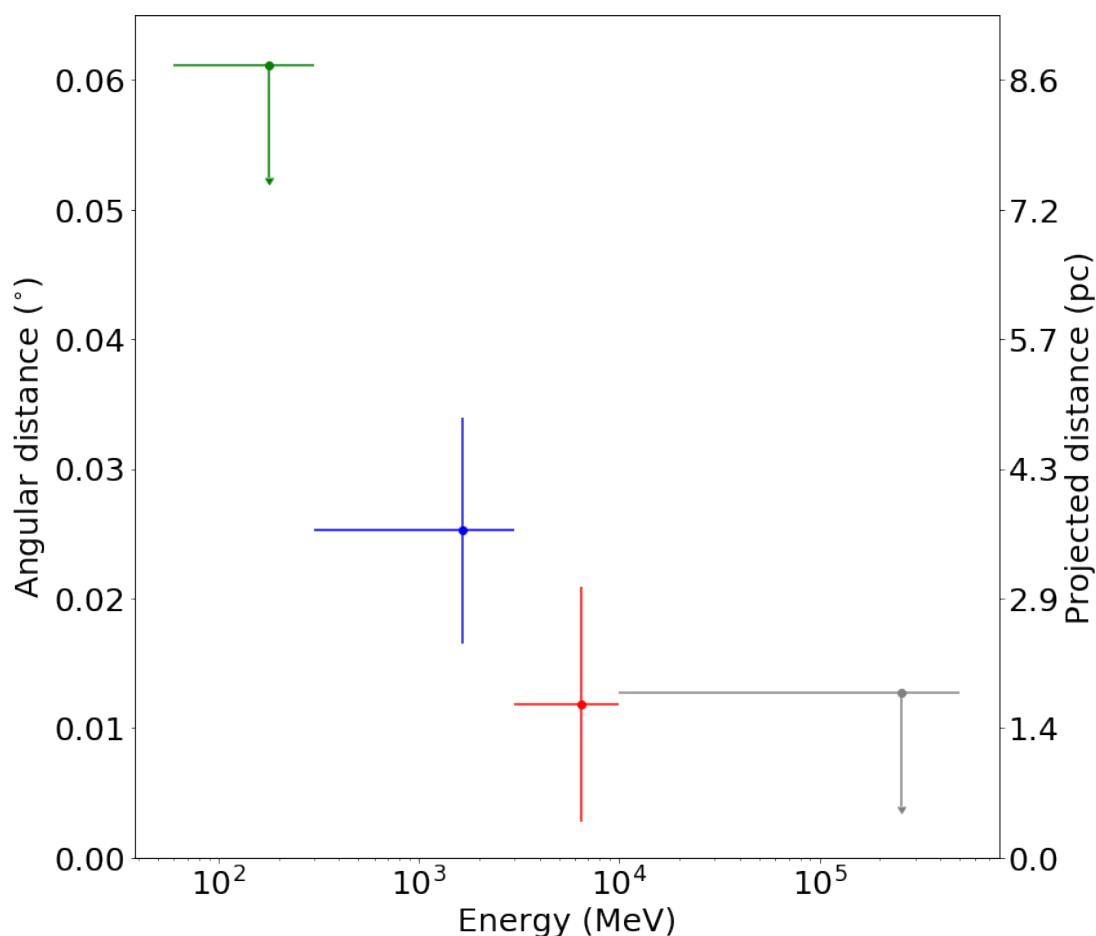


Figure 3.3: The distance between the central source and Sgr A* as a function of energy. Since the central source and Sgr A* are spatially coincident in the lowest and the highest energy bands, we show the ULs for these distances.

The positional uncertainties of the sources in the three highest-energy bands are on the order of $0.^{\circ}01$. This value is similar to the semi-major axis of the error ellipse at 68% confidence for 4FGL J1745.6–2859 in the 4FGL Catalog. It is smaller than the pixel size used in the analysis of these energy bands ($0.^{\circ}08$). We performed a simple statistical simulation to see if we could reproduce results with positional uncertainty smaller than the bin size. We generate a mock source with a size smaller than the bin size. We then computed the uncertainty and found that it can be smaller than the bin size, therefore this result is not unexpected.

We also tested the likelihood of the source being extended versus a point source using the `extension` tool. Figure 3.4 shows the 95% upper limits on the spatial extension of the

source for each energy range. Their numerical values can be found in the last column of Table 3.1.

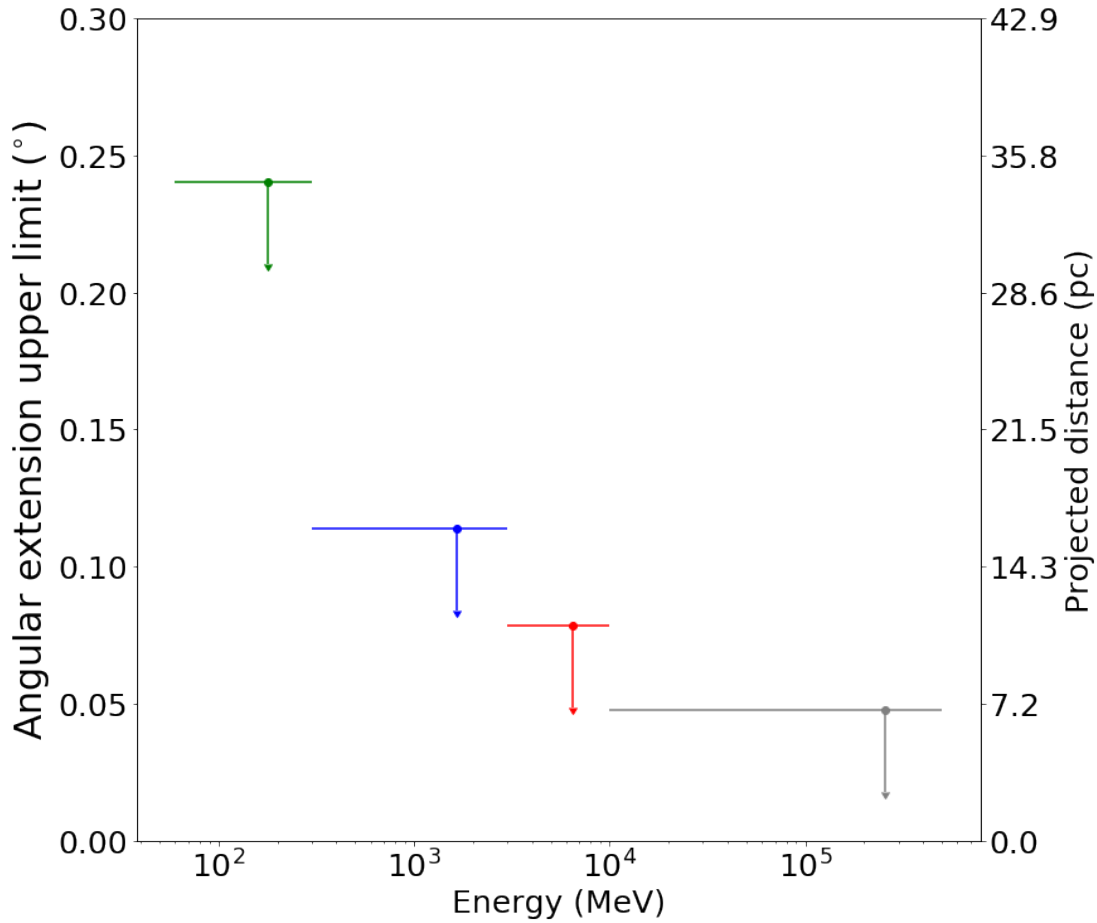


Figure 3.4: Upper limit on the spatial extension of the central source as a function of energy. Upper limits correspond to the 95% confidence level.

In Section 2.4 we explained the difficulties in assessing the extension of the central source in the energy bands we are studying, so we only report the ULs on the extension. We find no conclusive evidence for any spatially extended emission from the central source, for the following reasons. We start by comparing these ULs with the positional uncertainties of other sources in the 4FGL Catalog. The median positional uncertainties for high-latitude cataloged point-sources with $25 < TS < 100$ is of $\sim 0.^\circ 08$ (Figure 3.5). This value is larger than the ULs we obtained for the central source’s extension for the two highest energy bands. It is important to mention that the 4FGL Catalog was constructed in the energy range between 50 MeV and 1 TeV, a band much larger than the ones we are using and that covers energies in which *Fermi* LAT’s PSF is much better than in our low energy band. In order to have a fair comparison between the extension UL in the low energy band and the

positional uncertainties of known point sources, we refer to the first catalog of *Fermi*-LAT sources below 100 MeV (1FLE, Principe et al. 2018). In the 1FLE, the average and median positional uncertainties (95% confidence level) are of $0^\circ.245$ and $0^\circ.246$, respectively, which are larger than the extension UL we obtained in the lowest energy band of this work. The ULs we obtained, then, are compatible with the positional uncertainties of cataloged point sources observed with *Fermi*-LAT in similar energy ranges.

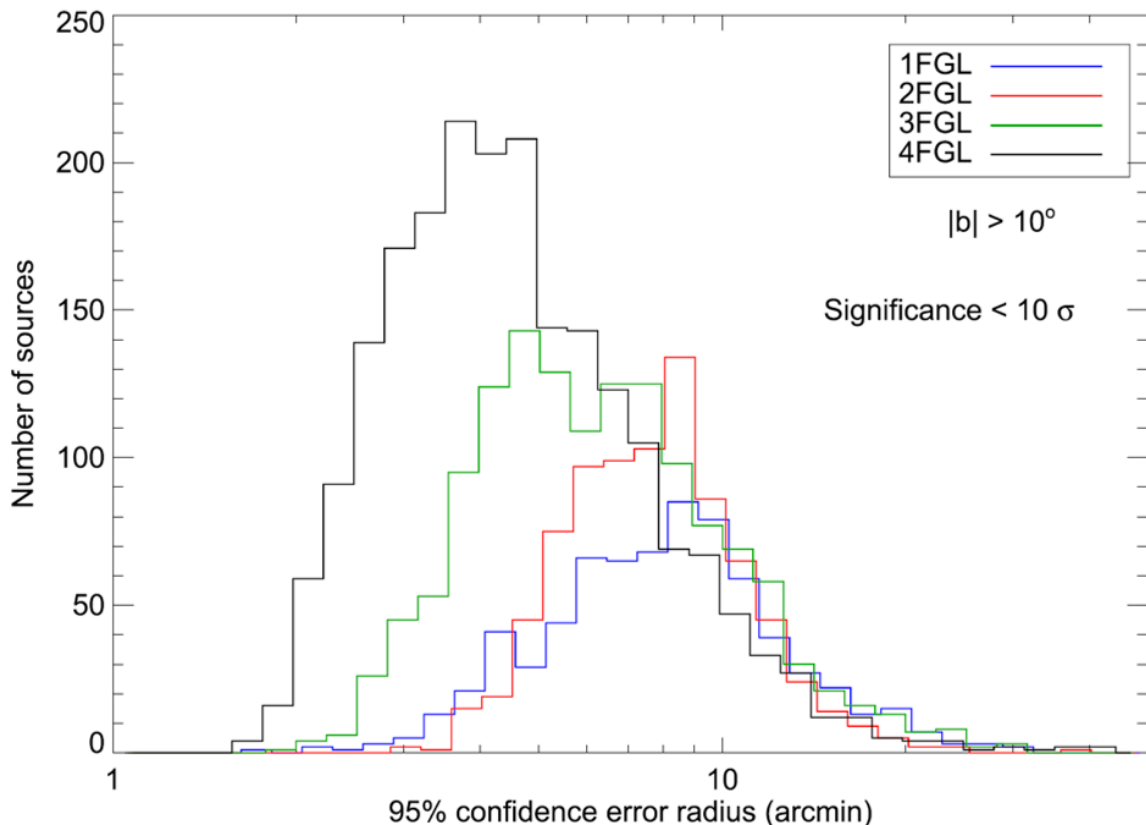


Figure 3.5: Distributions of the 95% confidence error radii for high-latitude sources with $TS < 100$ in the four versions of the *Fermi* Catalogues. The distribution for the 4FGL has median $\sim 0^\circ.08$.

3.3 Light curves

Here we present the LCs obtained in Section 2.5.1. We start with the 15 days bins LCs, followed by the LCs created using the tighter energy bands. We present the 45 days bins LCs, in Appendix K.

3.3.1 15 days bins, Universal Model

In the upper and bottom panels of Figure 3.6 we show, respectively, the 15 days bins energy and the photon flux LCs in the 100 MeV–500 GeV energy band, compared with the average fluxes. In all the LCs presented in this thesis, the error bars correspond to the 68% confidence level uncertainty. In the time bins with $TS < 16$, we show the 95% confidence level UL. In Appendix M we exhibit the TS values of every LC presented in this work.

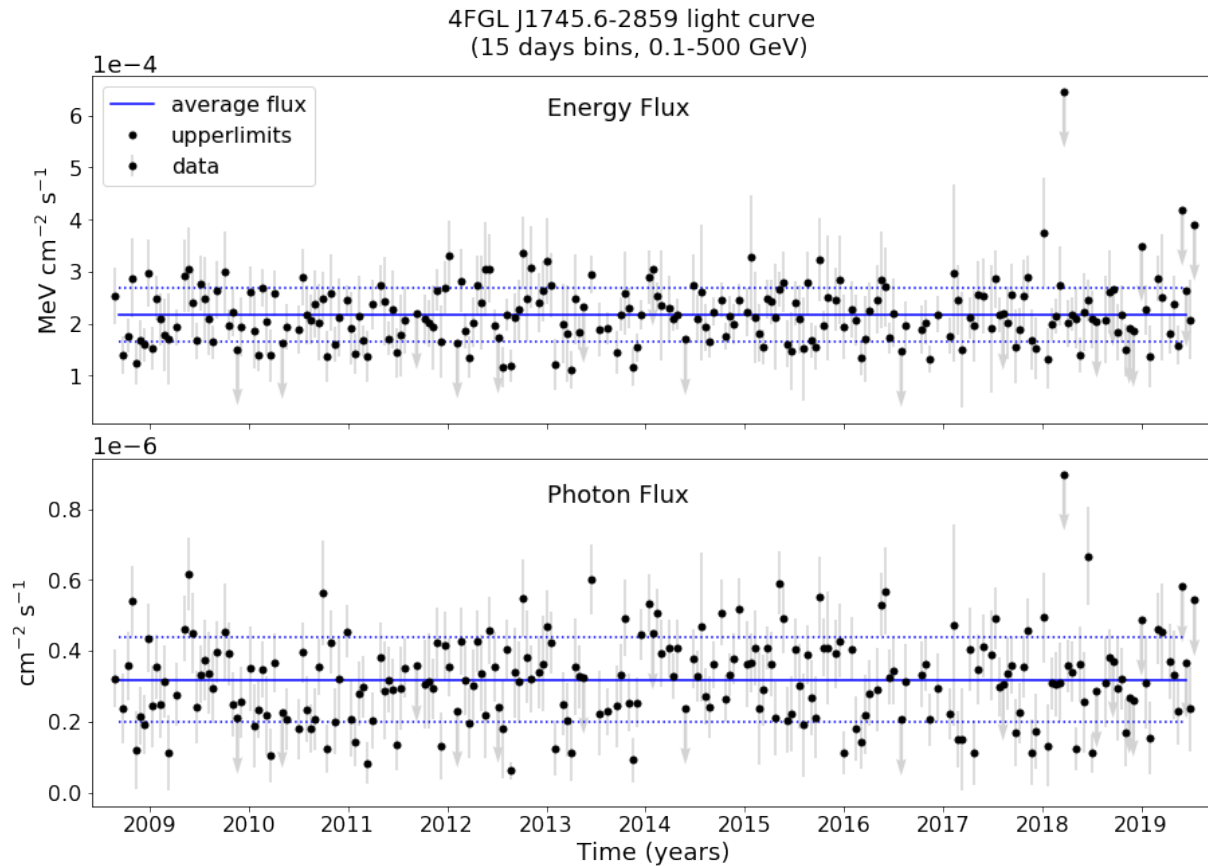


Figure 3.6: These are the same 15 days LCs of 4FGL J1745.6–2859 in the 100 MeV–500 GeV energy band shown in Figure 2.12 with the addition of the mean flux (blue line). The dotted blue lines correspond to the 1σ uncertainty of the average flux.

In most of the time bins of both panels of Figure 3.6 the flux is compatible with the average flux. This is an indication that the source is in a quiescent state most of the time, but it does not rule out the hypothesis of variability. We decided to use the rolling average of the flux to look for bins with fluxes significantly different than the neighboring bins. In the upper and bottom panels of Figure 3.7 we plot the energy and photon flux LCs with the 5 bins (= 75 days in total) rolling average. The rolling average values are plotted on

the date corresponding to the center of the 5 bins.

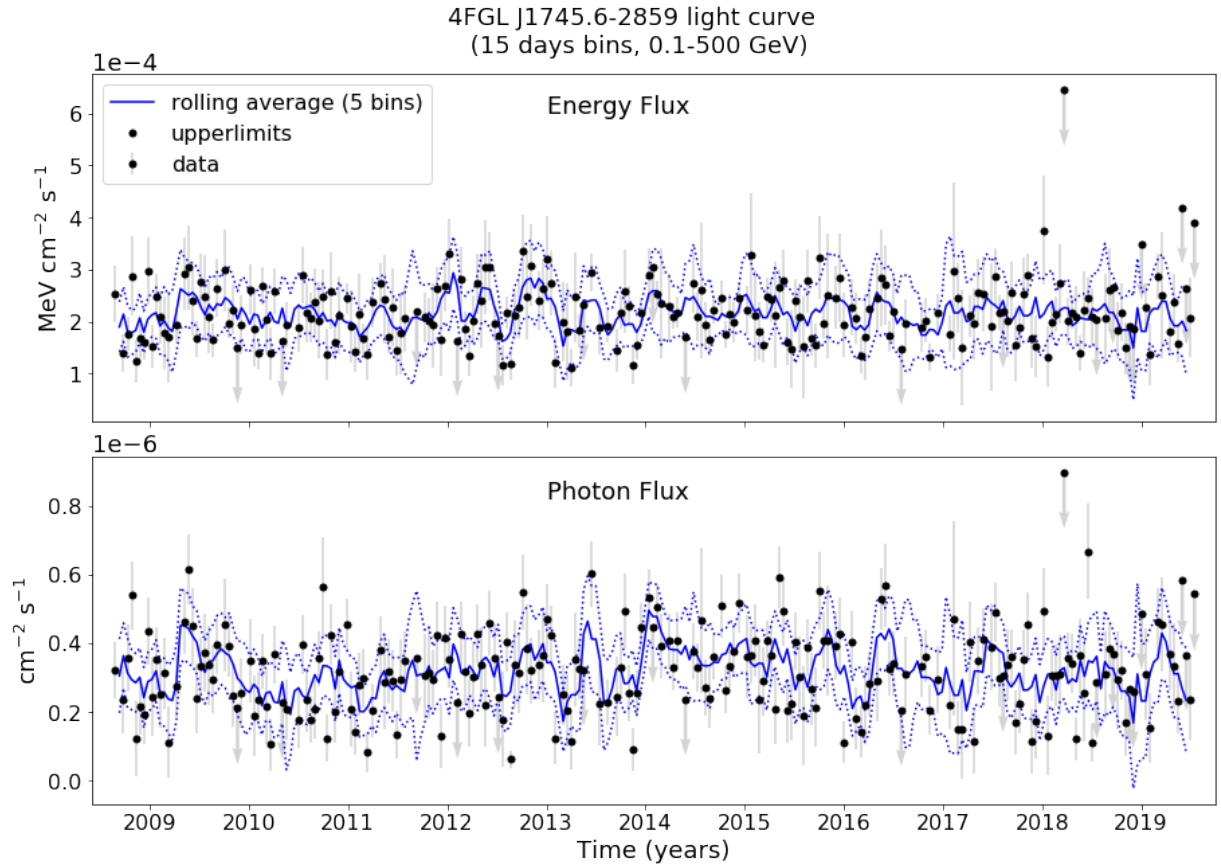


Figure 3.7: These are the same 15 days LCs of 4FGL J1745.6–2859 in the 100 MeV–500 GeV energy band shown in Figure 2.12 with the addition of the rolling average flux (blue line) of 5 bins. The dotted lines correspond to the 2σ uncertainty of the rolling average flux.

Of the whole 204 data points (not considering the ULs), in the energy flux LC (upper panel of Figure 3.7), only one is barely not compatible with the 2σ uncertainty of the 5 bins rolling average. The energy flux in this bin is smaller than the rolling average. The same method applied to the photon flux LC (bottom panel of Figure 3.7) reveals 7 (11) bins with fluxes only slightly above (below), the rolling average $\pm 2\sigma$.

To check if the variability observed in these LCs arises from a random process, we tested if the flux distribution is compatible with a Gaussian, representative of a normal random process, or a log-normal, consistent with a flaring source. In Figure 3.8 we show the histograms of the flux distribution. The energy flux distribution is shown in panel a) and the photon flux in panel b). Both distributions seen to be compatible with a Gaussian fit, shown by the red curves. In panel c) we plot the the logarithm of the photon flux distribution. The red curve in panel c) corresponds to a log-normal fit to the data (which

is simply a Gaussian in log space). The data does not seem to be compatible with a log-normal distribution.

In Tables 3.2 and 3.3 we show the results of 3 different tests used to quantify whether the data follow a Normal distribution. The Shapiro-Wilk and the D’Agostino’s K^2 test could not reject the null hypothesis that the Energy and the Photon fluxes follow a normal distribution. But it was possible to reject the log-normal distribution with a significance better than 95%. The same results were obtained with the Anderson-Darling normality test (Table 3.3). It was also not possible to reject the hypothesis that the Energy and Photon flux LCs are normally distributed even if we were willing to accept confidence levels as low as 85%. However, we could reject the null hypothesis that it is log-normally distributed with a confidence level of 99% ($\sim 3\sigma$).

The results shown in Tables 3.2 and 3.3 indicate that 4FGL J1745.6–2859’s flux distributions are compatible with Gaussian distributions, which means that the variability likely arises from a random process. It is incompatible with a log-normal distribution, expected in the case of a flaring source.

Table 3.2 - Results of the Shapiro-Wilk and the D’Agostino’s K^2 normality tests for the 15 days LCs in the 0.1 MeV–500 GeV energy range. The flux distribution is compatible with a Gaussian fit.

Test	Energy flux		Photon flux		Log(Photon flux)	
	H_0 : normal distribution		H_0 : normal distribution		H_0 : log-normal distribution	
	p-value	result	p-value	result	p-value	result
Shapiro-Wilk	0.1780	fail to reject H_0	0.1583	fail to reject H_0	0.000	reject H_0
D’Agostino’s K^2	0.245	fail to reject H_0	0.418	fail to reject H_0	0.000	reject H_0

Table 3.3 - Results of the Anderson-Darling normality test for the 15 days LCs in the 0.1 MeV–500 GeV energy range. The flux distribution is compatible with a Gaussian fit.

Significance level	Energy flux			Photon flux			Log(Photon flux)		
	H_0 : normal distribution			H_0 : normal distribution			H_0 : log-normal distribution		
	statistic	crit. value	result	statistic	crit. value	result	statistic	crit. value	result
15		0.565	fail to reject H_0		0.565	fail to reject H_0		0.565	reject H_0
10		0.644	fail to reject H_0		0.644	fail to reject H_0		0.644	reject H_0
5	0.4022	0.772	fail to reject H_0	0.4081	0.772	fail to reject H_0	3.331	0.772	reject H_0
2.5		0.901	fail to reject H_0		0.901	fail to reject H_0		0.901	reject H_0
1		1.072	fail to reject H_0		1.072	fail to reject H_0		1.072	reject H_0

Finally, we tested the presence of a global trend in the ~ 11.3 years of data collection. We simply fitted linear functions to the observed data. The results are in Figure 3.9. In Table 3.4 we show the linear and angular coefficients (with their uncertainties) obtained in

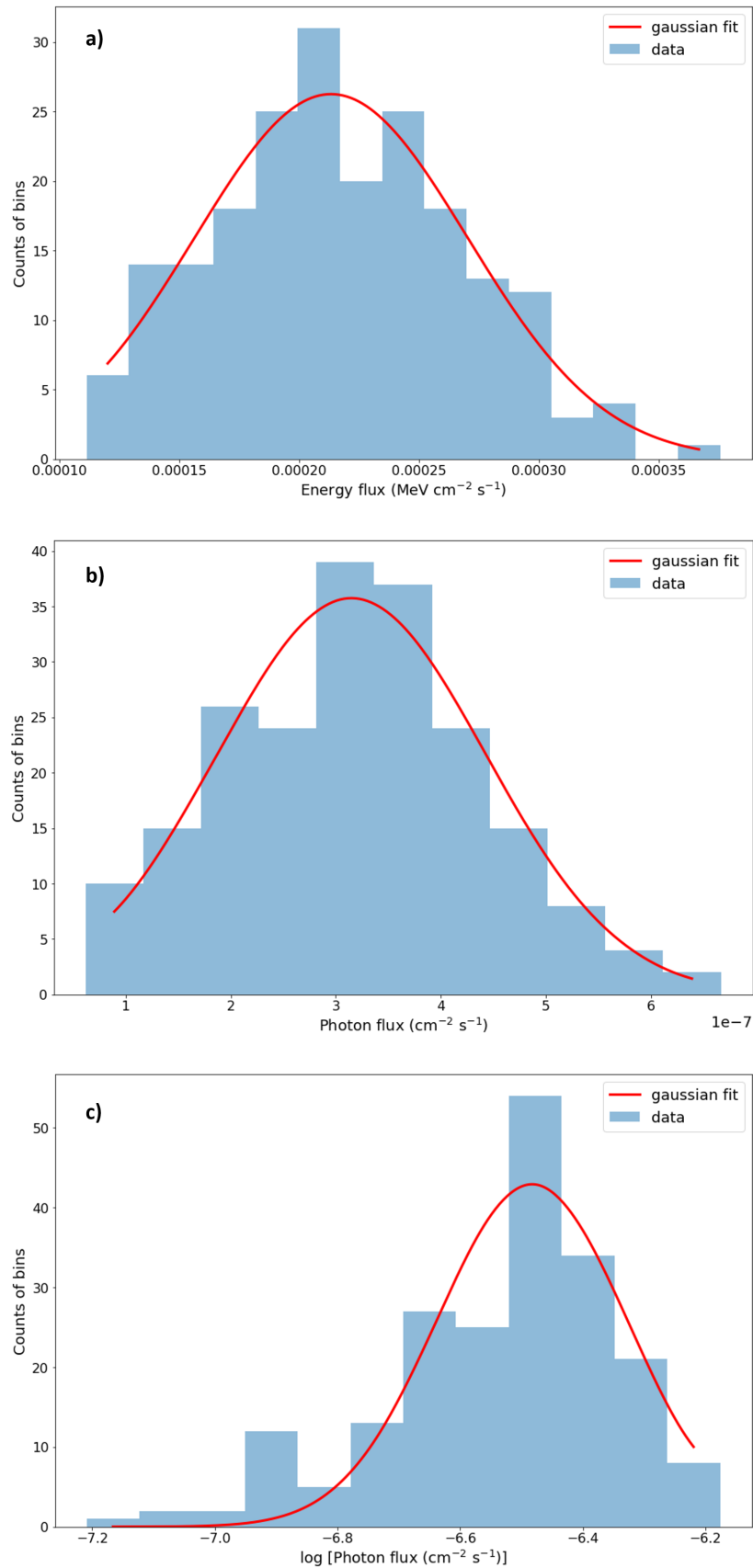


Figure 3.8: The flux distribution for the 15 days bins LCs in the 0.1 MeV–500 GeV. We show the distributions for the energy flux, the photon flux and the logarithm of the photon flux in panels a), b) and c), respectively. The red curve corresponds to the Gaussian fits to the distribution (a log-normal fit in panel c)). A Gaussian fit is clearly preferable for the fluxes distribution (see Tables 3.2 and 3.3).

these fits. Both LCs are compatible with constant flux for the duration of the observations (angular coefficient compatible with 0).

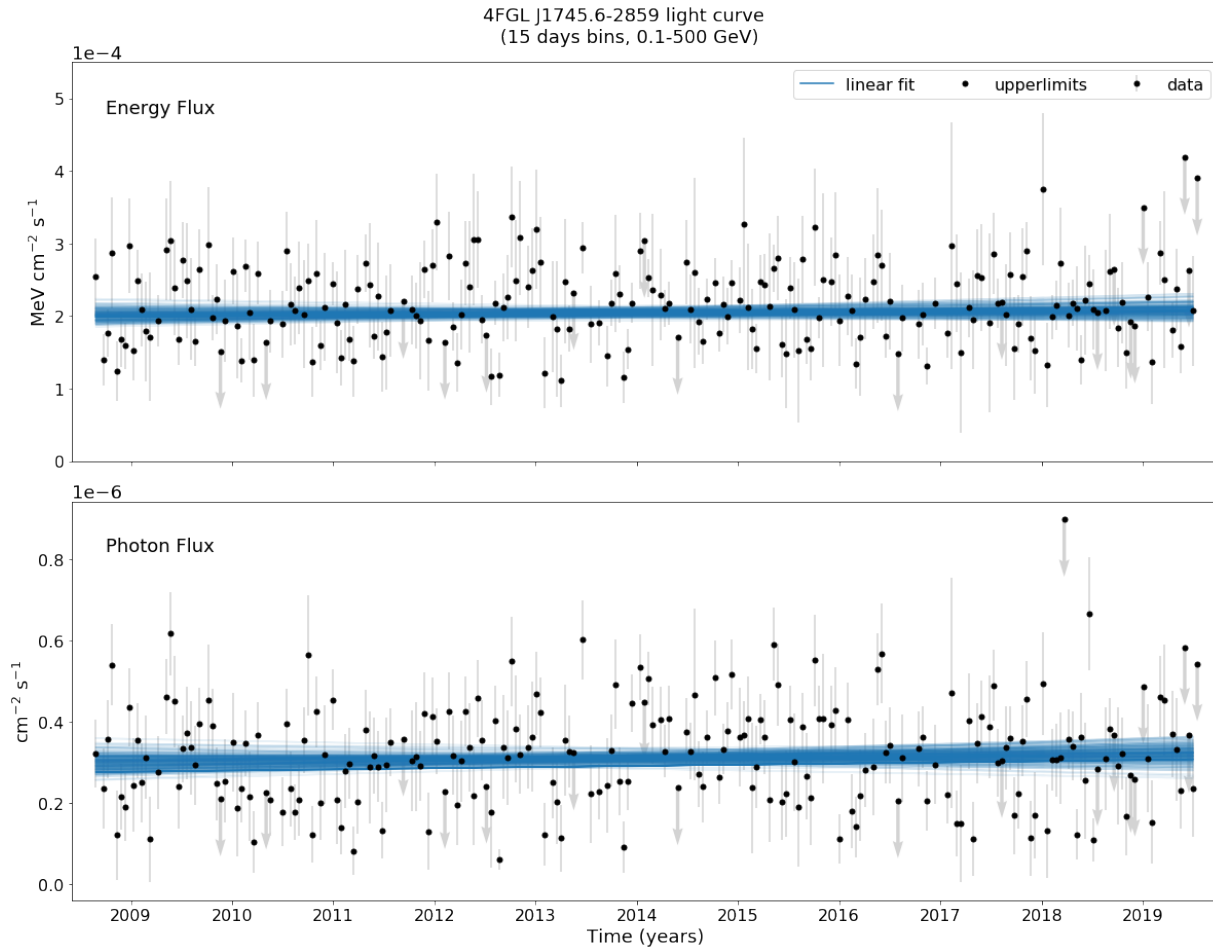


Figure 3.9: These are the same 15 days LCs of 4FGL J1745.6–2859 in the 100 MeV–500 GeV energy band shown in Figure 2.12 fitted with linear functions. We plotted in blue 200 randomized selected MCMC linear fits to the data.

Table 3.4 - Results of a linear fit to the 100 MeV–500 GeV energy range 15 days bins LCs.

Parameter	Light curve	
	Energy flux	Photon flux
Angular coefficient	$(2.5 \pm 4.2) \times 10^{-14}$	$(4.9 \pm 9.3) \times 10^{-17}$
Linear coefficient	$(1.93 \pm 0.18) \times 10^{-4}$	$(2.9 \pm 0.4) \times 10^{-7}$

The results obtained for the 15 days bins LCs are compatible with 4FGL J1745.6–2859’s flux being generated by a normal random process. Very few time bins have a flux significantly incompatible with the average flux. Also, there is no signal of a global trend in the data. In Section 4.2 we discuss these results in the context of Sgr A* as the source of the gamma-ray emission.

3.3.2 Separate energy intervals

We also created LCs for the models generated from the Universal model. We created 90-days bins LCs in the 300 MeV–3 GeV and in the 3–10 GeV energy bands. For the 10–500 GeV energy band we used 180 days time bins because of the low number of photon counts at higher energies, in order to have bins with $TS > 16$. In Appendix M we exhibit the TS values of these LCs.

We start with the LCs accompanied with the average flux. We show the energy and the photon flux LCs in growing order of energy in Figures 3.10 to 3.12. As in the 100 MeV–500 GeV LCs, very few points are incompatible within 1σ with the average flux.

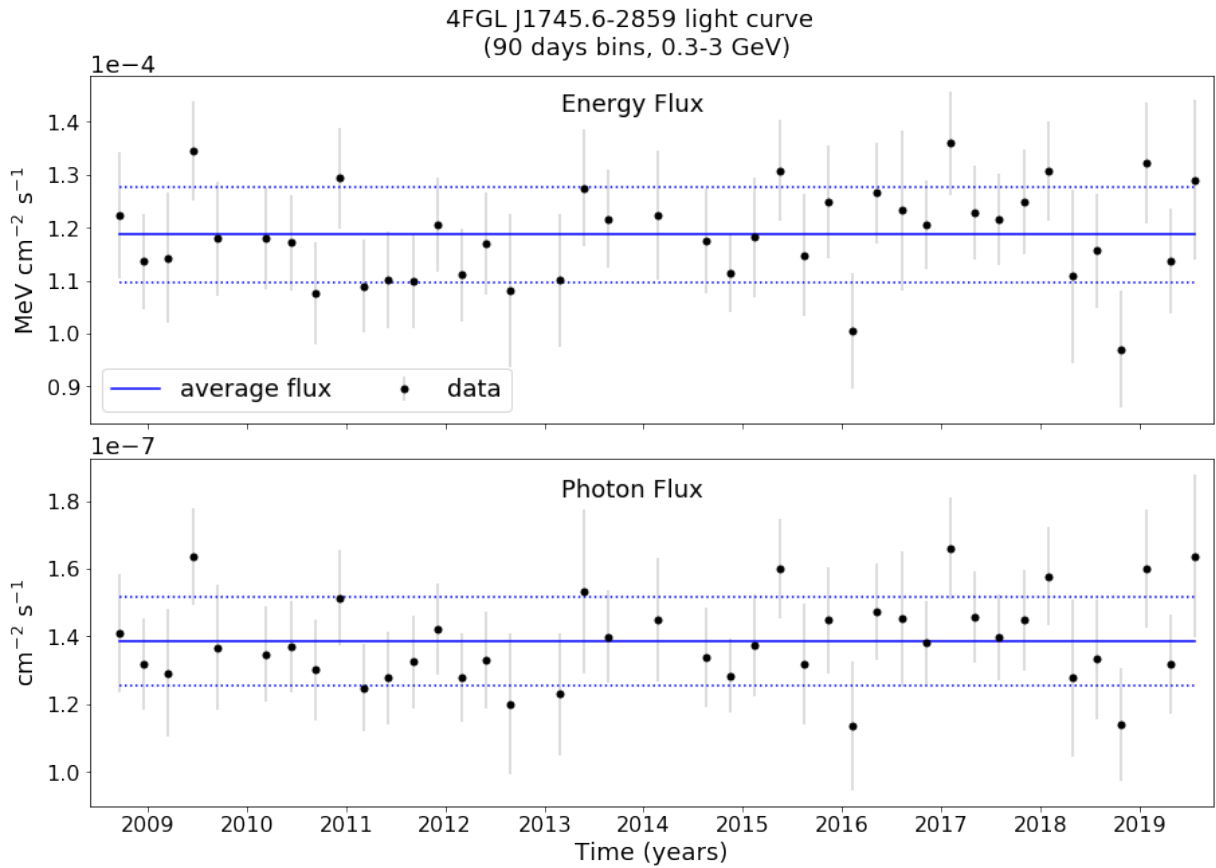


Figure 3.10: The 90 days LCs of 4FGL J1745.6–2859 in the 300 MeV–3 GeV energy band with the addition of the mean flux (blue line). The dotted blue lines correspond to the 1σ uncertainty of the average flux.

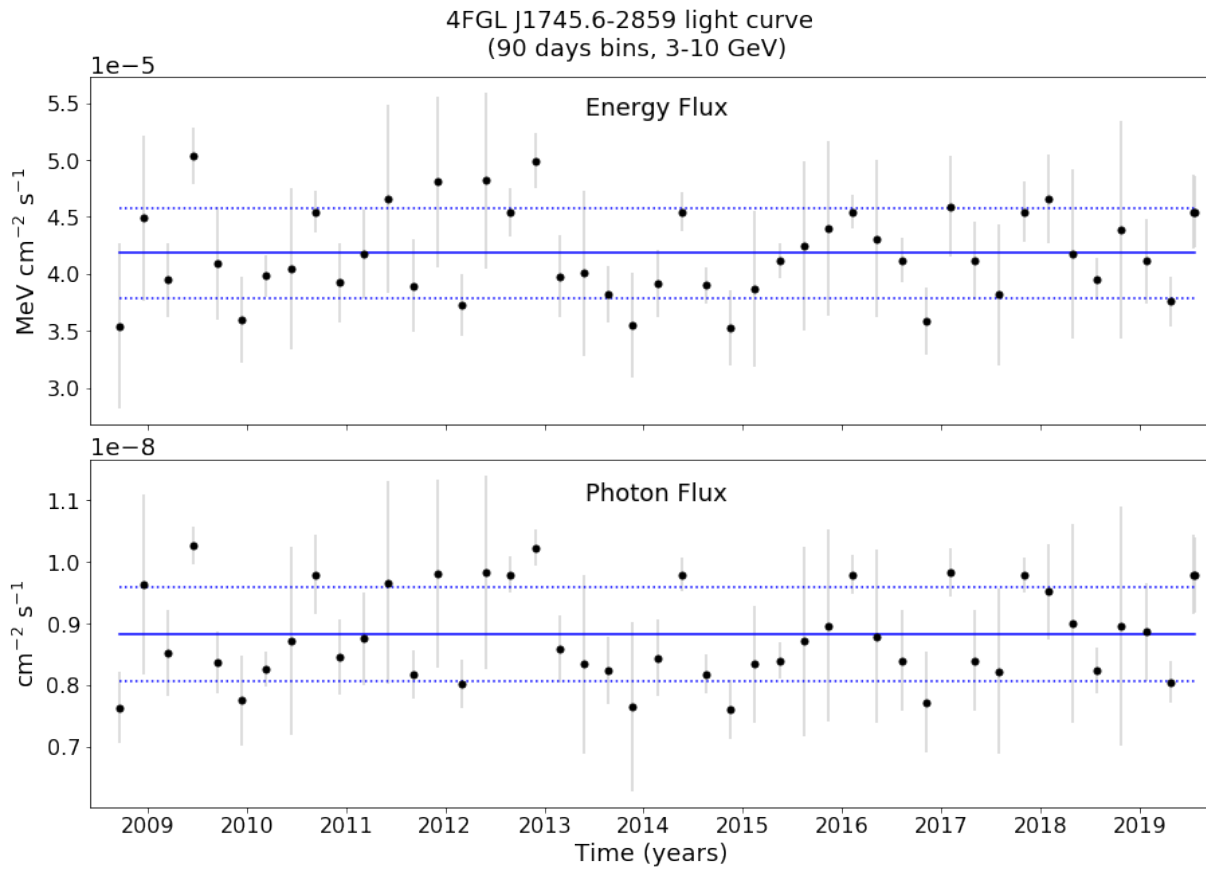


Figure 3.11: The 90 days LCs of 4FGL J1745.6–2859 in the 3–10 GeV energy band with the addition of the mean flux (blue line). The dotted blue lines correspond to the 1σ uncertainty of the average flux.

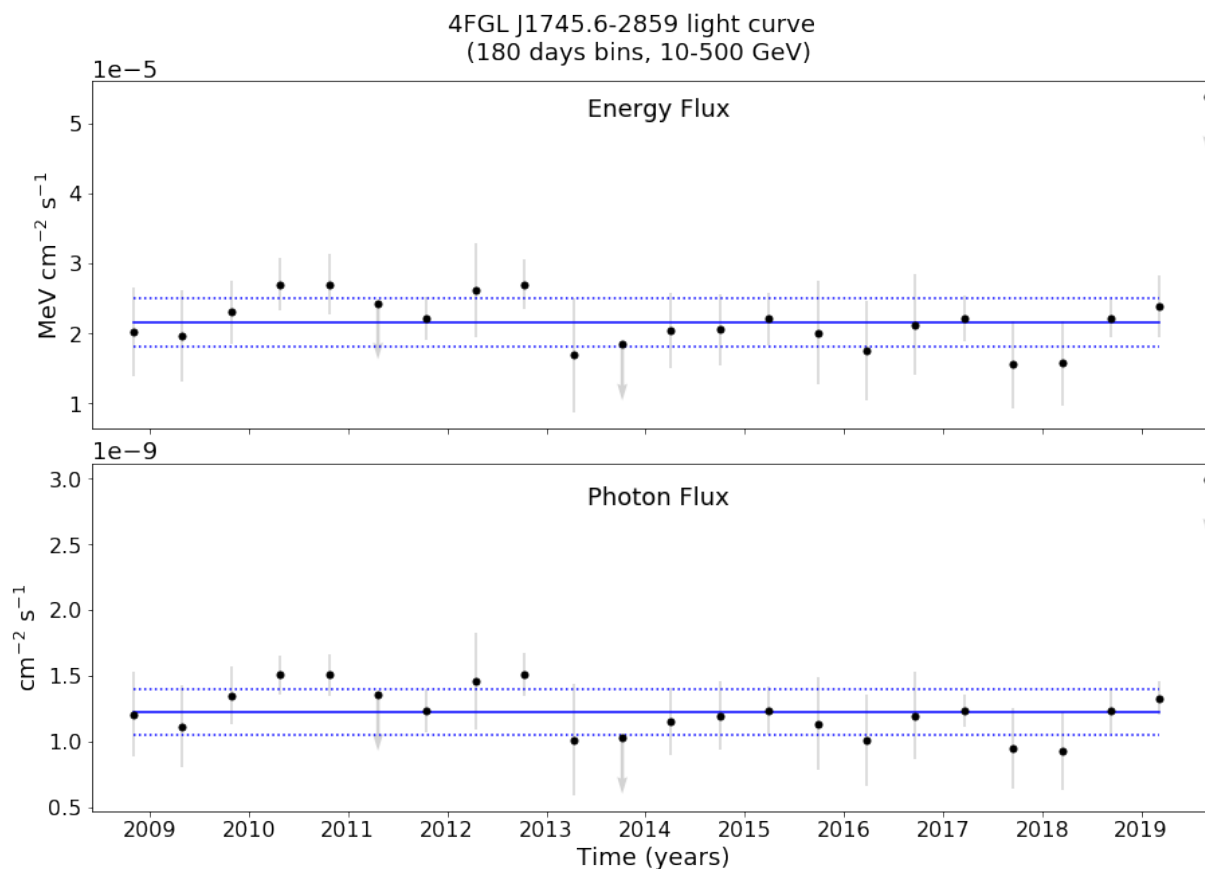


Figure 3.12: The 180 days LCs of 4FGL J1745.6–2859 in the 10–500 GeV energy band with the addition of the mean flux (blue line). The dotted blue lines correspond to the 1σ uncertainty of the average flux.

We also compared the fluxes with their 5 bins rolling average. The results are presented in Figures 3.13 to 3.15. Once again, with very few exceptions, the data points are compatible within 2σ with the rolling average fluxes. The exceptions are 2 data points, from a total of 45, in the 90 days bins LCs in the 3–10 GeV energy band (Figure 3.14 at $t \approx 2009.5$ and $t \approx 2014.5$). They are just barely outside the 2σ band with the 5 bins rolling average. It is unlikely that they represent a flare from 4FGL J1745.6–2859 since this behavior was not detected in other energy bands nor in the better time-resolved LCs with 15 days bins.

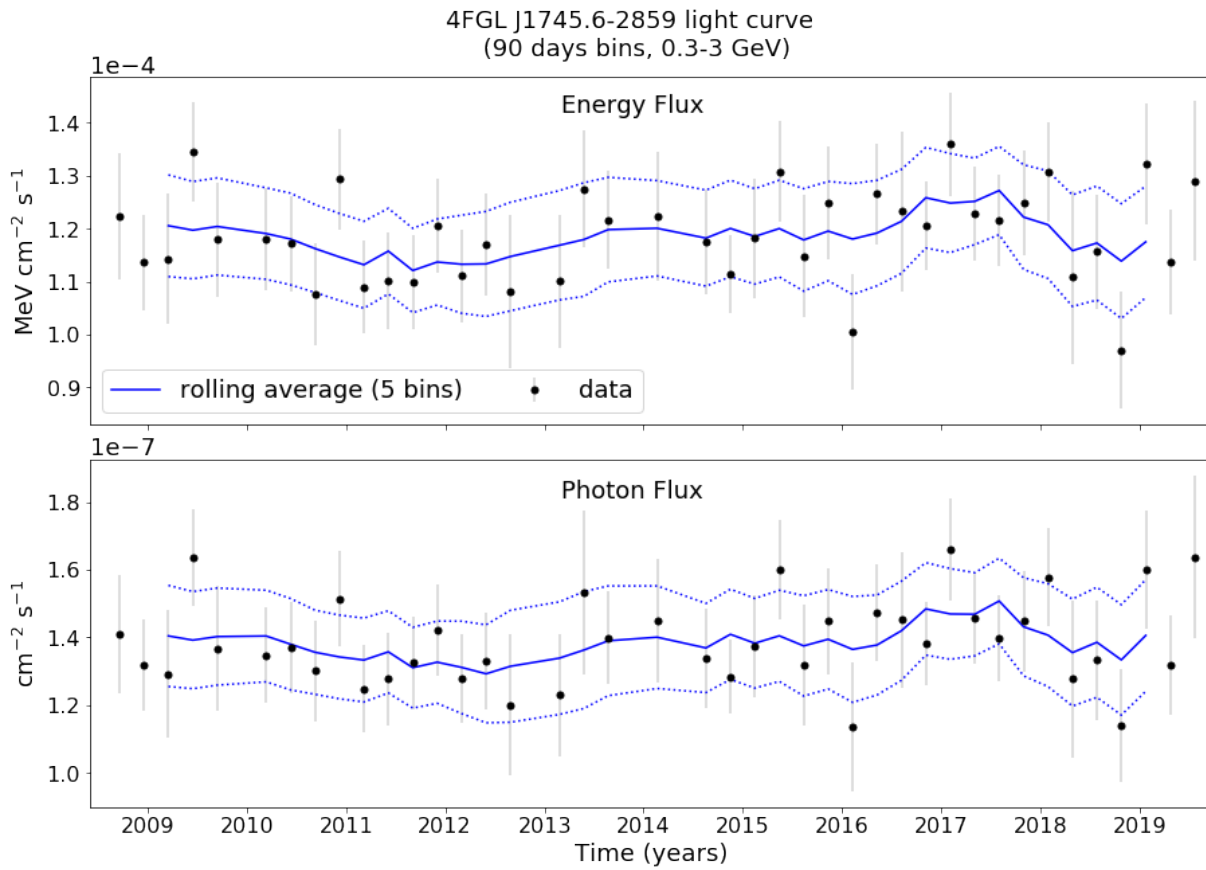


Figure 3.13: The 90 days LCs of 4FGL J1745.6–2859 in the 300 MeV–3 GeV energy band with the addition of the rolling average flux of 5 bins (blue line). The dotted lines correspond to the 2σ uncertainty of the rolling average flux.

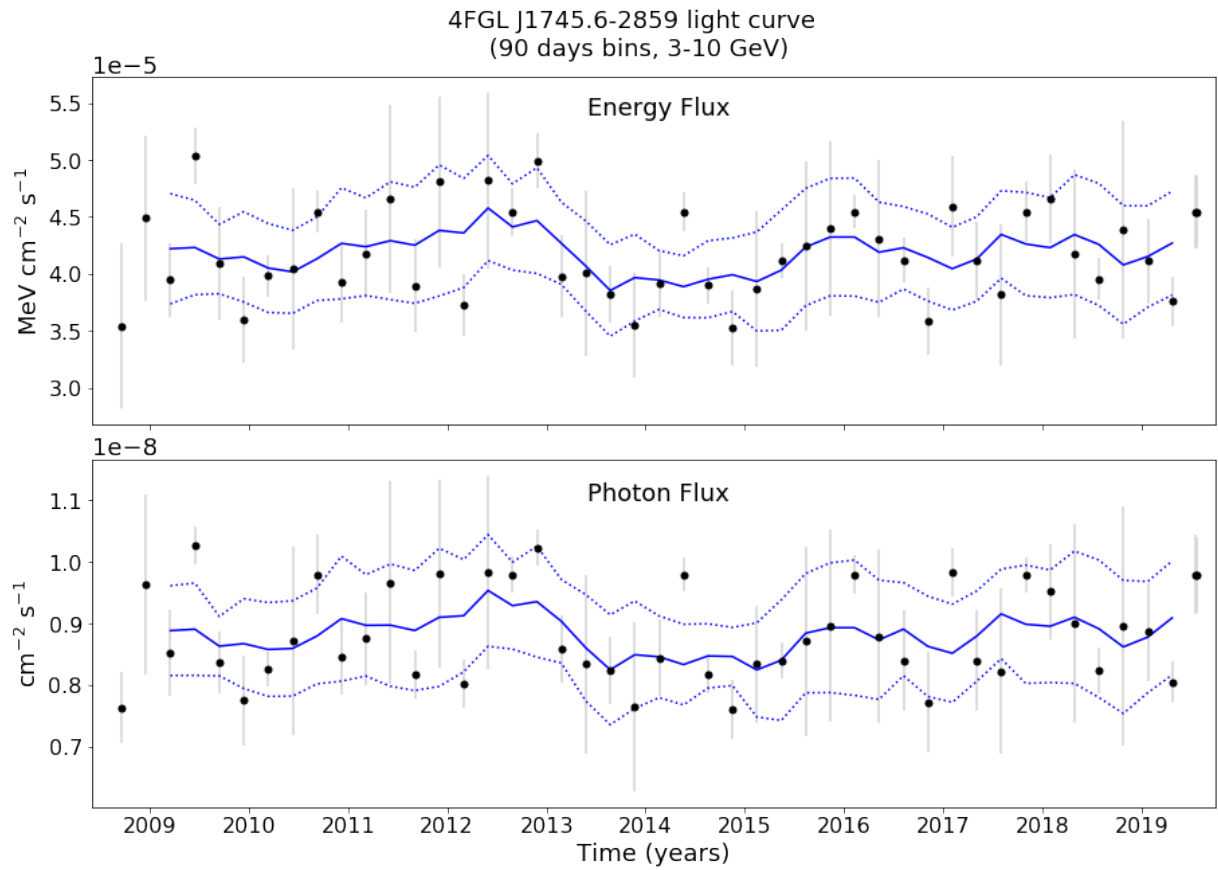


Figure 3.14: The 90 days LCs of 4FGL J1745.6–2859 in the 3–10 GeV energy band with the addition of the rolling average flux of 5 bins (blue line). The dotted lines correspond to the 2σ uncertainty of the rolling average flux.

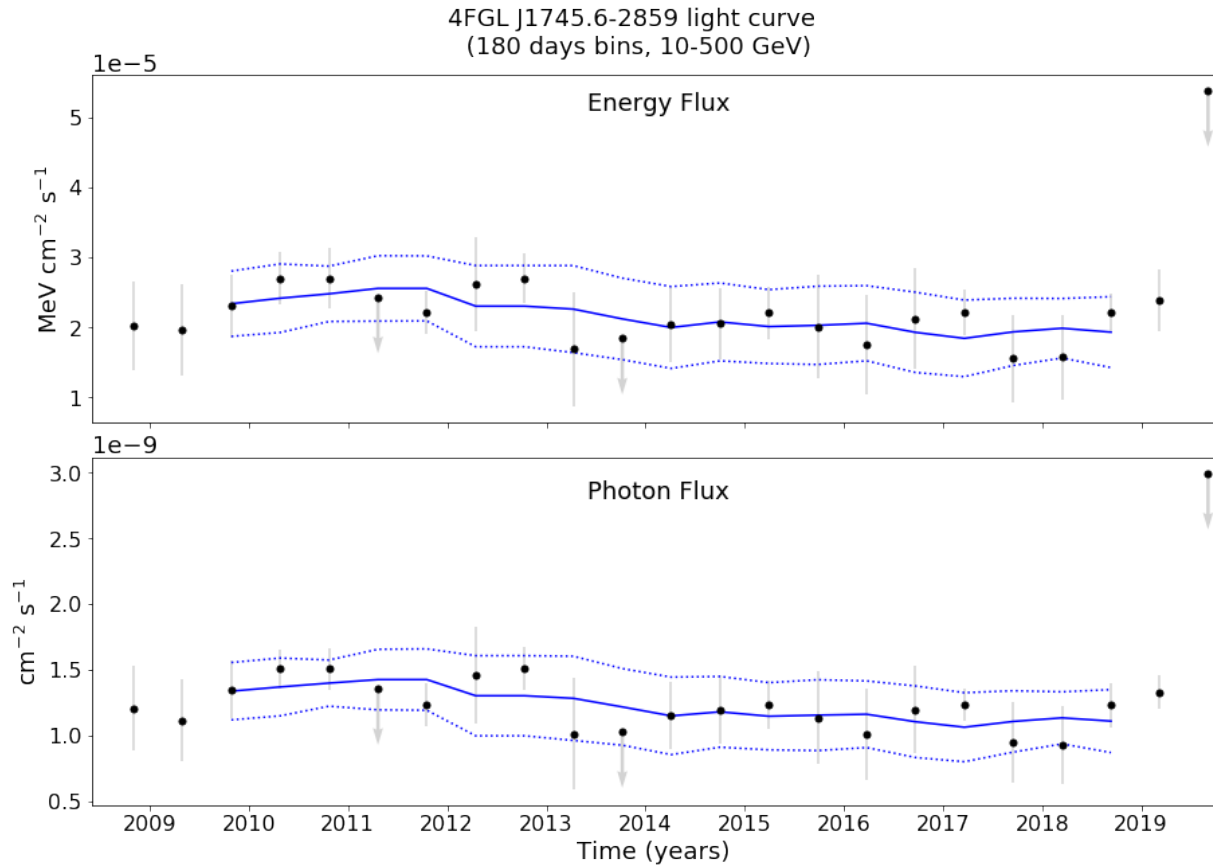


Figure 3.15: The 180 days LCs of 4FGL J1745.6–2859 in the 10–500 GeV energy band with the addition of the rolling average flux of 5 bins (blue line). The dotted lines correspond to the 2σ uncertainty of the rolling average flux.

The plots shown in Figures 3.10 to 3.15 indicate that 4FGL J1745.6–2859’s emission is also constant in time even in the tighter energy bands. We fitted linear functions to these LCs. Here we report the results, in Figures 3.16 to 3.18. In Table 3.5 we show the linear and angular coefficients obtained in these fits. With one exception, the LCs are compatible with constant flux for the duration of the observations since their angular coefficient is compatible with 0. The exception is the photon flux LC in the 10–500 GeV, whose angular coefficient, although not compatible with 0, is very small (on the order of -10^{-19}).

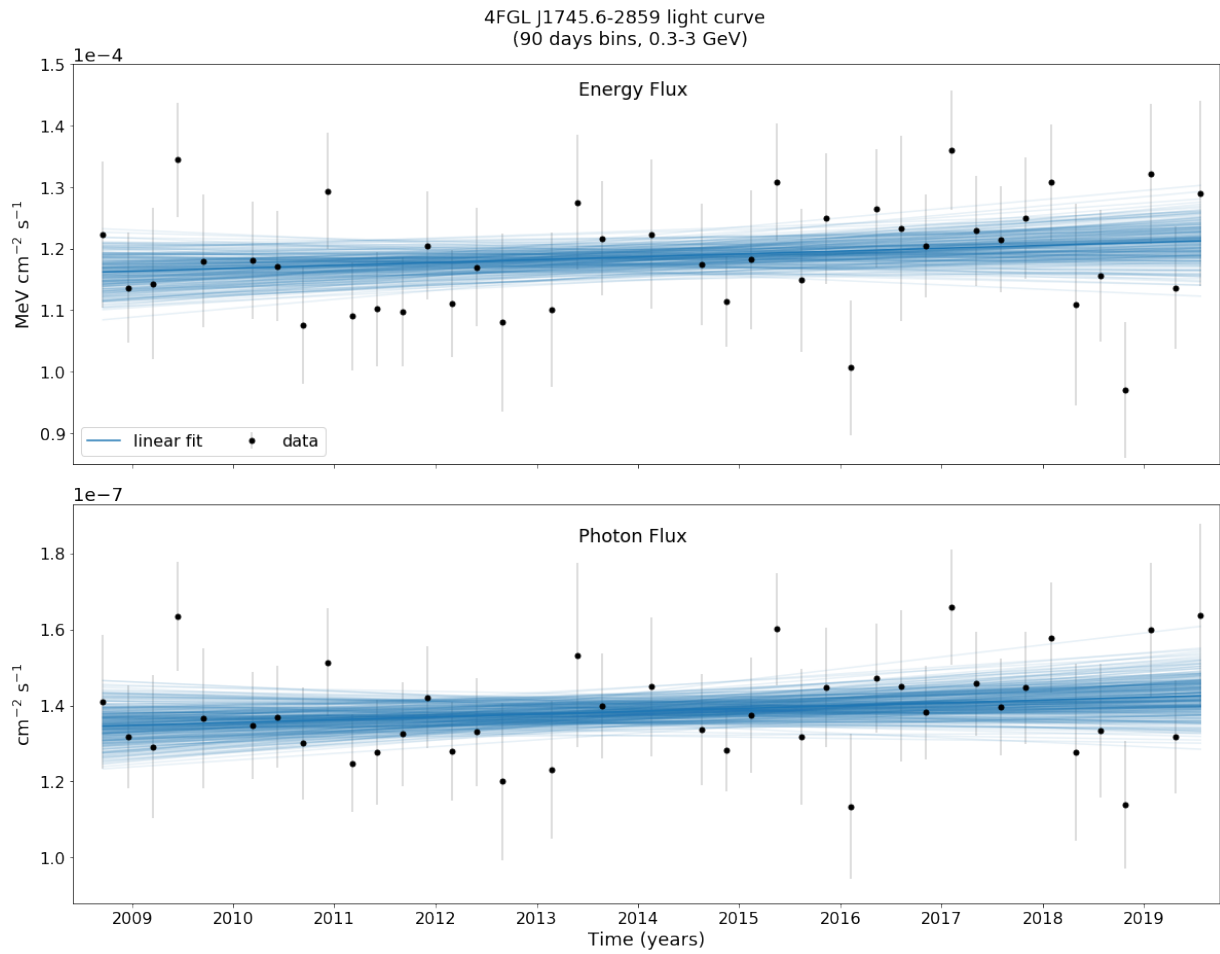


Figure 3.16: Linear fit to the 90 days bins LCs of 4FGL J1745.6–2859 in the 300 MeV–3 GeV energy band. We plotted in blue 200 randomized selected MCMC linear fits to the data.

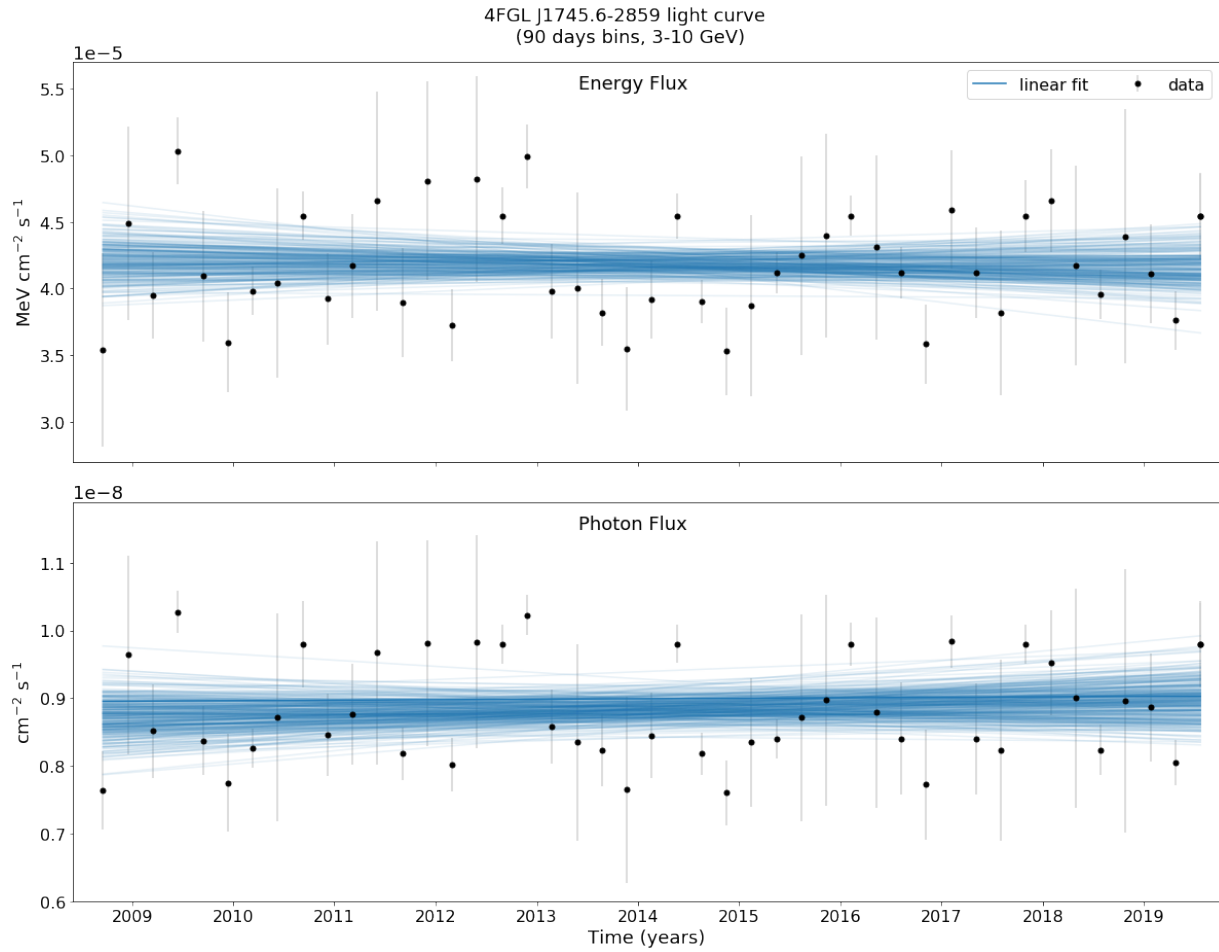


Figure 3.17: Linear fit to the 90 days bins LCs of 4FGL J1745.6–2859 in the 3–10 GeV energy band. We plotted in blue 200 randomized selected MCMC linear fits to the data.

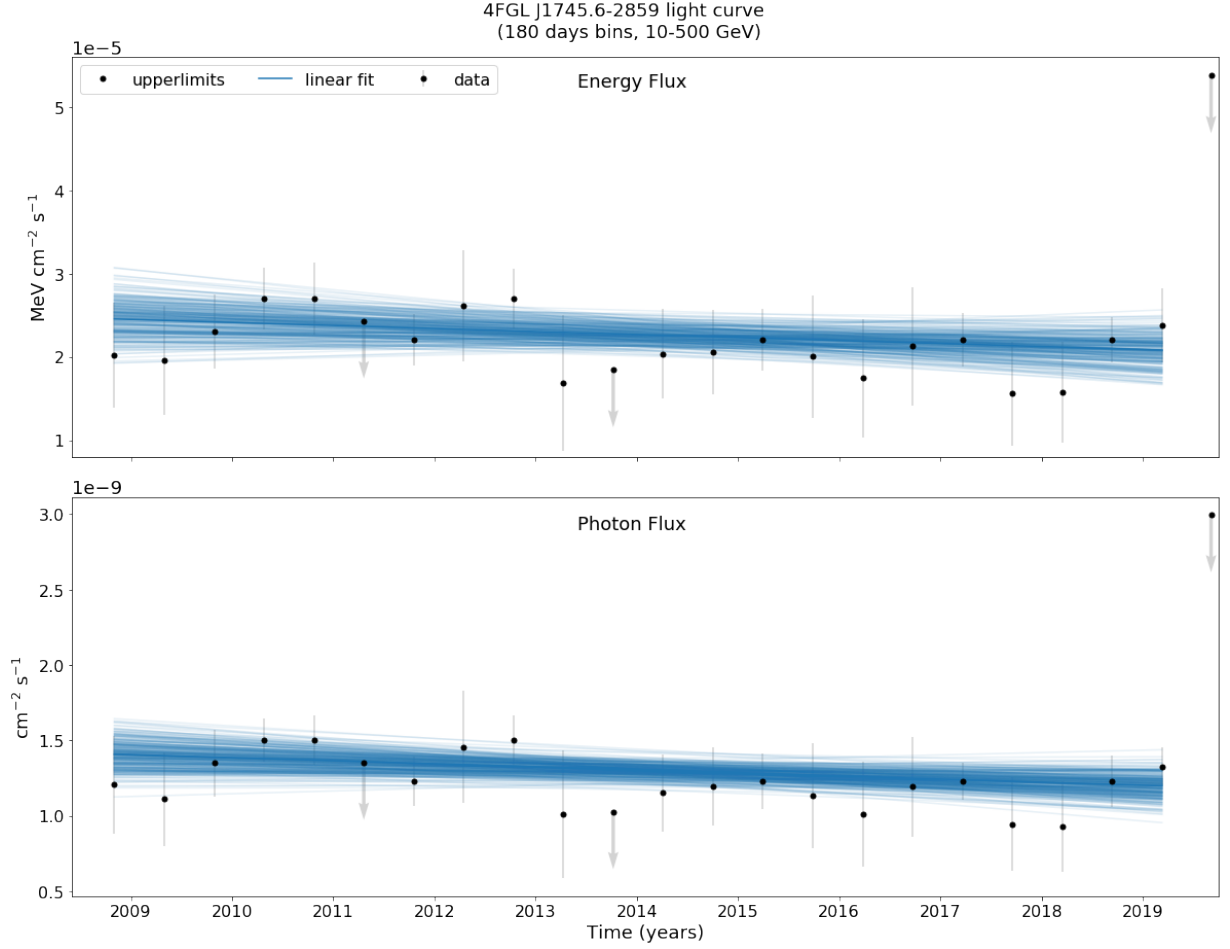


Figure 3.18: Linear fit to the 180 days bins LCs of 4FGL J1745.6–2859 in the 10–500 GeV energy band. We plotted in blue 200 randomized selected MCMC linear fits to the data.

Table 3.5 - Results of linear fits to the 300 MeV–3 GeV, 3–10 GeV and 10–500 GeV energy ranges LCs.

Parameter	Light curve					
	300 MeV–3 GeV		3–10 GeV		10–500 GeV	
	Energy Flux	Photon flux	Energy Flux	Photon flux	Energy Flux	Photon flux
Angular coeff.	$(1.0 \pm 1.8) \times 10^{-14}$	$(2.3 \pm 2.4) \times 10^{-17}$	$(-3.1 \pm 7.6) \times 10^{-15}$	$(7.3 \pm 7.5) \times 10^{-19}$	$(-1.2 \pm 1.7) \times 10^{-14}$	$(-6.4 \pm 4.2) \times 10^{-17}$
Linear coeff.	$(1.13 \pm 0.92) \times 10^{-4}$	$(1.29 \pm 0.10) \times 10^{-7}$	$(4.15 \pm 0.33) \times 10^{-5}$	$(8.90 \pm 0.61) \times 10^{-9}$	$(2.47 \pm 0.56) \times 10^{-5}$	$(1.57 \pm 0.20) \times 10^{-5}$

We did not test if the fluxes distributions are also compatible with a Gaussian random process because of the small number of time bins in these LCs and the consequent lack of statistics.

As reported in Section 3.2, the emission centroids in different energy ranges are displaced from Sgr A*’s position in reverse order of energy (see Figures 3.2 and 3.3). The main reason to create the LCs in these 3 energy bands was to search for “echoes” in the gamma-ray flux. They would be identified as variability in a higher energy LC being observed in a lower energy one after a period of time associated to the light crossing time

correspondent to the distance between their respective centroids. Since we found no signal of variability in the LCS, the possibility of echoes is unlikely. We further explain and discuss this hypothesis in Section 4.2.

3.4 SED

In Figure 3.19 we show the resulting SED. It was created based on the Universal Model (100 MeV–500 GeV energy range). The spectral model for the source (a log-parabola, Equation 1.2) is shown as a gray line, bounded by the 1σ uncertainty. For the energy bins in which 4FGL J1745.6–2859 was detected with $TS > 5$ ($\lesssim 2.2\sigma$) we show the energy flux ($E^2 dN/dE$) and the 68% confidence level uncertainties. Otherwise, we show the 95% confidence level UL.

The best fit model to the data is described as a log-parabola with the parameters $N_0 = (2.53 \pm 0.04) \times 10^{-12} \text{ cm}^{-2} \text{ s}^{-1} \text{ MeV}^{-1}$, $\alpha = 2.59 \pm 0.02$, $\beta = 0.260 \pm 0.010$ and the parameter E_0 was kept fixed during the analysis in its 4FGL value (i.e., it was not fit) of 4133 MeV.

In section 4.3 we compare this SED with several models for Sgr A* gamma-ray emission.

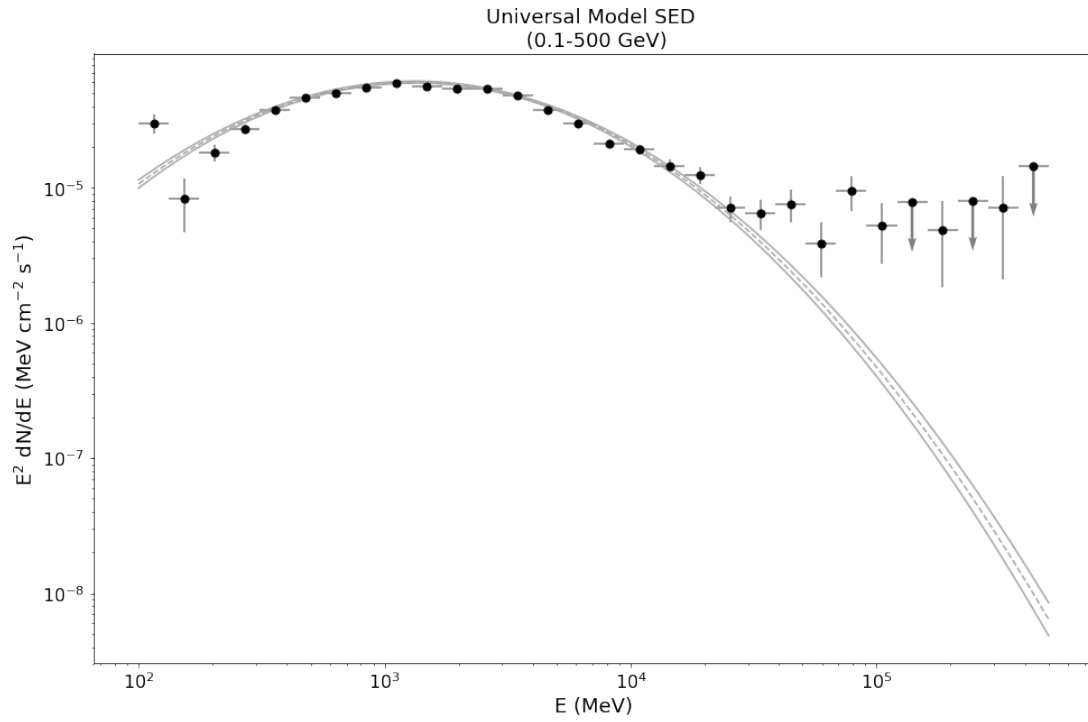


Figure 3.19: The resulting SED for the Universal Model. The dashed gray line is the spectral model for the source (a log-parabola), and the solid lines represent its 1σ uncertainty. The error bars represent the 68% confidence level uncertainties. For points in which the source was detected with significance $\lesssim 2.2\sigma$, we show the 95% confidence level UL.

Discussion

Here, we discuss the results presented in Section 3. We start with 4FGL J1745.6–2859’s energetics and position, which are compatible with Sgr A*. Then we discuss several candidates for the origin of the observed GC gamma-ray emission, of which Sgr A* is the most likely. Finally, we discuss a variety of models for the variability and SED.

4.1 *Energetics and centroid*

The gamma-ray photons observed with *Fermi* LAT do not contain any indicator of the distance from our planet at which they were produced. This realization makes it difficult to unequivocally pinpoint the physical nature and location of 4FGL J1745.6–2859 besides noting that its position in the sky approaches Sgr A*’s position as the photon energy increases.

The strong similarity between the electromagnetic energetics of 4FGL J1745.6–2859 and Sgr A*, combined with the positional coincidence, suggests that the gamma-ray point source investigated in this work is associated with the accreting SMBH. Nevertheless, the $0.1^\circ - 1^\circ$ PSF of *Fermi* LAT encompasses a region of size $\sim 10 - 100$ pc around the GC. Even the more constraining limit of $\lesssim 0.24^\circ$ for the central source’s extension upper limit (Figure 3.4) corresponds to $\lesssim 35$ pc at the distance of Sgr A*, thus allowing for several other potential candidates for the gamma-ray production site. Here, we list the most promising ones and, based on the results of our analysis in the four different energy bands and the energetics of the source derived from the Universal Model, we discuss their likelihood at accounting for 4FGL J1745.6–2859.

Evaluating the source with the Universal Model (100 MeV–500 GeV), we obtain a gamma-ray energy flux of $(3.26 \pm 0.05) \times 10^{-10}$ erg cm⁻² s⁻¹ (Section 3.1). By assuming a distance of 8.2 kpc for 4FGL J1745.6–2859 (i.e., that it is located at the GC) we obtain the interesting result that its gamma-ray luminosity is similar to Sgr A*’s radio to X-ray luminosity, which is about 10^{36} erg s⁻¹. Taken together with the positional coincidence with Sgr A* (and the other circumstantial evidence arising from the temporal behavior and emissions models compatible with the expected from Sgr A*, see Sections 4.2 and 4.3) it is a compelling suggestion that 4FGL J1745.6–2859 is associated with Sgr A*.

Also, when we use our flux results of the four energy bands (Section 3.1 and Table 3.1) to investigate other competing candidates for this emission, we find that Sgr A* is the most compelling contender (Section 4.1.1). Another information used in the evaluation of these potential candidates is the central source position as a function of energy, presented in Section 3.2 (Figure 3.2).

If we consider only the three highest-energy ranges used in this analysis, the centroid emission moves in the direction of Sgr A* as the photon energy is increased (Figures 3.2 and 3.3). Assuming a distance of 8.2 kpc, the projected distances to Sgr A* as a function of energy varies from 3.6 ± 1.3 pc (300 MeV–3 GeV) to 0.4 ± 1.4 pc (10–500 GeV) (Figure 3.3). This suggests that the particle populations responsible for the gamma-rays detected in the three bands are accelerated by the same process, originating in the surroundings of Sgr A*. The location centroid for the higher and the lower-energy bands are consistent within 1σ with Sgr A*’s.

As discussed in Section 1.5.3, the impact of source confusion on *Fermi*-LAT observations is greater at lower energies due to the PSF broadening. The localization uncertainties are considerable larger at low energies, as well as the limit on the angular extension, which creates the possibility that several other sources and processes are contributing to the lower energy flux.

In Figure 4.1 we show that the emission centroids are compatible with the gas distribution in the CND and mini-spiral in the inner parsecs of the GC. This coincidence may indicate that the gamma-ray arising from the GC is due to hadronic processes (Section 1.6.2). In this case, protons accelerated by (or very nearby) Sgr A* interact with the gas content in the CND generating pions and, consequently, gamma-ray photons. Scenarios in which the gamma-ray emission from the GC has a hadronic origin are further described

below.

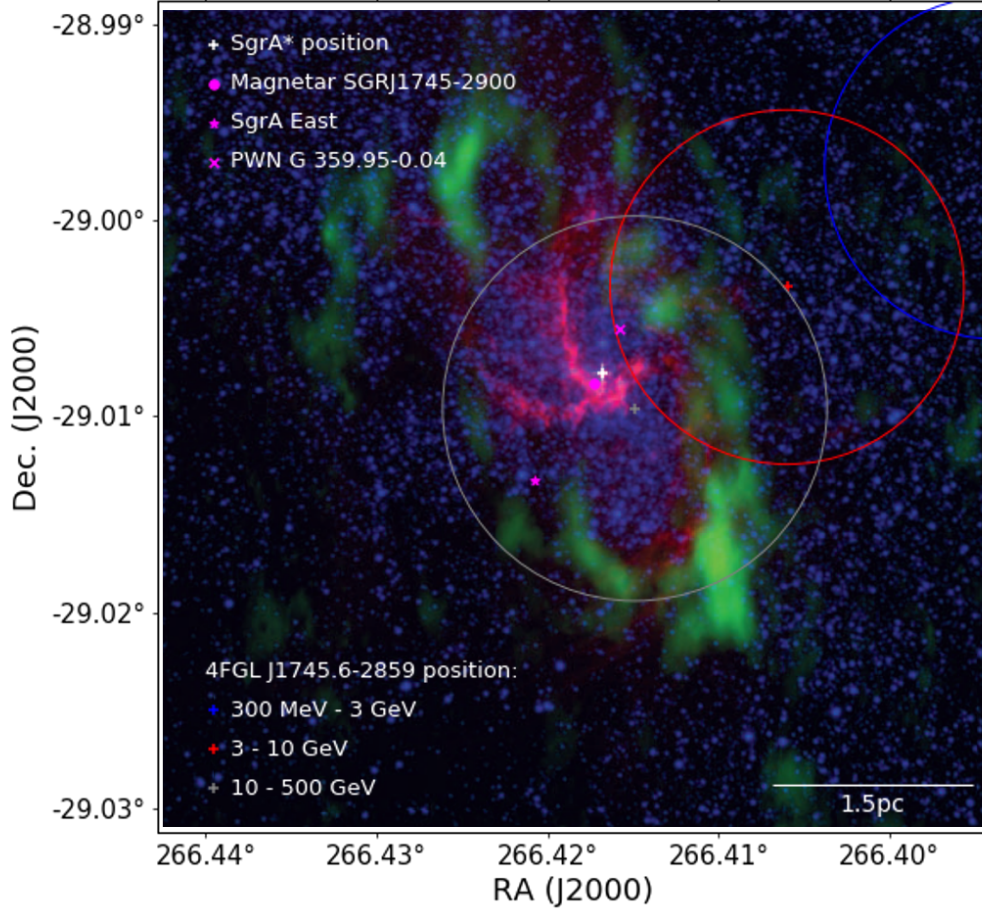


Figure 4.1: In this plot, we combine the position of the central source as a function of energy with a background showing the gas distribution in the CND and mini-spiral (adapted from Genzel et al. 2010). The circles follow the notation introduced in Figure 3.2 and the colors of the background are the same as in Figure 1.1.

4.1.1 Nature of emission

Other than Sgr A*, there are several other potential candidates for the gamma-ray production site. Here, we list the most promising ones and discuss whether which candidate model can successfully explain 4FGL J1745.6–2859.

The SMBH: Aharonian and Neronov (2005a) argue that due to Sgr A*’s low bolometric luminosity compared to other SBMHs, the gamma-rays produced at small radii can escape

the source and be detected by *Fermi* LAT because the absorption through photon-photon pair production should be unimportant. Aharonian and Neronov (2005a) considered three scenarios for the TeV photons detected by H.E.S.S., two being hadronic and one leptonic. The first hadronic model considers emission related to accelerated protons producing gamma-rays through synchrotron and curvature radiation. It predicts energy flux lower than a few 10^{-12} erg cm $^{-2}$ s $^{-1}$ in the energy range studied in this work, below the values we observed. The second hadronic scenario considers lower energy protons accelerated by the electric field close to the event horizon or by shocks in the accretion disks. Some parametrizations of this model predict very peaked SEDs in the energy ranges used in this work. Since these SEDs are very narrow, the energy fluxes they predict are consistent only with the observations in one of the four energy ranges we used in this work. Their leptonic model, in its turn, also fails to explain *Fermi*-LAT's observation of 4FGL J1745.6–2859: their leptonic-model SED shows $E^2 dN/dE \approx 4 \times 10^{-9}$ erg cm $^{-2}$ s $^{-1}$ at ~ 1 GeV thus overpredicting our observed energy flux at this energy by ~ 2 orders of magnitude.

A “plerion” in Sgr A*’s winds: Atoyan and Dermer (2004) propose a model for Sgr A* in which the quiescent radio and the flaring NIR and X-ray emission are generated by synchrotron radiation from the RIAF. The wind from the RIAF, in a process similar to pulsar-powered plerions¹, generates the quiescent X-ray and TeV emission at the wind termination shock at a distance of about 3×10^{16} cm ($\sim 25,000 R_S$) from the SMBH. Although it can explain H.E.S.S.’ TeV observations, their model is not sufficient to explain the MeV-GeV reported in this work. Even if we consider Sagittarius A West bremsstrahlung emission and the emission from a larger plerion (inflated to pc scales), which are prominent in the energy range used in this work (e.g., their Figure 1), the energy flux we detected is still about one order of magnitude higher. On the other hand, Kusunose and Takahara (2012) used 25 months of *Fermi* LAT’s data for the GC (reported by Chernyakova et al. 2011) and proposed a similar leptonic model in which electrons escaping from the vicinity of Sgr A* accumulate in a region with a size of 10^{18} cm where the gamma-rays are produced by IC scattering of soft photons emitted by stars and dust around the GC. Importantly, they obtain energy fluxes similar ($\sim 10^{-10}$ erg cm $^{-2}$ s $^{-1}$) to the values observed here.

¹ A plerion is a supernova remnant that, instead of being a shell, has its center is “filled” by energetic particles streaming from a rotating pulsar. The Crab Nebula is the archetypal plerion.

The interaction between the dense molecular clouds with cosmic rays: As an explanation for the gamma-ray emission from the GC, Aharonian and Neronov (2005b) presented a model of proton-proton interactions between the protons accelerated near the SMBH and the dense gas in the central 10 pc of the Galaxy which are followed by π^0 decay to gamma-rays. Aharonian & Neronov’s work was published before the beginning of operations of *Fermi* LAT. Their results are inconsistent with our observations, predicting energy fluxes ~ 1 order of magnitude lower than our observations.

More recent models take into account *Fermi*-LAT observations. For instance, Chernyakova et al. (2011) use the first 25 months of *Fermi*-LAT and H.E.S.S. data to create a hadronic model in which relativistic protons (presumably accelerated near Sgr A*) interact with the gas in the inner parsecs of the Galaxy. Linden et al. (2012) developed a similar model. Another hadronic model is proposed by Fatuzzo and Melia (2012) where they consider a two-phase environment surrounding Sgr A*: an inner high-density “torus” and the surrounding interstellar medium filled with shocked stellar winds which they call the “wind zone”. *Fermi* gamma-rays would be produced in the “torus” and the higher energies would come mostly from the “wind zone”. Guo et al. (2013) propose a hybrid model. In their scenario, protons and electrons are accelerated in the GC (possibly around Sgr A*). Collisions between the protons and the interstellar gas would produce the TeV gamma-rays and the electrons would IC scatter the soft background photons.

The four “Fermi-era” models mentioned above—as reported by Chernyakova et al. (2011); Linden et al. (2012); Fatuzzo and Melia (2012); Guo et al. (2013)—are consistent with our observations, except in the lower energy band we used. This energy band is the one most subject to source confusion and to the impacts of the Galactic diffuse emission. This could explain why we observe greater energy fluxes in the 60–300 MeV energy band than the prediction of these models: in addition to the gamma-rays created by the interaction between cosmic rays originated by (or nearby) Sgr A*, there is also a contribution from other sources. When Ahnen, M. L. et al. (2017) compared *Fermi* LAT’s data reported by Malyshev et al. (2015) with the “Fermi-era” models, the lower energy data ($\lesssim 200$ MeV) also showed greater fluxes than the models’ predictions.

The PWN G 359.95-0.04: This X-ray nebula was discovered by Wang et al. (2006) with a projected distance of only 0.32 pc from Sgr A* and was proposed as an explanation for the TeV emission observed in the GC. Hinton and Aharonian (2007) constructed theoretical

SEDs for this source based on Chandra X-Ray Observatory’s detection and supposing that the TeV emission of the H.E.S.S. source HESS J1745–290 is from the PWN. Their models (e.g., their Figure 4) predicts energy fluxes on the order of $\sim 10^{-12}$ erg cm $^{-2}$ s $^{-1}$ for the energy ranges studied in this work. This is more than one order of magnitude lower than the energy fluxes we measured for 4FGL J1745.6–2859. This indicates that G 359.95-0.04 is not a good candidate to explain 4FGL J1745.6–2859’s emission.

The supernova remnant Sagittarius A East: Sagittarius A East is a SNR located in the inner parsecs of the Galaxy. Crocker et al. (2005) proposed it as the source of the TeV γ -rays from the GC. On the other hand, Aharonian et al. (2009) and Acero et al. (2010) ruled out this association based on H.E.S.S. observations that show the origin of the TeV emission, although still coincident with Sagittarius A East’s extended radio shell, coming from a region where the radio flux is comparatively low and significantly displaced from the radio maximum, as indicated in Figure 3.2. The same argument can be used to rule out a physical link between the SNR and the 4FGL J1745.6–2859 in energies above 300 MeV.

The magnetar SGRJ 1745–2900: This object was first detected during a flare in 2013 with *Swift*’s X-Ray Telescope (Kennea et al., 2013) and NuSTAR (Mori et al., 2013). 4FGL J1745.6–2859’s gamma-ray light curve shows no sign of variability during this period (Section 3.3). Also, it is predicted that the high-energy portion of the spectra of magnetars peak at a few MeV (Thompson and Beloborodov, 2005), while our work clearly shows emission from 4FGL J1745.6–2859 at energies > 10 GeV.

Self-annihilating dark matter particles accumulating at the GC: Self-annihilating dark matter particles could explain the GC gamma-ray excess (Hooper and Goodenough, 2011; Hooper and Linden, 2011), a surplus of \sim GeV diffuse emission that cannot be explained by the known cataloged sources (and see Di Mauro 2021 for a recent analysis of the GC excess). But is not a satisfactory explanation for 4FGL J1745.6–2859 since this is a point-like source rather than spatially extended, as expected for dark matter emission.

A population of pulsars surrounding the GC: The gamma-ray spectra of pulsars and millisecond pulsars can be described as a power-law with an exponential cutoff above a few GeV (Abdo et al., 2010). de Menezes et al. (2019) studied the gamma-ray emission of globular clusters in the Milky Way—attributed to their large population of millisecond pulsars—and found no significant flux above ~ 10 GeV. In contrast with that, the point

source 4FGL J1745.6–2859 is detected at energies above that as indicated in Table 3 and Figure 2.8. Its hard spectrum is also not consistent with a pulsar (or population) in the line of sight.

A background blazar fortuitously aligned with Sgr A*: From the $\gtrsim 5000$ sources in the 4FGL Catalog, ~ 4000 are identified or associated with plausible counterparts observed at other wavelengths. More than 80% of these are blazars (The Fermi-LAT Collaboration, 2019). Here we consider the possibility of a background blazar, fortuitously aligned with Sgr A*, as the explanation for the central gamma-ray source. We should stress that the lack of evidence of this putative object in other wavelengths is already an indication that this is not a likely supposition. Here we consider the energetics obtained with the Universal Model (100 MeV–500 GeV) to assess if this is a satisfactory hypothesis. The average energy flux of the 4FGL blazars in the 100 MeV–100 GeV energy range is $(8.989 \pm 0.014) \times 10^{-12}$ erg cm $^{-2}$ s $^{-1}$. The energy flux we measured for the central source is $(3.26 \pm 0.05) \times 10^{-10}$ erg cm $^{-2}$ s $^{-1}$ (in the slightly larger energy band of 100 MeV–500 GeV). This would put the hypothesized source among the 0.2% brightest blazars in 4FGL (the 8th brightest in a list of $\gtrsim 3400$, see Figure 4.2). The fact that this bright blazar was never observed in other wavelengths (in particular radio) already rules out this possibility. The combination of three very unlikely events—i.e. an atypically bright gamma-ray blazar, that is also unusually dim (so far undetected) in other wavelengths and is perfectly aligned with the Galactic Center—would have to be acting in concert to explain the central source as a blazar. Another reason for discarding the blazar hypothesis is that we don’t see “blazar-like” variability from the GC (see Section 4.2). So we can safely rule out this possibility.

The central cluster of massive stars: A young and dense stellar cluster lies in the GC (Do et al., 2013). Quataert and Loeb (2005) propose a model in which shocks from stellar winds can efficiently accelerate electrons to relativistic energies. Then, they IC scatter the ambient radiation field producing gamma-rays from \sim GeV to \sim 10 TeV. Considering a distance of 8.2 kpc to the GC, their model predicts energy flux one order of magnitude lower than our observations. Aharonian et al. (2019) have discussed young stellar clusters as sources of cosmic rays. They suggest that the cosmic rays responsible for the diffuse very high energy gamma-ray from the GC are accelerated by the local stellar clusters. This emission, though, is extended while we did not find evidence of extension for 4FGL

J1745.6–2859.

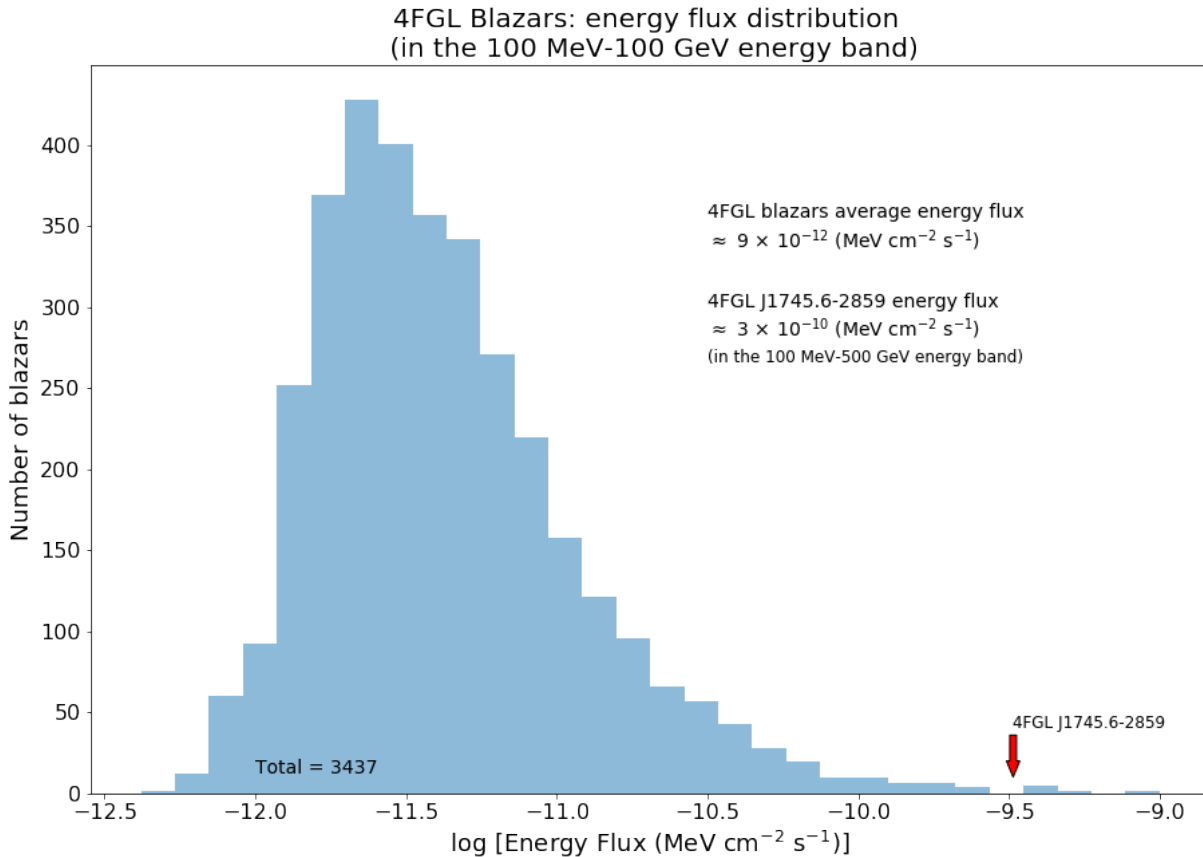


Figure 4.2: The energy flux distribution of the 3447 4FGL sources associated with blazars in the 100 MeV–100 GeV energy band. The GC source, 4FGL J1745.6–2859, energy flux is consistent with the top the 0.2% brightest blazars in the Catalog.

Except for the models constructed around *Fermi* LAT’s data (the “Fermi-era” models), most of the candidates listed above are unlikely to be solely responsible (if responsible at all) for 4FGL J1745.6–2859’s emission. It is possible that some of them could explain, individually or together, the lower energy emission where *Fermi* LAT’s PSF is broadest. One way to separate the contributions of different candidates at lower energies is through modeling the MeV-to-GeV spectral energy distribution of the point source. This is discussed in Section 4.3.

In Sections 4.2 and 4.3 we further discuss the “Fermi-era” models in view of 4FGL J1745.6–2859’s temporal variability and SED.

4.2 On the temporal flux evolution

Here, we discuss the time evolution of the 4FGL J1745.6–2859’s gamma-ray flux. We start this Section discussing the 15 days bins LC. After that, we analyze the LCs created for the models with tighter energy bands generated from the Universal model.

As stated in Table 2.1, the systematic uncertainties in our LCs are small, representing $\lesssim 10\%$ of the error bars’ sizes for every energy range used in this work (except for the 100–500 GeV energy band in which it is $< 20\%$). For this reason, their impact in the results are neglected in our discussion.

4.2.1 The 15 days bins LC

The 15 days bins flux distribution is compatible with a Gaussian, which indicates that it arises from a random process (see Tables 3.2 and 3.3). This, alone, does not exclude the possibility that the source, although in a steady state most of the time, has very short periods of variability. The results presented in both panels of Figure 3.7, though, indicate that this is not the case. Only very few data points incompatible within 2σ with the 5 bins rolling average flux. If the source is flaring in gamma-rays, the 15 days time resolution used in our work, close to the limit allowed by *Fermi*-LAT, is not enough to detect it.

The “Fermi-era” models try to explain the Fermi GC source as the manifestation of Sgr A*. Most of them were created taking into account the temporal behavior. We discuss them in view of our updated LCs.

Chernyakova et al. (2011) work was based on the *Fermi*-LAT source 1FGL J1745.6-2900 (See Table 1.2 for a list of the GC source in the different *Fermi*-LAT catalogs), together with H.E.S.S. observations, to create a hadronic model in which relativistic protons (presumably accelerated near Sgr A*) interact with the gas in the inner parsecs of the Galaxy. Their analysis of the Fermi data did not uncover any statistically significant variability of 1FGL J1745.6-2900 at GeV energies on the month timescale. This is compatible with our findings.

Fatuzzo and Melia (2012) proposes another hadronic model, described in Section 4.1.1. They suggest that the *Fermi*-LAT and H.E.S.S. data they used do not provide evidence for strong gamma-ray variability in Sgr A*, which is compatible with our updated and more detailed observations.

Since electrons have much shorter cooling time than protons, the use of leptonic models to explain a steady source is challenging. Kusunose and Takahara (2012) propose a leptonic model in which relativistic electrons supplied by flare events that occur near Sgr A* accumulate in a region with a size of 10^{18} cm. There the gamma-rays are produced by IC scattering of soft photons emitted by stars and dust around the GC. The parameters they use for the magnetic field and soft photon energy in the GC result in the electron cooling time being longer than the escape time which justifies their steady state homogeneous model. Also, since the flares intervals that accelerate the electrons are of only a few hours and much shorter than the dynamical timescale of the emission, they assume a continuous injection of electrons in their model.

Our results are also compatible with Malyshev et al. (2015) observations of the GC source 2FGL J1745.6-2858. This *Fermi*-LAT source was split into two different sources in the following version of the Catalog: 3FGL J1745.6-2859c and 3FGL J1745.3-2903c. They found no temporal variability on yearlong timescales in the 1–10 GeV energy range they used. This energy band is not exactly the same as any used in our work. But we have LCs in the 300 MeV–3 GeV and 3–10 GeV energy bands and both are also consistent with constant flux (i.e., can be fitted with a linear function with angular coefficient compatible with zero, see Table 3.5). Our work has the advantages of having shorter time bins (90 days *versus* 1 year), of using more data (11.3 *versus* 6 years) and of employing a more recent version of the *Fermi* Catalogs (4FGL *versus* 2FGL).

Malyshev et al. (2015) proposed a leptonic model for the GC source emission. The combination of the emission from electrons injected during a strong Sgr A*'s flare occurred between ~ 100 to 400 years ago (see Section 1.3.3.4) with emission from much weaker, recent activity. They propose ionisation, bremsstrahlung, IC, and synchrotron mechanisms as the main energy-loss channels. Their observations cover only the $\lesssim 6.2$ years of *Fermi* operation. For longer timescales, they made a testable prediction of a 5–10% decrease in the 1–10 GeV flux. Our ~ 11.3 years observations are not compatible with this prediction, since 4FGL J1745.6–2859 flux is constant either in the energy bands that cover Malyshev et al. (2015) LC and also in the whole energy band used in the Universal Model (100 MeV–500 GeV).

The steady emission is a characteristic of the gamma-ray flux from the GC. In addition to the *Fermi*-LAT data reported discussed above, the same is true for the IACT and EAS

observations. No variability has been detected yet in *Fermi*-LAT energy levels and above (Aharonian et al., 2009; Chernyakova et al., 2011; Malyshev et al., 2015; Ahnen, M. L. et al., 2017; H.E.S.S. Collaboration et al., 2018).

The flares from Sgr A* in longer wavelengths are frequent. They are typically daily in X-rays and even more frequent in the NIR. Also, they have short duration, lasting usually for tens of minutes in X-rays and NIR. See Section 1.3.3.3 for a description of the characteristics of the flares. If the same processes that generate them are also generating gamma-ray flares with similar rate and duration, these flares could not be identified with the 15 days bins LCs we created for this thesis. Unfortunately, smaller time bins lead to poor statistics because of the small number of counts and also the increased systematic uncertainties. At the same time that our results are compatible with a steady source in 15 days timescales, they do not rule out the possibility of variability on shorter timescales.

With this caveat in mind, the lack of coordinated variability in high and low energies arising from Sgr A* may indicate that the gamma-ray emission mechanism differs substantially from the low-energy regime. Models by which the longer wavelengths emission are generated very close to Sgr A* while the gamma-rays are produced farther away by high-energy protons interacting with the interstellar medium could explain our observations. This framework was originally proposed by Aharonian and Neronov (2005b) and explored in several models thereafter (e.g., Chernyakova et al. 2011; Linden et al. 2012; Fatuzzo and Melia 2012; Guo et al. 2013).

Here, we list a few examples of remarkable events that could enhance the gamma-ray emission from the GC or flares in different wavelengths originated by Sgr A* during the period covered by our LCs. There is no notable variability in the 100 MeV–500 GeV flux, as shown in Figures 4.4 and 4.5, in which we identify the following events:

1. The multiwavelength flare from April 1st 2009: Trap et al. (2011) reports concurrent X-ray, NIR, sub-mm, and gamma-ray (assuming 1FGL J1745.6-2900 is associated with the SMBH) observations of Sgr A*. In April 1st 2009 they detected a NIR flare (lasting for ~ 4.5 ks) followed (~ 12 ks after) by a sub-mm flare among the brightest ever detected (lasting for ~ 9 ks). They detected no significant peak in the GeV energy range, a result compatible with our LCs. Their LCs are show in Figure 4.3.
2. X-ray flare from February 9th 2012: Nowak et al. (2012) reported the brightest, at

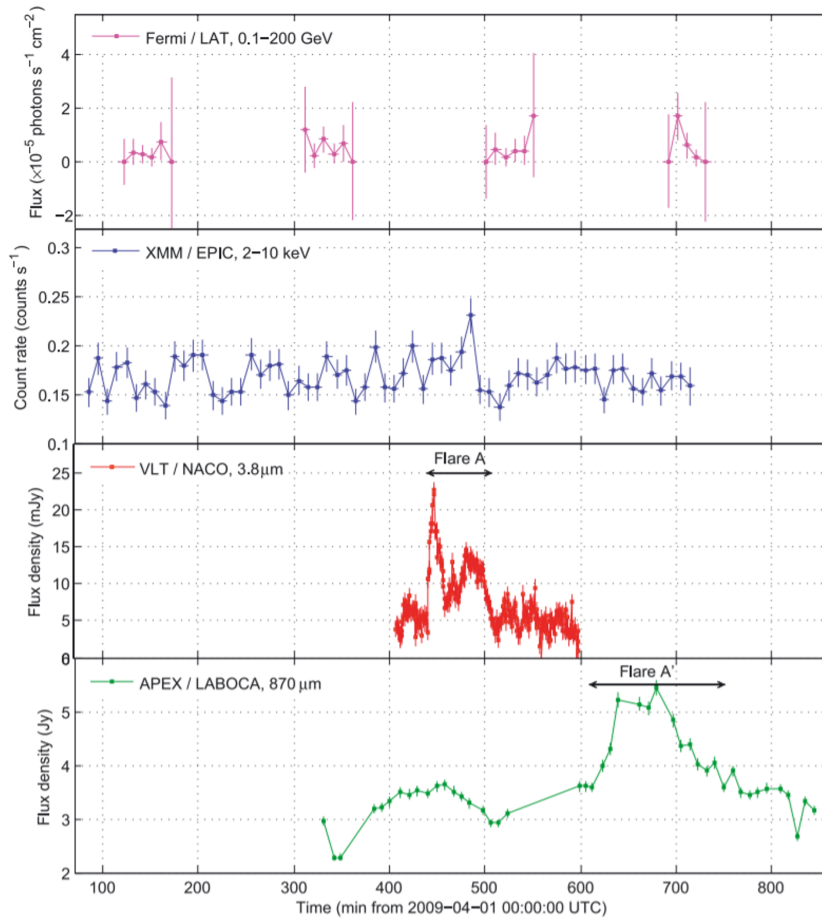


Figure 4.3: Trap et al. (2011) observations of Sgr A* from April 1st 2009. The upper panel corresponds to *Fermi*-LAT’s monitoring in the 100 MeV–200 GeV energy range. The next panel shows XMM-Newton observations in energies between 2–10 keV. The third panel shows, in red, the NIR flare detected by the VLT in the 3.8 μm wavelength. A flare was also observed in the 870 μm by the Atacama Pathfinder Experiment \sim 12ks later as shown in the bottom panel. Source: Trap et al. (2011).

the time, X-ray flare from Sgr A*, observed on February 9th 2012 with Chandra X-Ray Observatory. The flux rose to more than $100\times$ quiescence and lasted for \sim 5.6 ks. This flare is depicted in the left panel of Figure 1.7. The total energy released in the 2–10 keV energy band was estimated to be $\sim 10^{39}$ erg. Guo et al. (2013) made an order of magnitude estimate of the gamma-ray emission expected from this event supposing that the total energy of this accretion event is about four orders of magnitude higher than the X-ray emission, $\sim 10^{43}$ erg (Mezger et al., 1996), and that $\sim 10\%$ of it converted to acceleration of cosmic rays and the framework of their “Fermi-era” model. The total gamma-ray flux expected was too low to be detectable by the current astrophysical gamma-ray observatories.

3. X-ray flare from September 14th 2013: Reported by Haggard et al. (2019), this is the brightest Chandra X-Ray flare reported so far, reaching more than $600\times$ the quiescent X-ray emission. The flare lasted for 5.7 ks, with a rapid rise time of 1.5 ks and a decay time of 2.5 ks.
4. The pericenter of the G2 object orbit around Sgr A* on March 7th 2014: Plewa et al. (2017) reported the post pericenter (at $\approx 1560 R_S$) evolution of the G2 object (more details in Section 1.3.2) emission. They find no evidence of a drag force or any strong hydrodynamic interaction with the hot gas in the inner accretion zone.
5. The multiwavelength flare from June 18th 2014: This event, reported by Fazio et al. (2018) provides the first evidence of coeval structure between NIR and flux increase. It was composed by a double-peaked NIR flare that lasted for $\lesssim 4$ ks and a flare with much longer duration of $\lesssim 20$ ks. There was no good quality observations in X-rays, so it is not known whether the flare produced any emission at these frequencies. The authors could not rule out that the unusual simultaneous flares was just a coincidence.
6. X-ray flare from October 20th 2014: Also reported by Haggard et al. (2019), this flare peak luminosity was of more than $245\times$ the quiescent X-ray emission and lasted for 3.4 ks.
7. The multiwavelength flare from May 14th 2015: This is the first example of the sequence of , X-ray and NIR increase in Sgr A*'s flux, all occurring within ~ 1 hr (Fazio et al., 2018). In this unusual event, a single-peaked flare was coincident at X-ray (~ 500 s duration) and (~ 2 ks) wavelengths, but the NIR peak was delayed by ~ 4 ks (and lasted for ~ 2 ks). This flare is unprecedented in several aspects: the peak precedes the X-ray peak by ~ 1.6 ks, and the NIR peak is delayed from the peak of the emission. This has never been observed in previous events. The authors warn that observation time before and after the flare is very limited, and it is possible that the peaks at different wavelengths may be associated with other flares that either preceded or followed the observed flare.
8. The pericenter of the S2 star orbit around Sgr A* on May 19th 2018: GRAVITY Collaboration et al. (2020) report the first detection of the General Relativity Schwarzschild Precession in S2's orbit close to the pericenter (at $\approx 1400 R_S$) of its orbit. The

close encounter could provide a surplus of accreting material to the SMBH over the following few years by providing fuel due to the mass-loss from the star.

9. The unprecedented NIR flare of May, 13th 2019: Do et al. (2019) observed the brightest NIR ever recorded from Sgr A*. They observed a factor of 75 change in the NIR flux over a 2-hour time span. The maximum occurred at the beginning of the observations, suggesting that Sgr A* was likely even brighter earlier in the night. The authors suggested that the flare was a consequence of an increase in the SMBH mass accretion rate. On the other hand, we propose a model in which the flare was the result of particle acceleration to nonthermal energies, leading to an explosive event in the innermost parts of the accretion flow (Gutiérrez et al., 2020).

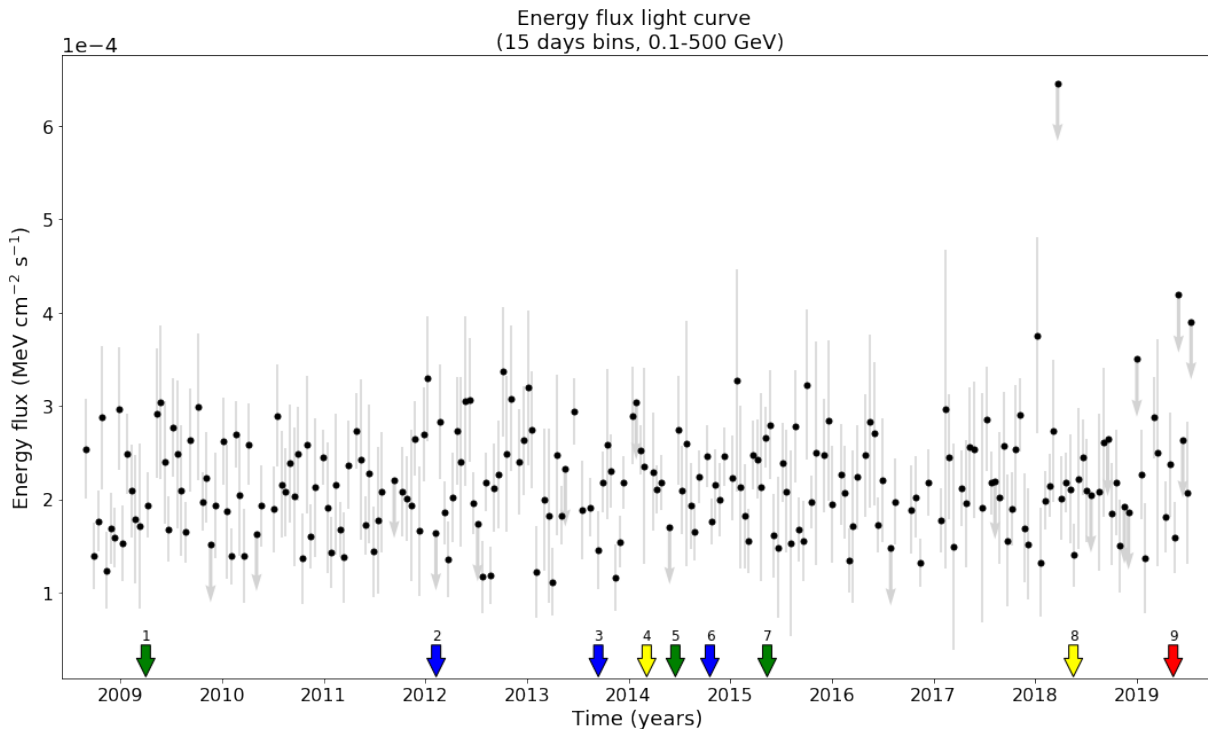


Figure 4.4: 15 days energy flux LC of 4FGL J1745.6–2859 in the 100 MeV–500 GeV energy band. This is the same as the upper panel of Figure 2.12, with the inclusion of several arrows at the bottom of the plot, indicating remarkable events associated to Sgr A*: multiwavelength flare (green), X-ray flares (blue), orbital ephemeris (yellow) and NIR flare (red). The number above the arrows relate to the events listed in Section 4.2.1.

Models for the emission above a few MeV from the GC must take into account that this emission shows no temporal variability since the first observations. Three of the “Fermi-*era*” models were created in this context, two hadronic (Chernyakova et al., 2011; Fatuzzo

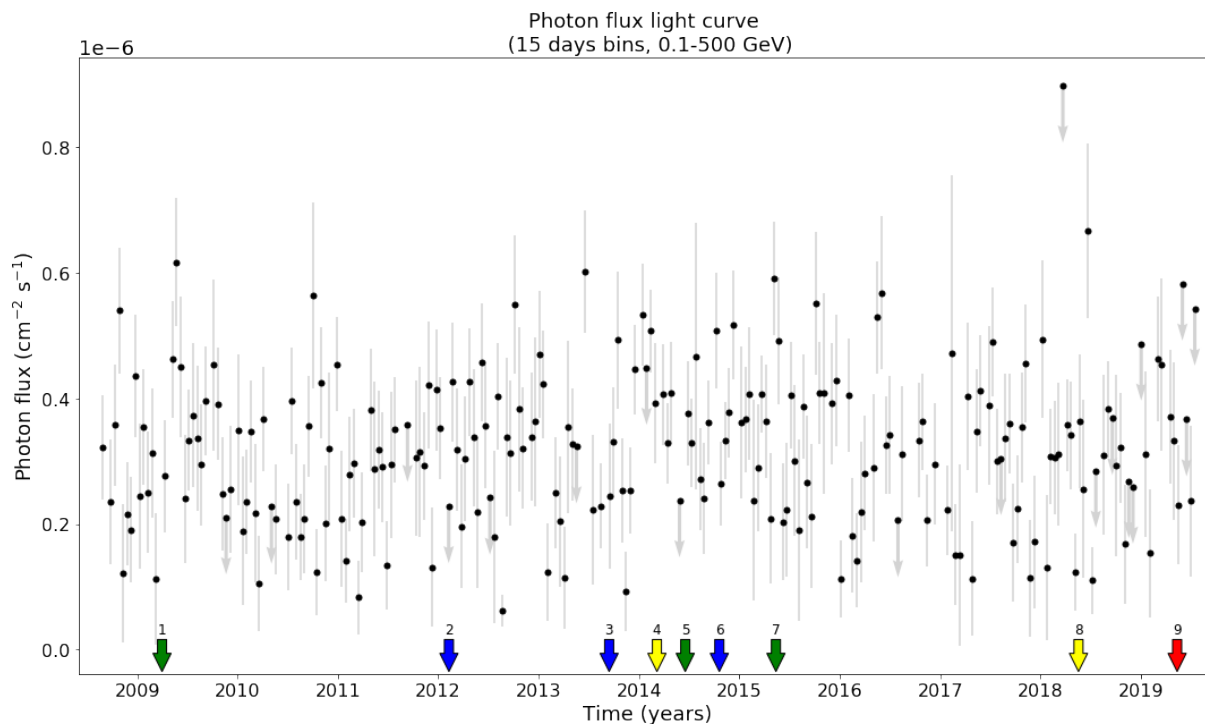


Figure 4.5: 15 days photon flux LC of 4FGL J1745.6–2859 in the 100 MeV–500 GeV energy band. This is identical to the LC shown in the bottom panel of Figure 2.12 with the addition of the same arrows described in Figure 4.4.

and Melia, 2012) and one leptonic (Kusunose and Takahara, 2012). This shows that both type of models can explain the lack of variability in the GC gamma-ray emission.

In this work, we also tried to incorporate the source imaging into this analysis. In the next Section, we describe our search of “echoes” in the LCs associated with different energy bands, whose centroids are displaced from Sgr A*’s position in inverse order of photon energy (Section 3.2).

4.2.2 The LCs created for the narrower energy bands

Here we discuss the LCs created for the Models in the narrower energy bands: 300 MeV–3 GeV, 3–10 GeV and 10–500 GeV. We already showed that the emission centroids in these bands are displaced from each other (see Figure 3.2).

Either for the leptonic and the hadronic astrophysical gamma-ray scenarios (Section 1.6) the cross sections governing the electromagnetic emission increase with the cosmic ray kinetic energy (Compton 1923; Kafexhiu et al. 2014, respectively). This could explain why the point source’s positions depart from Sgr A* in the lower energies (considering only the models above 300 MeV). If that is the case, we would expect the most energetic cosmic rays

accelerated by Sgr A* to interact first with photons (if leptonic) or gas (if hadronic) closer to their origin. A hypothetical fluctuation on the rate of energetic cosmic rays generated by Sgr A* would appear as “echoes” in the LCs with the variation manifesting first in higher energies and later, after the light crossing time between the centroids, in lower energies. Figure 4.6 shows a cartoonistic version of this simple model, considering the distances of the emission centroids exhibited in Figures 3.2 and 3.3 as examples. Although very naive, this model is easy to investigate since we have the LCs and the source’s centroid into three different energy bands.

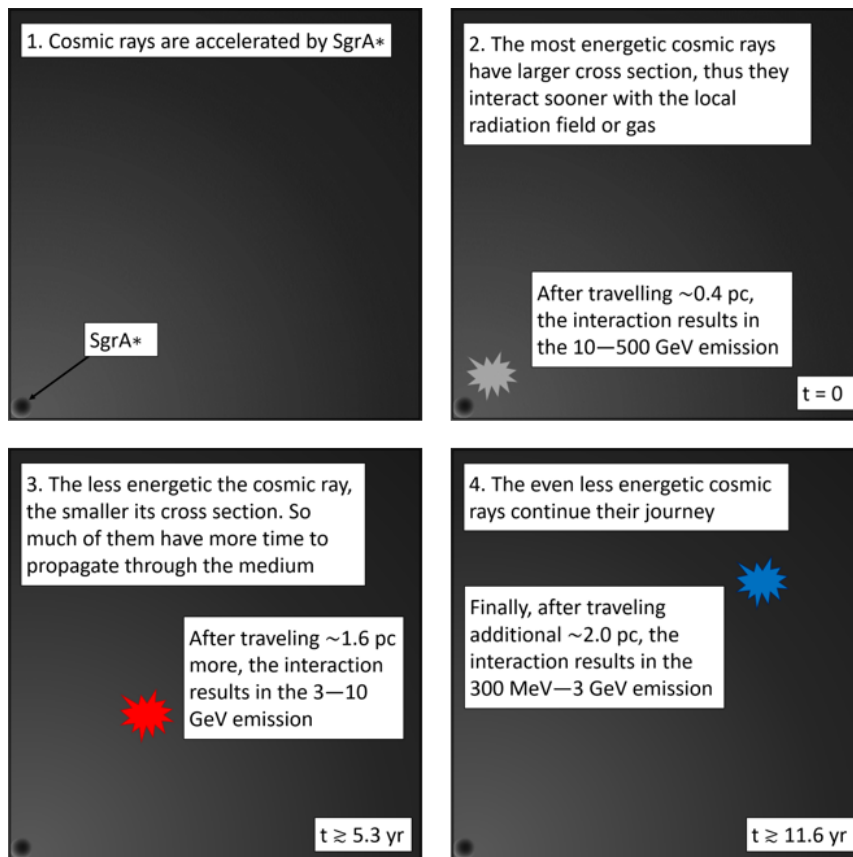


Figure 4.6: A cartoonistic version of the simple model suggested in the text. Cosmic rays accelerated by Sgr A* propagate through the GC region, interacting either with the radiation field or the local gas. More energetic cosmic rays have larger cross sections, thus they interact closer to Sgr A*. Less energetic ones have more time to travel before interacting. The time lengths exhibited at the bottom right part of the panels correspond to the approximate light crossing time for the distances indicated in the Figure text and were chosen based on the centroids distances to Sgr A* (see Figure 3.3).

In Figures 4.7 and 4.8 we show the energy and photon fluxes, respectively, of the three narrower energy bands models. We displaced the data according to the distance between the emission centroids in each energy band. We calculated it based on their angular distances and considering that they are at the GC. We, then, converted this distances into

time delays, defined as the light crossing time between the centroids separations. These delays are only lower bounds, since the cosmic rays, although relativistic, will take longer than light to spread through the GC. We started by displacing the 3–10 GeV data by ≈ 5.3 years. This corresponds to the light crossing time of the distance of ≈ 1.6 pc between the emission centroids in the 10–500 GeV and in the 3–10 GeV ranges (if they are at the GC distance). The data for the 300 MeV–3 GeV LC was displaced by ≈ 11.6 years with the addition of the light crossing time for 1.9 pc (the distance between the 3–10 GeV and the 300 MeV–3 GeV centroids). It means that fluctuations in the LCs caused by one population of cosmic rays in a panel will be approximately aligned with the potential variability generated by the same population in another panel. Because of the estimated time delays, we changed the horizontal axis to account for the time (in years) elapsed since the beginning of the data collection.

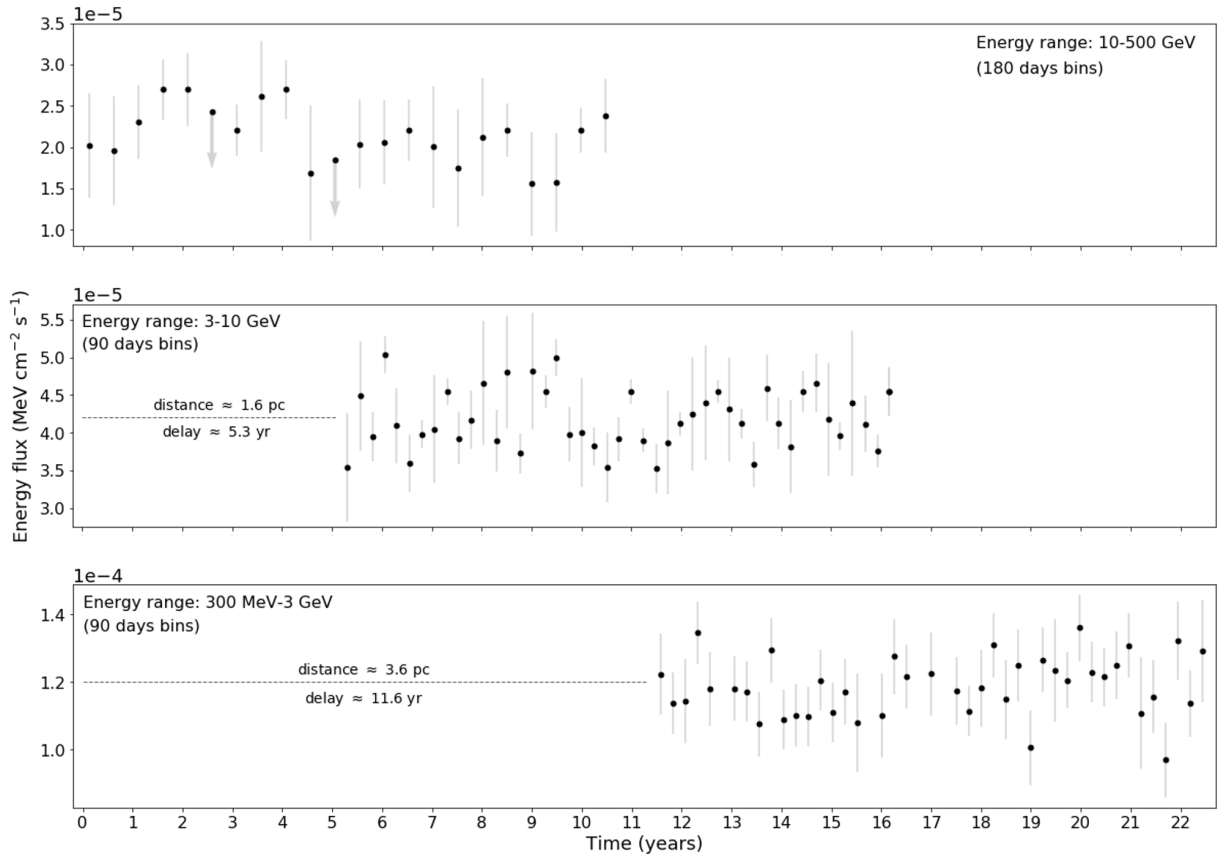


Figure 4.7: We show the energy flux LCs obtained for the narrower energy bands models used in this work: 10–500 GeV (with 180 days bins, in the upper panel), 3–10 GeV (with 90 days bins, in the central panel), and 300 MeV–3 GeV (with 90 days bins, in the lower panel). The LC in the central panel was displaced by ≈ 5.3 years, corresponding to the light crossing time between the emission centroids in the 10–500 GeV and the 3–10 GeV energy bands. The displacement in the lower panel is of ≈ 11.6 years to include the separation between the 3–10 GeV and the 300 MeV–3 GeV centroids.

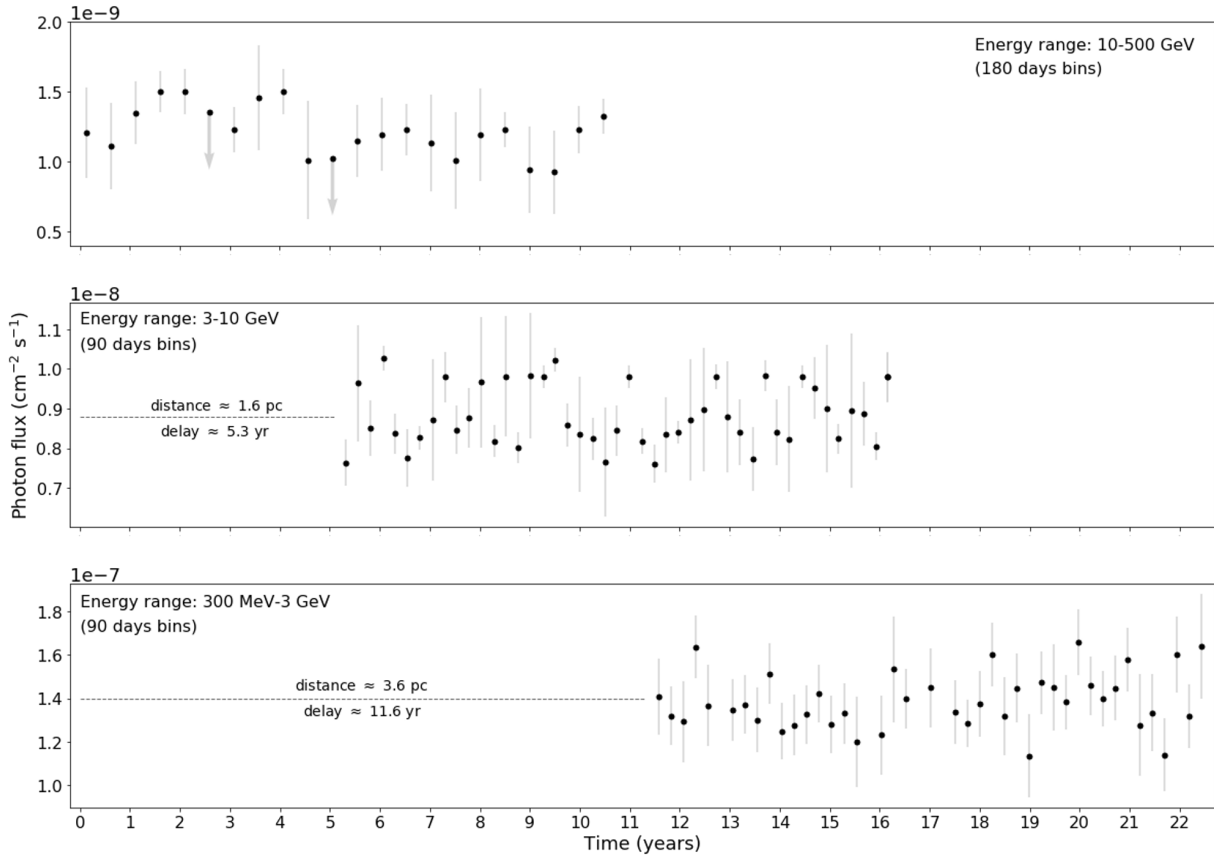


Figure 4.8: We show the photon flux LCs obtained for the narrower energy bands models used in this work: 10–500 GeV (upper panel), 3–10 GeV (central panel), and 300 MeV–3 GeV (lower panel). The bins sizes and displacements are the same as in Figure 4.7.

A visual inspection of Figures 4.7 and 4.8 is enough to rule out any detection of “echoes”. This is not surprising for two main reasons. The first is that the variability in these LCs are very similar with a random noise (although we did not test if these fluxes distributions are compatible with a Gaussian random process, as explained in Sections 2.5.3 and 3.3.2), which impose severe limitation on the possibility of correlating variation. Also, since we had to use large time bins in these LCs, the number of data points available to correlate is very limited.

4.3 SED and emission models

In Figure 4.9² we compare the GC source’s SED (presented in 3.19) with several models for the MeV to TeV emission from Sgr A*. The list includes the “Fermi-era” models and also a model from Ballantyne et al. (2011) in the TeV energy range, with only a minor overlap with the energy range used in our analysis. A quick comment about this model is that its spectrum is a result of intermittent CR acceleration close to Sgr A* at specific periods in the past. One prediction from Ballantyne et al. (2011) is variability in the emission on time scales of ~ 10 years. Ahnen, M. L. et al. (2017) find no evidence of this variability in the MAGIC observations. Also, our LCs in the 10–500 GeV energy range (see Figure 3.18), that partially overlaps with the low energy part of Ballantyne et al. (2011) model, show no significant evidence of variability. The “Fermi-era” models were already described in the discussion above (see Sections 4.1.1 and 4.2.1).

Our results are compatible (or close to) all of the models in the ~ 3 –500 GeV energy range. At lower energies, they depart from the “Fermi-era” hadronic models of: Chernyakova et al. (2011), Linden et al. (2012) and Fatuzzo and Melia (2012).

Kusunose and Takahara (2012) propose two parametrizations of their leptonic model, one to explain the TeV emission and another for the *Fermi*-LAT range. Finally, Guo and Mathews (2012) suggest a hybrid model with the TeV emission being hadronic while the electrons scatter off the soft background photons to the MeV–GeV energy range via IC. Our data are consistent with the low energy components of both models in the ~ 2 –500 GeV energy range.

Although our data is not totally coincident with any of the models, it is important to notice that they were constructed around *Fermi*-LAT data obtained during the 2FGL Catalog period. In our work, besides the much longer data collection period (which leads to better statistics), we are using a more recent version of `Fermitools`, Pass 8 response

² Figure 4.9 is an adaptation of a plot from Ahnen, M. L. et al. (2017). Originally, the *Fermi*-LAT data of this image was from Malyshev et al. (2015), but we replaced this with ours. Malyshev et al. (2015) data was created based on the 2FGL J1745.6–2858 source. Later, as discussed in Section 4.2.1 this source was split into two in the following versions of *Fermi* Catalogs. For this reason, their $E^2 dN/dE$ values are slightly higher than ours, especially in lower energies. Another reason to explain this difference is the improvement of the *galdiff* model through the years (Section 1.5.5.1). Malyshev et al. (2015) results might be more contaminated with the diffuse emission associated with gas in the Galactic disk than ours.

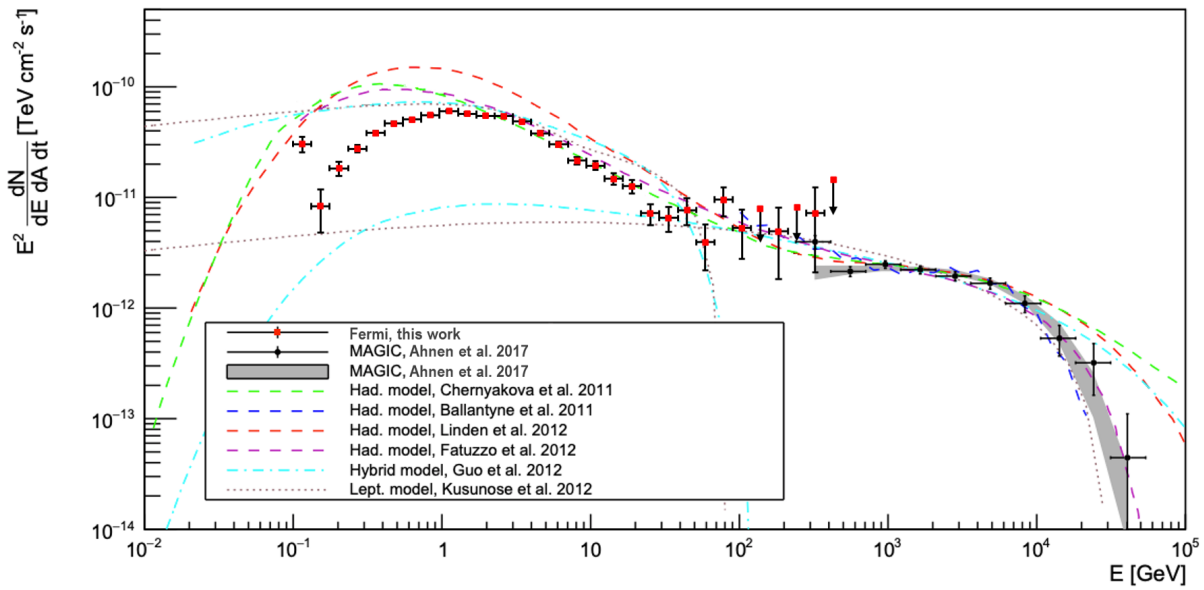


Figure 4.9: The 4FGL J1745.6–2859 SED created for the Universal Model (100 MeV–500 GeV) compared with several models for Sgr A* high energy emission. Source: adapted from Ahnen, M. L. et al. (2017).

functions and the preliminary version of 4FGL catalog (accompanied with improved versions of the diffuse models), all of which were released after these works were published. These improvements allow for much better discrimination between sources, especially the diffuse emission so prominent in the GC and in lower energies. Contamination of diffuse emission in our data is probably the culprit of our lowest energy point being displaced from the spectral model used for the source. This is easier to observe in Figure 3.19, where we also plot the spectral model.

Other than trying to find models that fit exactly to the data, we should be more interested in observing the shape of the observed and the theoretical SEDs. Every hadronic model exhibit a low-energy cut-off (Chernyakova et al., 2011; Linden et al., 2012; Fatuzzo and Melia, 2012). This is expected because of the energy threshold of the “pion-decay bump”, described in Section 1.6.2. And this feature is very clear in our data (except for the lowest energy bin). This SED shape is reported for the first time in this thesis and is a strong evidence of a hadronic origin for this emission. The previous versions of the *galdiff* and *Fermi*-LAT’s response function probably hindered the best assessment of the source’s SED in energies \lesssim a few GeV (e.g., Chernyakova et al. 2011; Malyshev et al. 2015; and our own unpublished former studies).

As explained in Section 1.6.2, the “pion-decay bump” is a signature expected in RIAFs.

In these environments, the protons are heated to very high temperatures, which leads to proton-proton collisions and, consequently, gamma-ray emission. For several decades, RIAFs models have been successfully used to explain Sgr A*’s observations (e.g. Narayan et al. 1995; Yuan et al. 2003, 2004) and our results fit nicely with this framework.

On the high energy end of our SED ($\gtrsim 20$ GeV photons), there is a considerable detachment from the log-parabola spectral model used in the analysis (Figure 3.19). The risk of contamination from nearby sources is low either because of the scarcity of candidates and also because of the intrinsically better PSF in higher energies (see the top row of Figure 1.14). In these energies, the *Fermi*-LAT data transition smoothly to the MAGIC data, as depicted in Figure 4.9, following the behavior of every “Fermi-era” hadronic model (including the hadronic component of the hybrid model from Guo and Mathews 2012); of the Ballantyne et al. (2011) hadronic model that only covers energies $\gtrsim 100$ GeV; and also of the high energy parametrization of the Kusunose and Takahara (2012) leptonic model.

The two-component spectrum at \sim GeV and \sim TeV energies is explained by the hadronic models with very similar arguments. The Chernyakova et al. (2011) spectrum is explained by the different effective velocities of the relativistic and non-relativistic protons accelerated near Sgr A*. Equivalently, Linden et al. (2012) explain their spectrum shape as an outcome of the way protons may propagate through the GC region: either rectilinearly or diffusively and undergoing many or fewer than one collision with the surrounding gas. At the ~ 10 TeV, the emission is dominated by a high energy proton population which propagates rectilinearly, while the \sim GeV emission is governed by less energetic protons propagating diffusively and undergoing Poissonian interactions. A related reason for the observed spectrum is proposed by the two-phase environment of Fatuzzo and Melia (2012). All these scenarios are compatible with the shape and the data of our SED \gtrsim tens GeV.

As a preliminary assessment of the robustness of our results, we inspected the 7 SEDs created based on different selection of free parameters (see Section 2.6). The “pion-decay bump” is conspicuous in all of them. This indicates that the feature in the SED is not a result of the fitting process. Other robustness tests are also possible, such as using alternative models for the Galactic diffuse gamma-ray emission to compare the resulting SED. These tests will be the performed in the near future.

We will discuss the SED in more detail in a forthcoming publication.

Conclusions

In this Section, we summarize the results of this thesis regarding the imaging, spectral and variability properties of 4FGL J1745.6–2859.

The spatial coincidence of 4FGL J1745.6–2859 with Sgr A* is a necessary but not sufficient condition for it to be considered the counterpart emission of the GC’s SMBH. In this respect, our imaging analysis showed that the source’s position is coincident with Sgr A*’s in the 60–300 MeV and in the 10–500 GeV energy bands. Also, when we consider only the three highest energy bands used in this work, the emission centroid approaches Sgr A*’s position as the photon energy increases. Furthermore, 4FGL J1745.6–2859’s luminosity in the 100 MeV–500 GeV is also similar to Sgr A*’s bolometric luminosity. The temporal analyses showed no variability in 15 days timescales. And the SED is compatible with a hadronic scenario. Taken together, these results support the picture in which the point source 4FGL J1745.6–2859 observed by *Fermi*-LAT at the GC is the manifestation of Sgr A* in the MeV–GeV range.

5.1 *The evidence points to Sagittarius A**

Our analysis of 4FGL J1745.6–2859 was split into three approaches. First, we evaluated its position (and extension) as function of the photon energy, then we studied its time evolution and, finally, we assessed its spectrum. Taken together, these analyses allow us to conclude that Sgr A* is the most likely candidate to explain 4FGL J1745.6–2859 and its properties.

The positional and energetics analyses attained the following four main results: (i) the

energetics of 4FGL J1745.6–2859 is comparable to the radio-to-X-ray bolometric luminosity of Sgr A*, (ii) among all the possible candidates for the gamma-ray flux of the point source, only the models invoking cosmic rays accelerated by Sgr A* or a nearby source can explain the observations, (iii) the emission centroid moves toward the position of Sgr A* as the energy is increased and is spatially associated with the CND, a region rich in dense molecular clouds and warm dust, and (iv) other processes not associated with the SMBH could be contributing to the flux at energies < 300 MeV (e.g. pulsars) due to the larger positional uncertainty of the source as the instrument PSF becomes larger at lower energies.

These results suggest that particles responsible for the gamma-ray detected in the three higher energy bands are accelerated by the same process that originates in the region of Sgr A*. A natural consequence of large emission regions is little temporal variability.

The time evolution of the source, observed for ~ 11.3 years, shows no signal of variability on 15 days timescales. This suggests that the source is steady in gamma-rays, hinting at a different emission process from the intrinsically variable ones in lower energies (X-rays, NIR and radio). We can not confidently rule out the possibility, though, that these processes are indeed associated but any variability in gamma-rays average out in the 15 days timescales of our bins. Although there are leptonic models constructed over a stable gamma-ray emission from Sgr A*, this behavior is better explained by hadronic processes. They result in inherently unvarying LCs since the emission regions are larger (than in leptonic scenarios) and the cooling time is much longer for protons.

Another strong evidence favoring hadronic process as the origin of the *Fermi*-LAT emission from the GC arises from its SED. It clearly shows a “pion-decay bump” and its shape is compatible with every “Fermi-era” hadronic model. The observed “pion-decay bump” is also compatible with the RIAF interpretation of Sgr A*, which is largely used in the literature, since RIAF’s environments favor proton-proton collisions and subsequent gamma-ray emission through pion decay.

Furthermore, we scrutinized all the potential candidates for the gamma-ray emission from the GC found in the literature. Only models that link the emission with Sgr A* are compatible with our results. Other candidates are likely to contribute only at low ($\lesssim 300$ MeV) energies.

Taken together, the evidence we gathered regarding 4FGL J1745.6–2859 emission point

in the direction of Sgr A*. An hadronic model, in which the accelerated protons interact with the gas content of the CND, is the most suitable: it naturally explains the steady LCs and the shape of the observed SED. Also, it is compatible with the emission positions and extension ULs.

There are still uncertainties regarding the association of 4FGL J1745.6–2859 with the SMBH. In the following Section we discuss future perspectives concerning our work with *Fermi*-LAT data and the advent of modern gamma-ray detectors, for the GC high energy study.

5.2 Future perspectives

Before we discuss the arrival of a new generation of astrophysical gamma-ray observatories and their impact on the high energy emission from the GC, we will focus on improvements in the context of our own work with *Fermi*-LAT data that could slightly improve the quality of this work.

The most obvious improvement that we could make in our analysis is to use what we learned with the SED. In Figure 3.19 we can clearly observe that the lowest energy point (that covers the 100–133 MeV energy range) is significantly displaced from the trend observed in higher energies. This is likely due to contamination from other sources, facilitated by *Fermi*-LAT’s broader PSF in lower energies and the ubiquity of low energy sources, including the *galdiff*. Excluding energies $\lesssim 130$ MeV from our analysis would help a better fit of the log-parabola spectral model to the data. It is evident from Figure 3.19 that the modeled cutoff in lower energies (represented by the gray line) is displaced from the SED data. We did not perform an analysis with this different energy selection, but we expect a better fitting of the model to the data, evidenced by higher likelihoods. The impact on the source position’s reported, for example, in Figure 3.2 would probably be negligible because we only used the Universal Model (100 MeV–500 GeV) to assess 4FGL J1745.6–2859’s position in energies > 300 MeV (the position in lower energies was obtained with an independent model). And the SED data is perfectly compatible with the fitted spectral model up to ~ 50 GeV. Any impact on the source’s position is expected to the higher energy band of our work (10–50 GeV). But, a combination of factors—*Fermi*-LAT’s better PSF

at high energies and the lack of other very high energy sources close to the GC—reduce the potential of this impact.

Figure 3.19 also indicates a displacement of the data from the log-parabola spectral model in energies $\gtrsim 50$ GeV. Excluding photons with these energies would also help in assessing the “pion-decay bump” shape in our work. The analysis focused in this higher energy emission could be performed separately. Different functions could be used in this energy range, such as a power-law and a log-parabola, and the model with the higher likelihood adopted. In Figure 4.9 it is clear that the high energy *Fermi*-LAT data transition smoothly to the ground-based telescopes (such as the MAGIC data). This is expected since every hadronic model consider that the GC gamma-ray emission is divided into two components and both contribute in the ~ 100 GeV energies.

We also plan on developing our own emission models, either hadronic and leptonic, based on the SED we obtained. This will allow us to better understand the high energy processes happening in the vicinity of Sgr A* and put constrains on the cosmic ray population of the GC.

The LCs were created with the whole energy range of the Universal Model. Eliminating photons with energies $\lesssim 130$ MeV, as we proposed above as an improvement for the quality of the SED, could impact the results obtained in the temporal analysis. Since the contaminating photons are likely poorly modeled *galdiff*'s photons, whose emission is expected to be constant in time, further avoiding this foreground emission could potentially evidence some very small—undetected in this work—variability. On the other hand, limiting the energy range also reduces the number of photons available for the analysis. A smaller number of counts in the LCs leads to points with smaller TS , which are consequently reported as ULs. The impact of this trade-off between a better analysis with a limited energy range and the consequent decrease of statistics is very hard to quantify. An empirical assessment is the better approach and, given that generating LCs is very time consuming, we let it to the future.

The LCs we presented in this work could also be improved, even if we keep the same energy range used in the Universal Model. We could use slightly smaller time bins in the LCs, as evidenced by the $TS > 16$ in most of the data points (see Appendix M). An outcome of reducing the bin sizes, is the decrease of the TS because of the fewer photons and consequence lack of statistics. For this reason, the bins sizes could be only moderately

reduced. If the source is variable in timescales much smaller than the 15 days bins we used in this work, the potential decrease in the bins sizes would not be enough to assess this variability.

The only way to obtain LCs with time bins that are short and also have high enough TS is to collect large amount of photons. Our results are very close to *Fermi*-LAT limit, which is governed by its effective area and sensitivity. The ground-based gamma-ray observatories have much larger collecting areas but they cover energy ranges higher than *Fermi*-LAT's; are localized in regions with low exposure to the GC (with the exception of H.E.S.S.); and operate in a very different way than *Fermi*, requiring an observing campaign to point to the GC. CTA South (located in the Paranal Observatory in the Atacama Desert in Chile) will have very good exposure to the GC, but has the same characteristics as the other ground-based detectors. Proposed gamma-ray space observatories, AMEGO (McEnery et al., 2019) and e-ASTROGAM (de Angelis et al., 2018), will cover energy ranges that overlap with *Fermi*-LAT's low energy limit, bridging the gap to the current generation of hard X-ray instruments. As *Fermi*, they will cover the whole sky periodically, being constantly exposed to the GC, which, combined with their high sensitivity, will potentially allow to LCs with higher temporal resolutions.

The new generation of gamma-ray telescopes will also have a positive impact on the imaging, positional and extension analyses that we performed. The advent of CTA will allow for a deep exposure of the GC in energies up to ~ 300 TeV. This will permit studies in spatial and spectral details unavailable today, with arc-minute resolution at energies above *Fermi*-LAT's operational range, potentially enabling a firmer association between the very high-energy point source in the GC with Sgr A* or other nearby candidate. CTA will be able to enhance significantly the assessment of the morphology of \sim TeV source, allowing for correlations with the gas density distribution in the GC (Linden et al., 2012). This could potentially confirm or deny the hadronic origin for the very high energy gamma-ray emission. Correspondingly, the AMEGO mission and e-ASTROGAM should help to better constrain the properties of the GC emission in the 60–300 MeV energy band and shed light on the contribution of Sgr A* in the low energy portion of our analysis.

Moving away from the gamma-ray detectors, future missions and results focused in the GC will also contribute to the understanding of the high energy processes associated to Sgr A*. The Extremely Large Telescope (ELT) will increase the probability of

finding S-star cluster members very close to Sgr A* with NIR observations. Recently, Fragione and Loeb (2020) placed an UL on the spin of Sgr A* based on the spatial distribution of the S-stars. ELT observations would help them to even better constrain their estimate. The EHT observational campaign of Sgr A* will also contribute to measure the SMBH spin. This measurement could help to determine the mechanism behind the *Fermi*-LAT observations of the GC. Leptonic models are dependent of a relatively high spin, necessary to enable the concentration of magnetic field lines and consequent acceleration of electrons to relativistic speeds and gamma-ray emission through IC scattering.

The recent history of astrophysics is conspicuously brimful of discoveries regarding BHs and the GC. In 2017, Rainer Weiss, Kip S. Thorne and Barry C. Barish shared the Nobel Prize in Physics for the direct detection of gravitational waves from the merger of two BHs. Two years later, the first image of a BH silhouette was captured using the EHT. The following year, Andrea Ghez and Reinhard Genzel were awarded the Nobel Prize in Physics for the discovery of Sgr A*. Jointly, Roger Penrose has also received the prize for his theoretical work robustly connecting BHs to the General Theory of Relativity. In this context, the present work serves the purpose of contributing as a building block to our understanding of those intriguing objects and their role in the cosmos.

Bibliography

- Abazajian, K. N., Horiuchi, S., Kaplinghat, M., Keeley, R. E., and Macias, O. (2020). Strong constraints on thermal relic dark matter from fermi-lat observations of the galactic center. *Phys. Rev. D*, 102:043012.
- Abazajian, K. N. and Kaplinghat, M. (2012). Detection of a gamma-ray source in the Galactic Center consistent with extended emission from dark matter annihilation and concentrated astrophysical emission. *Phys. Rev. D*, 86(8):083511.
- Abbott, B. P., Abbott, R., Abbott, T. D., Acernese, F., Ackley, K., et al. (2017a). Gw170817: Observation of gravitational waves from a binary neutron star inspiral. *Phys. Rev. Lett.*, 119:161101.
- Abbott, B. P., Abbott, R., Abbott, T. D., Acernese, F., Ackley, K., et al. (2017b). Multimessenger observations of a binary neutron star merger. *The Astrophysical Journal*, 848(2):L12.
- Abdo, A. A., Ackermann, M., Ajello, M., Allafort, A., Antolini, E., et al. (2010). Fermi large area telescope first source catalog. *ApJS*, 188(2):405.
- Abdo, A. A., Ackermann, M., Ajello, M., Atwood, W. B., Axelsson, M., et al. (2010). The First Fermi Large Area Telescope Catalog of Gamma-ray Pulsars. *ApJS*, 187(2):460–494.
- Acero, F., Ackermann, M., Ajello, M., Albert, A., Atwood, W. B., et al. (2015). Fermi Large Area Telescope Third Source Catalog. *ApJS*, 218:23.
- Acero, F., Aharonian, F., Akhperjanian, A. G., Anton, G., Barres de Almeida, U., et al. (2010). Localizing the VHE γ -ray source at the Galactic Centre. *MNRAS*, 402(3):1877–1882.

- Ackermann, M., Ajello, M., Albert, A., Allafort, A., Atwood, W. B., et al. (2012a). The Fermi Large Area Telescope on Orbit: Event Classification, Instrument Response Functions, and Calibration. *ApJS*, 203:4.
- Ackermann, M., Ajello, M., Albert, A., Atwood, W., Baldini, L., et al. (2017). The Fermi galactic center GeV excess and implications for dark matter. *The Astrophysical Journal*, 840(1):43.
- Ackermann, M., Ajello, M., Atwood, W. B., Baldini, L., Ballet, J., et al. (2012b). Fermi-LAT Observations of the Diffuse γ -Ray Emission: Implications for Cosmic Rays and the Interstellar Medium. *ApJ*, 750(1):3.
- Aharonian, F., Akhperjanian, A. G., Anton, G., Barres de Almeida, U., Bazer-Bachi, A. R., et al. (2009). Spectrum and variability of the Galactic center VHE γ -ray source HESS J1745-290. *A&A*, 503(3):817–825.
- Aharonian, F. and Neronov, A. (2005a). High-Energy Gamma Rays from the Massive Black Hole in the Galactic Center. *ApJ*, 619:306–313.
- Aharonian, F. and Neronov, A. (2005b). TeV gamma rays from the galactic center direct and indirect links to the massive black hole in sgr A*. *Astrophysics and Space Science*, 300(1):255–265.
- Aharonian, F., Yang, R., and de Oña Wilhelmi, E. (2019). Massive stars as major factories of Galactic cosmic rays. *Nature Astronomy*, 3:561–567.
- Aharonian, F., Akhperjanian, A. G., Aye, K.-M., Bazer-Bachi, A. R., Beilicke, M., et al. (2004). Very high energy gamma rays from the direction of Sagittarius A*. *A&A*, 425(1):L13–L17.
- Ahnen, M. L., Ansoldi, S., Antonelli, L. A., Antoranz, P., Arcaro, C., et al. (2017). Observations of Sagittarius A* during the pericenter passage of the G2 object with MAGIC. *A&A*, 601:A33.
- Ajello, M., Albert, A., Atwood, W., Barbiellini, G., Bastieri, D., et al. (2016). Fermi-lat observations of high-energy γ -ray emission toward the galactic center. *The Astrophysical Journal*, 819(1):44.

-
- Ajello, M., Angioni, R., Axelsson, M., Ballet, J., Barbiellini, G., et al. (2020). The fourth catalog of active galactic nuclei detected by the Fermi Large Area Telescope. *The Astrophysical Journal*, 892(2):105.
- Ajello, M., Atwood, W. B., Baldini, L., Ballet, J., Barbiellini, G., et al. (2017). 3FHL: The Third Catalog of Hard Fermi-LAT Sources. *ApJS*, 232(2):18.
- Akaike, H. (1974). A new look at the statistical model identification. *IEEE Transactions on Automatic Control*, 19(6):716–723.
- Albert, J., Aliu, E., Anderhub, H., Antoranz, P., Armada, A., et al. (2006). Observation of gamma rays from the galactic center with the MAGIC telescope. *The Astrophysical Journal*, 638(2):L101–L104.
- Almeida, I. and Nemmen, R. (2020). Winds and feedback from supermassive black holes accreting at low rates: hydrodynamical treatment. *Monthly Notices of the Royal Astronomical Society*, 492(2):2553–2571.
- Armillotta, L., Krumholz, M. R., Di Teodoro, E. M., and McClure-Griffiths, N. M. (2019). The life cycle of the Central Molecular Zone - I. Inflow, star formation, and winds. *Monthly Notices of the Royal Astronomical Society*, 490(3):4401–4418.
- Atoyan, A. and Dermer, C. D. (2004). TeV Emission from the Galactic Center Black Hole Plerion. *ApJ*, 617:L123–L126.
- Atwood, W., Albert, A., Baldini, L., Tinivella, M., Bregeon, J., et al. (2013). Pass 8: Toward the full realization of the fermi-lat scientific potential. *arXiv preprint arXiv:1303.3514*.
- Atwood, W. B., Abdo, A. A., Ackermann, M., Althouse, W., Anderson, B., et al. (2009). The Large Area Telescope on the Fermi Gamma-Ray Space Telescope Mission. *The Astrophysical Journal*, 697(2):1071–1102.
- Baganoff, F. K., Bautz, M. W., Brandt, W. N., Chartas, G., Feigelson, E. D., et al. (2001). Rapid X-ray flaring from the direction of the supermassive black hole at the Galactic Centre. *Nature*, 413:45–48.

- Baganoff, F. K., Maeda, Y., Morris, M., Bautz, M. W., Brandt, W. N., et al. (2003). Chandra X-Ray Spectroscopic Imaging of Sagittarius A* and the Central Parsec of the Galaxy. *ApJ*, 591:891–915.
- Balick, B. and Brown, R. L. (1974). Intense sub-arcsecond structure in the galactic center. *ApJ*, 194:265–270.
- Ball, D., Ozel, F., Psaltis, D., and kwan Chan, C. (2016). Particle Acceleration and the Origin Of X-Ray Flares In GRMHD Simulations Of Sgr A*. *The Astrophysical Journal*, 826(1):77.
- Ballantyne, D. R., Schumann, M., and Ford, B. (2011). Modelling the time-dependence of the TeV Gamma-ray source at the Galactic Centre. *Monthly Notices of the Royal Astronomical Society*, 410(3):1521–1526.
- Ballet, J., Burnett, T. H., Digel, S. W., and Lott, B. (2020). Fermi Large Area Telescope Fourth Source Catalog Data Release 2. *arXiv e-prints*, page arXiv:2005.11208.
- Barrière, N. M., Tomsick, J. A., Baganoff, F. K., Boggs, S. E., Christensen, F. E., et al. (2014). NuSTAR Detection of High-Energy X-Ray Emission and Rapid Variability From Sagittarius A* Flares. *The Astrophysical Journal*, 786(1):46.
- Becklin, E. E., Gatley, I., and Werner, M. W. (1982). Far-infrared observations of Sagittarius A - The luminosity and dust density in the central parsec of the Galaxy. *ApJ*, 258:135–142.
- Becklin, E. E., Matthews, K., Neugebauer, G., and Willner, S. P. (1978). Infrared observations of the galactic center. I. Nature of the compact sources. *ApJ*, 219:121–128.
- Becklin, E. E. and Neugebauer, G. (1968). Infrared Observations of the Galactic Center. *ApJ*, 151:145.
- Blum, R. D., Ramond, T. M., Conti, P. S., Figer, D. F., and Sellgren, K. (1997). H-Band Spectroscopic Classification of OB Stars. *AJ*, 113:1855–1859.
- Boehle, A., Ghez, A. M., Schodel, R., Meyer, L., Yelda, S., et al. (2016). An Improved Distance and Mass Estimate For Sgr A* From a Multistar Orbit Analysis. *The Astrophysical Journal*, 830(1):17.

-
- Bower, G. C., Falcke, H., Sault, R. J., and Backer, D. C. (2002). The spectrum and variability of circular polarization in Sagittarius A* from 1.4 to 15 GHz. *The Astrophysical Journal*, 571(2):843.
- Boyce, H., Haggard, D., Witzel, G., Willner, S. P., Neilsen, J., et al. (2019). Simultaneous X-Ray and Infrared Observations of Sagittarius A*s Variability. *The Astrophysical Journal*, 871(2):161.
- Brinkerink, C. D., Falcke, H., Law, C. J., Barkats, D., Bower, G. C., et al. (2015). ALMA and VLA measurements of frequency-dependent time lags in Sagittarius A*: evidence for a relativistic outflow. *A&A*, 576:A41.
- Broderick, A. E. and Loeb, A. (2005). Imaging bright-spots in the accretion flow near the black hole horizon of Sgr A*. *Monthly Notices of the Royal Astronomical Society*, 363(2):353–362.
- Broderick, A. E. and Loeb, A. (2006). Imaging optically-thin hotspots near the black hole horizon of Sgr A* at radio and near-infrared wavelengths. *Monthly Notices of the Royal Astronomical Society*, 367(3):905–916.
- Brown, R. L. (1982). Precessing jets in Sagittarius A: gas dynamics in the central parsec of the galaxy. *ApJ*, 262:110–119.
- Calderon, D., Cuadra, J., Schartmann, M., Burkert, A., and Russell, C. M. P. (2020). Stellar Winds Pump the Heart of the Milky Way. *ApJ*, 888(1):L2.
- Calore, F., Cholis, I., and Weniger, C. (2015). Background model systematics for the fermi GeV excess. *Journal of Cosmology and Astroparticle Physics*, 2015(03):038–038.
- Chen, Z., Gallego-Cano, E., Do, T., Witzel, G., Ghez, A. M., et al. (2019). Consistency of the Infrared Variability of SGR A* over 22 yr. *The Astrophysical Journal*, 882(2):L28.
- Cherenkov Telescope Array Consortium, Acharya, B. S., Agudo, I., Al Samarai, I., Alfaro, R., et al. (2019). *Science with the Cherenkov Telescope Array*.
- Chernyakova, M., Malyshev, D., Aharonian, F. A., Crocker, R. M., and Jones, D. I. (2011). The High-energy, Arcminute-scale Galactic Center Gamma-ray Source. *ApJ*, 726:60.

- Cholis, I., Evoli, C., Calore, F., Linden, T., Weniger, C., and Hooper, D. (2015). The galactic center GeV excess from a series of leptonic cosmic-ray outbursts. *Journal of Cosmology and Astroparticle Physics*, 2015(12):005–005.
- Christopher, M. H., Scoville, N. Z., Stolovy, S. R., and Yun, M. S. (2005). HCN and HCO+ Observations of the Galactic Circumnuclear Disk. *The Astrophysical Journal*, 622(1):346–365.
- Clavel, M., Terrier, R., Goldwurm, A., Morris, M. R., Ponti, G., Soldi, S., and Trap, G. (2013). Echoes of multiple outbursts of Sagittarius A* revealed by Chandra. *A&A*, 558:A32.
- Compton, A. H. (1923). A quantum theory of the scattering of x-rays by light elements. *Phys. Rev.*, 21:483–502.
- Crocker, R. M., Fatuzzo, M., Jokipii, J. R., Melia, F., and Volkas, R. R. (2005). The AGASA and SUGAR Anisotropies and TeV Gamma Rays from the Galactic Center: A Possible Signature of Extremely High Energy Neutrons. *ApJ*, 622:892–909.
- D’Agostino, R. (1971). An omnibus test of normality for moderate and large size samples. *Biometrika*, 58(2):341–348.
- D’Agostino, R. and Pearson, E. S. (1973). Tests for departure from normality. Empirical results for the distributions of b_2 and $\sqrt{b_1}$. *Biometrika*, 60(3):613–622.
- de Angelis, A. and Mallamaci, M. (2018). Gamma-ray astrophysics. *European Physical Journal Plus*, 133(8):324.
- de Angelis, A., Tatischeff, V., Grenier, I. A., McEnery, J., Mallamaci, M., et al. (2018). Science with e-ASTROGAM. A space mission for MeV-GeV gamma-ray astrophysics. *Journal of High Energy Astrophysics*, 19:1–106.
- de Menezes, R., Cafardo, F., and Nemmen, R. (2019). Milky Way globular clusters in Gamma-rays: analysing the dynamical formation of millisecond pulsars. *Monthly Notices of the Royal Astronomical Society*, 486(1):851–867.
- de Menezes, R., Nemmen, R., Finke, J. D., Almeida, I., and Rani, B. (2020). Gamma-ray observations of low-luminosity active galactic nuclei. *MNRAS*, 492(3):4120–4130.

- Dermer, C. and Menon, G. (2009). *High Energy Radiation from Black Holes: Gamma Rays, Cosmic Rays, and Neutrinos*. Princeton Series in Astrophysics. Princeton University Press.
- Di Mauro, M. (2021). The characteristics of the Galactic center excess measured with 11 years of Fermi-LAT data. *arXiv e-prints*, page arXiv:2101.04694.
- Dibi, S., Markoff, S., Belmont, R., Malzac, J., Barrière, N. M., and Tomsick, J. A. (2014). Exploring plasma evolution during Sagittarius A* flares. *MNRAS*, 441:1005–1016.
- Do, T., Ghez, A. M., Morris, M. R., Yelda, S., Meyer, L., et al. (2009). A Near-Infrared Variability Study of the Galactic Black Hole: A Red Noise Source With No Detected Periodicity. *The Astrophysical Journal*, 691(2):1021–1034.
- Do, T., Lu, J. R., Ghez, A. M., Morris, M. R., Yelda, S., et al. (2013). Stellar populations in the central 0.5 pc of the galaxy. i. a new method for constructing luminosity functions and surface-density profiles. *The Astrophysical Journal*, 764(2):154.
- Do, T., Witzel, G., Gautam, A. K., Chen, Z., Ghez, A. M., et al. (2019). Unprecedented Near-infrared Brightness and Variability of Sgr A*. *The Astrophysical Journal Letters*, 882(2):L27.
- Dodds-Eden, K., Gillessen, S., Fritz, T. K., Eisenhauer, F., Trippe, S., et al. (2011). The Two States of Sgr A* In The Near-Infrared: Bright Episodic Flares on Top Of Low-Level Continuous Variability. *The Astrophysical Journal*, 728(1):37.
- Dodds-Eden, K., Porquet, D., Trap, G., Quataert, E., Haubois, X., et al. (2009). Evidence for X-Ray Synchrotron Emission from Simultaneous Mid-Infrared to X-Ray Observations of a Strong Sgr A* Flare. *ApJ*, 698:676–692.
- Eckart, A., Baganoff, F., Morris, M., Bautz, M., Brandt, W. N., et al. (2004). First simultaneous NIR/X-ray detection of a flare from Sgr A*. *Astronomy & Astrophysics*, 427(1):1–11.
- Eckart, A., Baganoff, F., Morris, M., Kunneriath, D., Zamaninasab, M., et al. (2009). Modeling mm-to X-ray flare emission from Sagittarius A*. *Astronomy & Astrophysics*, 500(3):935–946.

- Eckart, A., García-Marín, M., Vogel, S., Teuben, P., Morris, M., et al. (2012). Millimeter to X-ray flares from Sagittarius A*. *Astronomy & Astrophysics*, 537:A52.
- Eckart, A., Hüttemann, A., Kiefer, C., Britzen, S., Zajaček, M., et al. (2017). The Milky Way's Supermassive Black Hole: How Good a Case Is It? *Foundations of Physics*, 47(5):553–624.
- Eckart, A., Schödel, R., García-Marín, M., Witzel, G., Weiss, A., et al. (2008). Simultaneous NIR/sub-mm observation of flare emission from Sagittarius A*. *Astronomy & Astrophysics*, 492(2):337–344.
- Eckart, A., Schodel, R., Meyer, L., Trippe, S., Ott, T., and Genzel, R. (2006). Polarimetry of near-infrared flares from Sagittarius A*. *A&A*, 455(1):1–10.
- Eckart, A., Zajacek, M., Parsa, M., Fazeli, E. H. N., Busch, G., et al. (2018). The Multi-frequency Behavior of Sagittarius A*. *arXiv e-prints*, page arXiv:1806.00284.
- Eisenhauer, F., Genzel, R., Alexander, T., Abuter, R., Paumard, T., et al. (2005). SINFONI in the Galactic Center: Young Stars and Infrared Flares in the Central Light-Month. *The Astrophysical Journal*, 628(1):246–259.
- Event Horizon Telescope Collaboration et al. (2019). First M87 Event Horizon Telescope Results. I. The Shadow of the Supermassive Black Hole. *ApJ*, 875(1):L1.
- Falcke, H., Goss, W. M., Matsuo, H., Teuben, P., Zhao, J.-H., and Zylka, R. (1998). The Simultaneous Spectrum of Sagittarius A* from 20 Centimeters to 1 Millimeter and the Nature of the Millimeter Excess. *The Astrophysical Journal*, 499(2):731–734.
- Fatuzzo, M. and Melia, F. (2003). A Kinship between the EGRET Supernova Remnants and Sagittarius A East. *The Astrophysical Journal*, 596(2):1035–1043.
- Fatuzzo, M. and Melia, F. (2012). Diffusive Cosmic-Ray Acceleration in Sagittarius A*. *ApJ*, 757(1):L16.
- Fazio, G. G., Hora, J. L., Witzel, G., Willner, S. P., Ashby, M. L. N., et al. (2018). Multiwavelength Light Curves of Two Remarkable Sagittarius A* Flares. *ApJ*, 864(1):58.
- Foreman-Mackey, D., Hogg, D. W., Lang, D., and Goodman, J. (2013). emcee: The MCMC Hammer. *PASP*, 125(925):306.

-
- Fragione, G. and Loeb, A. (2020). An Upper Limit on the Spin of SgrA* Based on Stellar Orbits in Its Vicinity. *The Astrophysical Journal*, 901(2):L32.
- Freitag, M., Amaro-Seoane, P., and Kalogera, V. (2006). Stellar remnants in galactic nuclei: Mass segregation. *The Astrophysical Journal*, 649(1):91–117.
- Genzel, R., Eisenhauer, F., and Gillessen, S. (2010). The Galactic Center massive black hole and nuclear star cluster. *Reviews of Modern Physics*, 82:3121–3195.
- Genzel, R., Hollenbach, D., and Townes, C. H. (1994). The nucleus of our galaxy. *Reports on Progress in Physics*, 57(5):417–479.
- Genzel, R., Pichon, C., Eckart, A., Gerhard, O. E., and Ott, T. (2000). Stellar dynamics in the Galactic Centre: proper motions and anisotropy. *Monthly Notices of the Royal Astronomical Society*, 317(2):348–374.
- Genzel, R., Schödel, R., Ott, T., Eckart, A., Alexander, T., Lacombe, F., et al. (2003). Near-infrared flares from accreting gas around the supermassive black hole at the Galactic Centre. *Nature*, 425:934–937.
- Genzel, R., Schödel, R., Ott, T., Eisenhauer, F., Hofmann, R., et al. (2003). The Stellar Cusp around the Supermassive Black Hole in the Galactic Center. *The Astrophysical Journal*, 594(2):812–832.
- Genzel, R., Thatte, N., Krabbe, A., Kroker, H., and Tacconi-Garman, L. E. (1996). The dark mass concentration in the central parsec of the milky way. *The Astrophysical Journal*, 472(1):153–172.
- Ghez, A. M., Salim, S., Weinberg, N. N., Lu, J. R., Do, T., et al. (2008). Measuring Distance and Properties of the Milky Way’s Central Supermassive Black Hole with Stellar Orbits. *ApJ*, 689:1044–1062.
- Ghez, A. M., Wright, S. A., Matthews, K., Thompson, D., Le Mignant, D., et al. (2004). Variable Infrared Emission from the Supermassive Black Hole at the Center of the Milky Way. *ApJ*, 601:L159–L162.

- Gillessen, S., Eisenhauer, F., Fritz, T. K., Bartko, H., Dodds-Eden, K., et al. (2009). The Orbit of the Star S2 Around Sgr A* From Very Large Telescope and Keck Data. *The Astrophysical Journal*, 707(2):L114–L117.
- Gillessen, S., Eisenhauer, F., Trippe, S., Alexander, T., Genzel, R., et al. (2009). Monitoring Stellar Orbits Around the Massive Black Hole in the Galactic Center. *ApJ*, 692:1075–1109.
- Gillessen, S., Genzel, R., Fritz, T. K., Eisenhauer, F., Pfuhl, O., et al. (2013). Pericenter Passage of the Gas Cloud G2 in the Galactic Center. *ApJ*, 774:44.
- Gillessen, S., Genzel, R., Fritz, T. K., Quataert, E., Alig, C., et al. (2012). A gas cloud on its way towards the supermassive black hole at the Galactic Centre. *Nature*, 481:51–54.
- Goodenough, L. and Hooper, D. (2009). Possible evidence for dark matter annihilation in the inner milky way from the fermi gamma ray space telescope. *arXiv preprint arXiv:0910.2998*.
- Goss, W. M., Brown, R. L., and Lo, K. Y. (2003). The Discovery of Sgr A*. *Astronomische Nachrichten Supplement*, 324(1):497–504.
- GRAVITY Collaboration et al. (2018a). Detection of orbital motions near the last stable circular orbit of the massive black hole SgrA*. *A&A*, 618:L10.
- GRAVITY Collaboration et al. (2018b). Detection of the gravitational redshift in the orbit of the star S2 near the Galactic centre massive black hole. *A&A*, 615:L15.
- GRAVITY Collaboration et al. (2019). A geometric distance measurement to the galactic center black hole with 0.3% uncertainty. *A&A*, 625:L10.
- GRAVITY Collaboration et al. (2020). Detection of the schwarzschild precession in the orbit of the star s2 near the galactic centre massive black hole. *A&A*, 636:L5.
- Grenier, I., Casandjian, J.-M., and Terrier, R. (2005). Unveiling extensive clouds of dark gas in the solar neighborhood. *Science (New York, N.Y.)*, 307:1292–5.
- Guesten, R., Genzel, R., Wright, M. C. H., Jaffe, D. T., Stutzki, J., and Harris, A. I. (1987). Aperture Synthesis Observations of the Circumnuclear Ring in the Galactic Center. *ApJ*, 318:124.

-
- Guo, F. and Mathews, W. G. (2012). The Fermi Bubbles. I. Possible Evidence for Recent AGN Jet Activity in the Galaxy. *ApJ*, 756:181.
- Guo, Y.-Q., Yuan, Q., Liu, C., and Li, A.-F. (2013). A hybrid model of GeV-TeV gamma ray emission from the Galactic center. *Journal of Physics G Nuclear Physics*, 40(6):065201.
- Gusten, R. and Downes, D. (1980). Formaldehyde in the Galactic Center region: interpretation. *A&A*, 87:6–19.
- Gutiérrez, E. M., Nemmen, R., and Cafardo, F. (2020). A Nonthermal Bomb Explains the Near-infrared Superflare of Sgr A*. *The Astrophysical Journal*, 891(2):L36.
- Habibi, M., Gillessen, S., Martins, F., Eisenhauer, F., Plewa, P. M., et al. (2017). Twelve Years of Spectroscopic Monitoring in the Galactic Center: The Closest Look at S-stars near the Black Hole. *The Astrophysical Journal*, 847(2):120.
- Haggard, D., Nynka, M., Mon, B., de la Cruz Hernandez, N., et al. (2019). Chandra Spectral and Timing Analysis of Sgr A*'s Brightest X-Ray Flares. *ApJ*, 886(2):96.
- Hales, C. A., Gaensler, B. M., Chatterjee, S., van der Swaluw, E., and Camilo, F. (2009). A Proper Motion for the Pulsar Wind Nebula G359.23-0.82, the “Mouse,” Associated with the Energetic Radio Pulsar J1747-2958. *ApJ*, 706(2):1316–1322.
- Hartman, R. C., Bertsch, D. L., Bloom, S. D., Chen, A. W., Deines-Jones, P., et al. (1999). The Third EGRET Catalog of High-Energy Gamma-Ray Sources. *The Astrophysical Journal Supplement Series*, 123(1):79–202.
- Hawley, J. F. and Balbus, S. A. (2002). The Dynamical Structure of Nonradiative Black Hole Accretion Flows. *ApJ*, 573:738–748.
- Heckman, T. M. and Best, P. N. (2014). The Coevolution of Galaxies and Supermassive Black Holes: Insights from Surveys of the Contemporary Universe. *ARA&A*, 52:589–660.
- Herold, L. and Malyshev, D. (2019). Hard and bright gamma-ray emission at the base of the Fermi bubbles. *arXiv e-prints*, page arXiv:1904.01454.
- Herrnstein, R. M., Zhao, J.-H., Bower, G. C., and Goss, W. M. (2004). The Variability of Sagittarius A* at Centimeter Wavelengths. *AJ*, 127(6):3399–3410.

- H.E.S.S. Collaboration et al. (2016). Acceleration of petaelectronvolt protons in the Galactic Centre. *Nature*, 531:476–479.
- H.E.S.S. Collaboration et al. (2018). Characterising the vhe diffuse emission in the central 200 parsecs of our galaxy with h.e.s.s. *A&A*, 612:A9.
- Hinton, J. A. and Aharonian, F. A. (2007). Inverse Compton Scenarios for the TeV Gamma-Ray Emission of the Galactic Center. *ApJ*, 657(1):302–307.
- Ho, L. C. (2008). Nuclear Activity in Nearby Galaxies. *ARA&A*, 46:475–539.
- Hogg, D., Bovy, J., and Lang, D. (2010). Data analysis recipes: Fitting a model to data. *ArXiv e-prints*.
- Hooper, D. and Dingus, B. (2005). Improving the angular resolution of EGRET and new limits on supersymmetric dark matter near the galactic center. *Advances in Space Research*, 35(1):130–134.
- Hooper, D. and Goodenough, L. (2011). Dark matter annihilation in the Galactic Center as seen by the Fermi Gamma Ray Space Telescope. *Physics Letters B*, 697:412–428.
- Hooper, D. and Linden, T. (2011). Origin of the gamma rays from the Galactic Center. *Phys. Rev. D*, 84(12):123005.
- Hooper, D. and Linden, T. (2016). The gamma-ray pulsar population of globular clusters: implications for the gev excess. *Journal of Cosmology and Astroparticle Physics*, 2016(08):018.
- Hora, J. L., Witzel, G., Ashby, M. L. N., Becklin, E. E., and Carey S. et al. (2014). Spitzer/IRAC Observations of the Variability of Sgr A* and the Object G2 at 4.5 microns. *The Astrophysical Journal*, 793(2):120.
- Hornstein, S. D., Matthews, K., Ghez, A. M., Lu, J. R., and Morris, M. et al. (2007). A Constant Spectral Index for Sagittarius A* during Infrared/X-Ray Intensity Variations. *The Astrophysical Journal*, 667(2):900–910.
- Igumenshchev, I. V. and Abramowicz, M. A. (1999). Rotating accretion flows around black holes: convection and variability. *MNRAS*, 303:309–320.

-
- Igumenshchev, I. V. and Abramowicz, M. A. (2000). Two-dimensional Models of Hydrodynamical Accretion Flows into Black Holes. *ApJS*, 130:463–484.
- Igumenshchev, I. V., Abramowicz, M. A., and Narayan, R. (2000). Numerical Simulations of Convective Accretion Flows in Three Dimensions. *ApJ*, 537:L27–L30.
- Igumenshchev, I. V., Narayan, R., and Abramowicz, M. A. (2003). Three-dimensional Magnetohydrodynamic Simulations of Radiatively Inefficient Accretion Flows. *ApJ*, 592:1042–1059.
- Jackson, J. M., Geis, N., Genzel, R., Harris, A. I., Madden, S., et al. (1993). Neutral Gas in the Central 2 Parsecs of the Galaxy. *ApJ*, 402:173.
- Kafexhiu, E., Aharonian, F., Taylor, A. M., and Vila, G. S. (2014). Parametrization of gamma-ray production cross sections for p p interactions in a broad proton energy range from the kinematic threshold to PeV energies. *Physical Review D*, 90(12):123014.
- Karssen, G. D., Bursa, M., Eckart, A., Valencia-S, M., Dovčiak, M., et al. (2017). Bright X-ray flares from Sgr A*. *Monthly Notices of the Royal Astronomical Society*, 472(4):4422–4433.
- Kennea, J. A., Burrows, D. N., Kouveliotou, C., Palmer, D. M., Gouguen, E., et al. (2013). Swift Discovery of a new soft gamma repeater, SGR J1745-29, near Sagittarius A*. *The Astrophysical Journal*, 770(2):L24.
- Koratkar, A. and Blaes, O. (1999). The Ultraviolet and Optical Continuum Emission in Active Galactic Nuclei: The Status of Accretion Disks. *PASP*, 111:1–30.
- Kormendy, J. and Richstone, D. (1995). Inward Bound—The Search For Supermassive Black Holes In Galactic Nuclei. *ARA&A*, 33:581.
- Kosack, K., Badran, H. M., Bond, I. H., Boyle, P. J., and Bradbury, S. M. et al. (2004). TeV Gamma-Ray Observations of the Galactic Center. *The Astrophysical Journal*, 608(2):L97–L100.
- Kusunose, M. and Takahara, F. (2012). A Leptonic Model of Steady High-energy Gamma-Ray Emission from Sgr A*. *ApJ*, 748(1):34.

- Lacy, J. H., Townes, C. H., Geballe, T. R., and Hollenbach, D. J. (1980). Observations of the motion and distribution of the ionized gas in the central parsec of the Galaxy. II. *ApJ*, 241:132–146.
- Lacy, J. H., Townes, C. H., and Hollenbach, D. J. (1982). The nature of the central parsec of the Galaxy. *ApJ*, 262:120–134.
- LaRosa, T. N., Kassim, N. E., Lazio, T. J. W., and Hyman, S. D. (2000). A Wide-Field 90 Centimeter VLA Image of the Galactic Center Region. *AJ*, 119(1):207–240.
- Linden, T., Lovegrove, E., and Profumo, S. (2012). The Morphology of Hadronic Emission Models for the Gamma-Ray Source at the Galactic Center. *ApJ*, 753(1):41.
- Lo, K. and Claussen, M. (1983). High-resolution observations of ionized gas in central 3 parsecs of the galaxy: possible evidence for infall. *Nature*, 306(5944):647–651.
- Lynden-Bell, D. (1969). Galactic Nuclei as Collapsed Old Quasars. *Nature*, 223:690–694.
- Macias, O., Gordon, C., Crocker, R. M., Coleman, B., and Paterson, D. et al. (2018). Galactic bulge preferred over dark matter for the Galactic centre gamma-ray excess. *Nature Astronomy*, 2(5):387–392.
- Macquart, J.-P., Bower, G. C., Wright, M. C. H., Backer, D. C., and Falcke, H. (2006). The Rotation Measure and 3.5 Millimeter Polarization of Sagittarius A*. *The Astrophysical Journal*, 646(2):L111–L114.
- MAGIC Collaboration et al. (2020). MAGIC observations of the diffuse γ -ray emission in the vicinity of the Galactic Centre. *arXiv e-prints*, page arXiv:2006.00623.
- Mahadevan, R., Narayan, R., and Krolik, J. (1997). Gamma-Ray Emission from Advection-dominated Accretion Flows around Black Holes: Application to the Galactic Center. *ApJ*, 486:268.
- Malyshev, D., Chernyakova, M., Neronov, A., and Walter, R. (2015). Leptonic origin of the 100 MeV γ -ray emission from the Galactic centre. *A&A*, 582:A11.
- Marrone, D. P., Baganoff, F. K., Morris, M. R., Moran, J. M., and Ghez, A.M. et al. (2008). An X-Ray, Infrared, and Submillimeter Flare of Sagittarius A*. *ApJ*, 682:373–383.

- Marrone, D. P., Moran, J. M., Zhao, J.-H., and Rao, R. (2006). Interferometric Measurements of Variable 340 GHz Linear Polarization in Sagittarius A*. *ApJ*, 640:308–318.
- Mattox, J. R., Bertsch, D., Chiang, J., Dingus, B., Digel, S., Esposito, J., Fierro, J., Hartman, R., Hunter, S., Kanbach, G., et al. (1996). The likelihood analysis of EGRET data. *The Astrophysical Journal*, 461:396.
- Mauerhan, J. C., Morris, M., Walter, F., and Baganoff, F. K. (2005). Intraday Variability of Sagittarius A* at 3 Millimeters. *ApJ*, 623:L25–L28.
- Mayer-Hasselwander, H. A., Bertsch, D. L., Dingus, B. L., Eckart, A., Esposito, J. A., et al. (1998). High-energy gamma-ray emission from the Galactic Center. *A&A*, 335:161–172.
- McEney, J., van der Horst, A., Dominguez, A., Moiseev, A., Marcowith, A., et al. (2019). All-sky Medium Energy Gamma-ray Observatory: Exploring the Extreme Multimessenger Universe. In *Bulletin of the American Astronomical Society*, volume 51, page 245.
- Meyer, L., Do, T., Ghez, A., Morris, M. R., Witzel, G., et al. (2008). A 600 Minute Near-Infrared Light Curve of Sagittarius A*. *The Astrophysical Journal*, 688(1):L17–L20.
- Meyer, L., Eckart, A., Schödel, R., Duschl, W. J., Muzi'c, K., et al. (2006a). Near-infrared polarimetry setting constraints on the orbiting spot model for Sgr A* flares. *A&A*, 460(1):15–21.
- Meyer, L., Schödel, R., Eckart, A., Duschl, W. J., Karas, V., and Dovciak, M. (2007). On the orientation of the Sagittarius A* system. *A&A*, 473(3):707–710.
- Meyer, L., Schödel, R., Eckart, A., Karas, V., Dovciak, M., and Duschl, W. J. (2006b). K-band polarimetry of an Sgr A* flare with a clear sub-flare structure. *A&A*, 458(2):L25–L28.
- Mezger, P. G., Duschl, W. J., and Zylka, R. (1996). The Galactic Center: a laboratory for AGN? *The Astronomy and Astrophysics Review*, 7(4):289–388.
- Mezger, P. G. and Wink, J. E. (1986). Dynamics of the ionized gas within 2 PC of the galactic center. I. First results of a radio recombination line survey. *A&A*, 157:252–266.

- Miyazaki, A., Tsutsumi, T., and Tsuboi, M. (2004). Intraday Variation of Sagittarius A* at Short Millimeter Wavelengths. *The Astrophysical Journal*, 611(2):L97–L100.
- Miyoshi, M., Moran, J., Herrnstein, J., Greenhill, L., Nakai, N., et al. (1995). Evidence for a black hole from high rotation velocities in a sub-parsec region of NGC4258. *Nature*, 373:127–129.
- Mori, K., Gotthelf, E. V., Zhang, S., An, H., et al. (2013). NuStar Discovery of A 3.76s Transient Magnetar Near Sagittarius A*. *The Astrophysical Journal*, 770(2):L23.
- Mori, M. (2003). CANGAROO Project for High-Energy Gamma-Ray Astrophysics. *Progress of Theoretical Physics Supplement*, 151:85–94.
- Morris, M. and Serabyn, E. (1996). The galactic center environment. *Annual Review of Astronomy and Astrophysics*, 34(1):645–701.
- Morris, M. R., Meyer, L., and Ghez, A. M. (2012). Galactic center research: manifestations of the central black hole. *Research in Astronomy and Astrophysics*, 12(8):995–1020.
- Mouawad, N., Eckart, A., Pfalzner, S., Schodel, R., Moultaqa, J., and Spurzem, R. (2005). Weighing the cusp at the Galactic Center. *Astron. Nachr.*, 326:83.
- Muno, M. P., Baganoff, F. K., Bautz, M. W., Feigelson, E. D., Garmire, G. P., et al. (2004). Diffuse X-Ray Emission in a DeepChandraImage of the Galactic Center. *The Astrophysical Journal*, 613(1):326–342.
- Murchikova, E. M., Phinney, E. S., Pancoast, A., and Blandford, R. D. (2019). A cool accretion disk around the galactic centre black hole. *Nature*, 570(7759):83–86.
- Narayan, R. (2002). Why Do AGN Lighthouses Switch Off? In Gilfanov, M., Sunyeav, R., and Churazov, E., editors, *Lighthouses of the Universe: The Most Luminous Celestial Objects and Their Use for Cosmology*, page 405.
- Narayan, R., Mahadevan, R., Grindlay, J. E., Popham, R. G., and Gammie, C. (1998). Advection-dominated accretion model of Sagittarius A*: evidence for a black hole at the Galactic center. *ApJ*, 492:554–568.
- Narayan, R. and McClintock, J. E. (2008). Advection-dominated accretion and the black hole event horizon. *New Astron. Rev.*, 51:733–751.

-
- Narayan, R., Yi, I., and Mahadevan, R. (1995). Explaining the spectrum of Sagittarius A* with a model of an accreting black hole. *Nature*, 374:623–625.
- Navarro, J. F., Frenk, C. S., and White, S. D. M. (1997). A universal density profile from hierarchical clustering. *The Astrophysical Journal*, 490(2):493–508.
- Neilsen, J., Markoff, S., Nowak, M. A., Dexter, J., Witzel, G., et al. (2015). The X-Ray Flux Distribution of Sagittarius A* as Seen by Chandra. *ApJ*, 799:199.
- Neilsen, J., Nowak, M. A., Gammie, C., Dexter, J., Markoff, S., et al. (2013). A Chandra/HETGS Census of X-Ray Variability from Sgr A* during 2012. *ApJ*, 774:42.
- Nolan, P. L., Abdo, A. A., Ackermann, M., Ajello, M., Allafort, A., et al. (2012). Fermi Large Area Telescope Second Source Catalog. *ApJS*, 199:31.
- Nowak, M. A., Neilsen, J., Markoff, S. B., Baganoff, F. K., Porquet, D., et al. (2012). Chandra/HETGS Observations of the Brightest Flare Seen From Sgr A*. *The Astrophysical Journal*, 759(2):95.
- Oka, K. and Manmoto, T. (2003). Gamma-ray emission from an accretion flow around a Kerr black hole. *MNRAS*, 340:543–550.
- O’Leary, R. M., Kistler, M. D., Kerr, M., and Dexter, J. (2015). Young pulsars and the galactic center gev gamma-ray excess. *arXiv preprint arXiv:1504.02477*.
- Paumard, T., Genzel, R., Martins, F., Nayakshin, S., Beloborodov, A. M., et al. (2006). The Two Young Star Disks in the Central Parsec of the Galaxy: Properties, Dynamics, and Formation. *The Astrophysical Journal*, 643(2):1011–1035.
- Paumard, T., Maillard, J.-P., and Stolovy, S. (2003). New results on the galactic center helium stars. *Astronomische Nachrichten*, 324(S1):303–307.
- Peißker, F., Eckart, A., Zajaček, M., Ali, B., and Parsa, M. (2020). S62 and S4711: Indications of a Population of Faint Fast-moving Stars inside the S2 Orbit-S4711 on a 7.6 yr Orbit around Sgr A*. *The Astrophysical Journal*, 899(1):50.
- Petrov, L., Kovalev, Y. Y., Fomalont, E. B., and Gordon, D. (2011). The Very Long Baseline Array Galactic Plane Survey—VGaPS. *AJ*, 142(2):35.

- Petrovic, J., Serpico, P. D., and Zaharijaš, G. (2014). Galactic center gamma-ray “excess” from an active past of the galactic centre? *Journal of Cosmology and Astroparticle Physics*, 2014(10):052.
- Phifer, K., Do, T., Meyer, L., Ghez, A. M., Witzel, G., et al. (2013). Keck Observations of the Galactic Center Source G2: Gas Cloud or Star? *ApJ*, 773:L13.
- Plambeck, R., Dexter, J., Bower, G. C., Kelly, B., Marrone, D. P., and Stone, J. (2014). An 8h characteristic time-scale in submillimetre light curves of Sagittarius A*. *Monthly Notices of the Royal Astronomical Society*, 442(3):2797–2808.
- Plewa, P. M., Gillessen, S., Pfuhl, O., Eisenhauer, F., Genzel, R., et al. (2017). The Post-pericenter Evolution of the Galactic Center Source G2. *The Astrophysical Journal*, 840(1):50.
- Ponti, G., De Marco, B., Morris, M. R., Merloni, A., Muñoz-Darias, T., et al. (2015). Fifteen years of XMM-Newton and Chandra monitoring of Sgr A*: evidence for a recent increase in the bright flaring rate. *MNRAS*, 454:1525–1544.
- Ponti, G., George, E., Scaringi, S., Zhang, S., Jin, C., and et al. (2017). A powerful flare from Sgr A* confirms the synchrotron nature of the X-ray emission. *Monthly Notices of the Royal Astronomical Society*, 468(2):2447–2468.
- Ponti, G., Terrier, R., Goldwurm, A., Belanger, G., and Trap, G. (2010). Discovery of a Superluminal Fe K Echo at the Galactic Center: The Glorious Past of Sgr A* Preserved by Molecular Clouds. *ApJ*, 714:732–747.
- Porquet, D., Grosso, N., Predehl, P., Hasinger, G., Yusef-Zadeh, F., et al. (2008). X-ray hiccups from Sagittarius A* observed by XMM-Newton-The second brightest flare and three moderate flares caught in half a day. *Astronomy & Astrophysics*, 488(2):549–557.
- Porquet, D., Predehl, P., Aschenbach, B., Grosso, N., Goldwurm, A., et al. (2003). XMM-Newton observation of the brightest X-ray flare detected so far from Sgr A*. *Astronomy & Astrophysics*, 407(1):L17–L20.
- Principe, G., Malyshev, D., Ballet, J., and Funk, S. (2018). The first catalog of Fermi-LAT sources below 100 MeV. *A&A*, 618:A22.

-
- Quataert, E. (2003). Radiatively Inefficient Accretion Flow Models of Sgr A*. *Astronomische Nachrichten*, 324(S1):435–443.
- Quataert, E., Dorland, W., and Hammett, G. W. (2002). The Magnetorotational Instability in a Collisionless Plasma. *ApJ*, 577:524–533.
- Quataert, E. and Loeb, A. (2005). Nonthermal THz to TeV emission from stellar wind shocks in the galactic center. *The Astrophysical Journal*, 635(1):L45–L48.
- Reid, M. J. and Brunthaler, A. (2004). The Proper Motion of Sagittarius A*. II. The Mass of Sagittarius A*. *The Astrophysical Journal*, 616(2):872–884.
- Ressler, S. M., Quataert, E., and Stone, J. M. (2018). Hydrodynamic simulations of the inner accretion flow of Sagittarius A* fuelled by stellar winds. *Monthly Notices of the Royal Astronomical Society*, 478(3):3544–3563.
- Rieke, G. H. and Lebofsky, M. J. (1985). The interstellar extinction law from 1 to 13 microns. *ApJ*, 288:618–621.
- Rieke, G. H., Rieke, M. J., and Paul, A. E. (1989). Origin of the Excitation of the Galactic Center. *ApJ*, 336:752.
- Roberts, D. A. and Goss, W. M. (1993). Multiconfiguration VLA H92 alpha Observations of Sagittarius A West at 1 Arcsecond Resolution. *ApJS*, 86:133.
- Rubilar, G. F. and Eckart, A. (2001). Periastron shifts of stellar orbits near the Galactic Center. *A&A*, 374:95–104.
- Saitoh, T. R., Makino, J., Asaki, Y., Baba, J., Komugi, S., et al. (2012). Flaring up of the Compact Cloud G2 during the Close Encounter with Sgr A*. *ArXiv e-prints*.
- Sądowski, A., Narayan, R., Penna, R., and Zhu, Y. (2013). Energy, momentum and mass outflows and feedback from thick accretion discs around rotating black holes. *MNRAS*, 436:3856–3874.
- Schartmann, M., Burkert, A., Alig, C., Gillessen, S., Genzel, R., and et al. (2012). Simulations of the Origin and Fate of the Galactic Center Cloud G2. *ApJ*, 755:155.

- Schödel, R., Eckart, A., Alexander, T., Merritt, D., Genzel, R., et al. (2007). The structure of the nuclear stellar cluster of the Milky Way. *A&A*, 469:125–146.
- Schödel, R., Merritt, D., and Eckart, A. (2009). The nuclear star cluster of the Milky Way: proper motions and mass. *A&A*, 502:91–111.
- Shah, Z., Mankuzhiyil, N., Sinha, A., Misra, R., Sahayanathan, S., and Iqbal, N. (2018). Log-normal flux distribution of bright Fermi blazars. *Research in Astronomy and Astrophysics*, 18(11):141.
- Shapiro, S. S. and Wilk, M. B. (1965). An analysis of variance test for normality (complete samples). *Biometrika*, 52(3-4):591–611.
- Sinha, A., Shukla, A., Saha, L., Acharya, B. S., Anupama, G. C., Bhattacharjee, P., Britto, R. J., Chitnis, V. R., Prabhu, T. P., Singh, B. B., and Vishwanath, P. R. (2016). Long-term study of mkn 421 with the hagar array of telescopes. *A&A*, 591:A83.
- Stecker, F. W. (1971). *Cosmic gamma rays*, volume 249. Scientific and Technical Information Office, National Aeronautics and Space.
- Stephens, M. A. (1974). Edf statistics for goodness of fit and some comparisons. *Journal of the American Statistical Association*, 69(347):730–737.
- Stone, J. M., Marrone, D. P., Dowell, C. D., Schulz, B., Heinke, C. O., and Yusef-Zadeh, F. (2016). Far Infrared Variability of Sagittarius A*: 25.5 hr of Monitoring with Herschel. *The Astrophysical Journal*, 825(1):32.
- Stone, J. M., Pringle, J. E., and Begelman, M. C. (1999). Hydrodynamical non-radiative accretion flows in two dimensions. *MNRAS*, 310:1002–1016.
- Su, M., Slatyer, T. R., and Finkbeiner, D. P. (2010). Giant Gamma-ray Bubbles from Fermi-LAT: Active Galactic Nucleus Activity or Bipolar Galactic Wind? *ApJ*, 724:1044–1082.
- Swanenburg, B. N., Bennett, K., Bignami, G., Buccheri, R., Caraveo, P., et al. (1981). Second COS B catalog of high-energy gamma-ray sources. *The Astrophysical Journal*, 243:L69–L73.

-
- Tanner, A., Figer, D. F., Najarro, F., Kudritzki, R. P., Gilmore, D., et al. (2006). High Spectral Resolution Observations of the Massive Stars in the Galactic Center. *The Astrophysical Journal*, 641(2):891–904.
- The Fermi-LAT Collaboration (2019). Fermi Large Area Telescope Fourth Source Catalog. *arXiv e-prints*, page arXiv:1902.10045.
- The Fermi-LAT Collaboration et al. (2017). Characterizing the population of pulsars in the inner Galaxy with the Fermi Large Area Telescope. *arXiv preprint arXiv:1705.00009*.
- The IceCube Collaboration, Fermi-LAT, MAGIC, AGILE, ASAS-SN, et al. (2018). Multimessenger observations of a flaring blazar coincident with high-energy neutrino IceCube-170922A. *Science*.
- Thompson, C. and Beloborodov, A. M. (2005). High-Energy Emission from Magnetars. *ApJ*, 634:565–569.
- Trap, G., Goldwurm, A., Dodds-Eden, K., Weiss, A., Terrier, R., et al. (2011). Concurrent X-ray, near-infrared, sub-millimeter, and GeV gamma-ray observations of Sagittarius A*. *A&A*, 528:A140.
- Trippe, S., Paumard, T., Ott, T., Gillessen, S., Eisenhauer, F., et al. (2007). A polarized infrared flare from Sagittarius A* and the signatures of orbiting plasma hotspots*. *Monthly Notices of the Royal Astronomical Society*, 375(3):764–772.
- Tsuchiya, K., Enomoto, R., Ksenofontov, L. T., Mori, M., Naito, T., et al. (2004). Detection of Sub-TeV Gamma Rays from the Galactic Center Direction by CANGAROO-II. *ApJ*, 606(2):L115–L118.
- Uttley, P. and McHardy, I. M. (2001). The flux-dependent amplitude of broadband noise variability in X-ray binaries and active galaxies. *MNRAS*, 323:L26–L30.
- Vasiliev, E. and Zelnikov, M. (2008). Dark matter dynamics in the galactic center. *Phys. Rev. D*, 78:083506.
- Virtanen, P., Gommers, R., Oliphant, T. E., Haberland, M., SciPy 1.0 Contributors, et al. (2020). SciPy 1.0: Fundamental Algorithms for Scientific Computing in Python. *Nature Methods*, 17:261–272.

- von Fellenberg, S. D., Gillessen, S., Graciá-Carpio, J., Fritz, T. K., Dexter, J., et al. (2018). A Detection of Sgr A* in the Far Infrared. *The Astrophysical Journal*, 862(2):129.
- Wang, Q. D., Lu, F. J., and Gotthelf, E. V. (2006). G359.95-0.04: an energetic pulsar candidate near Sgr A*. *MNRAS*, 367(3):937–944.
- Wardle, M. (2011). X-ray Echoes of Infrared Flaring in Sgr A*. In Morris, M., Wang, Q., and Yuan, F., editors, *Galactic Center*, Astronomical Society of the Pacific Conference Series, pages 450–455. Astronomical Society of the Pacific.
- Witzel, G., Eckart, A., Bremer, M., Zamaninasab, M., Shahzamanian, B., et al. (2012). Source-intrinsic Near-Infrared Properties of Sgr A*: Total Intensity Measurements. *The Astrophysical Journal Supplement Series*, 203(2):18.
- Witzel, G., Martinez, G., Hora, J., Willner, S. P., Morris, M. R., et al. (2018). Variability Timescale and Spectral Index of Sgr A* in the Near Infrared: Approximate Bayesian Computation Analysis of the Variability of the Closest Supermassive Black Hole. *The Astrophysical Journal*, 863(1):15.
- Wollman, E. R., Geballe, T. R., Lacy, J. H., Townes, C. H., and Rank, D. M. (1977). Ne II 12.8 micron emission from the galactic center. II. *ApJ*, 218:L103–L107.
- Wood, M., Caputo, R., Charles, E., Di Mauro, M., Magill, J., et al. (2017). Fermipy: An open-source Python package for analysis of Fermi-LAT Data. *arXiv preprint arXiv:1707.09551*.
- Xu, Y.-D., Narayan, R., Quataert, E., Yuan, F., and Baganoff, F. K. (2006). Thermal X-Ray Iron Line Emission from the Galactic Center Black Hole Sagittarius A*. *The Astrophysical Journal*, 640(1):319–326.
- Yang, H. Y., Ruszkowski, M., and Zweibel, E. (2018). Unveiling the Origin of the Fermi Bubbles. *Galaxies*, 6(1):29.
- Yuan, F. and Narayan, R. (2014). Hot Accretion Flows Around Black Holes. *ARA&A*, 52:529–588.
- Yuan, F., Quataert, E., and Narayan, R. (2003). Nonthermal Electrons in Radiatively Inefficient Accretion Flow Models of Sagittarius A*. *ApJ*, 598:301–312.

-
- Yuan, F., Quataert, E., and Narayan, R. (2004). On the Nature of the Variable Infrared Emission from Sagittarius A*. *ApJ*, 606:894–899.
- Yusef-Zadeh, F., Bushouse, H., Dowell, C. D., Wardle, M., Roberts, D., et al. (2006). A Multiwavelength Study of Sgr A*: The Role of Near-IR Flares in Production of X-Ray, Soft γ -Ray, and Submillimeter Emission. *The Astrophysical Journal*, 644(1):198–213.
- Yusef-Zadeh, F., Bushouse, H., Wardle, M., Heinke, C., Roberts, D. A., et al. (2009). Simultaneous Multi-Wavelength Observations of Sgr A* During 2007 April 1-11. *ApJ*, 706:348–375.
- Yusef-Zadeh, F., Morris, M., Slee, O. B., and Nelson, G. J. (1986). Nonthermal Radio Emission from the Galactic Center Arc. *ApJ*, 310:689.
- Yusef-Zadeh, F., Roberts, D., Wardle, M., Heinke, C. O., and Bower, G. C. (2006). Flaring Activity of Sagittarius A* at 43 and 22 GHz: Evidence for Expanding Hot Plasma. *ApJ*, 650:189–194.
- Yusef-Zadeh, F., Wardle, M., Dodds-Eden, K., Heinke, C. O., Gillessen, S., et al. (2012). An Inverse Compton Scattering Origin of X-Ray Flares from Sgr A*. *The Astronomical Journal*, 144(1):1.
- Yusef-Zadeh, F., Wardle, M., Heinke, C., Dowell, C. D., Roberts, D., et al. (2008). Simultaneous Chandra, CSO, and VLA Observations of Sgr A*: The Nature of Flaring Activity. *The Astrophysical Journal*, 682(1):361–372.
- Zamaninasab, M., Eckart, A., Witzel, G., Dovciak, M., Karas, V., et al. (2010). Near infrared flares of Sagittarius A* - Importance of near infrared polarimetry. *A&A*, 510:A3.
- Zhang, S., Baganoff, F. K., Ponti, G., Neilsen, J., Tomsick, J. A., et al. (2017). Sagittarius High-energy X-Ray Flare Properties during NuStar Monitoring of the Galactic Center from 2012 to 2015. *The Astrophysical Journal*, 843(2):96.
- Zhao, J.-H. and Goss, W. M. (1998). Radio Continuum Structure of IRS 13 and Proper Motions of Compact H [CSC]ii/[CSC] Components at the Galactic Center. *The Astrophysical Journal*, 499(2):L163–L167.

Zhao, J.-H., Young, K. H., Herrnstein, R. M., Ho, P. T. P., Tsutsumi, T., et al. (2003). Variability of Sagittarius A*: Flares at 1 Millimeter. *ApJ*, 586:L29–L32.

Zucker, S., Alexander, T., Gillessen, S., Eisenhauer, F., and Genzel, R. (2006). Probing Post-Newtonian Physics near the Galactic Black Hole with Stellar Redshift Measurements. *The Astrophysical Journal*, 639(1):L21–L24.

Appendix

Appendix A

Article: Fermi LAT observations of Sagittarius A*: I - Imaging Analysis

Here we reproduce the draft version of an Article as submitted in August 19th 2020 to *The Astrophysical Journal* which describe a significant part of the work presented in this Thesis. The PhD candidate is the first author and leader of the research presented in the document.

2 *Fermi* LAT observations of Sagittarius A*: I - Imaging Analysis3 FABIO CAFARDO ¹ AND RODRIGO NEMMEN ¹
4 (FERMI LAT COLLABORATION)5 ¹*Universidade de São Paulo, Instituto de Astronomia, Geofísica e Ciências Atmosféricas, Departamento de Astronomia, São Paulo, SP*
6 *05508-090, Brazil*

7 (Received XXXX; Revised XXXX; Accepted XXXX)

8 Submitted to ApJ

9 ABSTRACT

10 Sagittarius A* (Sgr A*)—the supermassive black hole (SMBH) in the center of our galaxy—has been
11 observed in most of the electromagnetic spectrum, from radio to X-rays. Diffuse γ -ray emission has
12 been observed around Sgr A* and a γ -ray point source has been detected coinciding with the SMBH’s
13 position, although there is no definitive association between the two. In this work, we have used ~ 11
14 years of *Fermi* Large Area Telescope (LAT) observations of the point source 4FGL J1745.6–2859 and
15 performed a detailed imaging analysis across four energy bands. Our goal is to elucidate the nature of
16 the γ -ray emission at the Galactic Center (GC) and whether it is associated with the SMBH. We find
17 that the centroid of the emission approaches Sgr A*’s location as the energy increases. Assuming that
18 the γ -ray point source is located at the GC, we estimate a luminosity of 2.61×10^{36} erg s^{−1} in the 100
19 MeV to 500 GeV energy range. This is consistent with Sgr A*’s bolometric luminosity. Based on the
20 point source properties, we ruled out several potential candidates for its nature and favor a cosmic ray
21 origin either from protons, electrons or both, accelerated by—or in the vicinity of—the SMBH. Our
22 results indicate that the point source at the GC is indeed the γ -ray counterpart of Sgr A* in the GeV
23 range.24 *Keywords:* Galaxy: center - Sagittarius A* - γ -rays

25 1. INTRODUCTION

26 The center of our galaxy hosts a SMBH with a mass of
27 $\sim 10^6 M_{\odot}$ (Ghez et al. 2008; Genzel et al. 2010; Boehle
28 et al. 2016) located at a distance of 8.2 kpc (Abuter
29 et al. 2019). Like the Milky Way, it is believed that ev-
30 ery sufficiently massive galaxy harbors a SMBH in its
31 center (Lynden-Bell 1969; Kormendy & Richstone 1995;
32 Miyoshi et al. 1995; Heckman & Best 2014). The first
33 observations of a source that would later be associated
34 with Sgr A*—the SMBH in our GC—were made by Bal-
35 ick & Brown (1974) in radio wavelengths. Almost fifty
36 years later, there are several observations that confirm
37 the presence of the SMBH. The most convincing are
38 those obtained by Eisenhauer et al. (2005) and Gillessen
39 et al. (2009) monitoring stellar orbits and the detection40 of orbital motions of a “hot spot” in the accretion flow
41 near the last stable circular orbit of Sgr A* (Gravity
42 Collaboration et al. 2018). Results of the Event Hori-
43 zon Telescope observational campaign to reveal the im-
44 age of the shadow of Sgr A* on the accretion flow are
45 still anxiously anticipated (e.g. Event Horizon Telescope
46 Collaboration et al. 2019).47 The electromagnetic radiation from Sgr A* has been
48 seen in several wavelengths (e.g. Genzel et al. 2010; Mor-
49 ris et al. 2012; Eckart et al. 2018). It is highly variable
50 in the infrared (Genzel et al. 2003; Ghez et al. 2004;
51 Hornstein et al. 2007; Dodds-Eden et al. 2009; Witzel
52 et al. 2012; Hora et al. 2014; Witzel et al. 2018; von Fel-
53 lenberg et al. 2018; Fazio et al. 2018; Boyce et al. 2018)
54 and X-rays (Baganoff et al. 2001; Nowak et al. 2012;
55 Neilsen et al. 2013; Barrière et al. 2014; Neilsen et al.
56 2015; Ponti et al. 2015; Fazio et al. 2018; Boyce et al.
57 2018), which suggests a compact source. Variability has
58 also been reported in longer wavelengths (Zhao et al.

2003; Miyazaki et al. 2004; Mauerhan et al. 2005; Macquart et al. 2006; Yusef-Zadeh et al. 2006; Marrone et al. 2008; Yusef-Zadeh et al. 2009; Plambeck et al. 2014; Brinkerink et al. 2015; Stone et al. 2016). The γ -ray flux, though, does not seem to be variable (Chernyakova et al. 2011; Malyshev et al. 2015; Ahnen et al. 2017) and there is still no definitive association between this emission and Sgr A*.

Following the H.E.S.S. TeV detections of the GC, several candidates have been proposed for this γ -ray flux: Sgr A* itself—either from its immediate vicinity (Aharonian & Neronov 2005a) or from a “plerion” produced by the SMBH winds (Atoyan & Dermer 2004; Kusunose & Takahara 2012)—; the interaction between the dense molecular clouds in the GC with cosmic rays accelerated by Sgr A* and/or by some other nearby source (Aharonian & Neronov 2005b; Ballantyne et al. 2011; Chernyakova et al. 2011; Linden et al. 2012; Fatuzzo & Melia 2012; Guo et al. 2013); the pulsar wind nebula (PWN) G359.95-0.04 (Wang et al. 2006; Hinton & Aharonian 2007); the supernova remnant Sagittarius A East (Crocker et al. 2005) (but see Aharonian et al. 2009; Acero et al. 2010); the magnetar SGR J1745–2900 (Kennea et al. 2013; Mori et al. 2013) orbiting Sgr A*; self-annihilating dark matter particles accumulating at the GC (Hooper & Goodenough 2011; Hooper & Linden 2011) and an as-yet undetected pulsar (or population of pulsars) (Hooper & Linden 2011).

It is believed that the quiescent state of Sgr A*, observed from radio to X-rays, is due to a radiatively inefficient accretion flow (RIAF) (e.g. Narayan et al. 1995; Yuan & Narayan 2014). The broadband spectrum is dominated by the radio-to-submm emission which is understood as synchrotron radiation from a thermal population of electrons, with temperatures between ~ 5 –20 MeV, as well as a small fraction (a few percent) of non-thermal electrons (Yuan et al. 2003). In its steady state, Sgr A* emits $\sim 10^{36}$ erg s $^{-1}$ (e.g. Genzel et al. 2010). The X-ray flare emission has been interpreted as Inverse Compton (IC) upscattered photons by the mildly relativistic, nonthermal electrons (Yusef-Zadeh et al. 2009; Ball et al. 2016). Alternatively, X-ray flare emission has been argued to be due to synchrotron emission (Dodds-Eden et al. 2009).

Prominent gamma-ray emission from MeV to TeV energies coincident with Sgr A*’s position is observed by *Fermi* LAT. Since the beginning of *Fermi*’s operations, a point source has been observed coinciding with the position of Sgr A*. This source was studied by Chernyakova et al. (2011) with 25 months of *Fermi* observations. They found no temporal variability at GeV energies and proposed a model in which the γ -ray emission in the in-

ner 10 pc of the Galaxy arises from relativistic proton interactions. Later, Malyshev et al. (2015) analyzed the same source using 74 months of data and the Second Catalogue of *Fermi* LAT Sources (Nolan et al. 2012). They also found no variability in the flux, and considered the observed spectrum as consistent with IC scattering of high-energy electrons.

Ahnen et al. (2017) collected several models for the MeV to TeV emission from Sgr A*. The list includes leptonic (Kusunose & Takahara 2012), hadronic (Fatuzzo & Melia 2012; Linden et al. 2012; Ballantyne et al. 2011; Chernyakova et al. 2011) and hybrid (Guo et al. 2013) models. We call the models in this list “Fermi-era”, since they were all constructed taking in consideration *Fermi*-LAT’s data.

The TeV emission observed by H.E.S.S. indicates the presence of PeV protons within the central 10 pc of the Galaxy (HESS Collaboration et al. 2016). They propose that a more active phase of Sgr A* in the past could have accelerated this population of high-energy protons. There is also tantalizing evidence for an enhanced level of activity in the recent past of Sgr A* through the *Fermi* Bubbles (Su et al. 2010) which should have formed 1–3 Myr ago and endured for 0.1–0.5 Myr (Guo & Mathews 2012; Yang et al. 2018). The origin of the bubbles is still debated and could be also due to a previous starburst in addition to the activity of the SMBH. Further evidence for higher levels of activity in Sgr A* comes from X-ray observations of circumnuclear clouds (Ponti et al. 2010). Concretely, X-ray observations since the 1990s show rapid variations in the 6.4 keV of Fe K α line propagating through molecular clouds in the inner Galactic regions. These variations are likely the result of a highly variable active phase of Sgr A* within the past few hundred years, which is echoing through the clouds. Models indicate at least two luminous outbursts (~ 100 and 400 years ago) on few-year timescales during which the luminosity of Sgr A* went up to at least 10^{39} erg s $^{-1}$ (Ponti et al. 2010; Clavel et al. 2013). In summary, it seems that Sgr A* was 10^3 times more active within the past few centuries compared to current levels.

The GC is the closest example of a galactic nucleus and a compelling laboratory to investigate the physical processes responsible for accelerating particles to TeV and PeV energies. Of the several sources near the GC in the Fourth catalog of *Fermi* LAT sources (4FGL, Abdollahi et al. 2020), 4FGL J1745.6–2859 is the brightest and the closest to Sgr A* at a distance of $\sim 0.01^\circ$. Here, we report an imaging analysis for this point source. In section 2, we describe the observations and data analysis procedure. In section 3 we describe the results from the imaging analysis for the point source in four different

163 energy ranges between 60 MeV–500 GeV. In section 4
 164 we discuss the possible candidates that can explain the
 165 observed γ -ray emission. Finally, in section 5 we sum-
 166 marize our main findings. In a forthcoming paper, we
 167 will describe a light curve and spectral analysis for this
 168 point source, with the overall goal of understanding the
 169 nature of the processes responsible for the high-energy
 170 emission of this source.

171 2. OBSERVATIONS AND DATA ANALYSIS

172 In this work, we divided the analysis into four en-
 173 ergy bands: 60–300 MeV, 300 MeV–3 GeV, 3–10 GeV
 174 and 10–500 GeV. The goals were to study the impact of
 175 photon energy on the location of the source, to measure
 176 4FGL J1745.6–2859’s γ -ray emission in different parts
 177 of the electromagnetic spectrum to allow comparisons
 178 with predictions of several models that try to explain
 179 the GC’s γ -ray flux (Section 4) and also to take ad-
 180 vantage of the better *Fermi*-LAT point-spread function
 181 (PSF) at higher energies.

182 The investigations of the three highest-energy bands
 183 are based on an analysis (which we call “universal
 184 model”) performed with energies between 100 MeV and
 185 500 GeV. The lowest-energy band used a custom model.
 186 Figure 1 shows how we split the analysis into different
 187 energy bands and models.

188 In this Section we show how the universal model
 189 (and its descendants) and the low-energy custom model
 190 were created and how they were used to assess 4FGL
 191 J1745.6–2859’s γ -ray flux and position in different en-
 192 ergies.

193 2.1. The universal model and its descendants

194 Here we describe the process for the creation of a spa-
 195 tial/spectral model with photons between 100 MeV and
 196 500 GeV. This model was used to evaluate the γ -ray
 197 photon and energy fluxes of the source. Also, it was
 198 used as the basis for three different analyses considering
 199 only photons with energies between 300 MeV–3 GeV,
 200 3–10 GeV and 10–500 GeV.

201 In this part of the work, we used ~ 11.3 years (from
 202 2008 August to 2019 December) of *Fermi*-LAT (Atwood
 203 et al. 2009) data. We considered a region of $20^\circ \times 20^\circ$
 204 square centered on the point source 4FGL J1745.6–2859
 205 coincident with Sgr A* and rotated $\sim 58^\circ.6$ to the East
 206 in Galactic coordinates.

207 Data were binned to a pixel size of $0^\circ.08$. We chose
 208 the recommended¹ value of $\geq 90^\circ$ for the zenith angle
 209 cut.

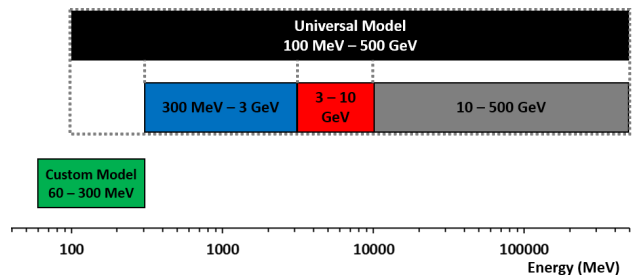


Figure 1. We divided our analyses into four energy bands (60–300 MeV, 300 MeV–3 GeV, 3–10 GeV and 10–500 GeV). The models for the three highest-energy bands were created based on an analysis that considered energies in the range 100 MeV–500 GeV. The lowest-energy band was studied with a custom model.

210 The region was modeled based on the sources’ posi-
 211 tions and spectral models in the preliminary re-
 212 lease of 4FGL (`gll_psc_v20.fit`, Abdollahi et al.
 213 2020), the updated model of interstellar γ -ray emission,
 214 `gll_iem_v07.fits`, and standard isotropic spectral tem-
 215 plates selected according to the *event types* and *event*
 216 *class* used in this work. We performed a binned like-
 217 lihood analysis using `Fermitools` conda package version
 218 1.2.1, `Fermipy` python package version 0.17.4 (Wood
 219 et al. 2017) and Pass 8 release 3 Version 2 response
 220 functions (Atwood et al. 2013). Energy dispersion was
 221 disabled for the isotropic diffuse component only.

222 The *Fermi*-LAT PSF varies considerably with photon
 223 energy. It ranges from $\gtrsim 10^\circ$ (68% containment for pho-
 224 tons with *event class* SOURCE) for photons with energies
 225 $\gtrsim 100$ MeV to $\lesssim 1^\circ$ for $\gtrsim 10$ GeV photons. In this work,
 226 we use photons classified as SOURCE.

227 *Fermi*-LAT photons are classified in different *event*
 228 *types*. They can be categorized according to the location
 229 where they converted in the detector (photons converted
 230 in the front of the equipment have better-measured direc-
 231 tions than those converted in the back) or according
 232 to the quality of the reconstructed direction (the pho-
 233 tons are divided in quartiles depending on the quality of
 234 this reconstruction). In this work we chose to consider
 235 only the 75% photons with the best-reconstructed direc-
 236 tions (*event types* PSF1, PSF2 and PSF3). We performed
 237 a joint likelihood analysis with three components ac-
 238 counting for the isotropic emission because *event types*
 239 PSF1, PSF2 and PSF3 have different isotropic spectral
 240 templates.

241 To perform a likelihood analysis with *Fermi*-LAT
 242 data, it is necessary to create a model of the γ -ray emit-
 243 ting sources in the region of interest (RoI). To generate
 244 the model, we included the 4FGL sources inside a square
 245 larger than the size of the RoI (with 25° side) to account
 246 for *Fermi*-LAT’s PSF. We started by creating the uni-

¹ https://fermi.gsfc.nasa.gov/ssc/data/analysis/documentation/Cicerone/Cicerone_Data_Exploration/Data_preparation.html

versal model with energies between 100 MeV and 500 GeV.

We began the analysis using `Fermipy`'s `optimize` method. This tool fits the spectral models of all sources within the RoI through an iterative strategy: it starts by simultaneously fitting the normalization parameters of the brightest sources, then individually fits the normalization of every source not included in the first step, and finishes by individually fitting the normalizations and indexes of sources with the largest TS. After that we started fitting the sources in the RoI. Since the GC region is very rich in sources—there are 196 4FGL sources in the central 10° of the Galaxy—we used an iterative approach for fitting of the RoI, always taking care to limit the number of free parameters to $\lesssim 15$ as recommended by the optimizer's (MINUIT) manual. Several iterations were performed in order to fit the brightest sources closest to 4FGL J1745.6–2859. In all iterations, the normalization of our source of interest was allowed to vary as well as the normalizations of the Galactic diffuse emission model (`galdiff`) and of the isotropic spectral template (`isodiff`). The normalizations of selected sources were also iteratively freed based on their proximity to the center of the RoI and their brightness in γ -rays, measured by the number of predicted photons in each energy interval. We performed several iterations to fit the desired sources. Only the best-quality fits (Quality: 3, Status: 0) were considered. Fits that did not converge or with lower quality were disregarded. In this case we would go back to the previous step of the fitting procedure and continue from there with fewer free sources.

The next step was to use the `Fermipy` function `find_sources`. Twenty-nine new sources were found with this tool in the energy range between 100 MeV and 500 GeV. We used power-law spectral models for each of the new sources. This spectral model was selected because it is typically adequate for relatively faint sources, and in fact the majority of sources in 4FGL are modeled with a power-law spectrum. Finding and characterizing new sources is not a goal of this work. The aim of this source-finding step was to improve the quality of the model. Some of the newly found sources are likely spurious detection due to unmodeled background emission. The new sources are listed in Appendix A.

In between these steps we evaluated the quality of our fitting procedures by two approaches:

- Residual maps: built by subtracting the modeled counts from the data and searching for regions with significant residuals.

- Test Statistics (TS, [Mattox et al. 1996](#)) maps: searching for the presence of an additional source component in each spatial bin of the RoI.

Maps that show no regions with $TS \gtrsim 25$ and Residuals $\gtrsim |4\sigma|$ were considered well modeled. Regions with excesses above these levels were fitted again. In these cases, the normalizations of sources close to excesses in those maps were allowed to vary, together with the normalizations of 4FGL J1745.6–2859 and of the diffuse components. Usually, mainly in the case of negative residuals, this additional round of fitting was enough to lessen the excesses in the maps while also increasing the likelihood of the model. In the case of regions with positive TS, some of the excesses were reduced only after using the `find_sources` tool.

The last step was fitting the spectral indexes of the central source. The approach was the same as described above. We performed different iterations of fitting, always with the normalization and the indexes of 4FGL J1745.6–2859 as free parameters together with other free parameters that usually included the normalization and the spectral indexes of nearby bright sources and the Galactic and isotropic diffuse models. Only iterations with the best fit quality were considered.

These steps led to the creation of the universal model with photons between 100 MeV and 500 GeV. Then, it was used as an initial model for the analysis in three energy bands (300 MeV–3 GeV, 3–10 GeV and 10–500 GeV). In each energy band, the only sources that were allowed to vary in a new round of fitting were 4FGL J1745.6–2859 (normalization and index) and the Galactic and isotropic diffuse models (normalization only). This “minimal fitting” was used with the objective of keeping a similar model in the three energy bands.

To determine the centroid of the γ -ray emission of the central point source for each energy range and calculate the likelihood of it being spatially extended, we used `Fermipy`'s `extension` method. In addition to finding the location of the point source, it computes the likelihood of the source being extended with respect to it being pointlike. Also, it gives the best-fit model for extension. We chose to use a 2D Gaussian as the putative extended spatial model for the central source.

2.2. The low-energy model

Using the universal model as a starting point for a new model at lower energies proved to be challenging. We could not obtain a good-quality model with the same minimal fitting used to “split” the universal model in 3 energy bands (described at the end of Section 2.1) nor with several additional rounds of fitting: in both cases we ended up with models whose Residuals and TS maps

348 showed many regions with excesses above the acceptable
 349 levels. So we decided to use a model created specifically
 350 for the 60–300 MeV energy band. We already had this
 351 model prepared from previous studies. As will be de-
 352 scribed below, some features of this model’s data are
 353 different from the universal model’s. This is not a seri-
 354 ous issue because, in this work, we treat the results for
 355 each energy band independently, avoiding comparisons
 356 between each other.

357 We considered data inside a $30^\circ \times 30^\circ$ square also cen-
 358 tered on the point source 4FGL J1745.6–2859 and with
 359 the same orientation as the one used to the universal
 360 model. This choice of size for the RoI is appropriate for
 361 modeling the distribution of lower-energy photons given
 362 the broad PSF. We used $0^\circ.1$ pixel size and the recom-
 363 mended value of $\geq 90^\circ$ for the zenith angle cut. About
 364 10.5 years of *Fermi* LAT data was considered (from 2008
 365 August to 2019 February).

366 We modeled the region using the preliminary re-
 367 lease of 4FGL (`gll_psc_v17.fit`, Abdollahi et al.
 368 2020), the updated model of interstellar γ -ray emission,
 369 `gll_iem_v07.fits`, and standard isotropic spectral tem-
 370 plates. We included in the model all 4FGL sources in a
 371 region with 35° side to account for *Fermi*-LAT’s PSF.
 372 Energy dispersion was disabled for the isotropic and
 373 Galactic diffuse components.

374 As for the analysis described in Section 2.1 we used
 375 *event class* SOURCE, *event types* PSF1, PSF2 and PSF3 and
 376 performed a joint likelihood analysis with three compo-
 377 nents accounting for the isotropic emission.

378 Before starting the analysis we changed the Spectrum
 379 Type of 4FGL J1745.6–2859. It is catalogued as log-
 380 parabola but we adopted a power-law in this low-energy
 381 model. We used results obtained in previous analy-
 382 sis using the Third Fermi LAT catalog (3FGL, Acero
 383 et al. 2015) as the starting values for the parameters
 384 that were later refitted with the new data. The main
 385 reason for the change was the ease of fitting power-law
 386 spectra, which have one less parameter compared to log-
 387 parabolas. This change is appropriate since in narrow
 388 energy bands (like the ones we are using here) a log-
 389 parabola can be approximated by a power law.

390 After this, we followed the same process described
 391 in Section 2.1 to fit the model. During this pro-
 392 cess, we found 14 new sources with *Fermipy*’s func-
 393 tion `find_sources` in regions associated with $TS > 25$.
 394 But in new rounds of fitting, several of them showed a
 395 reduction of their TS to values below 25. Since *Fermi*-
 396 LAT’s PSF is broader at lower energies, we decided
 397 to exclude—one at a time—the new sources in this
 398 condition from the model to avoid them interfering
 399 in the results of our source of interest. We started

400 by excluding the farthest from the center of the RoI
 401 and refitted the model. The normalizations of the
 402 sources closest to the excluded one were left free, to-
 403 gether with the normalizations of the Galactic diffuse
 404 emission model, of the isotropic spectral template and
 405 of 4FGL J1745.6–2859. We repeated this process until
 406 there were no new sources with $TS < 25$ in the model.
 407 After excluding these sources, we ended up with 5 new
 408 sources. They are listed in Appendix B. As we men-
 409 tioned in Section 2.1, these new sources may be spurious
 410 detections due to inaccuracies in the models. Finally,
 411 we used *Fermipy*’s `extension` method to assess the lo-
 412 cation of 4FGL J1745.6-2859 in this energy range.

413
 414 This study has some similarities to the work of Maly-
 415 shev et al. (2015), with several improvements. The most
 416 obvious is the longer time baseline of the photon data—
 417 more than 10.5 years of observations versus 6 years—
 418 which provides better statistics. This allows for sharper
 419 images and better modelling with reduced source con-
 420 fusion. Also, we are using more-recent versions of *Fer-*
 421 *mitools*, Pass 8 response functions and the preliminary
 422 version of 4FGL catalog (accompanied with improved
 423 versions of the diffuse models), all of which were released
 424 after their work. Finally, we chose to use a stricter *event*
 425 *type* selection than Malyshhev et al. (2015).

426 3. RESULTS

427 In our work, we subdivided the analysis into four
 428 energy ranges. In Figure 2 we compare the results
 429 of these four models with the log-parabola spectral
 430 model adopted in the 4FGL Catalogue for 4FGL
 431 J1745.6–2859. We can see there is a considerable dis-
 432 crepancy between the low (60–300 MeV) and higher
 433 energy (>300 MeV) spectral models. This is the result
 434 of the different modelling for the 60–300 MeV band,
 435 as discussed in Section 2. Only part of this difference
 436 can be explained by the addition in our 60–300 MeV
 437 model of a new source (not included in 4FGL but listed
 438 as PS J1750.6-2723 in Appendix B) at a distance $<2^\circ$
 439 from 4FGL J1745.6–2859. This difference means that
 440 the γ -ray flux for this energy band might be underesti-
 441 mated. It is important to notice that the GC is among
 442 the most complicated regions in the sky to study with
 443 *Fermi* data: in addition to the high density of sources,
 444 the region is also engulfed by the Galactic diffuse emis-
 445 sion. These factors are enhanced in lower energies due
 446 to the large PSF.

447 The results of our fitting steps discussed in Section
 448 2 can be seen in Figure 3. These residual maps are
 449 useful to assess goodness-of-fit. The colors indicate the

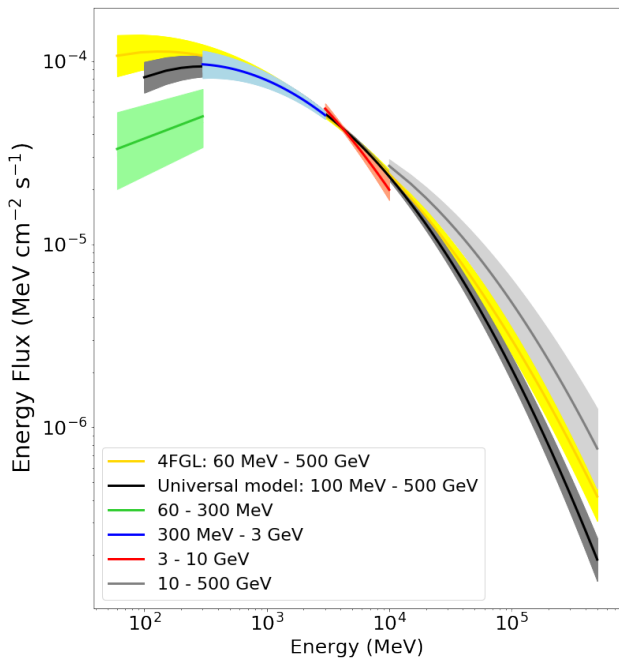


Figure 2. Comparison of spectral models for 4FGL J1745.6–2859. The black line shows the universal model created in the 100 MeV–500 GeV energy range. It was later used as basis to create models in three different energy bands: 300 MeV–3 GeV (blue), 3–10 GeV (red) and 10–500 GeV (gray). They were created with log-parabolas templates. A power-law model was used in the 60–300 MeV energy range (green). The log-parabola spectral model used by the 4FGL Catalogue for this source is also shown (yellow).

significance² (σ) of the residual (calculated as the difference between the data and the model) in each energy band used in this work. Positive residuals indicate regions that are underpredicted whereas negative ones indicate overpredicted regions. There are some regions with $|\sigma| > 5$ in the models with energies > 300 MeV, especially in the 300 MeV–3 GeV energy band. They are the result of the minimal fitting we did when splitting the analysis in the different energy bands. This prevented us from getting better models but provided models that are comparable between the 3 highest-energy bands. To assess the impact of this modelling on the results, we created unique models from scratch for each energy band and performed the same analysis. The results we got were compatible in 1σ with the ones presented within this work both in terms of the γ -ray fluxes and the position of the source.

² For a description on how σ is calculated:
<https://fermipy.readthedocs.io/en/latest/advanced/residmap.html>

The four panels in Figure 4 show the TS map for each energy range. They were constructed using the `tmap` tool. This tool moves a putative point source through the RoI and performs a maximum likelihood fit at each point. We used a power-law spectral model with a spectral index of -2 (with $dN/dE \propto E^\alpha$ where dN/dE is the differential photon flux and α is the spectral index). In the maps, the source position in each energy range is marked by a colored circle in the center of the images. The central point source itself is not visible in the maps since it is part of the model. For the 60–300 MeV range there is no region with $TS \geq 25$ (i.e. no emission consistent with a point source with a power-law spectrum with index -2 has significance $\gtrsim 5\sigma$). This shows that the models include all significant sources in this field. But in the maps of the high-energy (> 300 MeV) models this is not true. These models were created with minimal fitting based on the universal model (Section 2.1) which led to regions that could be better modeled if its sources were refitted. Nevertheless, the results we got for these energy models are compatible within 1σ with the ones obtained through models created specifically for each energy band (and that had no residual $TS > 25$).

The central source was detected in the four energy ranges used in the analysis with TS varying from ≈ 300 to ≈ 10000 , corresponding to detections with significance above background ranging from $\approx 17\sigma$ to $\approx 100\sigma$. Its photon and energy flux were also measured and the results are shown in Table 1.

Assuming a distance to 4FGL J1745.6–2859 of 8.2 kpc (Abuter et al. 2019) and isotropic emission, the energy flux of $(3.26 \pm 0.05) \times 10^{-10}$ erg cm⁻² s⁻¹ measured in the 100 MeV to 500 GeV energy range corresponds to a γ -ray luminosity of $(2.61 \pm 0.05) \times 10^{36}$ erg s⁻¹. This luminosity is comparable to the observed radio-to-X-ray luminosity of Sgr A* $\sim 10^{36}$ erg s⁻¹ (Genzel et al. 2010).

The four panels of Figure 5 show the TS maps of the inner $8^\circ \times 8^\circ$ of the RoI, showing the presence of the central point source. They were constructed using the `tmap` tool (again considering a putative point with a spectral index of -2) and excluding the source 4FGL J1745.6–2859 from the models. TS excesses are observed in every panel and are always coincident with 4FGL J1745.6–2859’s position. The apparent size of the excess in the TS maps seems to decrease with energy, but this does not correspond to any variation of the physical extension of the source. It is, instead, an outcome of the improvement of *Fermi* LAT’s PSF with energy, as mentioned in Section 2.

The same diagnostic plots shown in Figures 3, 4 and 5 for the different energy bands were used to evaluate

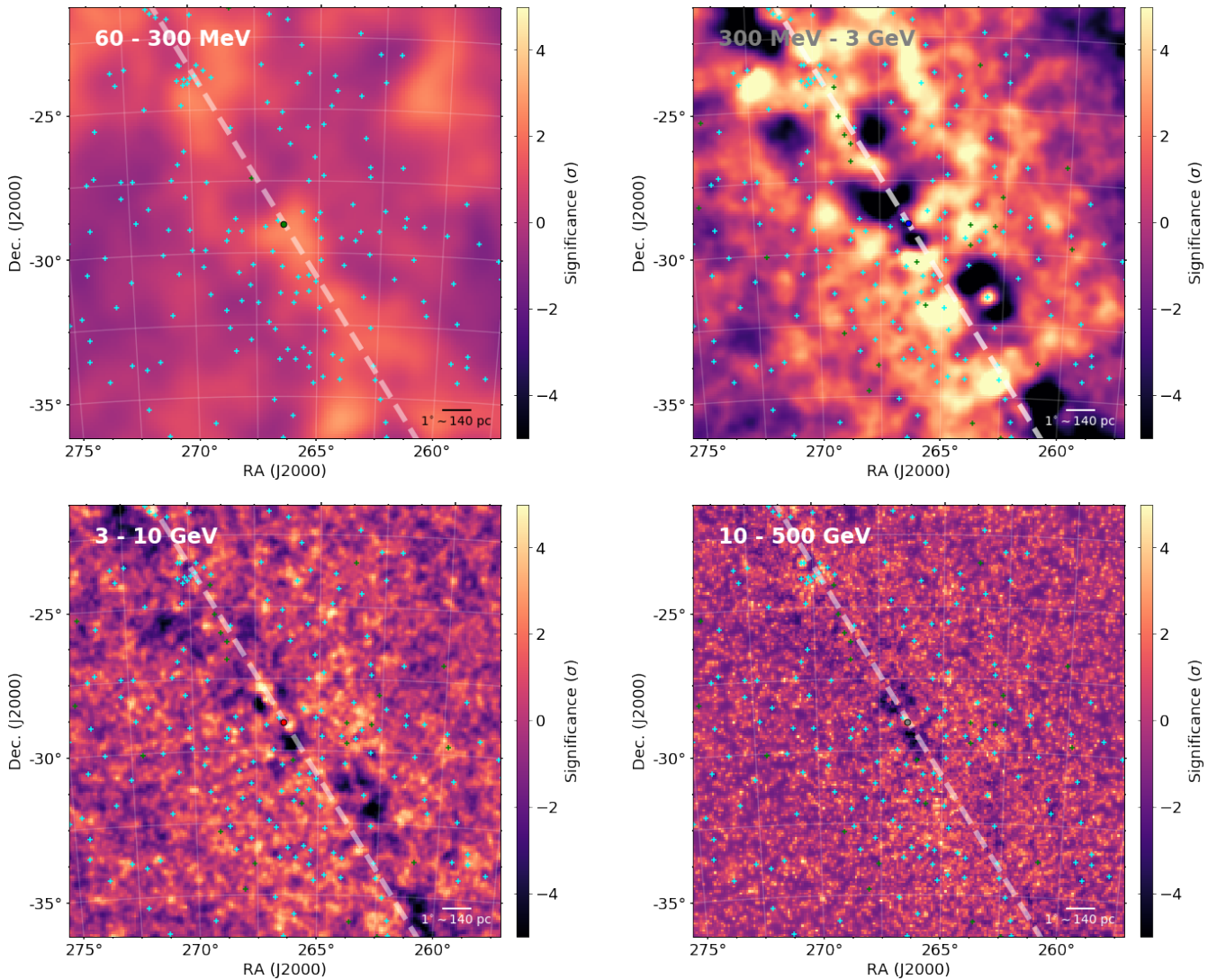


Figure 3. Residual maps for the four different energy ranges. The colors show the significance of the residual. The point at the center of each panel corresponds to the central source position obtained in each energy range. 4FGL point sources are displayed as cyan crosses and new sources found during the analysis as green crosses. The gray dashed lines indicate the direction of the Galactic equator. An angular separation of 1° corresponds to ~ 140 pc at Sgr A*'s distance (8.2 kpc).

519 the quality of the fit of the universal model. They are
 520 shown in Appendix C.

521 We used the `localize` tool to constrain the point
 522 source location in each energy range. Figure 6 shows
 523 the dependence of the source location on energy, to-
 524 gether with the radio position of Sgr A* as measured
 525 by the Very Long Baseline Array (Petrov et al. 2011)
 526 and locations of other potential γ -ray emitters in the
 527 GC.

528 To calculate the total errors Δ_{tot} on the location of
 529 the source we followed the approach used by Abdollahi
 530 et al. (2020) for the creation of the 4FGL Catalog:

$$\Delta_{tot}^2 = (f_{rel}\Delta_{stat})^2 + \Delta_{abs}^2 \quad (1)$$

531 For the absolute precision Δ_{abs} we used the value of
 532 $0.^\circ0068$ (Abdollahi et al. 2020) in the two energy bands
 533 below 3 GeV and $0.^\circ0075$ (Ajello et al. 2017) for higher-
 534 energy bands. For the systematic factor f_{rel} we used
 535 1.1 for the three lower-energy bands and 1.2 for the
 536 10–500 GeV band, these are conservative values based
 537 on *Fermi*-LAT's reported PSF systematic uncertainty³.

³ https://fermi.gsfc.nasa.gov/ssc/data/analysis/LAT_caveats.html

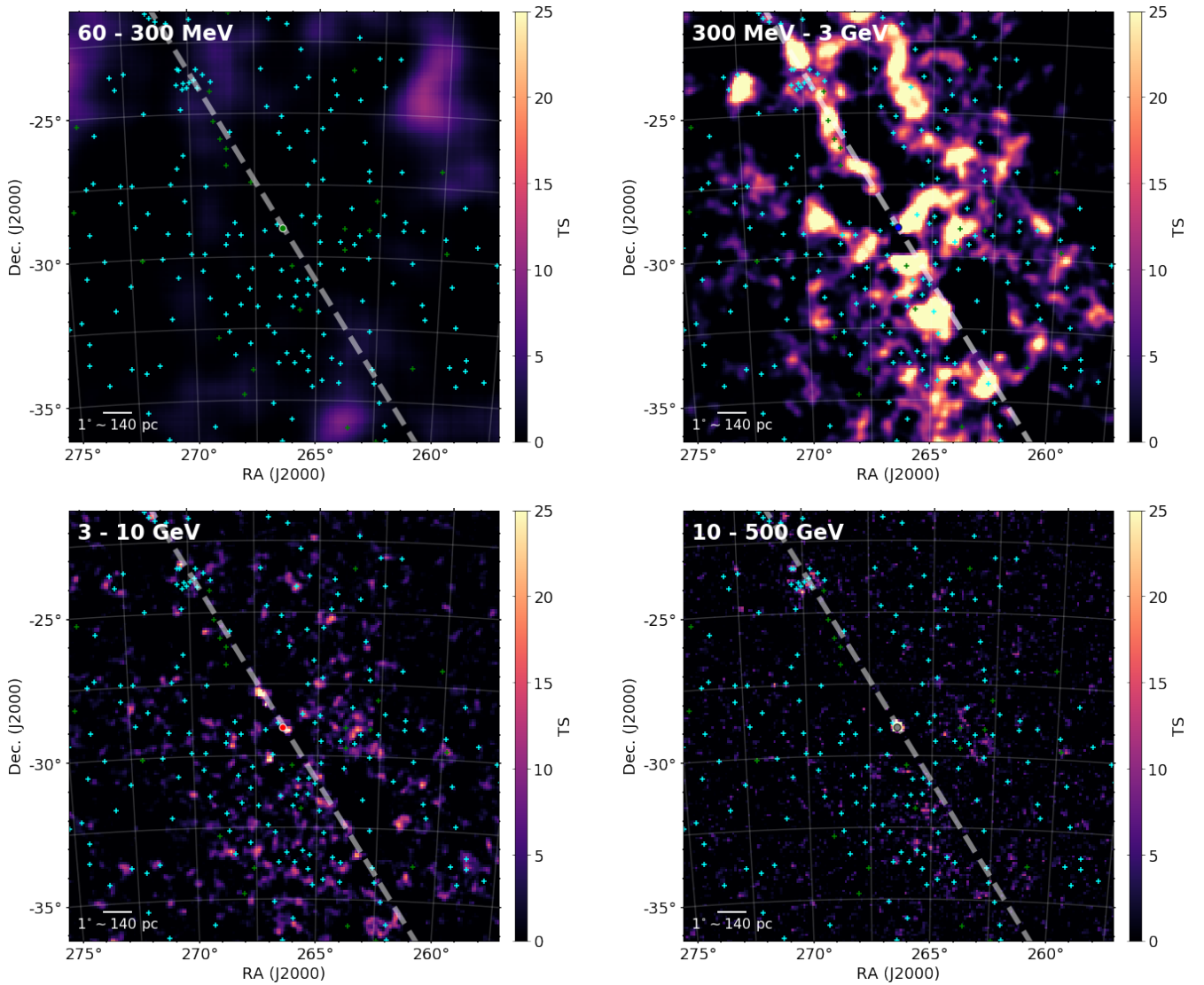


Figure 4. TS maps of the RoI for the four different energy ranges. The central point source is not prominent in these maps since it is part of the model. The circles at the center of the panels correspond to the central point source position obtained in each energy range. 4FGL point sources are displayed as cyan crosses and new sources found during the analysis as green crosses. The gray dashed lines indicate the direction of the Galactic equator. An angular separation of 1° corresponds to ~ 140 pc at Sgr A*'s distance (8.2 kpc).

538 The statistical errors Δ_{stat} are the 68% positional un-
 539 certainties obtained reported by the `localize` tool.

540 In Figure 6 we can see that the position uncertainty of
 541 the source in the lowest energy range is the largest. This
 542 is the result of a combination of factors: the broadening
 543 of *Fermi* LAT's PSF at lower energies, the energy de-
 544 pendence of the instrument's field of view and effective
 545 area, the central source's spectrum and the impact of
 546 the Galactic diffuse emission which is more prominent
 547 at lower energies. The position of the source is consis-
 548 tent within 1σ with Sgr A* in the energy ranges 60–300
 549 MeV and 10–500 GeV. The γ -centroid recedes from Sgr

550 A* as the energy decreases. This is also seen in Figure 7,
 551 which shows the distance between 4FGL J1745.6–2859
 552 and Sgr A* as a function of energy.

553 We also tested the likelihood of the source being ex-
 554 tended versus a point source using the `extension` tool.
 555 Figure 8 shows the 95% upper limits on the spatial ex-
 556 tension of the source for each energy range. We find no
 557 conclusive evidence for any spatially extended emission
 558 from the central source.

4. DISCUSSION

Energy range (GeV)	TS ¹	Photon flux (cm ⁻² s ⁻¹)	Energy flux (erg cm ⁻² s ⁻¹)	Centroid ² (°)	Positional Uncertainty ³ (°)	
					statistical	total
0.06 - 0.3	2246	$(5.17 \pm 0.16) \times 10^{-7}$	$(1.06 \pm 0.03) \times 10^{-10}$	266.407, -29.013	0.045	0.050
0.3 - 3	10522	$(1.49 \pm 0.17) \times 10^{-7}$	$(1.99 \pm 0.20) \times 10^{-10}$	266.394, -28.997	0.005	0.009
3 - 10	3618	$(8.94 \pm 0.22) \times 10^{-9}$	$(6.69 \pm 0.17) \times 10^{-11}$	266.406, -29.003	0.005	0.009
10 - 500	321	$(1.23 \pm 0.11) \times 10^{-9}$	$(3.45 \pm 0.35) \times 10^{-11}$	266.415, -29.010	0.005	0.010
0.1 - 500	14724	$(2.83 \pm 0.08) \times 10^{-7}$	$(3.26 \pm 0.05) \times 10^{-10}$			

¹ $\sqrt{TS} \approx$ detection significance of the source in each energy range

² RA and Dec (in the J2000 epoch) corresponding to the emission centroid in degrees

³ 68% positional uncertainty

Table 1. Results from the likelihood modeling of central point source. The last line presents the results for the universal model. The photon and energy flux uncertainties are statistical only.

By assuming a distance of 8.2 kpc for 4FGL J1745.6–2859 (i.e., that it is located at the GC) we obtain the interesting result that its γ -ray luminosity is similar to Sgr A*’s radio to X-ray luminosity, about 10^{36} erg s⁻¹. The strong similarity between the electromagnetic energetics of 4FGL J1745.6–2859 and Sgr A*, combined with the positional coincidence, naturally suggests that the γ -ray point source investigated in this work is associated with the accreting SMBH. Nevertheless, the $0.1^\circ - 1^\circ$ PSF of *Fermi* LAT encompasses a region of size $\sim 10 - 100$ pc around the GC. Even the more constraining limit of $\lesssim 0^\circ.24$ for the central source’s extension upper limit (Figure 8) corresponds to $\lesssim 35$ pc at the distance of Sgr A*, thus allowing for several other potential candidates for the γ -ray production site. Here, we list the most promising ones and discuss their likelihood at accounting for 4FGL J1745.6–2859.

The SMBH: Aharonian & Neronov (2005a) argue that due to Sgr A*’s low bolometric luminosity compared to other SBMHs, the γ -rays produced close to the event horizon—or in the inner parts of the accretion flow—can escape the source and be detected by *Fermi* LAT because the absorption through photon-photon pair production is low. Aharonian & Neronov (2005a) considered three scenarios for the TeV photons detected by H.E.S.S., two being hadronic and one leptonic. The first hadronic model considers emission related to accelerated protons producing γ -rays through synchrotron and curvature radiation. It predicts an energy flux lower than a few 10^{-12} erg cm⁻² s⁻¹ in the energy range studied in this work, below the values we observed. The second hadronic scenario considers lower energy protons accelerated by the electric field close to the event horizon or by shocks in the accretion disks. Some parametrizations of this model predict very peaked spectral energy distributions (SEDs) in the energy ranges used in this work. Since these SEDs are very narrow, the energy fluxes they predict are consistent only with the observations in one of the four energy ranges we used in this

work. Their leptonic model, in its turn, also fails to explain *Fermi*-LAT’s observation of 4FGL J1745.6–2859: its SED shows $E^2 dN/dE \approx 4 \times 10^{-9}$ erg cm⁻² s⁻¹ at ≈ 1 GeV, thus overpredicting our observed energy flux around this energy.

A “plerion” produced by electrons in Sgr A*’s winds: Atoyan & Dermer (2004) propose a model for Sgr A* in which the quiescent radio and the flaring NIR and X-ray emissions are generated by synchrotron radiation from the RIAF. The wind from the RIAF, in a process similar to pulsar-powered plerions, generates the quiescent X-ray and TeV emissions at the wind termination shock at about 3×10^{16} cm from the SMBH. Although it can explain H.E.S.S.’ TeV observations, their model is not sufficient to explain the MeV-GeV reported in this work. Even if we consider Sagittarius A West bremsstrahlung emission and the emission from a larger plerion (inflated to pc scales), which are prominent in the energy range used in this work (e.g., their Figure 1), the energy flux we detected is still about one order of magnitude higher. On the other hand, Kusunose & Takahara (2012) used 25 months of *Fermi* LAT’s data for the GC (reported by Chernyakova et al. 2011) and proposed a similar leptonic model in which electrons escaping from the vicinity of Sgr A* accumulate in a region with a size of 10^{18} cm where the γ -rays are produced by IC scattering of soft photons emitted by stars and dust around the GC. Importantly, they obtain energy fluxes similar ($\sim 10^{-10}$ erg cm⁻² s⁻¹) to the values observed here.

The interaction between the dense molecular clouds with cosmic rays: As an explanation for the γ -ray emission from the GC, Aharonian & Neronov (2005b) presented a model of proton-proton interactions between the protons accelerated near the SMBH and the dense gas in the central 10 pc of the Galaxy which are followed by π^0 decay to γ -rays. Aharonian & Neronov’s work was published before the beginning of operations of *Fermi* LAT. Their results are inconsistent with our observations.

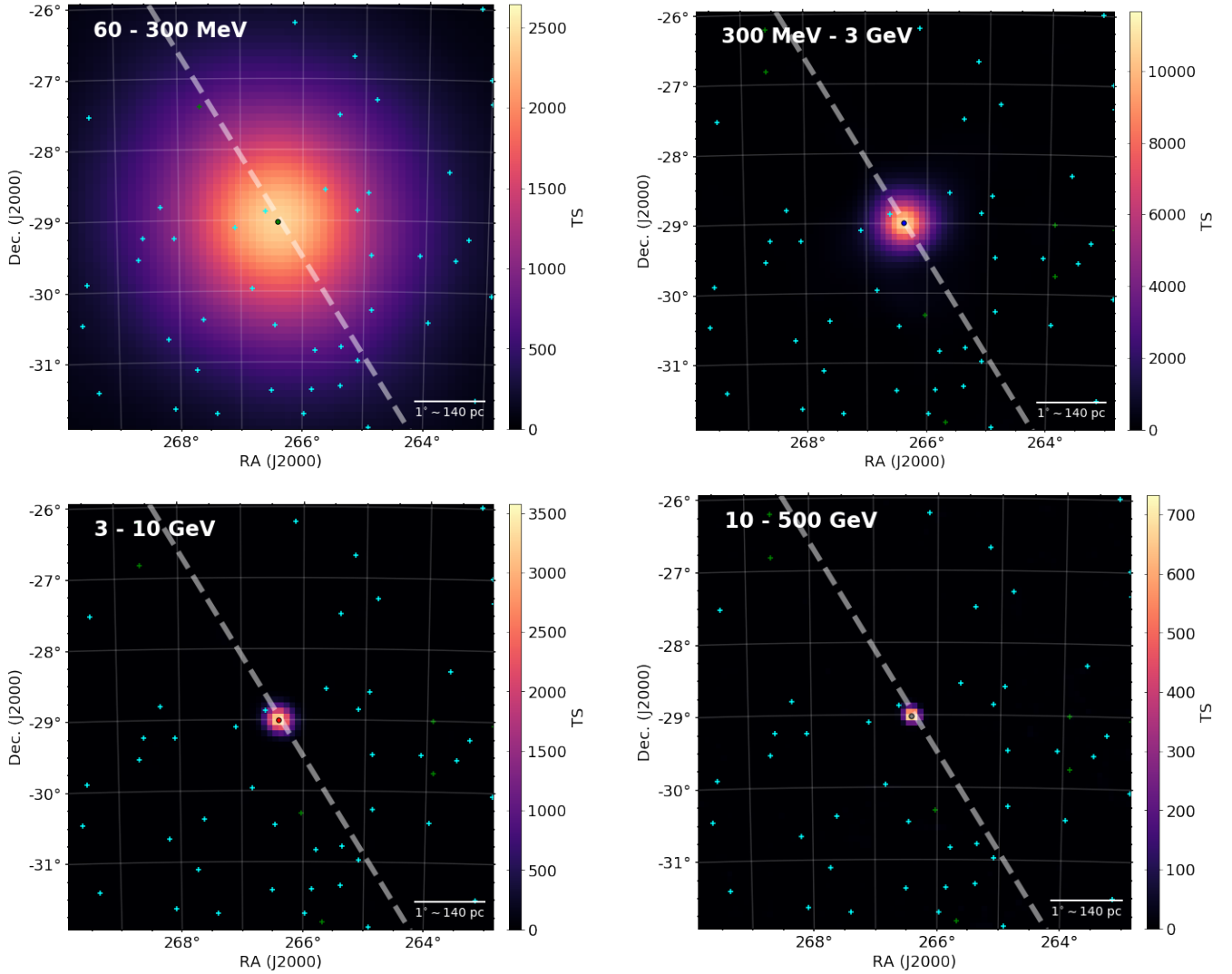


Figure 5. TS maps of the inner $8^\circ \times 8^\circ$ of the RoI showing the contribution of the central point source. They were constructed after excluding 4FGL J1745.6–2859 from the models, as explained in the text. The point at the center of each panel corresponds to the source position obtained in each energy range. The other 4FGL point sources are shown as cyan crosses and new sources found during the analysis are shown as green crosses. The apparent sizes of the excesses decrease with energy, but this does not mean any variation of the physical extension of the source. Instead, it is an outcome of the broadening of *Fermi* LAT’s PSF in low energies. The gray dashed lines indicate the direction of the Galactic equator. An angular separation of 1° corresponds to ~ 140 pc at Sgr A*’s distance (8.2 kpc).

638 More recent models take into account *Fermi*-LAT ob-
 639 servations. For instance, Chernyakova et al. (2011) use
 640 the first 25 months of *Fermi*-LAT and H.E.S.S. data
 641 to create a hadronic model in which relativistic protons
 642 (presumably accelerated near Sgr A*) interact with the
 643 gas in the inner parsecs of the Galaxy. Linden et al.
 644 (2012) developed a similar model. Another hadronic
 645 model is proposed by Fatuzzo & Melia (2012) where
 646 they consider a two-phase environment surrounding Sgr
 647 A*: an inner high-density “torus” and the surround-
 648 ing interstellar medium filled with shocked stellar winds

649 which they call the “wind zone”. *Fermi* γ -rays would be
 650 produced in the “torus” and the higher energies would
 651 come mostly from the “wind zone”. Guo et al. (2013)
 652 propose a hybrid model. In their scenario, protons and
 653 electrons are accelerated in the GC (possibly around Sgr
 654 A*). Collisions between the protons and the interstel-
 655 lar gas would produce the TeV γ -rays and the electrons
 656 would IC scatter the soft background photons.

657 The four “Fermi-era” models mentioned above—
 658 namely, Chernyakova et al. 2011; Linden et al. 2012;
 659 Fatuzzo & Melia 2012; Guo et al. 2013—are consistent

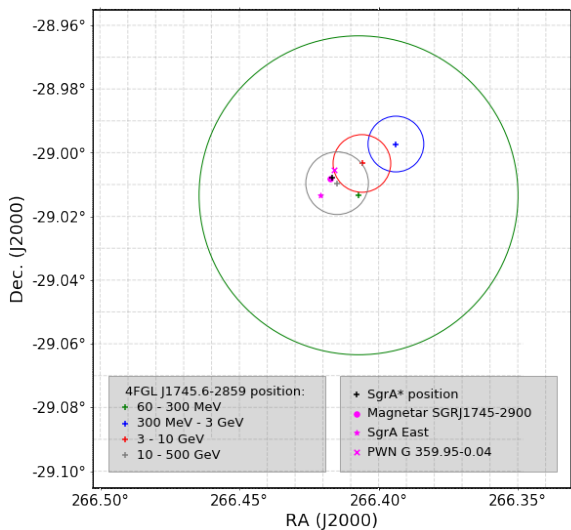


Figure 6. The position of the central source as a function of the energy range used in the analysis: green (100–300 MeV), blue (300 MeV–3 GeV), red (3–10 GeV) and gray (10–500 GeV). The circles represent the 68% positional uncertainty. The radio position of Sgr A* is indicated by the black cross. The positions of other γ -ray-emitters in the GC are also indicated.

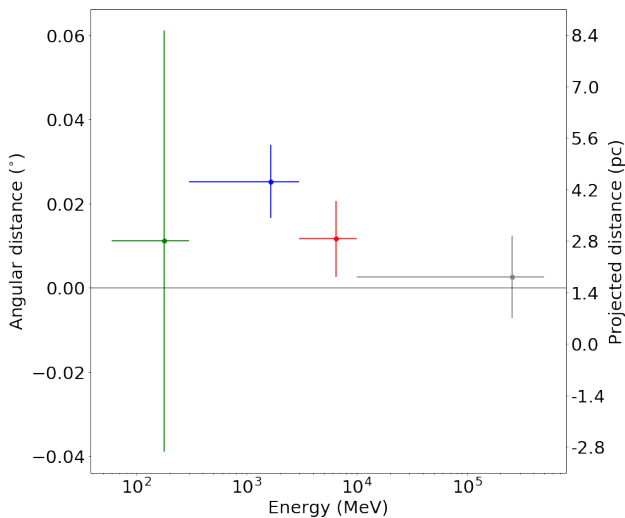


Figure 7. The distance between the central source and Sgr A* as a function of energy.

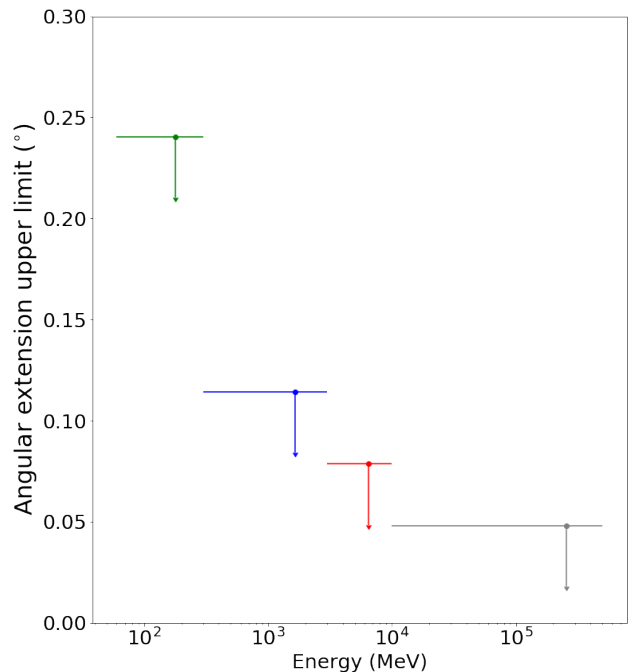


Figure 8. Upper limit on the spatial extension of 4FGL J1745.6–2859 as a function of energy. Upper limits correspond to the 95% confidence level.

660 with our observations, except in the lower energy band
 661 we used. This energy band is the one most subject
 662 to source confusion and to the impacts of the Galactic
 663 diffuse emission. This could explain why we observe
 664 greater energy fluxes in the 60–300 MeV energy band
 665 than the prediction of these models: in addition to the
 666 γ -rays created by the interaction between cosmic rays
 667 originated by (or nearby) Sgr A*, there is also a contri-

668 bution from other sources. When Ahnen et al. (2017)
 669 compared *Fermi* LAT’s data reported by Malyshev et al.
 670 (2015) with the “Fermi-era” models, the lower energy
 671 data ($\lesssim 200$ MeV) also showed greater fluxes than the
 672 models’ predictions.

673 The PWN G 359.95-0.04: This X-ray nebula was dis-
 674 covered by Wang et al. (2006) with a projected distance
 675 of only 0.32 pc from Sgr A* and was proposed
 676 as an explanation for the TeV emission observed in the
 677 GC. Hinton & Aharonian (2007) constructed theoret-
 678 ical SEDs for this source based on Chandra’s detection
 679 and supposing that the TeV emission of the H.E.S.S.
 680 source HESS J1745–290 is from the PWN. Their mod-
 681 els (e.g., their Figure 4) predicts energy fluxes on the
 682 order of $\sim 10^{-12}$ erg cm $^{-2}$ s $^{-1}$ for the energy ranges
 683 studied in this work. This is more than one order of
 684 magnitude lower than the energy fluxes we measured for
 685 4FGL J1745.6–2859. This indicates that G 359.95-0.04
 686 is not a good candidate to explain 4FGL J1745.6–2859’s
 687 emission.

688 The supernova remnant Sagittarius A East: Sagit-
 689 tarius A East is usually explained as a supernova rem-
 690 nant, although other interpretations have also been sug-
 691 gested (Yusef-Zadeh & Morris 1987; Mezger et al. 1989;
 692 Khokhlov & Melia 1996). It is located in the inner par-
 693 secs of the Galaxy. Crocker et al. (2005) proposed it as
 694 the source of the TeV γ -rays from the GC. On the other

695 hand, Aharonian et al. (2009) and Acero et al. (2010)
 696 ruled out this association based on H.E.S.S. observations
 697 that show the origin of this emission as significantly dis-
 698 placed from the position of Sagittarius A East. Posi-
 699 tions of the central source found for the energy bands
 700 300 MeV–3 GeV and 3–10 GeV suggest the same con-
 701 clusion, as shown in Figure 6. But that is not the case
 702 for the lowest and the highest energy bands (whose po-
 703 sitions are coincident with Sagittarius A East). So we
 704 can not completely rule out the association of the central
 705 source with Sagittarius A East, although the connection
 706 appears weak.

707 The magnetar SGR J1745–2900: This object was first
 708 detected during a flare in 2013 with *Swift*'s X-Ray Tele-
 709 scope (Kennea et al. 2013) and NuSTAR (Mori et al.
 710 2013). 4FGL J1745.6–2859's γ -ray light curve shows
 711 no sign of variability during this period (Malyshev et al.
 712 2015; Ahnen et al. 2017; Cafardo et al., in preparation).
 713 Also, it is predicted that the high-energy portion of the
 714 spectra of magnetars peak at a few MeV (Thompson &
 715 Beloborodov 2005), while our work clearly shows emis-
 716 sion from 4FGL J1745.6–2859 at energies > 10 GeV.

717 Self-annihilating dark matter particles accumulating
 718 at the GC: Self-annihilating dark matter particles could
 719 explain the GC γ -ray excess (Hooper & Goodenough
 720 2011; Hooper & Linden 2011 and see Di Mauro 2020,
 721 in preparation, for a recent analysis of the GC excess),
 722 a surplus of \sim GeV diffuse emission that cannot be ex-
 723 plained by the known catalogued sources. But is not a
 724 satisfactory explanation for 4FGL J1745.6–2859 since
 725 this is a point-like source rather than extended in space.

726 A population of pulsars surrounding the GC: The γ -
 727 ray spectra of pulsars and millisecond pulsars can be
 728 described as a power-law with an exponential cutoff
 729 above a few GeV (Abdo et al. 2010). de Menezes et al.
 730 (2019) studied the γ -ray emission of globular clusters in
 731 the Milky Way—attributed to their large population of
 732 millisecond pulsars—and found no significant flux above
 733 ~ 10 GeV. In contrast with that, the point source 4FGL
 734 J1745.6–2859 is detected at energies above that as indi-
 735 cated in Table 1 and Figure 5. Its hard spectrum is also
 736 not consistent with a pulsar (or population of them) in
 737 the line of sight.

738
 739 Except for the models constructed around *Fermi*
 740 LAT's data, most of the candidates listed above are
 741 unlikely to be solely responsible (if responsible at all)
 742 for 4FGL J1745.6–2859's emission. It is possible that
 743 some of them could explain, individually or together,
 744 the lower energy emission where *Fermi* LAT's PSF is
 745 broadest. One way to separate the contributions of
 746 different candidates at lower energies is through model-

747 ing the MeV-to-GeV spectral energy distribution of the
 748 point source. This is beyond the scope of the present
 749 paper, and left for a forthcoming work.

750 From this work, we have the following main three re-
 751 sults: (i) the energetics of 4FGL J1745.6–2859 is com-
 752 parable to the radio-to-X-ray bolometric luminosity of
 753 Sgr A*, (ii) among all the possible candidates for the
 754 γ -ray flux of the point source, only the models invoking
 755 cosmic rays accelerated by Sgr A* or a nearby source can
 756 explain the observations and (iii) the emission centroid
 757 moves toward the position of Sgr A* as the energy is in-
 758 creased. From these results, we conclude that Sgr A* is
 759 the most likely candidate to explain 4FGL J1745.6–2859
 760 and its properties.

761 If we consider only the three highest-energy ranges
 762 used in this analysis, the centroid emission moves in the
 763 direction of Sgr A* as the photon energy is increased
 764 (Figures 6 and 7). Assuming a distance of 8.2 kpc, the
 765 projected distances to Sgr A* as a function of energy
 766 varies from 3.6 ± 1.3 pc (300 MeV–3 GeV) to 0.4 ± 1.4
 767 pc (10–500 GeV). This suggests that the particle popu-
 768 lations responsible for the γ -rays detected in the three
 769 bands are accelerated by the same process, originating
 770 in the surroundings of Sgr A*. The location centroid for
 771 the lower-energy band is also consistent within 1σ with
 772 Sgr A*'s.

773 As discussed in Section 2, the impact of source con-
 774 fusion on *Fermi*-LAT observations is greater at lower
 775 energies due to the PSF broadening. The localization
 776 uncertainties are considerably larger at low energies, as
 777 well as the limit on the angular extension, which creates
 778 the possibility that several other sources and processes
 779 are contributing to the lower-energy flux.

780 We performed extension analysis of the source in the
 781 four energy bands used in this work. In Figure 8, we re-
 782 port the 95% confidence level upper limit for the spatial
 783 extension of the source. Again, we observe the impact of
 784 energy on the results: in lower energies the source tends
 785 to be more spatially extended. This can be a result of
 786 the degradation of *Fermi*'s PSF and source confusion.

787 5. SUMMARY

788 Sgr A*—the accreting SMBH at the center of our
 789 galaxy—has been observed in virtually every band of
 790 the electromagnetic spectrum. In γ -rays, H.E.S.S. and
 791 *Fermi* LAT detected point sources coincident with Sgr
 792 A*. Nevertheless the connection between these point
 793 sources and Sgr A* remained inconclusive. In this work
 794 we have used about 10.5 years of *Fermi* LAT observa-
 795 tions of the point source 4FGL J1745.6–2859 at the
 796 Galactic Center with the aim of constraining the na-
 797 ture of its emission. We divided the analysis into four

798 different energy bands between 60 MeV and 500 GeV,
799 performing a detailed imaging analysis of the surround-
800 ings of the point source. Our main conclusions can be
801 summarized as follows:

802 (i) The 0.1–500 GeV luminosity of the point source
803 is $(2.61 \pm 0.05) \times 10^{36}$ erg s⁻¹ assuming it is located
804 at the Galactic Center; this value is comparable to the
805 observed luminosity of Sgr A* from radio to X-rays.

806 (ii) The point source location approaches Sgr A*'s po-
807 sition as the photon energy is increased. For instance,
808 at energies > 10 GeV the source location is consistent
809 with Sgr A* within 1σ .

810 (iii) Among several possible candidates to the γ -ray
811 flux of the point source, only models invoking cosmic
812 rays—either hadronic or leptonic—accelerated by Sgr
813 A* or a nearby source can explain our observations.

814 (v) Other processes not associated with the SMBH
815 could be contributing to the flux at energies < 300 MeV
816 (e.g., pulsars) due to the larger positional uncertainty of
817 the source as the instrument PSF deteriorates at lower
818 energies.

819 Taken together, our results support the picture in
820 which the point source 4FGL J1745.6–2859 observed
821 by *Fermi* LAT at the GC is the manifestation of Sgr A*
822 in the MeV-to-GeV range.

823 The advent of the Cherenkov Telescope Array (CTA,
824 [Cherenkov Telescope Array Consortium et al. 2019](#)) will
825 allow for a deep exposure of the GC in energies up
826 to ~ 300 TeV. This will permit studies in spatial and
827 spectral details unavailable today, with arc-minute reso-
828 lution at energies above *Fermi*'s operational range, po-
829 tentially enabling a firmer association between the very
830 high-energy point source in the GC with Sgr A* or other
831 nearby candidate. Correspondingly, proposed γ -ray
832 missions focusing on MeV bands such as the AMEGO
833 mission ([McEnery et al. 2019](#)) and e-ASTROGAM ([de](#)
834 [Angelis et al. 2018](#)) should improve the observational
835 sensitivity, helping to better constrain the properties of
836 the GC emission in the 60–300 MeV energy band and
837 shed light on the contribution of Sgr A*.

838
839 In a forthcoming work, we will analyze the γ -ray vari-
840 ability and SED of 4FGL J1745.6–2859 in order to fur-
841 ther constrain its physical origin.

842 ACKNOWLEDGMENTS

843 We acknowledge useful discussions with John Hewitt,
844 Raniere de Menezes, Teddy Cheung, Matthew Kerr, Ju-
845 lia C. Santos., Giacomo Principe Jeremy S. Perkins and
846 Seth Digel.

847 This work was supported by CNPq (Conselho Na-
848 cional de Desenvolvimento Científico e Tecnológico) un-

849 der grant 142320/2016-1 and FAPESP (Fundação de
850 Amparo à Pesquisa do Estado de São Paulo) under grant
851 2017/01461-2.

852 The *Fermi* LAT Collaboration acknowledges gener-
853 ous ongoing support from a number of agencies and
854 institutes that have supported both the development
855 and the operation of the LAT as well as scientific data
856 analysis. These include the National Aeronautics and
857 Space Administration and the Department of Energy in
858 the United States, the Commissariat à l'Énergie Atom-
859 ique and the Centre National de la Recherche Scien-
860 tifique / Institut National de Physique Nucléaire et de
861 Physique des Particules in France, the Agenzia Spaziale
862 Italiana and the Istituto Nazionale di Fisica Nucleare in
863 Italy, the Ministry of Education, Culture, Sports, Sci-
864 ence and Technology (MEXT), High Energy Accelerator
865 Research Organization (KEK) and Japan Aerospace Ex-
866 ploration Agency (JAXA) in Japan, and the K. A. Wal-
867 lenberg Foundation, the Swedish Research Council and
868 the Swedish National Space Board in Sweden.

869 Additional support for science analysis during the
870 operations phase is gratefully acknowledged from the
871 Istituto Nazionale di Astrofisica in Italy and the Cen-
872 tre National d'Études Spatiales in France. This work
873 performed in part under DOE Contract DE-AC02-
874 76SF00515.

875 *Facilities:* *Fermi* LAT

876 *Software:* Fermipy ([Wood et al. 2017](#)), APLpy ([Ro-](#)
877 [bitaille & Bressert 2012](#); [Robitaille 2019](#)).

APPENDIX

A. NEW SOURCES FOUND IN THE ANALYSIS BETWEEN 100 MEV AND 500 GEV

Here we present the new sources encountered in the RoI with `Fermipy's find_sources` function in the energy range between 100 MeV and 500 GeV. The maximum likelihood parameters for the power-law (with $dN/dE \propto N_0 \times E^\alpha$, where dN/dE is the differential photon flux, N_0 is the prefactor and α is the spectral index) used to model their spectra are also shown, together with their TS and position.

Some of these newly detected source might be spurious due to unmodeled or inadequately modeled background emission.

Source name	Index	Prefactor	TS	RA	Dec
PS J1719.1–2945	−5.0	2.8×10^{-14}	236	259.80	−29.75
PS J1720.6–2655	−2.1	4.5×10^{-13}	40	260.16	−26.93
PS J1723.8–3347	−2.0	5.8×10^{-13}	31	260.95	−33.79
PS J1729.5–3623	−1.9	4.7×10^{-13}	40	262.39	−36.40
PS J1730.5–2801	−2.0	3.8×10^{-13}	31	262.64	−28.03
PS J1731.6–2903	−1.8	2.9×10^{-13}	34	262.92	−29.05
PS J1733.8–2114	−2.0	2.8×10^{-13}	30	263.47	−21.24
PS J1734.4–3555	−2.2	5.8×10^{-13}	34	263.62	−35.93
PS J1734.6–2328	−2.2	4.9×10^{-13}	37	263.66	−23.48
PS J1735.5–2944	−1.8	3.3×10^{-13}	31	263.88	−29.74
PS J1735.6–2900	−5.0	1.6×10^{-14}	36	263.91	−29.01
PS J1742.7–3150	−2.0	8.0×10^{-13}	50	265.68	−31.85
PS J1744.1–3019	−2.2	2.7×10^{-12}	124	266.03	−30.32
PS J1747.2–2114	−2.3	5.8×10^{-13}	40	266.81	−21.25
PS J1750.4–3355	−2.2	5.6×10^{-13}	40	267.61	−33.93
PS J1752.0–3447	−2.2	4.1×10^{-13}	34	268.02	−34.79
PS J1752.6–2105	−5.0	4.0×10^{-14}	303	268.15	−21.09
PS J1754.4–2612	−2.1	7.6×10^{-13}	32	268.60	−26.21
PS J1754.4–2649	−2.0	5.8×10^{-13}	30	268.60	−26.82
PS J1754.7–3730	−2.2	3.7×10^{-13}	38	268.70	−37.51
PS J1755.3–2553	−2.0	9.3×10^{-13}	49	268.83	−25.90
PS J1756.0–3248	−2.1	4.1×10^{-13}	31	269.02	−32.81
PS J1756.3–2515	−2.3	2.1×10^{-12}	99	269.08	−25.25
PS J1756.8–2413	−1.9	5.4×10^{-13}	36	269.21	−24.22
PS J1758.0–2421	−2.2	1.1×10^{-12}	38	269.52	−24.36
PS J1808.2–3003	−2.2	4.5×10^{-13}	45	272.06	−30.05
PS J1817.4–2516	−2.4	5.7×10^{-13}	50	274.35	−25.27
PS J1818.6–2812	−2.6	5.0×10^{-13}	57	274.65	−28.22
PS J1823.9–2341	−2.4	5.1×10^{-13}	47	275.99	−23.69

Table 2. New sources found in the 100 MeV to 500 GeV energy range. RA and Dec are in the J2000 epoch.

886 B. NEW SOURCES FOUND IN THE ANALYSIS WITH THE CUSTOM MODEL BETWEEN 60 AND 300 MEV

887 Five new sources were encountered in the RoI with `Fermipy`'s `find_sources` function in the energy range between
 888 60 and 300 MeV. They are listed in Table 3. The best parameters for the power-law (with $dN/dE \propto N_0 \times E^\alpha$, where
 889 dN/dE is the differential photon flux, N_0 is the prefactor and α is the spectral index) used to model their spectra are
 890 also shown, together with their TS and position.

891 These might be spurious findings due to imperfections in the model.

Source name	Index	Prefactor	TS	RA	Dec
PS J1639.5–2448	–1.7	4.4×10^{-12}	37	249.90	–24.81
PS J1750.6–2723	–2.0	4.8×10^{-12}	27	267.65	–27.40
PS J1753.7–2127	–0.9	2.9×10^{-12}	57	268.44	–21.47
PS J1820.5–2113	–2.0	4.3×10^{-12}	61	275.14	–21.22
PS J1835.0–1804	–5.0	8.8×10^{-15}	183	278.76	–18.07

Table 3. New sources found in the 60 to 300 MeV energy range. RA and Dec are in the J2000 epoch.

C. DIAGNOSTIC PLOTS FOR THE UNIVERSAL MODEL

892

893 We present the residual map, the TS maps with and without 4FGL J1745.6–2859 in the universal model created in
 894 the 100 MeV to 500 GeV energy range.

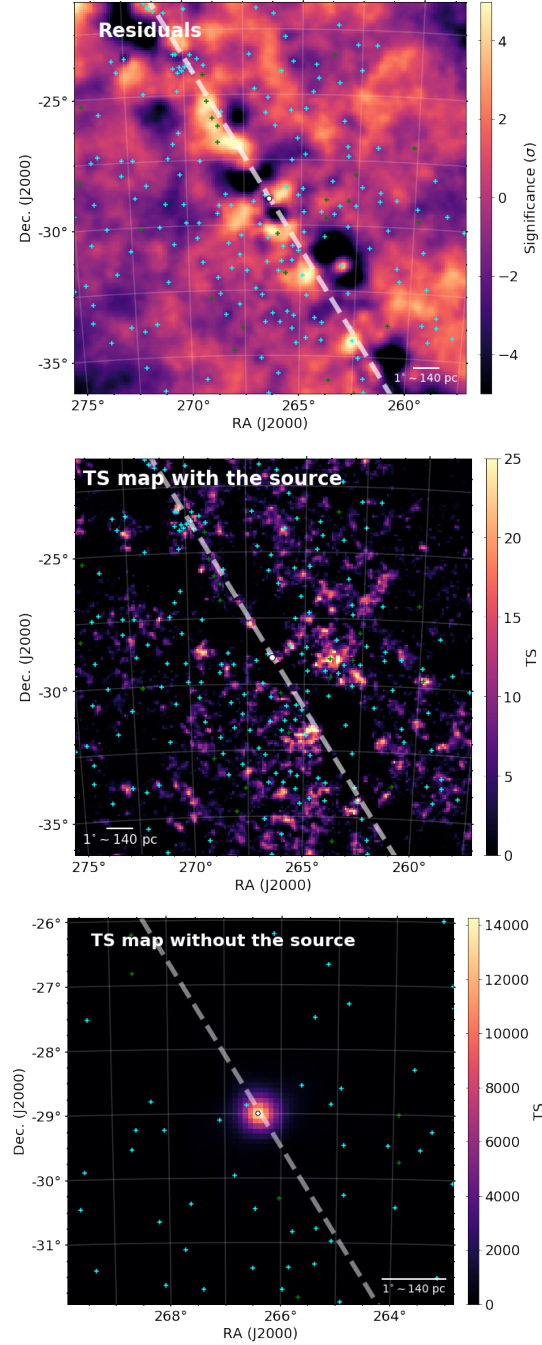


Figure 9. Diagnostic plots for the universal model. In the upper panel, the colors show the significance of the residual. On the other panels, the colors indicate the TS value in each position. The point at the center of each panel corresponds to 4FGL J1745.6–2859 position in the 4FGL Catalogue. 4FGL point sources are displayed as cyan crosses and new sources found during the analysis as green crosses. The gray dashed lines indicate the direction of the Galactic equator. An angular separation of 1° corresponds to ~ 140 pc at Sgr A*'s distance (8.2 kpc).

REFERENCES

- 895 Abdo, A. A., Ackermann, M., Ajello, M., et al. 2010, *ApJS*,
896 187, 460, doi: [10.1088/0067-0049/187/2/460](https://doi.org/10.1088/0067-0049/187/2/460)
- 897 Abdollahi, S., Acero, F., Ackermann, M., et al. 2020, *The*
898 *Astrophysical Journal Supplement Series*, 247, 33,
899 doi: [10.3847/1538-4365/ab6bcb](https://doi.org/10.3847/1538-4365/ab6bcb)
- 900 Abuter, R., Amorim, A., Bauboeck, M., et al. 2019, arXiv
901 e-prints, arXiv:1904.05721.
902 <https://arxiv.org/abs/1904.05721>
- 903 Acero, F., Aharonian, F., Akhperjanian, A. G., et al. 2010,
904 *MNRAS*, 402, 1877,
905 doi: [10.1111/j.1365-2966.2009.16014.x](https://doi.org/10.1111/j.1365-2966.2009.16014.x)
- 906 Acero, F., Ackermann, M., Ajello, M., et al. 2015, *ApJS*,
907 218, 23, doi: [10.1088/0067-0049/218/2/23](https://doi.org/10.1088/0067-0049/218/2/23)
- 908 Aharonian, F., & Neronov, A. 2005a, *ApJ*, 619, 306,
909 doi: [10.1086/426426](https://doi.org/10.1086/426426)
- 910 —. 2005b, *Astrophysics and Space Science*, 300, 255,
911 doi: [10.1007/s10509-005-1209-4](https://doi.org/10.1007/s10509-005-1209-4)
- 912 Aharonian, F., Akhperjanian, A. G., Anton, G., et al. 2009,
913 *A&A*, 503, 817, doi: [10.1051/0004-6361/200811569](https://doi.org/10.1051/0004-6361/200811569)
- 914 Ahnen, M. L., Ansoldi, S., Antonelli, L. A., et al. 2017,
915 *A&A*, 601, A33, doi: [10.1051/0004-6361/201629355](https://doi.org/10.1051/0004-6361/201629355)
- 916 Ajello, M., Atwood, W. B., Baldini, L., et al. 2017, *ApJS*,
917 232, 18, doi: [10.3847/1538-4365/aa8221](https://doi.org/10.3847/1538-4365/aa8221)
- 918 Atoyan, A., & Dermer, C. D. 2004, *ApJL*, 617, L123,
919 doi: [10.1086/427390](https://doi.org/10.1086/427390)
- 920 Atwood, W., Albert, A., Baldini, L., et al. 2013, arXiv
921 preprint arXiv:1303.3514
- 922 Atwood, W. B., Abdo, A. A., Ackermann, M., et al. 2009,
923 *ApJ*, 697, 1071, doi: [10.1088/0004-637X/697/2/1071](https://doi.org/10.1088/0004-637X/697/2/1071)
- 924 Baganoff, F. K., Bautz, M. W., Brandt, W. N., et al. 2001,
925 *Nature*, 413, 45, doi: [10.1038/35092510](https://doi.org/10.1038/35092510)
- 926 Balick, B., & Brown, R. L. 1974, *ApJ*, 194, 265,
927 doi: [10.1086/153242](https://doi.org/10.1086/153242)
- 928 Ball, D., Özel, F., Psaltis, D., & Chan, C.-k. 2016, *ApJ*,
929 826, 77, doi: [10.3847/0004-637X/826/1/77](https://doi.org/10.3847/0004-637X/826/1/77)
- 930 Ballantyne, D. R., Schumann, M., & Ford, B. 2011,
931 *Monthly Notices of the Royal Astronomical Society*, 410,
932 1521, doi: [10.1111/j.1365-2966.2010.17533.x](https://doi.org/10.1111/j.1365-2966.2010.17533.x)
- 933 Barrière, N. M., Tomsick, J. A., Baganoff, F. K., et al.
934 2014, *The Astrophysical Journal*, 786, 46,
935 doi: [10.1088/0004-637x/786/1/46](https://doi.org/10.1088/0004-637x/786/1/46)
- 936 Boehle, A., Ghez, A. M., Schödel, R., et al. 2016, *ApJ*, 830,
937 17, doi: [10.3847/0004-637X/830/1/17](https://doi.org/10.3847/0004-637X/830/1/17)
- 938 Boyce, H., Haggard, D., Witzel, G., et al. 2018, arXiv
939 e-prints, arXiv:1812.05764.
940 <https://arxiv.org/abs/1812.05764>
- 941 Brinkerink, C. D., Falcke, H., Law, C. J., et al. 2015, *A&A*,
942 576, A41, doi: [10.1051/0004-6361/201424783](https://doi.org/10.1051/0004-6361/201424783)
- 943 Cherenkov Telescope Array Consortium, Acharya, B. S.,
944 Agudo, I., et al. 2019, *Science with the Cherenkov*
945 *Telescope Array*, doi: [10.1142/10986](https://doi.org/10.1142/10986)
- 946 Chernyakova, M., Malyshev, D., Aharonian, F. A., Crocker,
947 R. M., & Jones, D. I. 2011, *ApJ*, 726, 60,
948 doi: [10.1088/0004-637X/726/2/60](https://doi.org/10.1088/0004-637X/726/2/60)
- 949 Clavel, M., Terrier, R., Goldwurm, A., et al. 2013, *A&A*,
950 558, A32, doi: [10.1051/0004-6361/201321667](https://doi.org/10.1051/0004-6361/201321667)
- 951 Crocker, R. M., Fatuzzo, M., Jokipii, J. R., Melia, F., &
952 Volkas, R. R. 2005, *ApJ*, 622, 892, doi: [10.1086/427972](https://doi.org/10.1086/427972)
- 953 de Angelis, A., Tatischeff, V., Grenier, I. A., et al. 2018,
954 *Journal of High Energy Astrophysics*, 19, 1,
955 doi: [10.1016/j.jheap.2018.07.001](https://doi.org/10.1016/j.jheap.2018.07.001)
- 956 de Menezes, R., Cafardo, F., & Nemmen, R. 2019, *Monthly*
957 *Notices of the Royal Astronomical Society*, 486, 851,
958 doi: [10.1093/mnras/stz898](https://doi.org/10.1093/mnras/stz898)
- 959 Dodds-Eden, K., Porquet, D., Trap, G., et al. 2009, *ApJ*,
960 698, 676, doi: [10.1088/0004-637X/698/1/676](https://doi.org/10.1088/0004-637X/698/1/676)
- 961 Eckart, A., Zajacek, M., Parsa, M., et al. 2018, arXiv
962 e-prints, arXiv:1806.00284.
963 <https://arxiv.org/abs/1806.00284>
- 964 Eisenhauer, F., Genzel, R., Alexander, T., et al. 2005, *The*
965 *Astrophysical Journal*, 628, 246, doi: [10.1086/430667](https://doi.org/10.1086/430667)
- 966 Event Horizon Telescope Collaboration, Akiyama, K.,
967 Alberdi, A., et al. 2019, *ApJ*, 875, L1,
968 doi: [10.3847/2041-8213/ab0ec7](https://doi.org/10.3847/2041-8213/ab0ec7)
- 969 Fatuzzo, M., & Melia, F. 2012, *ApJ*, 757, L16,
970 doi: [10.1088/2041-8205/757/1/L16](https://doi.org/10.1088/2041-8205/757/1/L16)
- 971 Fazio, G. G., Hora, J. L., Witzel, G., et al. 2018, *ApJ*, 864,
972 58, doi: [10.3847/1538-4357/aad4a2](https://doi.org/10.3847/1538-4357/aad4a2)
- 973 Genzel, R., Eisenhauer, F., & Gillessen, S. 2010, *Reviews of*
974 *Modern Physics*, 82, 3121,
975 doi: [10.1103/RevModPhys.82.3121](https://doi.org/10.1103/RevModPhys.82.3121)
- 976 Genzel, R., Schödel, R., Ott, T., et al. 2003, *Nature*, 425,
977 934, doi: [10.1038/nature02065](https://doi.org/10.1038/nature02065)
- 978 Ghez, A. M., Wright, S. A., Matthews, K., et al. 2004,
979 *ApJL*, 601, L159, doi: [10.1086/382024](https://doi.org/10.1086/382024)
- 980 Ghez, A. M., Salim, S., Weinberg, N. N., et al. 2008, *ApJ*,
981 689, 1044, doi: [10.1086/592738](https://doi.org/10.1086/592738)
- 982 Gillessen, S., Eisenhauer, F., Trippe, S., et al. 2009, *ApJ*,
983 692, 1075, doi: [10.1088/0004-637X/692/2/1075](https://doi.org/10.1088/0004-637X/692/2/1075)
- 984 Gravity Collaboration, Abuter, R., Amorim, A., et al. 2018,
985 *A&A*, 618, L10, doi: [10.1051/0004-6361/201834294](https://doi.org/10.1051/0004-6361/201834294)
- 986 Guo, F., & Mathews, W. G. 2012, *ApJ*, 756, 181,
987 doi: [10.1088/0004-637X/756/2/181](https://doi.org/10.1088/0004-637X/756/2/181)
- 988 Guo, Y.-Q., Yuan, Q., Liu, C., & Li, A.-F. 2013, *Journal of*
989 *Physics G Nuclear Physics*, 40, 065201,
990 doi: [10.1088/0954-3899/40/6/065201](https://doi.org/10.1088/0954-3899/40/6/065201)

- 991 Heckman, T. M., & Best, P. N. 2014, *ARA&A*, 52, 589,
992 doi: [10.1146/annurev-astro-081913-035722](https://doi.org/10.1146/annurev-astro-081913-035722)
- 993 HESS Collaboration, Abramowski, A., Aharonian, F., et al.
994 2016, *Nature*, 531, 476, doi: [10.1038/nature17147](https://doi.org/10.1038/nature17147)
- 995 Hinton, J. A., & Aharonian, F. A. 2007, *ApJ*, 657, 302,
996 doi: [10.1086/510283](https://doi.org/10.1086/510283)
- 997 Hooper, D., & Goodenough, L. 2011, *Physics Letters B*,
998 697, 412, doi: [10.1016/j.physletb.2011.02.029](https://doi.org/10.1016/j.physletb.2011.02.029)
- 999 Hooper, D., & Linden, T. 2011, *PhRvD*, 84, 123005,
1000 doi: [10.1103/PhysRevD.84.123005](https://doi.org/10.1103/PhysRevD.84.123005)
- 1001 Hora, J. L., Witzel, G., Ashby, M. L. N., et al. 2014, *The*
1002 *Astrophysical Journal*, 793, 120,
1003 doi: [10.1088/0004-637x/793/2/120](https://doi.org/10.1088/0004-637x/793/2/120)
- 1004 Hornstein, S. D., Matthews, K., Ghez, A. M., et al. 2007,
1005 *The Astrophysical Journal*, 667, 900, doi: [10.1086/520762](https://doi.org/10.1086/520762)
- 1006 Kennea, J. A., Burrows, D. N., Kouveliotou, C., et al. 2013,
1007 *The Astrophysical Journal*, 770, L24,
1008 doi: [10.1088/2041-8205/770/2/L24](https://doi.org/10.1088/2041-8205/770/2/L24)
- 1009 Khokhlov, A., & Melia, F. 1996, *ApJL*, 457, L61,
1010 doi: [10.1086/309895](https://doi.org/10.1086/309895)
- 1011 Kormendy, J., & Richstone, D. 1995, *ARA&A*, 33, 581,
1012 doi: [10.1146/annurev.aa.33.090195.003053](https://doi.org/10.1146/annurev.aa.33.090195.003053)
- 1013 Kusunose, M., & Takahara, F. 2012, *ApJ*, 748, 34,
1014 doi: [10.1088/0004-637X/748/1/34](https://doi.org/10.1088/0004-637X/748/1/34)
- 1015 Linden, T., Lovegrove, E., & Profumo, S. 2012, *ApJ*, 753,
1016 41, doi: [10.1088/0004-637X/753/1/41](https://doi.org/10.1088/0004-637X/753/1/41)
- 1017 Lynden-Bell, D. 1969, *Nature*, 223, 690,
1018 doi: [10.1038/223690a0](https://doi.org/10.1038/223690a0)
- 1019 Macquart, J.-P., Bower, G. C., Wright, M. C. H., Backer,
1020 D. C., & Falcke, H. 2006, *The Astrophysical Journal*,
1021 646, L111, doi: [10.1086/506932](https://doi.org/10.1086/506932)
- 1022 Malyshev, D., Chernyakova, M., Neronov, A., & Walter, R.
1023 2015, *A&A*, 582, A11, doi: [10.1051/0004-6361/201526120](https://doi.org/10.1051/0004-6361/201526120)
- 1024 Marrone, D. P., Baganoff, F. K., Morris, M. R., et al. 2008,
1025 *ApJ*, 682, 373, doi: [10.1086/588806](https://doi.org/10.1086/588806)
- 1026 Mattox, J. R., Bertsch, D. L., Chiang, J., et al. 1996, *ApJ*,
1027 461, 396, doi: [10.1086/177068](https://doi.org/10.1086/177068)
- 1028 Mauerhan, J. C., Morris, M., Walter, F., & Baganoff, F. K.
1029 2005, *ApJL*, 623, L25, doi: [10.1086/429960](https://doi.org/10.1086/429960)
- 1030 McEnery, J., van der Horst, A., Dominguez, A., et al. 2019,
1031 in *Bulletin of the American Astronomical Society*,
1032 Vol. 51, 245
- 1033 Mezger, P. G., Zylka, R., Salter, C. J., et al. 1989, *A&A*,
1034 209, 337
- 1035 Miyazaki, A., Tsutsumi, T., & Tsuboi, M. 2004, *The*
1036 *Astrophysical Journal*, 611, L97, doi: [10.1086/424004](https://doi.org/10.1086/424004)
- 1037 Miyoshi, M., Moran, J., Herrnstein, J., et al. 1995, *Nature*,
1038 373, 127, doi: [10.1038/373127a0](https://doi.org/10.1038/373127a0)
- 1039 Mori, K., Gotthelf, E. V., Zhang, S., et al. 2013, *The*
1040 *Astrophysical Journal*, 770, L23,
1041 doi: [10.1088/2041-8205/770/2/L23](https://doi.org/10.1088/2041-8205/770/2/L23)
- 1042 Morris, M. R., Meyer, L., & Ghez, A. M. 2012, *Research in*
1043 *Astronomy and Astrophysics*, 12, 995,
1044 doi: [10.1088/1674-4527/12/8/007](https://doi.org/10.1088/1674-4527/12/8/007)
- 1045 Narayan, R., Yi, I., & Mahadevan, R. 1995, *Nature*, 374,
1046 623, doi: [10.1038/374623a0](https://doi.org/10.1038/374623a0)
- 1047 Neilsen, J., Nowak, M. A., Gammie, C., et al. 2013, *ApJ*,
1048 774, 42, doi: [10.1088/0004-637X/774/1/42](https://doi.org/10.1088/0004-637X/774/1/42)
- 1049 Neilsen, J., Markoff, S., Nowak, M. A., et al. 2015, *ApJ*,
1050 799, 199, doi: [10.1088/0004-637X/799/2/199](https://doi.org/10.1088/0004-637X/799/2/199)
- 1051 Nolan, P. L., Abdo, A. A., Ackermann, M., et al. 2012,
1052 *ApJS*, 199, 31, doi: [10.1088/0067-0049/199/2/31](https://doi.org/10.1088/0067-0049/199/2/31)
- 1053 Nowak, M. A., Neilsen, J., Markoff, S. B., et al. 2012, *The*
1054 *Astrophysical Journal*, 759, 95,
1055 doi: [10.1088/0004-637x/759/2/95](https://doi.org/10.1088/0004-637x/759/2/95)
- 1056 Petrov, L., Kovalev, Y. Y., Fomalont, E. B., & Gordon, D.
1057 2011, *AJ*, 142, 35, doi: [10.1088/0004-6256/142/2/35](https://doi.org/10.1088/0004-6256/142/2/35)
- 1058 Plambeck, R., Dexter, J., Bower, G. C., et al. 2014,
1059 *Monthly Notices of the Royal Astronomical Society*, 442,
1060 2797, doi: [10.1093/mnras/stu1039](https://doi.org/10.1093/mnras/stu1039)
- 1061 Ponti, G., Terrier, R., Goldwurm, A., Belanger, G., & Trap,
1062 G. 2010, *ApJ*, 714, 732,
1063 doi: [10.1088/0004-637X/714/1/732](https://doi.org/10.1088/0004-637X/714/1/732)
- 1064 Ponti, G., De Marco, B., Morris, M. R., et al. 2015,
1065 *MNRAS*, 454, 1525, doi: [10.1093/mnras/stv1537](https://doi.org/10.1093/mnras/stv1537)
- 1066 Robitaille, T. 2019, *APLpy v2.0: The Astronomical*
1067 *Plotting Library in Python*, doi: [10.5281/zenodo.2567476](https://doi.org/10.5281/zenodo.2567476).
1068 <https://doi.org/10.5281/zenodo.2567476>
- 1069 Robitaille, T., & Bressert, E. 2012, *APLpy: Astronomical*
1070 *Plotting Library in Python, Astrophysics Source Code*
1071 *Library*. <http://ascl.net/1208.017>
- 1072 Stone, J. M., Marrone, D. P., Dowell, C. D., et al. 2016,
1073 *The Astrophysical Journal*, 825, 32,
1074 doi: [10.3847/0004-637x/825/1/32](https://doi.org/10.3847/0004-637x/825/1/32)
- 1075 Su, M., Slatyer, T. R., & Finkbeiner, D. P. 2010, *ApJ*, 724,
1076 1044, doi: [10.1088/0004-637X/724/2/1044](https://doi.org/10.1088/0004-637X/724/2/1044)
- 1077 Thompson, C., & Beloborodov, A. M. 2005, *ApJ*, 634, 565,
1078 doi: [10.1086/432245](https://doi.org/10.1086/432245)
- 1079 von Fellenberg, S. D., Gillessen, S., Graciá-Carpio, J., et al.
1080 2018, *The Astrophysical Journal*, 862, 129,
1081 doi: [10.3847/1538-4357/aac44b](https://doi.org/10.3847/1538-4357/aac44b)
- 1082 Wang, Q. D., Lu, F. J., & Gotthelf, E. V. 2006, *MNRAS*,
1083 367, 937, doi: [10.1111/j.1365-2966.2006.09998.x](https://doi.org/10.1111/j.1365-2966.2006.09998.x)
- 1084 Witzel, G., Eckart, A., Bremer, M., et al. 2012, *The*
1085 *Astrophysical Journal Supplement Series*, 203, 18,
1086 doi: [10.1088/0067-0049/203/2/18](https://doi.org/10.1088/0067-0049/203/2/18)

- 1087 Witzel, G., Martinez, G., Hora, J., et al. 2018, The
1088 Astrophysical Journal, 863, 15,
1089 doi: [10.3847/1538-4357/aace62](https://doi.org/10.3847/1538-4357/aace62)
- 1090 Wood, M., Caputo, R., Charles, E., et al. 2017, arXiv
1091 preprint arXiv:1707.09551
- 1092 Yang, H. Y., Ruszkowski, M., & Zweibel, E. 2018, Galaxies,
1093 6, 29, doi: [10.3390/galaxies6010029](https://doi.org/10.3390/galaxies6010029)
- 1094 Yuan, F., & Narayan, R. 2014, ARA&A, 52, 529,
1095 doi: [10.1146/annurev-astro-082812-141003](https://doi.org/10.1146/annurev-astro-082812-141003)
- 1096 Yuan, F., Quataert, E., & Narayan, R. 2003, ApJ, 598, 301,
1097 doi: [10.1086/378716](https://doi.org/10.1086/378716)
- 1098 Yusef-Zadeh, F., & Morris, M. 1987, ApJ, 320, 545,
1099 doi: [10.1086/165572](https://doi.org/10.1086/165572)
- 1100 Yusef-Zadeh, F., Roberts, D., Wardle, M., Heinke, C. O., &
1101 Bower, G. C. 2006, ApJ, 650, 189, doi: [10.1086/506375](https://doi.org/10.1086/506375)
- 1102 Yusef-Zadeh, F., Bushouse, H., Wardle, M., et al. 2009,
1103 ApJ, 706, 348, doi: [10.1088/0004-637X/706/1/348](https://doi.org/10.1088/0004-637X/706/1/348)
- 1104 Zhao, J.-H., Young, K. H., Herrnstein, R. M., et al. 2003,
1105 ApJL, 586, L29, doi: [10.1086/374581](https://doi.org/10.1086/374581)

Additional Publications

Other than the publications already mentioned in Section 1.7, and whose results are the core of this work, there were additional achievements, in terms of publications, obtained during this PhD.

The first one is Gutiérrez et al. (2020) (already mentioned in Section 1.3.3.3 and reproduced in the following pages), from which the doctoral candidate was a coauthor. The Article explains an unprecedented NIR flare from Sgr A* in May 2019 as the result of particle acceleration to nonthermal energies in the innermost parts of the accretion flow. It was published in the *The Astrophysical Journal Letters* in March 2020. The results of this work are not part of this thesis: it is only mentioned as part of the literature in Section 1.3.3.3 and in this Section for the sake of completeness.

A contribution with Dr. Raniere de Menezes, who recently completed his PhD at this Institute and presented these results in his thesis, was also an accomplishment of the PhD. In this work (de Menezes et al., 2019) the gamma-ray emission of every known globular cluster in the Milky Way was estimated with *Fermi*-LAT data. This emission is attributed to their populations of millisecond pulsars, which are efficient gamma-ray emitters, and can be used as a tool to explore the dynamical processes leading to binary system formation in these environments. Although this work is not immediately related to the subject of this thesis, the observational characteristics of the gamma-ray emission of millisecond pulsars were used in Section 4.1.1 to rule out the possibility that the observed emission of 4FGL J1745.6–2859 is from one of these objects (or population) in the line of sight. This work was published in the *Monthly Notices of the Royal Astronomical Society* in March 2019.




Finally, as a member of the *Fermi*-LAT Collaboration, the doctoral candidate made a minor contribution in Ajello et al. (2020). This work is also not directly related to the

major theme of this thesis. It is a catalog of AGNs detected by *Fermi*-LAT, published in *The Astrophysical Journal*, in April 2020. The candidate contribution was part of a collaborative effort to identify the synchrotron peak in the SED of sources candidates to be part of this catalog. The identification was performed visually as a first step for a following stricter fitting of the fitting.

In the following pages, we reproduce the published version of an Article lead by M.Sc. Eduardo Gutiérrez, and with this PhD candidate as a coauthor, which was published in *The Astrophysical Journal Letters* in March 2020.



A Nonthermal Bomb Explains the Near-infrared Superflare of Sgr A*

Eduardo M. Gutiérrez¹ , Rodrigo Nemmen² , and Fabio Cafardo² 

¹ Instituto Argentino de Radioastronomía (IAR, CCT La Plata, CONICET/CIC), C.C.5, (1984) Villa Elisa, Buenos Aires, Argentina; emgutierrez@iar.unlp.edu.ar

² Universidade de São Paulo, Instituto de Astronomia, Geofísica e Ciências Atmosféricas, Departamento de Astronomia, São Paulo, SP 05508-090, Brazil
Received 2019 December 20; revised 2020 February 22; accepted 2020 February 24; published 2020 March 12

Abstract

The Galactic center supermassive black hole, Sgr A*, has experienced a strong, unprecedented flare in 2019 May when its near-infrared luminosity reached much brighter levels than ever measured. We argue that an explosive event of particle acceleration to nonthermal energies in the innermost parts of the accretion flow—a nonthermal bomb—explains the near-infrared light curve. We discuss potential mechanisms that could explain this event such as magnetic reconnection and relativistic turbulence acceleration. Multiwavelength monitoring of such superflares in radio, infrared, and X-rays should allow a concrete test of the nonthermal bomb model and put better constraints on the mechanism that triggered the bomb.

Unified Astronomy Thesaurus concepts: Galactic center (565); Black hole physics (159); Non-thermal radiation sources (1119); Accretion (14)

1. Introduction

At the center of the Milky Way lies Sagittarius A* (Sgr A*), a supermassive black hole (SMBH) with a mass of $M = 4 \times 10^6 M_\odot$ located at a distance of 8.2 kpc (Abuter et al. 2019). Given its proximity, Sgr A* presents one of the best laboratories for studying the physics of black hole (BH) accretion flows (Falcke & Markoff 2013). Sgr A* has been detected in most of the electromagnetic spectrum (e.g., Dibi et al. 2014). The extremely low accretion rate and low luminosity observed in its quiescent state ($L_{\text{bol}} \sim 10^{36} \text{ erg s}^{-1} \sim 2 \times 10^{-9} L_{\text{Edd}}$ where L_{Edd} is the Eddington luminosity) implies that the accretion flow is in a radiatively inefficient accretion flow (RIAF) state (e.g., Yuan & Narayan 2014).

On top of the quiescent emission, Sgr A* also exhibits frequent flares in X-rays (e.g., Neilsen et al. 2013; Ponti et al. 2015) and near-infrared (NIR; e.g., Genzel et al. 2003; Boyce et al. 2018). About one X-ray flare is seen per day with a typical duration of a few tens of minutes (Neilsen et al. 2013). The brightest observed X-rays flares are ~ 100 times above the quiescent level (e.g., Nowak et al. 2012). The NIR flares are even more frequent. X-ray flares usually follow the NIR ones after a few tens of minutes, but there are multiple NIR flares without an X-ray counterpart (e.g., Eckart et al. 2006; Yusef-Zadeh et al. 2012; Ponti et al. 2017; but see Fazio et al. 2018). Flares are also observed in millimeter and submillimeter wavelengths (e.g., Yusef-Zadeh et al. 2006; Stone et al. 2016). They last from hours to days with amplitudes of $\sim 25\%$ of the quiescent level (Yusef-Zadeh et al. 2008; Fazio et al. 2018).

In 2019 May, Do et al. (2019) observed an unprecedented NIR flare from Sgr A*—hereafter the “superflare”—with the Keck telescope. The peak flux exceeded the maximum historical value by a factor of two and the light curve (LC) afterward showed a factor of 75 drop in flux over a 2 hr time span. Do et al. (2019) suggested that an increase in the SMBH accretion rate \dot{M} could be responsible for the superflare, possibly due to additional gas deposited by the passage of the G2 object in 2014 or a windy star such as S0-2 in 2018. Nevertheless, Ressler et al. (2018) argued that the effect of S0-2 on the RIAF structure should be negligible. This, combined with the fact that the S-star cluster has no known stars more

massive than S0-2 close to Sgr A* spells trouble for the “windy star” scenario.

Here, we propose an entirely different scenario for the superflare that does not rely on an \dot{M} -increase: an explosive event of particle acceleration to nonthermal energies in the innermost parts of the accretion flow—a nonthermal bomb. This model explains quantitatively the NIR LC and makes testable predictions at other wavelengths.

2. Model

Our model for the emission involves an RIAF with populations of thermal and nonthermal electrons, following the height-integrated approach of Yuan et al. (2003). For simplicity, we assume that the dynamical structure of the flow (i.e., ρ , v , T) does not vary with time, but we consider the possibility that an unspecified acceleration mechanism may change the number of particles following a nonthermal energy distribution.

We take into account the presence of outflows by allowing the accretion rate to decrease with radius as $\dot{M}(r) = \dot{M}_{\text{max}}(r/r_{\text{max}})^s$ (Blandford & Begelman 1999), with $s = 0.25$. We are only interested in the inner parts of the flow, so we only consider the accretion flow up to $r_{\text{max}} = 10^3 r_S$ where we set $\dot{M}_{\text{out}} \approx 10^{-7} M_\odot \text{ yr}^{-1}$. The other parameters are the fraction of turbulent energy directly transferred to electrons $\delta = 0.33$, the viscosity parameter $\alpha = 0.1$, and the gas pressure to magnetic pressure ratio $\beta = 9$.

2.1. Quiescent State

To reproduce the quiescent state of the spectral energy distribution (SED), we assume that in each shell of the RIAF a fraction $\eta_q = 0.4\%$ of the thermal energy density of electrons is in a nonthermal population with a broken power-law distribution:

$$N_q(\gamma; r) = \begin{cases} K_q(r) \gamma^{-p}, & \text{if } \gamma_{\text{min}} \leq \gamma \leq \gamma_c, \\ K_q(r)(p-1)\gamma_c \gamma^{-(p+1)}, & \text{if } \gamma_c \leq \gamma \leq \gamma_{\text{max}}, \end{cases} \quad (1)$$

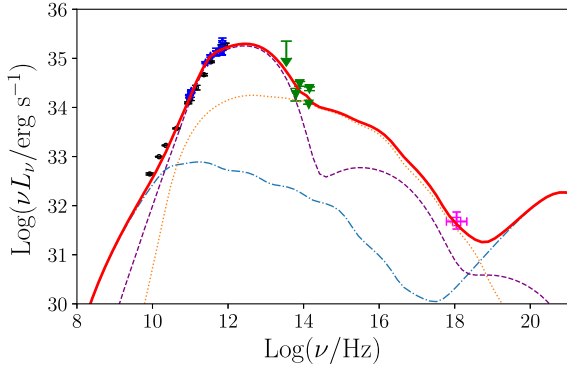


Figure 1. SED of Sgr A* in the quiescent state. The dotted line is the emission of nonthermal electrons from the inner parts of the flow ($r < 15r_S$). The dashed line is the thermal synchrotron and inverse Compton emission. The dotted-dashed line is the emission from the outer parts of the flow ($r > 15r_S$), including thermal bremsstrahlung and nonthermal synchrotron. The solid line is the total emission.

where N_q is the number density of electrons in the quiescent state, γ is the electron Lorentz factor, p is the spectral index at injection, γ_c is the “cooling break” Lorentz factor at which the accretion time is equal to the cooling time, $t_{\text{acc}} = t_{\text{cool}}(\gamma_c)$ (cf. Section 4), and γ_{min} and γ_{max} denote the minimum and maximum Lorentz factors, respectively. We assume that thermal electrons radiate locally through synchrotron, bremsstrahlung, and inverse Compton processes. For nonthermal electrons, we only consider synchrotron emission and adopt $p = 3.6$.

Figure 1 shows the quiescent state SED for the parameters given above. The observations are from Liu et al. (2016) (radio, dark circles), Shcherbakov et al. (2012) (radio, blue dots), Schödel et al. (2011) (IR, green triangles), and Roberts et al. (2017) (X-rays, magenta square). The submillimeter bump is due to thermal synchrotron, and the radio and IR excess are nonthermal synchrotron radiation.

2.2. Flare

Our model for flaring emission assumes that an unspecified process converts a fraction of electrons from the Maxwellian distribution to a nonthermal one during a short burst—a “nonthermal bomb.” In Section 4 we discuss about the possible physical mechanisms that might have produced such an event.

We consider that the burst occurs over an extended region ranging from radius r_{in} to r_{out} . The injection function of nonthermal particles during a burst is

$$\dot{N}_b(\gamma, r; t) = \dot{N}_b(\gamma, r)\delta(t), \quad (2)$$

where $\dot{N}_b(\gamma, r) = K_b(r)\gamma^{-p_b}$, and $K_b(r)$ is determined imposing that at each shell a fraction $\eta_b > \eta_q$ of the thermal energy goes to nonthermal particles. We follow the population while it is accreted onto the event horizon and compute the time evolution of the synchrotron emission. The transport equation that governs the evolution of this population is

$$\frac{\partial N_b(\gamma, r; t)}{\partial t} + \frac{1}{r^2} \frac{\partial}{\partial r} [r^2 v(r) N_b(\gamma, r; t)] + \frac{\partial}{\partial \gamma} \left[\left(\frac{d\gamma}{dt} \right)_{\text{syn}} N_b(\gamma, r; t) \right] = \dot{N}_b(\gamma, r)\delta(t), \quad (3)$$

where $d\gamma/dt(\gamma, r)$ is the rate of energy losses by synchrotron emission and $v(r)$ is the radial velocity of the flow. We solve Equation (3) by the method of characteristics. There are five free parameters in the flare model: η_b , the spectral index p_b , r_{in} , r_{out} , and t_0 , which is the time at which the burst occurs.

3. Results

Figure 2 contains the main result of this Letter: we successfully explain the unprecedented bright state of Sgr A* observed in the NIR in 2019 May as an injection burst of nonthermal particles in the RIAF, which subsequently undergo radiative cooling as they get advected onto the BH. The figure shows three models with different initial sizes of the burst region that reproduce well the decay in the NIR emission. The models reproduce the abrupt decrease in the flux in the last 10 minutes of observations. This is interpreted as the accretion of the last nonthermal particles accelerated in the burst—those near r_{out} at $t = 0$.

Our nonthermal bomb model predicts that the duration of the flare—determined by the accretion time—is the same across all wavelengths. The model also predicts that the slope of the LC following the initial burst depends on the wavelength. Both of these features are seen in Figure 3, which shows LCs in three different wavelengths: NIR, 1.3 mm (the Event Horizon Telescope wavelength), and 2–8 keV (the *Chandra* and *XMM-Newton* energy band). The NIR LC is relatively insensitive to the slope of the electron energy distribution function, such that $L_{\text{NIR}} \propto t^{-0.7}$. On the other hand, we find that the radio emission at millimeter wavelengths depends modestly on the power-law index p_b . This dependence can be approximated as $L_{\text{mm}} \propto t^{0.4-0.25p_b}$. The X-ray LC follows $L_X \propto t^{0.4}$ and depends weakly on p_b . Therefore, a campaign of multiwavelength monitoring of Sgr A*’s LC following a superflare in radio, NIR, and X-rays should allow a concrete test of our model.

Figure 3 also demonstrates that there is more than one combination of parameters capable of reproducing the NIR observations. For instance, the effect of the parameters p_b and η_b on the LC is degenerate: a change in any of these parameters affects only the total luminosity at the K_s band but does not modify the slope of the LC. This degeneracy can be broken by monitoring Sgr A* following the outset of the nonthermal bomb at other wavelengths. A change in η_b only, leaving p_b fixed, modifies the total amount of energy in the bomb, and thus the luminosity at all times and wavelengths. This is shown in Figure 3.

4. Discussion

4.1. Acceleration Mechanism

What is the mechanism responsible for triggering the nonthermal bomb in Sgr A*? BH accretion flows are highly turbulent, highly magnetized, relativistic environments (e.g., Porth et al. 2019). Thus, plausible culprits are magnetic reconnection events and/or turbulence acceleration. In fact, magnetic reconnection has been invoked to explain the recurring IR and X-ray flares observed in Sgr A* (e.g., Ball et al. 2018). Shocks are unlikely because while being efficient at dissipating energy, they do not accelerate particles far beyond thermal energies (e.g., Sironi et al. 2015).

Numerical solutions of the Vlasov equation for astrophysical plasmas—i.e., particle-in-cell (PIC) simulations—are showing

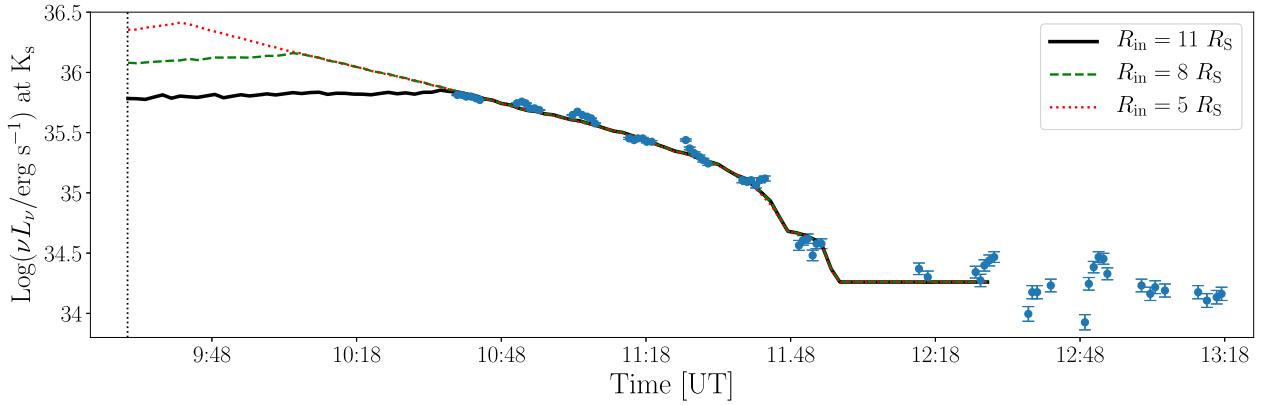


Figure 2. NIR LC of the superflare of Sgr A*. Points correspond to the Keck Telescope observations of Do et al. (2019) and lines indicate different nonthermal bomb models. The model parameters are $\eta_b = 0.25$, $p_b = 2.05$, and $r_{\text{out}} = 16r_s$, for three different values of r_{in} .

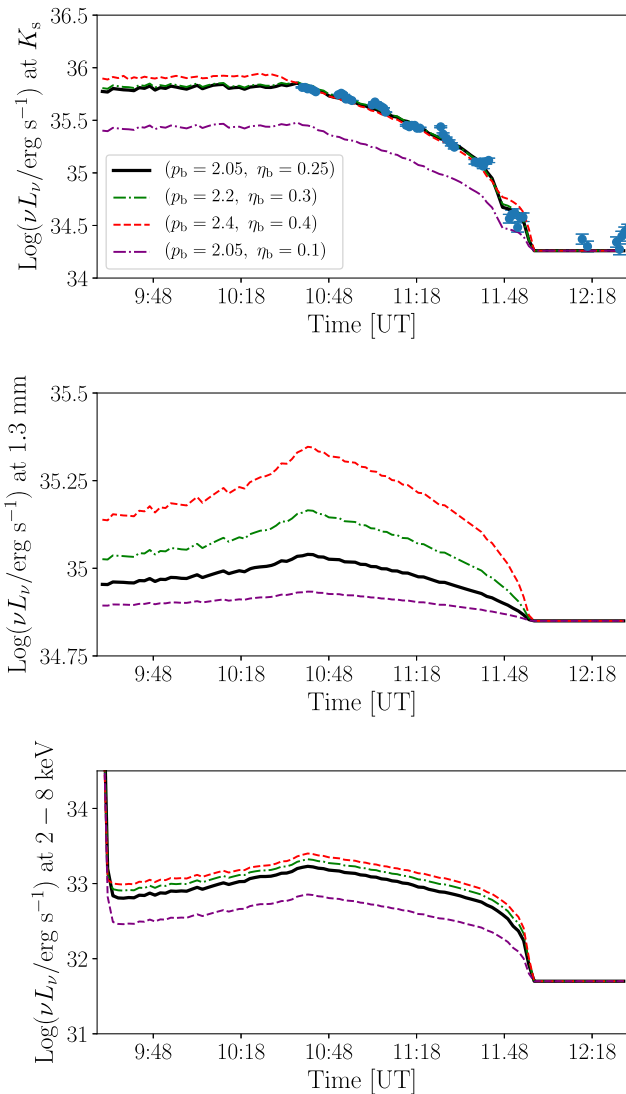


Figure 3. Predicted flare emission at three wavelengths: NIR (upper panel), 1.3 mm (middle panel), and X-rays (2–8 keV; lower panel). Three different values of the spectral index of the nonthermal distribution are displayed plus a model with the same spectral index as our fiducial model but with a lower value of η_b .

that: (i) magnetic reconnection events with high magnetizations³ of $\sigma \gtrsim 10$ lead to particles following power-law energy distributions with an index p ranging from 1 to 2 (e.g.,

Guo et al. 2014; Sironi & Spitkovsky 2014), (ii) the presence of relativistic⁴ turbulence acceleration leads to a power-law index closer to 2 (Comisso & Sironi 2019), and (iii) reconnection can deposit a large fraction (up to about 50%) of the dissipated energy in nonthermal electrons.

We have found that models with p between 2 and 2.5 and $\eta_b \approx 0.25$ can account for the NIR flare evolution. Energy distributions with these parameters are consistent with having been produced within 10 gravitational radii of the event horizon by either a magnetic reconnection event, or a reconnection event followed by relativistic turbulence acceleration.

For instance, according to the PIC simulations of Petropoulou et al. (2016) a lone reconnection event with $\sigma \approx 10$ should produce nonthermal electrons with the required values of p and η_b . Global GRMHD simulations such as those carried out by Ball et al. (2018) demonstrate that σ is correlated with the plasma- β , $\beta \equiv P_{\text{gas}}/P_{\text{magnetic}}$. The values of $\sigma \gtrsim 10$ required to explain the superflare are only attained in configurations with high amounts of magnetic flux near the event horizon—i.e., the magnetically arrested disk (MAD) state—in regions of the accretion flow at which $\beta \sim 0.1$ (Ball et al. 2018). In our fiducial LC model, the total amount of magnetic energy involved in the burst is $\sim 3 \times 10^{40}$ erg s⁻¹. The MAD models of Ball et al. reach at most $\sim 10^{39}$ erg s⁻¹ for $\sigma \approx 10$; therefore, a nonthermal bomb needs unusually large values of B —three times larger than the peak values of B reached in MAD models. This would explain why superflares such as the one observed in 2019 May should be quite rare.

4.2. Timescales

The relevant timescales for our problem are the electron cooling time and the accretion time. Interestingly, during the nonthermal bomb these timescales should be comparable. The synchrotron cooling time for an electron of Lorentz factor γ is

$$t_{\text{syn}} \approx 7.74 \times 10^6 \left(\frac{B}{10 \text{ G}} \right)^{-2} \gamma^{-1} \text{ s}. \quad (4)$$

³ The magnetization parameter is defined as $\sigma \equiv B^2/4\pi\rho c^2$, where B is the magnetic field intensity and ρ is the mass density—all quantities measured in the rest frame of the fluid.

⁴ Hereafter, by relativistic we mean that the mean magnetic energy per particle is larger than the rest-mass energy.

The cooling time corresponds to

$$t_{\text{syn}} \approx \left(\frac{B}{10 \text{ G}} \right)^{-3/2} \text{ hr.} \quad (5)$$

For magnetic fields of the order of 10 G, as appropriate for Sgr A* at $\approx 10r_S$, the cooling time is of the order of one hour. The accretion timescale is defined as $t_{\text{acc}} = R/|v|$. Using the self-similar RIAF solution (Narayan & Yi 1994) we obtain a first-order estimate of this timescale as

$$t_{\text{acc}} \approx 3\alpha r^{3/2} \text{ hr.} \quad (6)$$

For $\alpha = 0.1$ and $r \approx 10$, $t_{\text{acc}} \sim 10$ hr. In the models displayed in Figure 2, the duration of the flare is determined mainly by the accretion time, but the slope also depends on the electron cooling. However, we find that a model only taking into account cooling with electrons remaining at a fixed distance from the hole—i.e., undergoing convective motion—also fits well the data. This shows that cooling can have an effect as important as accretion in our model.

5. Summary

Sgr A* has experienced a strong, unprecedented flare in 2019 May when its near-IR luminosity reached much brighter levels than ever measured. We have explained this superflare with a nonthermal bomb model, where an unspecified process accelerates over a very short time a small fraction of the electrons into a nonthermal distribution; these electrons subsequently cool and are advected onto the BH. Besides explaining the NIR LC, our model predicts that the radio and X-ray fluxes should decay over time in a similar fashion. In particular, the radio LC at millimeter wavelengths is sensitive to the particle energy distribution and dissipation efficiency.

The nonthermal bomb detonated in a region spanning a length $5R_S$ in the innermost parts of the accretion flow, and is likely due to a magnetic reconnection event involving unusually strong magnetic fields and high magnetization, i.e., $\sigma \gtrsim 10$, or such a reconnection event followed by turbulence acceleration.

A multiwavelength monitoring of such superflares in radio, NIR, and X-rays should allow a concrete test of the nonthermal bomb model and better constrain the mechanism that triggered the bomb. Future theoretical research should investigate the observational signatures of relativistic reconnection and relativistic turbulence acceleration using realistic magnetic field configurations appropriate for the SMBH in our Galactic Center, combining the tools of multidimensional GRMHD and PIC simulations.

We thank Reinaldo Santos de Limia for useful discussions, Fan Guo for providing us useful references, and the anonymous

referee for very constructive comments that led to improvements in this Letter. E.G. thanks Gustavo Romero and Florencia Vieyro for useful discussions about relativistic processes in the vicinity of black holes. This work was supported by the Argentine National Scientific and Technical Research Council (CONICET, grant PIP 2014-00338), the National Agency for Scientific and Technological Promotion (PICT 2017-0898), Fundação de Amparo à Pesquisa do Estado de São Paulo (FAPESP, grant 2017/01461-2), and Conselho Nacional de Desenvolvimento Científico e Tecnológico (CNPq, grant 142320/2016-1).

ORCID iDs

Eduardo M. Gutiérrez  <https://orcid.org/0000-0001-7941-801X>

Rodrigo Nemmen  <https://orcid.org/0000-0003-3956-0331>

Fabio Cafardo  <https://orcid.org/0000-0002-7910-2282>

References

- Abuter, R., Amorim, A., Bauboeck, M., et al. 2019, in Proc. XIII Scientific Meeting of the Spanish Astronomical Society, Highlights on Spanish Astrophysics X, ed. B. Montesinos et al. (Berlin: Springer), 609
- Ball, D., Özel, F., Psaltis, D., Chan, C.-K., & Sironi, L. 2018, *ApJ*, **853**, 184
- Blandford, R. D., & Begelman, M. C. 1999, *MNRAS Letters*, **303**, L1
- Boyce, H., Haggard, D., Witzel, G., et al. 2018, arXiv:1812.05764
- Comisso, L., & Sironi, L. 2019, *ApJ*, **886**, 122
- Dibi, S., Markoff, S., Belmont, R., et al. 2014, *MNRAS*, **441**, 1005
- Do, T., Witzel, G., Gautam, A. K., et al. 2019, *ApJL*, **882**, L27
- Eckart, A., Baganoff, F. K., Schödel, R., et al. 2006, *A&A*, **450**, 535
- Falcke, H., & Markoff, S. B. 2013, *CQGra*, **30**, 244003
- Fazio, G. G., Hora, J. L., Witzel, G., et al. 2018, *ApJ*, **864**, 58
- Genzel, R., Schödel, R., Ott, T., et al. 2003, *Natur*, **425**, 934
- Guo, F., Li, H., Daughton, W., & Liu, Y.-H. 2014, *PhRvL*, **113**, 155005
- Liu, H. B., Wright, M. C. H., Zhao, J.-H., et al. 2016, *A&A*, **593**, A107
- Narayan, R., & Yi, I. 1994, *ApJL*, **428**, L13
- Neilsen, J., Nowak, M. A., Gammie, C., et al. 2013, *ApJ*, **774**, 42
- Nowak, M. A., Neilsen, J., Markoff, S. B., et al. 2012, *ApJ*, **759**, 95
- Petropoulou, M., Giannios, D., & Sironi, L. 2016, *MNRAS*, **462**, 3325
- Ponti, G., De Marco, B., Morris, M. R., et al. 2015, *MNRAS*, **454**, 1525
- Ponti, G., George, E., Scaringi, S., et al. 2017, *MNRAS*, **468**, 2447
- Porth, O., Chatterjee, K., Narayan, R., et al. 2019, *ApJS*, **243**, 26
- Ressler, S. M., Quataert, E., & Stone, J. M. 2018, *MNRAS*, **478**, 3544
- Roberts, S. R., Jiang, Y.-F., Wang, Q. D., & Ostriker, J. P. 2017, *MNRAS*, **466**, 1477
- Schödel, R., Morris, M. R., Muzic, K., et al. 2011, *A&A*, **532**, A83
- Shcherbakov, R. V., Penna, R. F., & McKinney, J. C. 2012, *ApJ*, **755**, 133
- Sironi, L., Keshet, U., & Lemoine, M. 2015, *SSRv*, **191**, 519
- Sironi, L., & Spitkovsky, A. 2014, *ApJL*, **783**, L21
- Stone, J. M., Marrone, D. P., Dowell, C. D., et al. 2016, *ApJ*, **825**, 32
- Yuan, F., & Narayan, R. 2014, *ARA&A*, **52**, 529
- Yuan, F., Quataert, E., & Narayan, R. 2003, *ApJ*, **598**, 301
- Yusef-Zadeh, F., Arendt, R., Bushouse, H., et al. 2012, *ApJL*, **758**, L11
- Yusef-Zadeh, F., Roberts, D., Wardle, M., Heinke, C. O., & Bower, G. C. 2006, *ApJ*, **650**, 189
- Yusef-Zadeh, F., Wardle, M., Heinke, C., et al. 2008, *ApJ*, **682**, 361

Appendix C

New sources found in the analysis between 100 MeV and 500 GeV

Here we present the new sources encountered in the RoI with `Fermipy's find_sources` function in the energy range between 100 MeV and 500 GeV (our Universal Model). The best parameters for the power-law used to model their spectra are also shown together with their TS and position.

Source name	Index	Prefactor	Scale	TS	RA	Dec
PS J1719.1-2945	-5.0	2.8×10^{-14}	1000	236	259.80	-29.75
PS J1720.6-2655	-2.1	4.5×10^{-13}	1000	40	260.16	-26.93
PS J1723.8-3347	-2.0	5.8×10^{-13}	1000	31	260.95	-33.79
PS J1729.5-3623	-1.9	4.7×10^{-13}	1000	40	262.39	-36.40
PS J1730.5-2801	-2.0	3.8×10^{-13}	1000	31	262.64	-28.03
PS J1731.6-2903	-1.8	2.9×10^{-13}	1000	34	262.92	-29.05
PS J1733.8-2114	-2.0	2.8×10^{-13}	1000	30	263.47	-21.24
PS J1734.4-3555	-2.2	5.8×10^{-13}	1000	34	263.62	-35.93
PS J1734.6-2328	-2.2	4.9×10^{-13}	1000	37	263.66	-23.48
PS J1735.5-2944	-1.8	3.3×10^{-13}	1000	31	263.88	-29.74
PS J1735.6-2900	-5.0	1.6×10^{-14}	1000	36	263.91	-29.01
PS J1742.7-3150	-2.0	8.0×10^{-13}	1000	50	265.68	-31.85
PS J1744.1-3019	-2.2	2.7×10^{-12}	1000	124	266.03	-30.32
PS J1747.2-2114	-2.3	5.8×10^{-13}	1000	40	266.81	-21.25
PS J1750.4-3355	-2.2	5.6×10^{-13}	1000	40	267.61	-33.93
PS J1752.0-3447	-2.2	4.1×10^{-13}	1000	34	268.02	-34.79
PS J1752.6-2105	-5.0	4.0×10^{-14}	1000	303	268.15	-21.09
PS J1754.4-2612	-2.1	7.6×10^{-13}	1000	32	268.60	-26.21
PS J1754.4-2649	-2.0	5.8×10^{-13}	1000	30	268.60	-26.82
PS J1754.7-3730	-2.2	3.7×10^{-13}	1000	38	268.70	-37.51
PS J1755.3-2553	-2.0	9.3×10^{-13}	1000	49	268.83	-25.90
PS J1756.0-3248	-2.1	4.1×10^{-13}	1000	31	269.02	-32.81
PS J1756.3-2515	-2.3	2.1×10^{-12}	1000	99	269.08	-25.25
PS J1756.8-2413	-1.9	5.4×10^{-13}	1000	36	269.21	-24.22
PS J1758.0-2421	-2.2	1.1×10^{-12}	1000	38	269.52	-24.36
PS J1808.2-3003	-2.2	4.5×10^{-13}	1000	45	272.06	-30.05
PS J1817.4-2516	-2.4	5.7×10^{-13}	1000	50	274.35	-25.27
PS J1818.6-2812	-2.6	5.0×10^{-13}	1000	57	274.65	-28.22
PS J1823.9-2341	-2.4	5.1×10^{-13}	1000	47	275.99	-23.69

Table C.1 - New sources found in the 100 MeV to 500 GeV energy range.

Appendix D

Examples of discontinuous models

Here we show, for the sake of clarity only, a few examples of discontinuous models that we obtained in analyses in which the “minimal fitting” procedure was not used. In Figure D.1 we plot 4 examples of the energy flux models ($E^2 dN/dE$) we obtained for single sources. Each energy range was treated as an isolated analysis. It is possible to see that the models are not continuous in every energy band (we are not showing the statistical uncertainties). These models were not used in our work. We developed the “minimal fitting” methodology to avoid results like these.

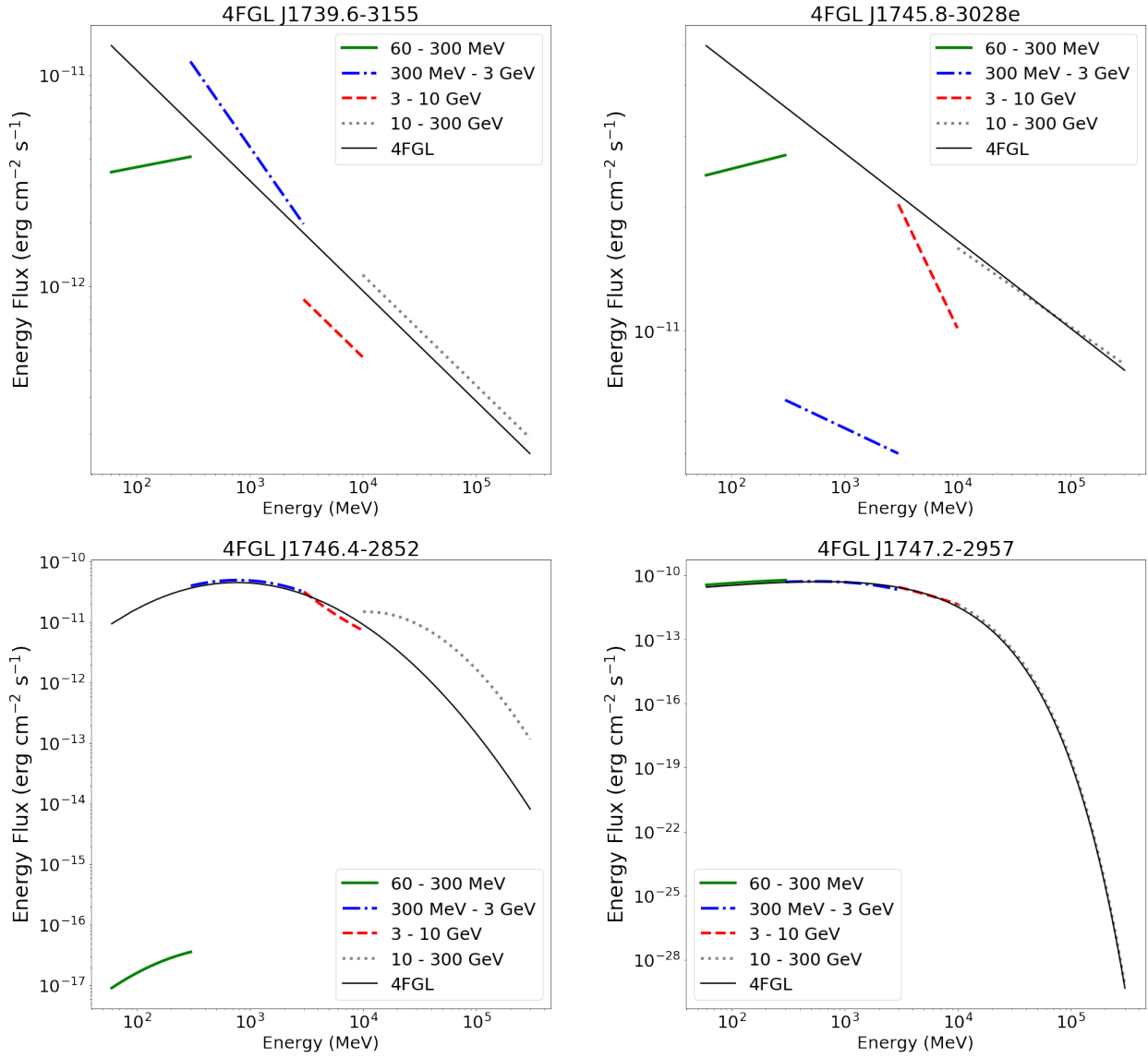


Figure D.1: Examples of energy flux models ($E^2 dN/dE$) we obtained for single sources when we separated the analyses into four independent energy band. These models were not used in our work.

Comparing the results obtained through the minimal fitting method to a more standard approach

Here we present the results of previous analyses performed for the three energy bands (i.e., 300 MeV–3GeV, 3–10 GeV and 10–500 GeV), based on models created from scratch to each one. In other words: models that were not created by splitting the Universal Model into tighter bands with the minimal fitting.

The photon selection for these analyses were very similar with the one used for the Universal Model, but not exactly equal: mainly, we used only ~ 10.5 years of data and, for the two highest energy bands only, we used all *event types* available: $PSF0 + PSF1 + PSF2 + PSF3$, which means all photons. Regardless these (and other minor) differences in the data selection and in the analyses, the results we obtained were coincident within 1σ with the what we achieve with the reported in the Section 3.

We start with the diagnostic plots. In Figure E.1 we show the residual maps for the models created from scratch for these 3 energy bands. In Figure E.2 we show the TS maps with the central source included in the models. And, in Figure E.3 we show the TS maps without the source in the models. These Figures were created following the same procedure described in Section 2.3.3 for the creation of Figures 2.4, 2.6 and 2.8, respectively.

The gamma-ray fluxes measured in these previous analyses are presented in Table E.1. All of them are compatible within 1σ with the results presented in Table 3.1, that we obtained through the splitting of the Universal Model.

We can conclude, then, that the results we obtained with the offspring of the Universal Model are consistent even though their diagnostic plots are not flawless.

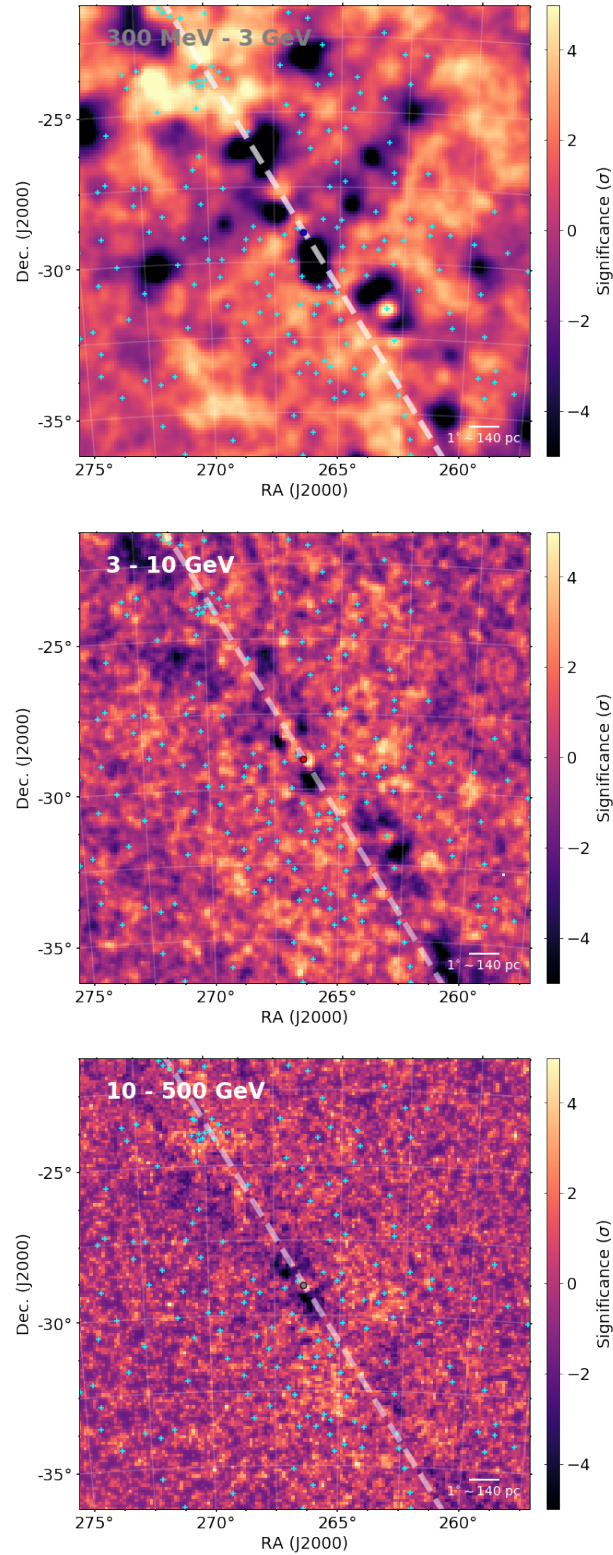


Figure E.1: Residuals maps for previous analyses in the 3 highest energy ranges. The colors show the significance of the residual. The point at the center of each panel corresponds to the source position obtained in each energy range. 4FGL point sources are displayed as cyan crosses. The white dashed lines indicate the direction of the Galactic plane.

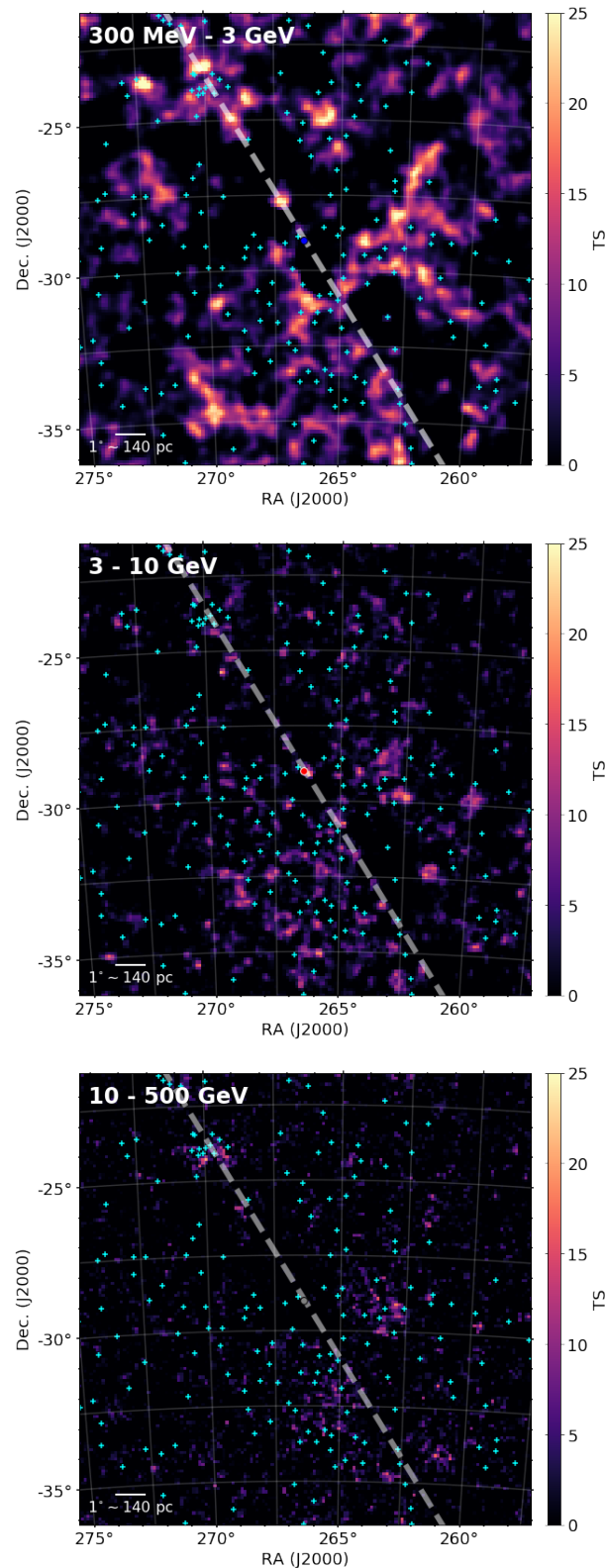


Figure E.2: TS maps of the RoI for previous analyses in the 3 highest energy ranges. The circles at the center of the panels correspond to the central point source position obtained in each energy range. 4FGL point sources are displayed as cyan crosses. The white dashed lines indicate the direction of the Galactic plane.

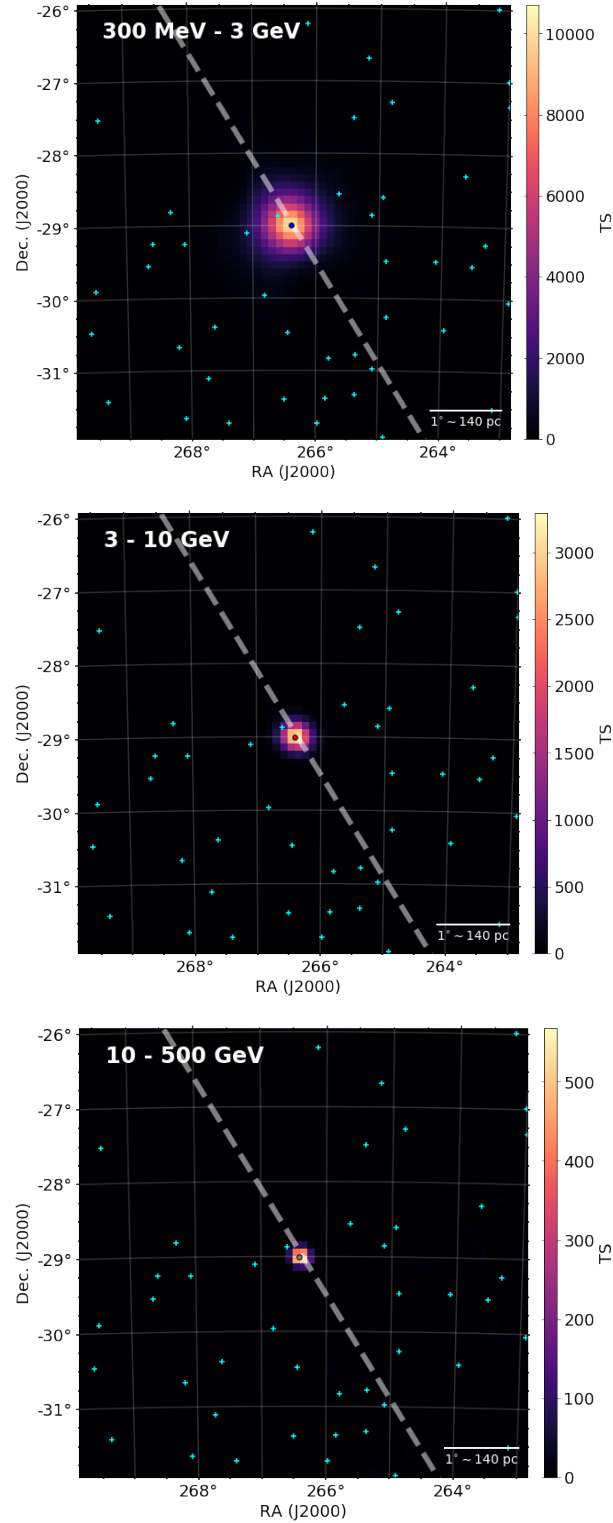


Figure E.3: TS maps of the inner $8^\circ \times 8^\circ$ of the RoI evidencing the contribution of the central point source. They were constructed after excluding 4FGL J1745.6–2859 from the models, as explained in Section 2.3.3. The point at the center of each panel corresponds to the source position obtained in each energy range. The other 4FGL point sources are shown as cyan crosses. The white dashed lines indicate the direction of the Galactic plane.

Table E.1 - Results from likelihood modeling of the central point source for previous analyses in the 3 highest energy bands. The photon and energy flux uncertainties are statistical only. All the results are compatible within 1σ with the results presented in Table 3.1.

Energy range (GeV)	TS ¹	Photon flux (cm ⁻² s ⁻¹)	Energy flux (erg cm ⁻² s ⁻¹)	Centroid ² (°)	Positional Uncertainty ³	
					statistical (°)	total (°)
0.3 - 3	10132	$(1.67 \pm 0.03) \times 10^{-7}$	$(2.04 \pm 0.03) \times 10^{-10}$	266.403, -28.995	0.005	0.009
3 - 10	3398	$(8.86 \pm 0.24) \times 10^{-9}$	$(6.66 \pm 0.18) \times 10^{-11}$	266.404, -29.002	0.005	0.009
10 - 500	720	$(1.14 \pm 0.07) \times 10^{-9}$	$(4.22 \pm 0.42) \times 10^{-11}$	266.411, -29.006	0.006	0.010

¹ $\sqrt{TS} \approx$ detection significance of the source in each energy range

² RA and Dec. corresponding to the emission centroid in degrees

³ 68% positional uncertainty

Appendix F

New sources found in the analysis between 60 and 300 MeV

Five new sources were encountered in the RoI with `Fermipy's find_sources` function in the energy range between 60 and 300 MeV. They are listed in this section. The best parameters for the power-law used to model their spectra are also shown together with their TS and position.

Table F.1 - New sources found in the 60 to 300 MeV energy range.

Source name	Index	Prefactor	Scale	TS	RA	Dec
PS J1639.5-2448	-1.7	4.4×10^{-12}	1000	37	249.90	-24.81
PS J1750.6-2723	-2.0	4.8×10^{-12}	1000	27	267.65	-27.40
PS J1753.7-2127	-0.9	2.9×10^{-12}	1000	57	268.44	-21.47
PS J1820.5-2113	-2.0	4.3×10^{-12}	1000	61	275.14	-21.22
PS J1835.0-1804	-5.0	8.8×10^{-15}	1000	183	278.76	-18.07

Comparing different *event type* selection for the low energy model

Here we present the results we obtained with preliminary analyses for the 60–300 MeV energy range. We were interested in testing the impact of different *event types* selection. The *event types* we used in the preliminary tests were:

- *PSF1 + PSF2 + PSF3*: which is the selection we decided to use in the main analysis
- *PSF2 + PSF3*: which means the 50% photons with better PSF in the data
- *front*: that consider only the events that converted in the *Fermi*-LAT’s “front”, a part of the instrument that provides counts with better spatial resolution, as explained in section 1.5.1

Since these were just tests, we tried to be as quick as possible. So we performed only a few rounds of fitting, among other differences in the modeling process presented in Section 2 (for instance, we did not use `Fermipy`’s function `find_sources` and did not change the log-parabola spectral model to a power-law).

In Figure G.1 we show the position of the source in the three tests and, also, the position we are reporting in this work (Section 3.2). The results are very similar among every photon selection: the point sources are all coincident within their 68% positional uncertainty (statistical and systematic uncertainties).

The tests results are all clustered in the same region, about $\sim 0.05^\circ$ away from the result we obtained later with a complete fitting (green line). The fact that the result of the test with *event type* *PSF1 + PSF2 + PSF3* is also clustered with the others tests indicates

that the offset of our final result was not caused by the photon selection but, instead, is a result of the better modeling.

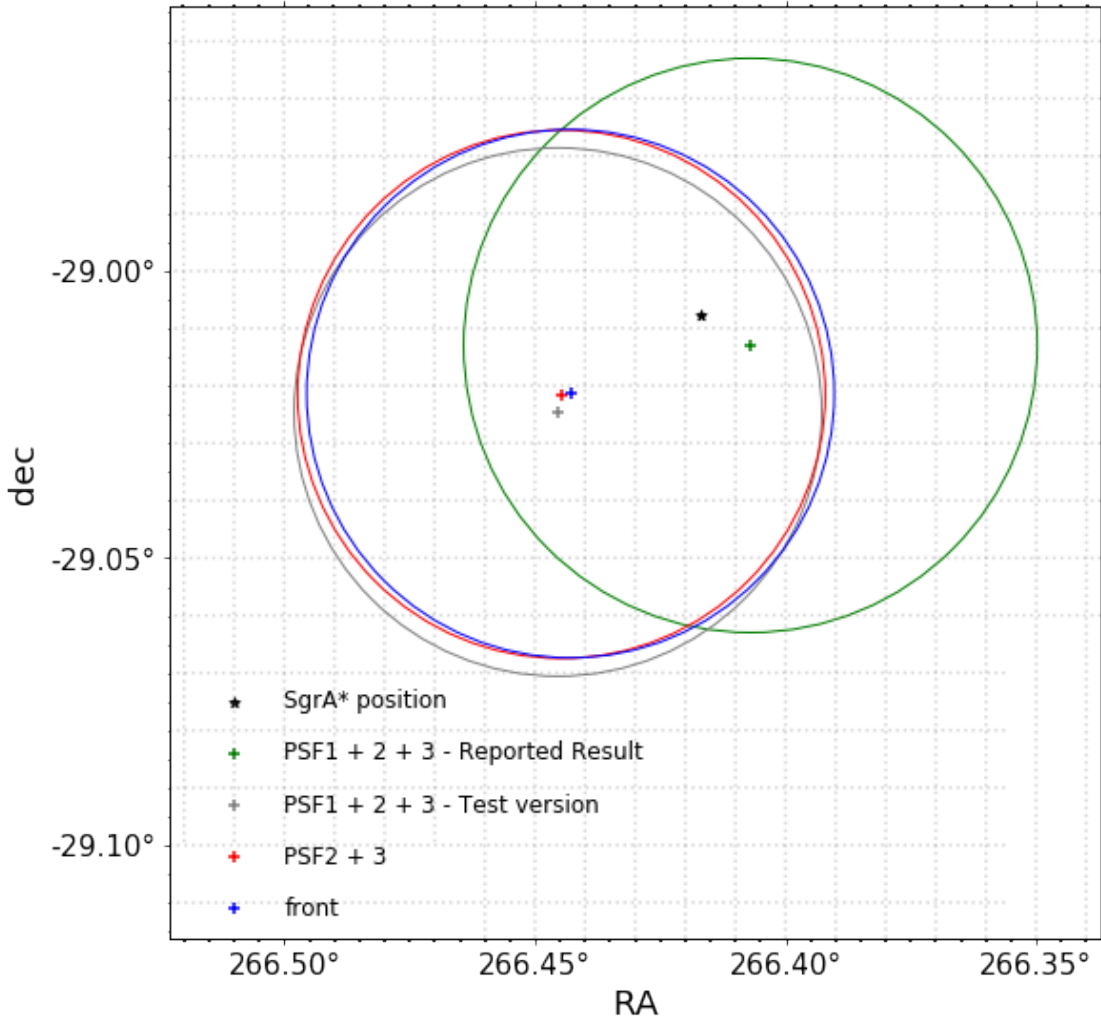


Figure G.1: The position of the central source in the 60–3000 MeV energy band for as reported in this work (green) and for the *event type* tests (gray, red and blue). The circles represent the 68% positional uncertainty. The radio position of Sgr A* is indicated by the black cross.

In Table G.1 we report the results we obtained for the central source’s photon and energy fluxes in these tests. All the results for the $PSF1 + PSF2 + PSF3$ test are compatible within 1σ with the final results presented in Table 3.1 for the 60–300 MeV. For the other tests, only the photon flux is compatible within 1σ , while the energy flux is compatible within 2σ with the results presented in Table 3.1 for the same energy range. We are reporting only the statistical uncertainties, so they are likely underestimated.

Table G.1 - Results from the *event types* testing for the 60–300 MeV energy interval. The photon and energy flux uncertainties are statistical only. All the results for the *PSF1 + PSF2 + PSF3* test are compatible within 1σ with the results presented in Table 3.1. For the other tests, only the photon flux is compatible within 1σ , while the energy flux is compatible within 2σ with the results presented in Table 3.1 for the same energy range.

<i>Event type</i>	TS ¹	Photon flux (cm ⁻² s ⁻¹)	Energy flux (erg cm ⁻² s ⁻¹)
<i>PSF1 + PSF2 + PSF3</i>	2525	$(5.25 \pm 0.13) \times 10^{-7}$	$(1.09 \pm 0.02) \times 10^{-10}$
<i>PSF2 + PSF3</i>	2250	$(5.50 \pm 0.17) \times 10^{-7}$	$(1.14 \pm 0.04) \times 10^{-10}$
<i>front</i>	2302	$(5.62 \pm 0.21) \times 10^{-7}$	$(1.17 \pm 0.04) \times 10^{-10}$

¹ $\sqrt{TS} \approx$ detection significance of the source in each energy range

Appendix H

Residuals distribution for the Universal Model offspring

In Figure H.1 we show the resulting residuals distribution after fitting the three offspring of the Universal Models.

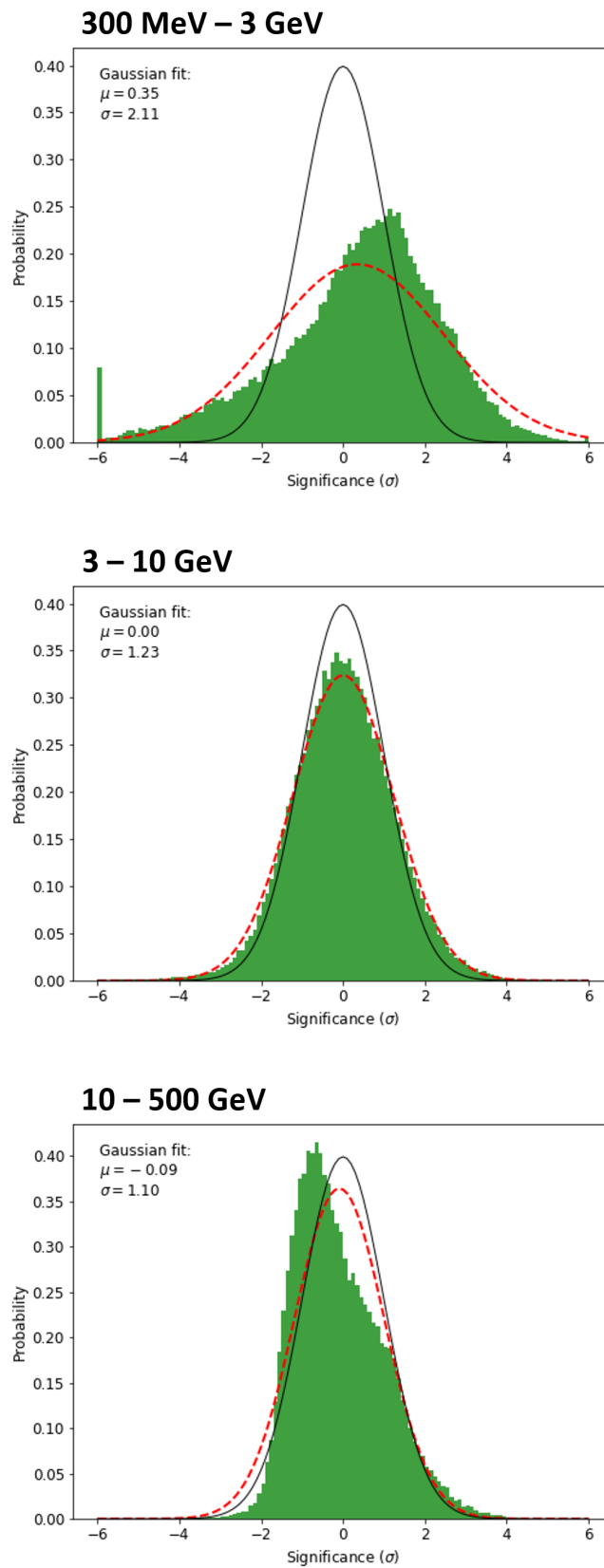


Figure H.1: Resulting residuals histograms obtained after fitting the three offspring of the Universal Model (i.e., top: 300 MeV–3 GeV, middle: 3–10 GeV and bottom: 10–500 GeV). The black lines are a standard normal distribution and the red dashed lines are the distributions for the best-fit Gaussian to the data.

Appendix I

Estimating the systematic uncertainties in the 15 days photon flux LC

Here we perform the same analysis as in Section 2.5.2, but for the photon flux LC of 4FGL J1747.2-2957 in order to estimate the systematic uncertainty in the 15 days LC created with data in the 100 MeV–500 GeV energy range. We will only focus on showing the relevant plots, since the details of the analysis are in the main text.

As a result of this analysis, we obtained a systematic uncertainty of 14.8% for the photon flux 15 days LC.

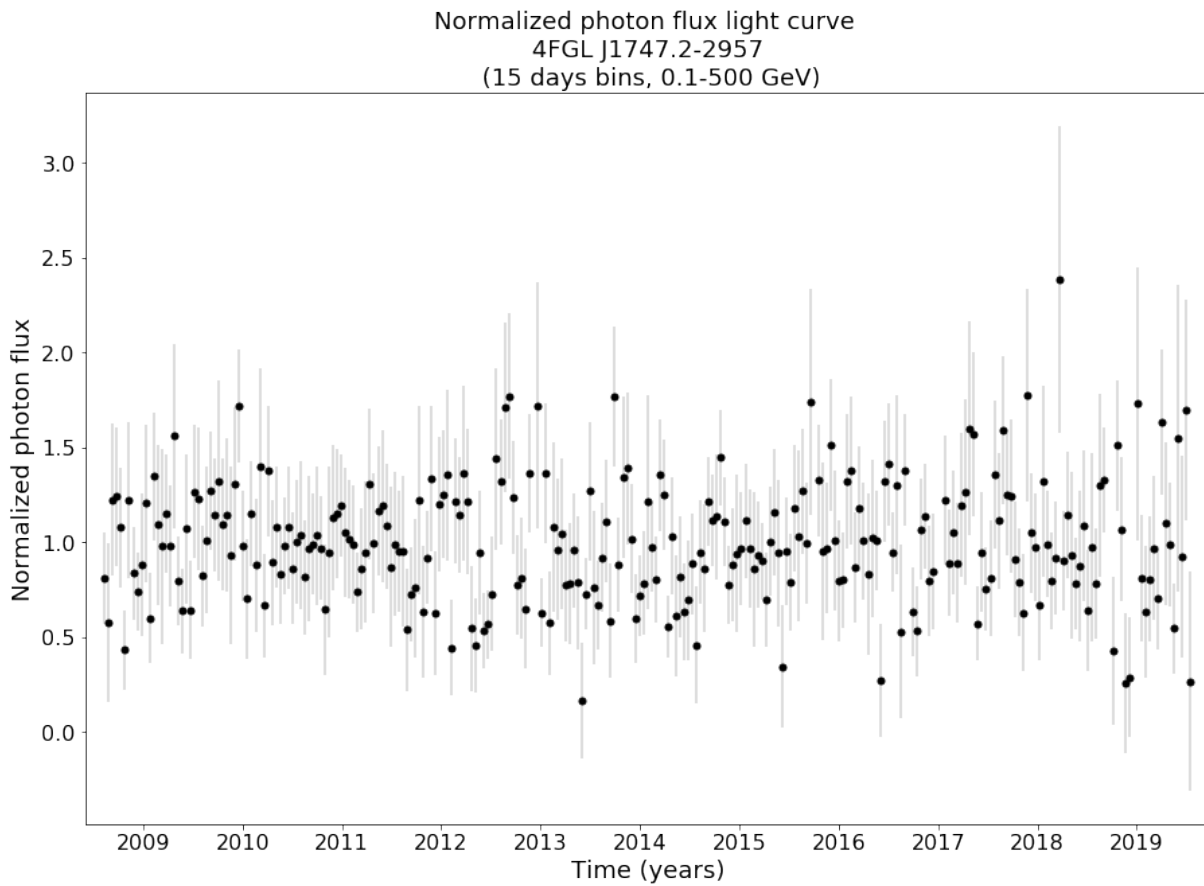


Figure I.1: 15 days average normalized photon flux LC of 4FGL J1747.2-2957 (pulsar PSR J1747-2958). This is a presumably steady sources and its flux variability is used to estimate the systematic uncertainty in the data. This LC was created following the exact same data selection and methods used to create 4FGL J1745.6–2859 LC.

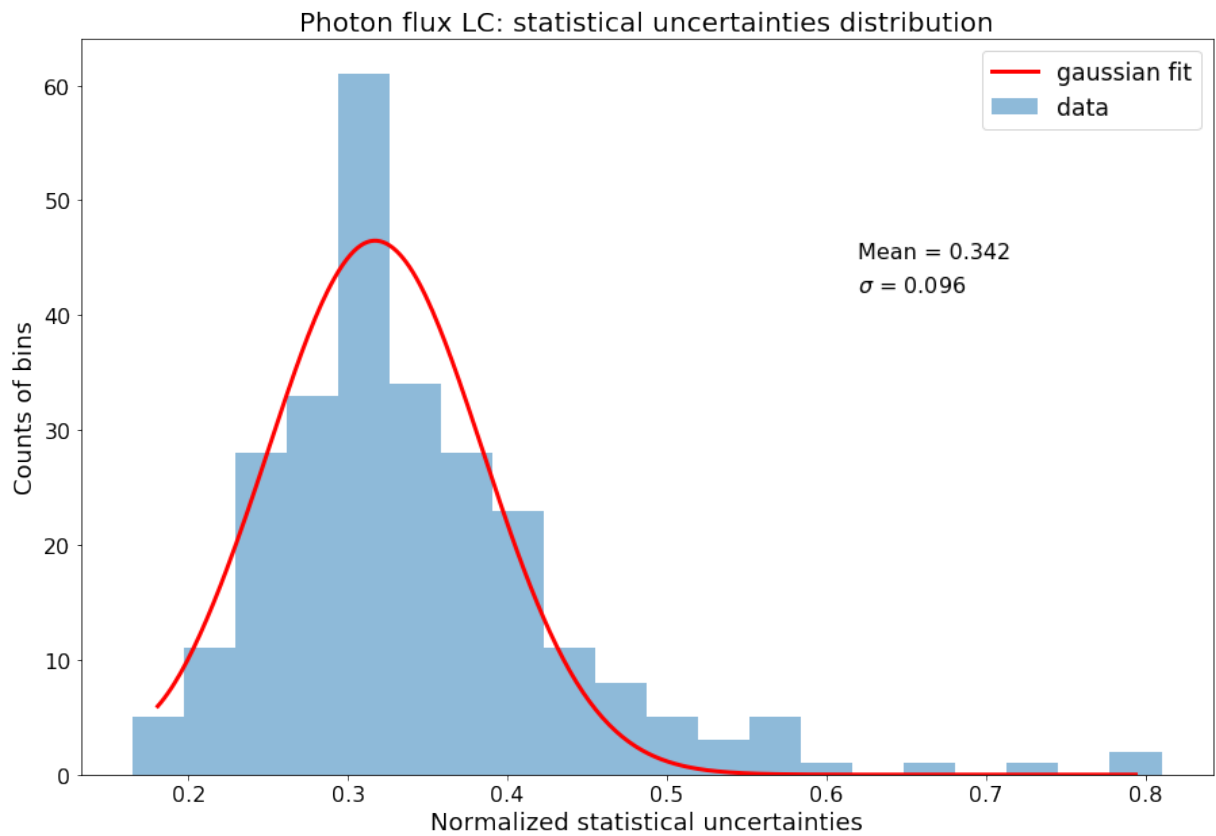


Figure I.2: Histogram of the statistical uncertainties of the 15 days average normalized photon flux LC of 4FGL J1747.2-2957 (Figure I.1). The dotted red line is a normal distribution with the same mean and standard deviation of the statistical uncertainties (the values are shown in the Figure).

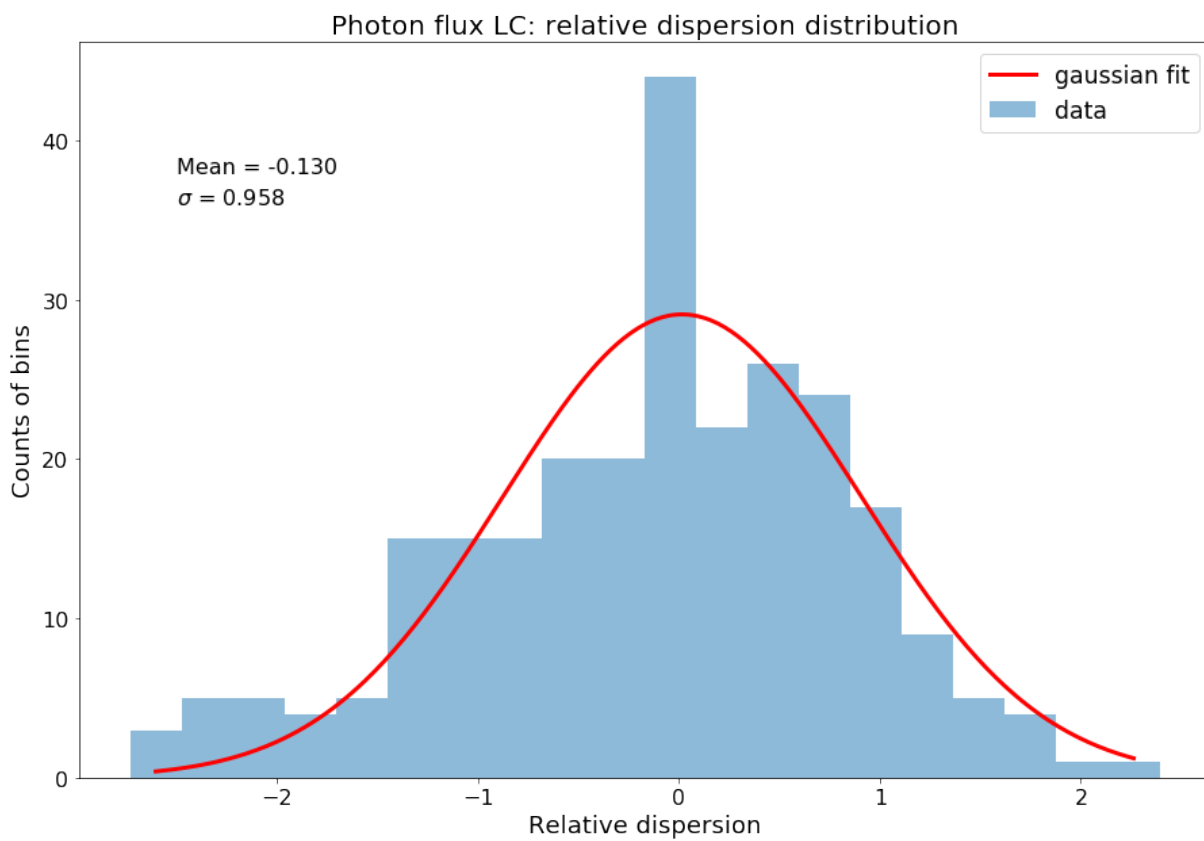


Figure I.3: Histogram of the relative dispersion distribution of the 15 days average normalized photon flux LC of 4FGL J1747.2-2957 (Figure I.1) calculated following Equation 2.13. The mean and standard deviation of this distribution are also shown in the Figure.

Estimating the systematic uncertainties in the LCs

Here we perform the same analysis as in Section 2.5.2, but for the different LCs intervals and energy ranges, in order to estimate the systematic uncertainty in the data. We will only focus on showing the relevant plots, since the details of the analysis are in the main text.

J.1 Systematic uncertainties in the 45 days LC

Below, the systematic uncertainties estimate of the LCs in the 100 MeV–500 GeV energy range and with 45 days bins.

J.1.1 Energy flux

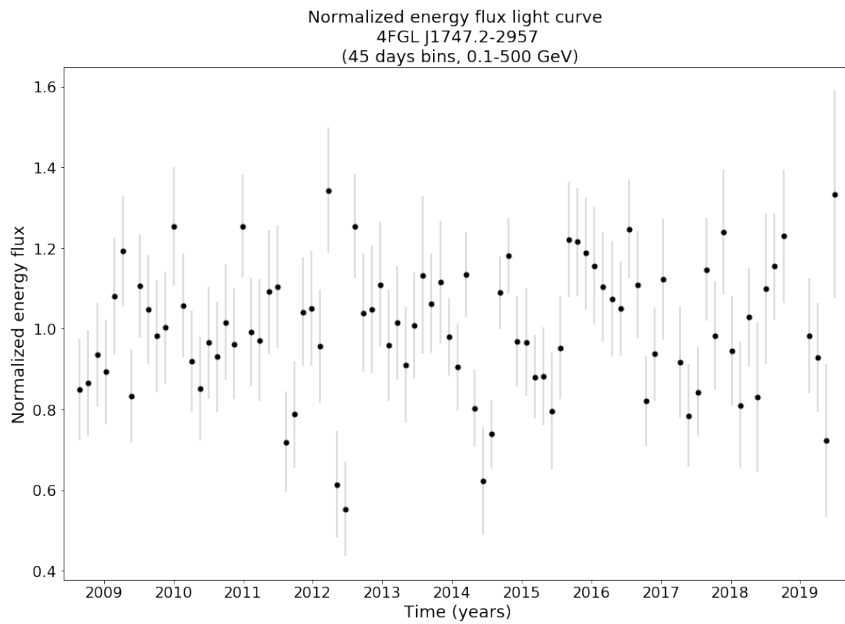


Figure J.1: 15 days average normalized energy flux LC of 4FGL J1747.2-2957 (pulsar PSR J1747-2958) in the 100 MeV–500 GeV energy range.

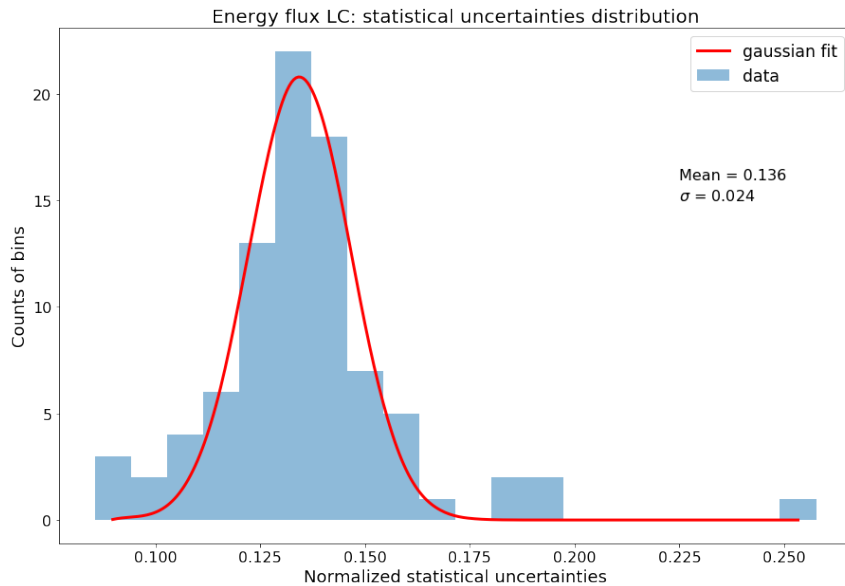


Figure J.2: Histogram of the statistical uncertainties of the 45 days average normalized energy flux LC of 4FGL J1747.2-2957 in the 100 MeV–500 GeV energy range. The red line is a normal distribution with the same mean and standard deviation of the statistical uncertainties (the values are shown in the Figure).

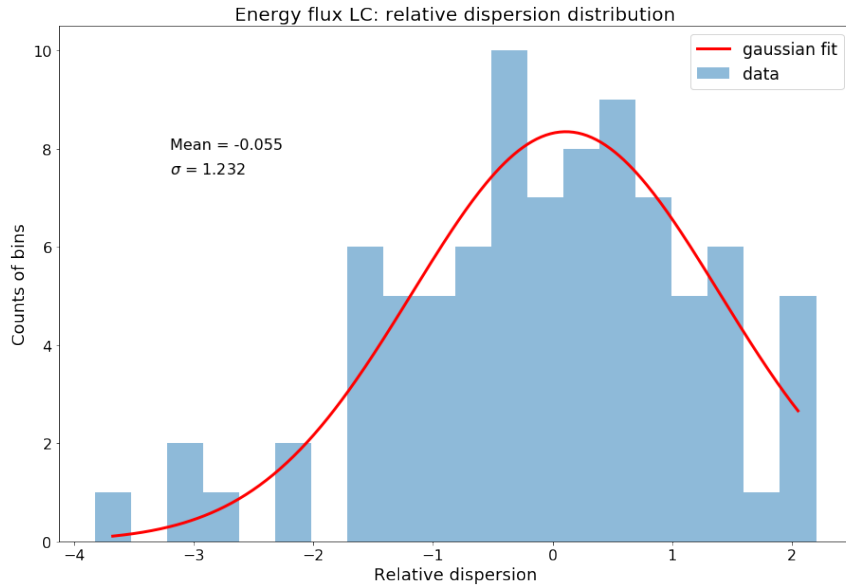


Figure J.3: Histogram of the relative dispersion distribution of the 45 days average normalized energy flux LC of 4FGL J1747.2-2957 in the 100 MeV–500 GeV energy range. The mean and standard deviation of this distribution are also shown in the Figure.

J.1.2 Photon flux

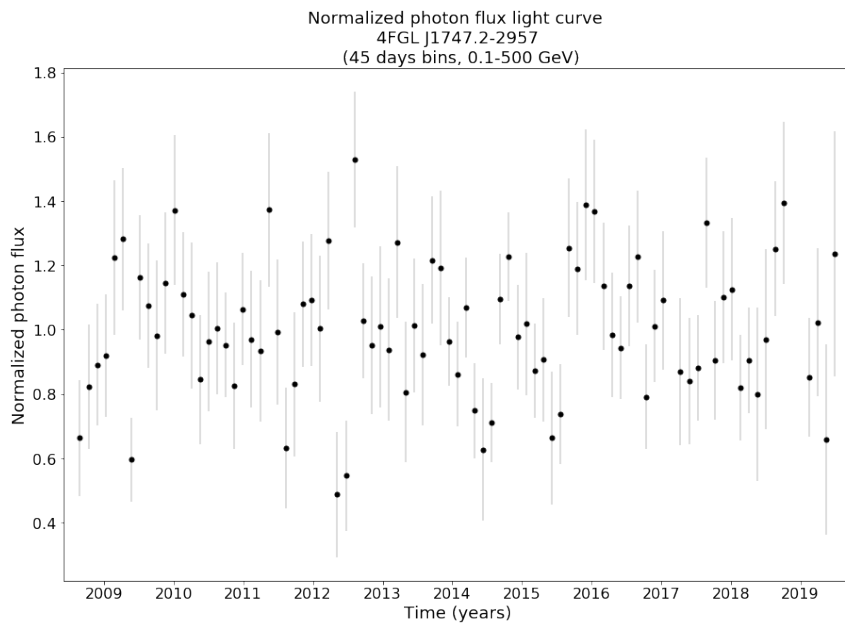


Figure J.4: 15 days average normalized photon flux LC of 4FGL J1747.2-2957 (pulsar PSR J1747-2958) in the 100 MeV–500 GeV energy range.

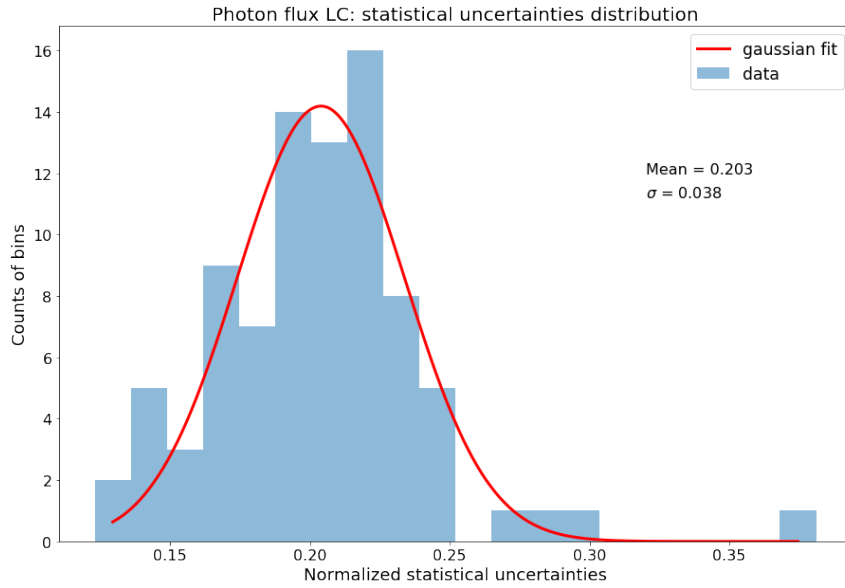


Figure J.5: Histogram of the statistical uncertainties of the 45 days average normalized photon flux LC of 4FGL J1747.2-2957 in the 100 MeV–500 GeV energy range. The red line is a normal distribution with the same mean and standard deviation of the statistical uncertainties (the values are shown in the Figure).

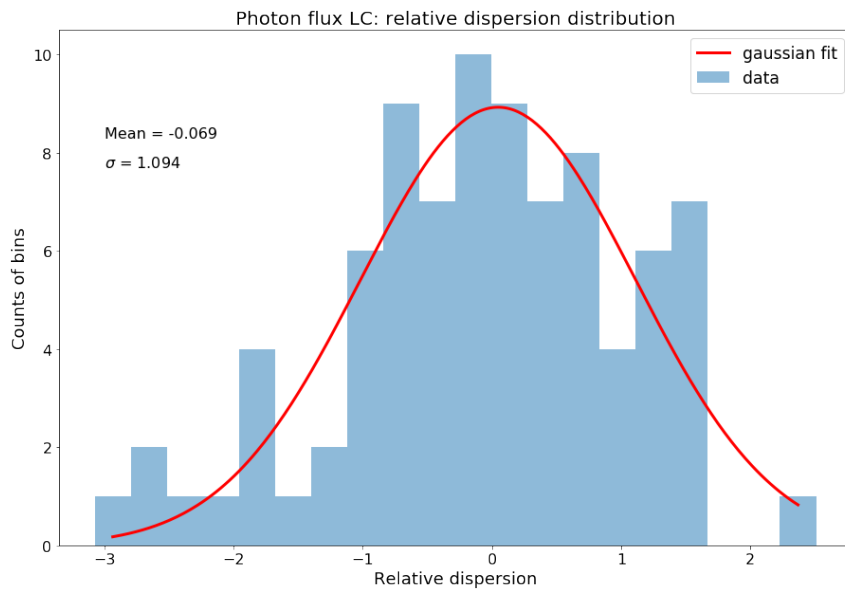


Figure J.6: Histogram of the relative dispersion distribution of the 45 days average normalized photon flux LC of 4FGL J1747.2-2957 in the 100 MeV–500 GeV energy range. The mean and standard deviation of this distribution are also shown in the Figure.

J.2 Systematic uncertainties in the 90 days, 300 MeV–3 GeV LC

Below, the systematic uncertainties estimate of the LCs in the 300 MeV–3 GeV energy range and with 90 days bins.

J.2.1 Energy flux

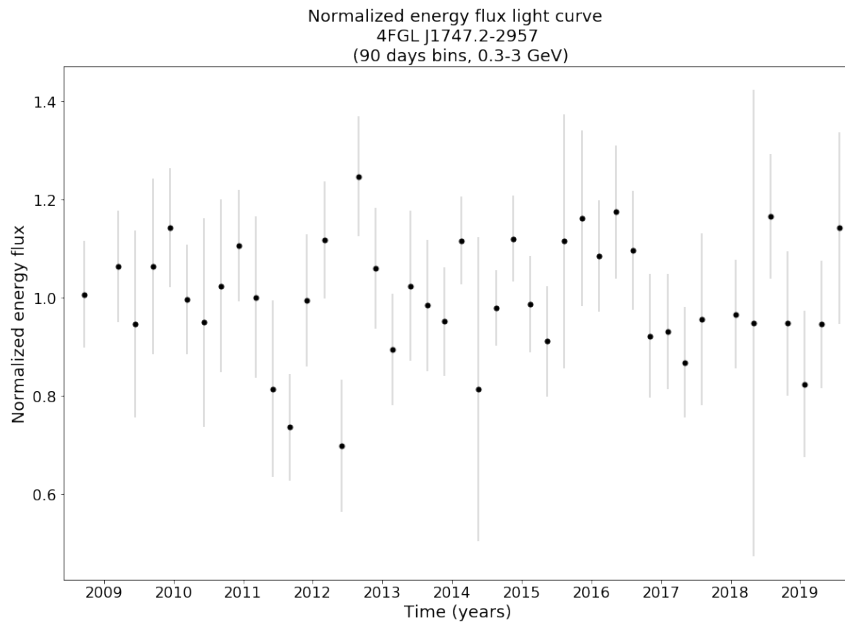


Figure J.7: 90 days average normalized energy flux LC of 4FGL J1747.2-2957 (pulsar PSR J1747-2958) in the 300 MeV–3 GeV energy range.

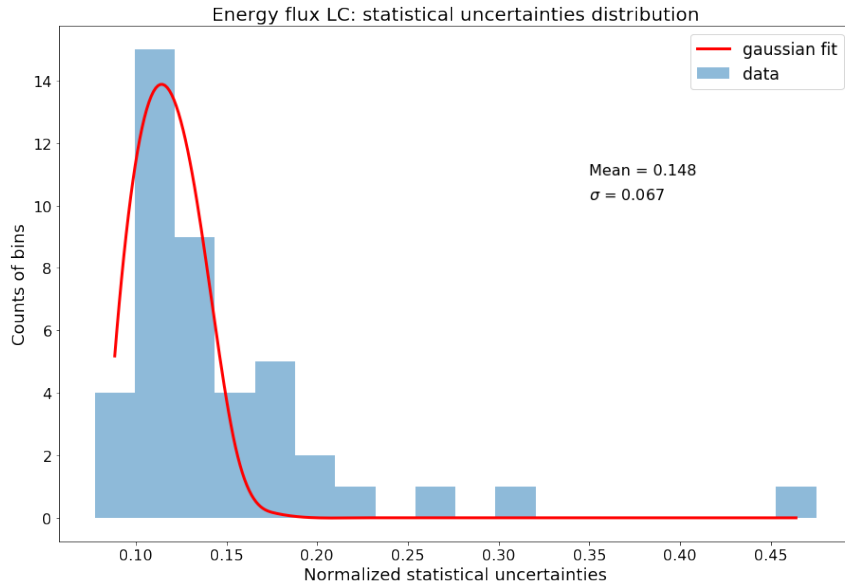


Figure J.8: Histogram of the statistical uncertainties of the 90 days average normalized energy flux LC of 4FGL J1747.2-2957 in the 300 MeV–3 GeV energy range. The red line is a normal distribution with the same mean and standard deviation of the statistical uncertainties (the values are shown in the Figure).

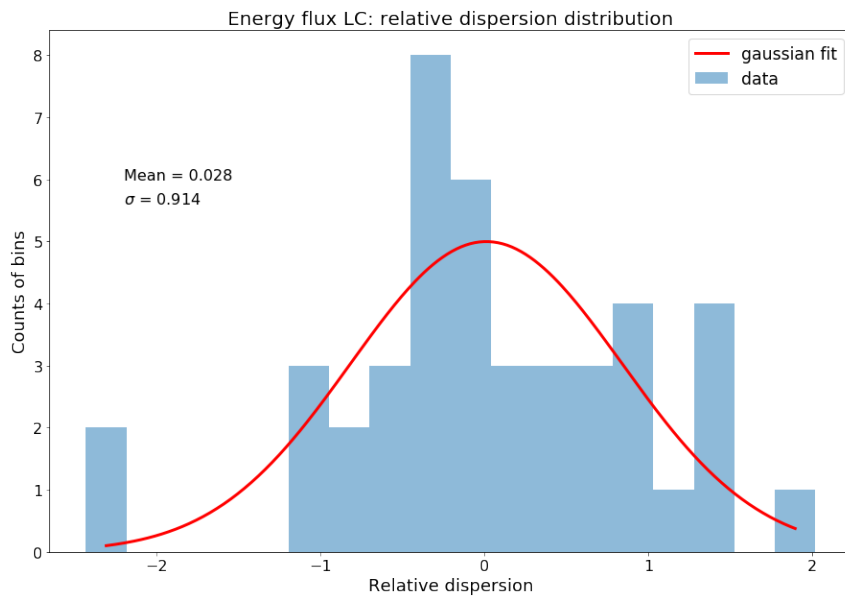


Figure J.9: Histogram of the relative dispersion distribution of the 90 days average normalized energy flux LC of 4FGL J1747.2-2957 in the 300 MeV–3 GeV energy range. The mean and standard deviation of this distribution are also shown in the Figure.

J.2.2 Photon flux

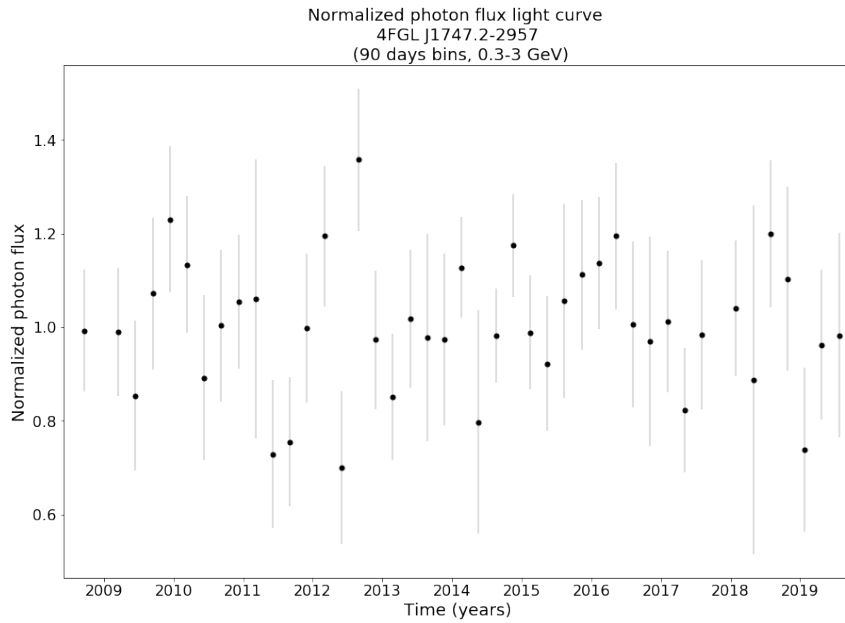


Figure J.10: 90 days average normalized photon flux LC of 4FGL J1747.2-2957 (pulsar PSR J1747-2958) in the 300 MeV–3 GeV energy range.

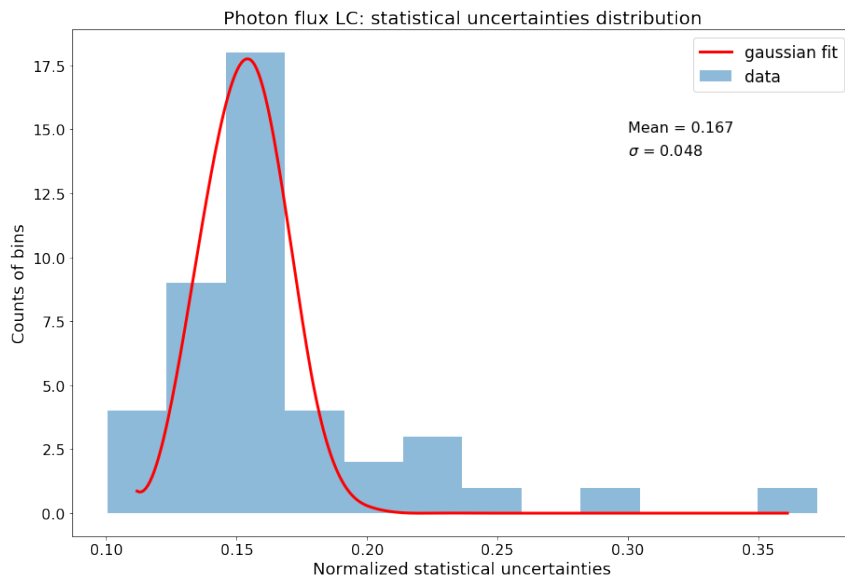


Figure J.11: Histogram of the statistical uncertainties of the 90 days average normalized photon flux LC of 4FGL J1747.2-2957 in the 300 MeV–3 GeV energy range. The red line is a normal distribution with the same mean and standard deviation of the statistical uncertainties (the values are shown in the Figure).

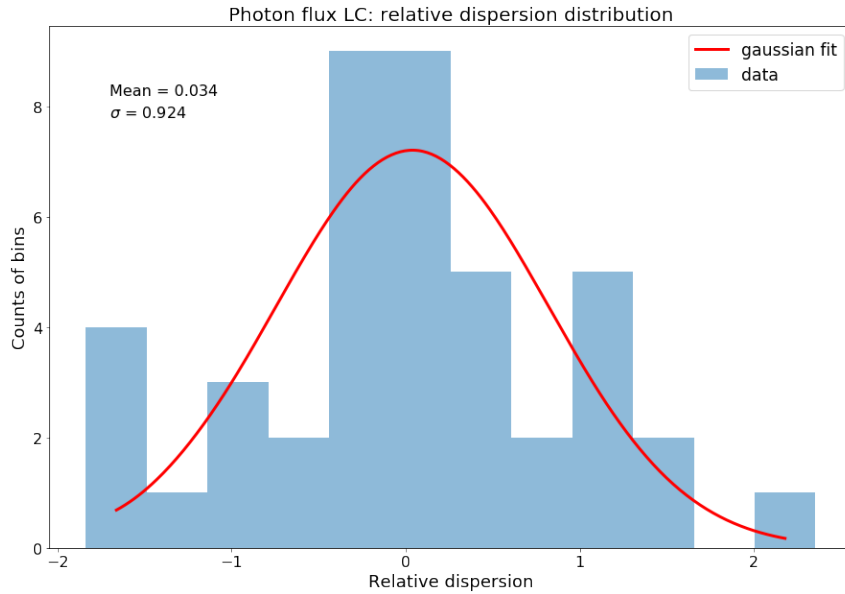


Figure J.12: Histogram of the relative dispersion distribution of the 90 days average normalized photon flux LC of 4FGL J1747.2-2957 in the 300 MeV–3 GeV energy range calculated following Equation 2.13. The mean and standard deviation of this distribution are also shown in the Figure.

J.3 Systematic uncertainties in the 90 days, 3–10 GeV LC

Below, the systematic uncertainties estimate of the LCs in the 3–10 GeV energy range and with 90 days bins.

J.3.1 Energy flux

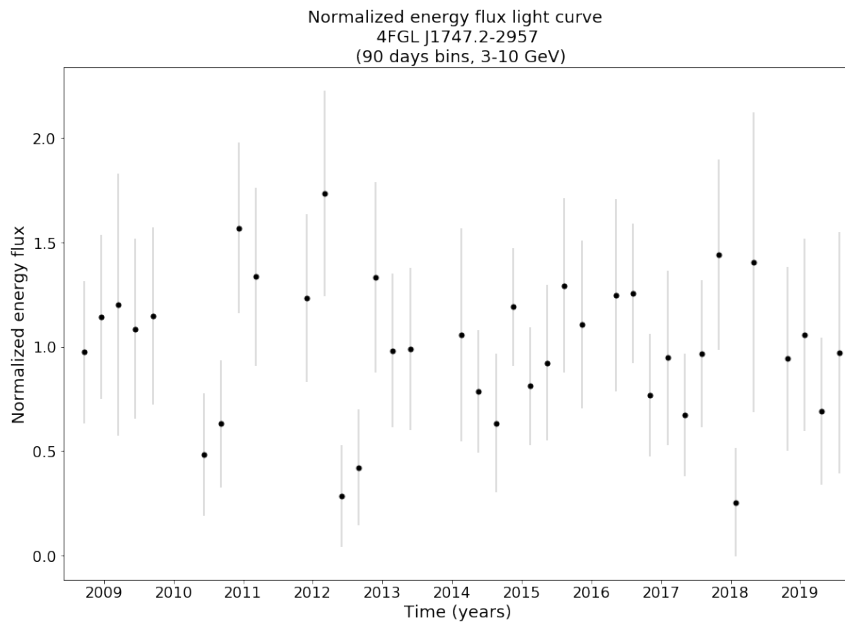


Figure J.13: 90 days average normalized energy flux LC of 4FGL J1747.2-2957 (pulsar PSR J1747-2958) in the 3–10 GeV energy range.

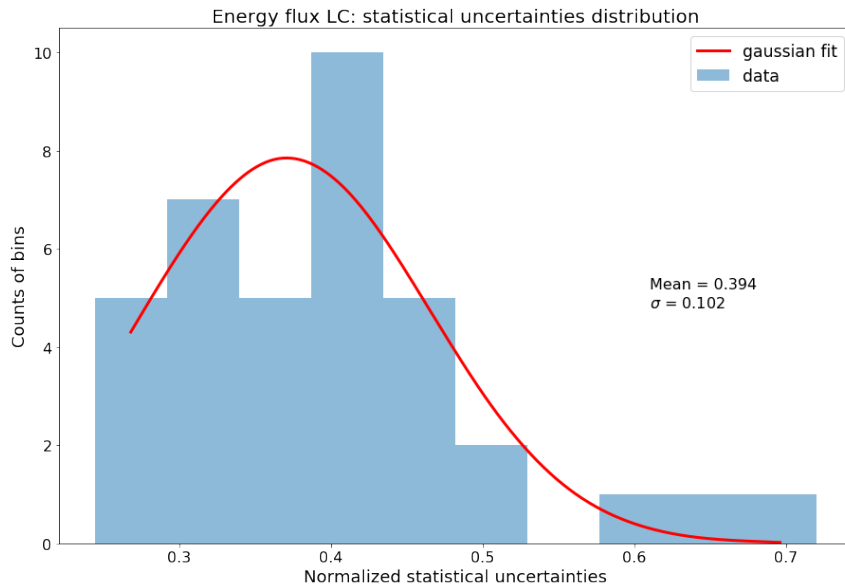


Figure J.14: Histogram of the statistical uncertainties of the 90 days average normalized energy flux LC of 4FGL J1747.2-2957 in the 3–10 GeV energy range. The red line is a normal distribution with the same mean and standard deviation of the statistical uncertainties (the values are shown in the Figure).

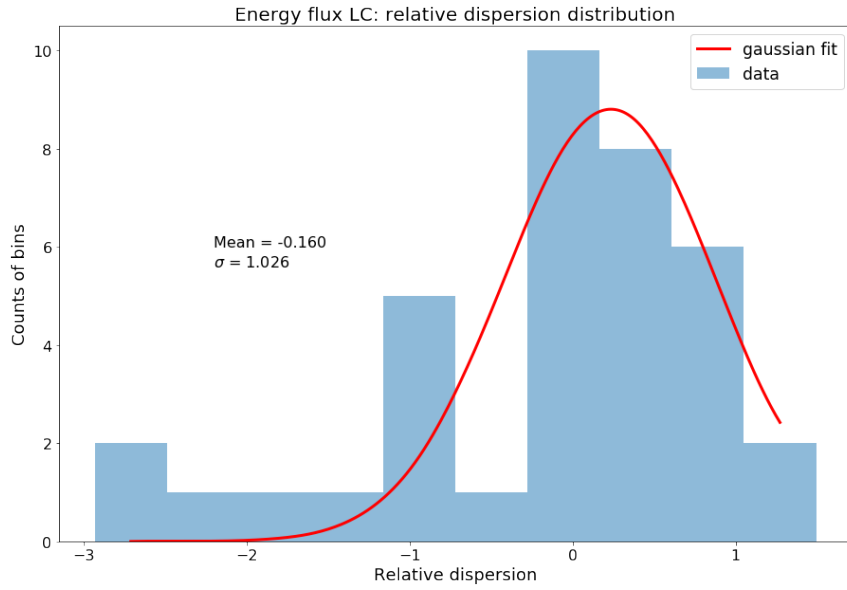


Figure J.15: Histogram of the relative dispersion distribution of the 90 days average normalized energy flux LC of 4FGL J1747.2-2957 in the 3–10 GeV energy range. The mean and standard deviation of this distribution are also shown in the Figure.

J.3.2 Photon flux

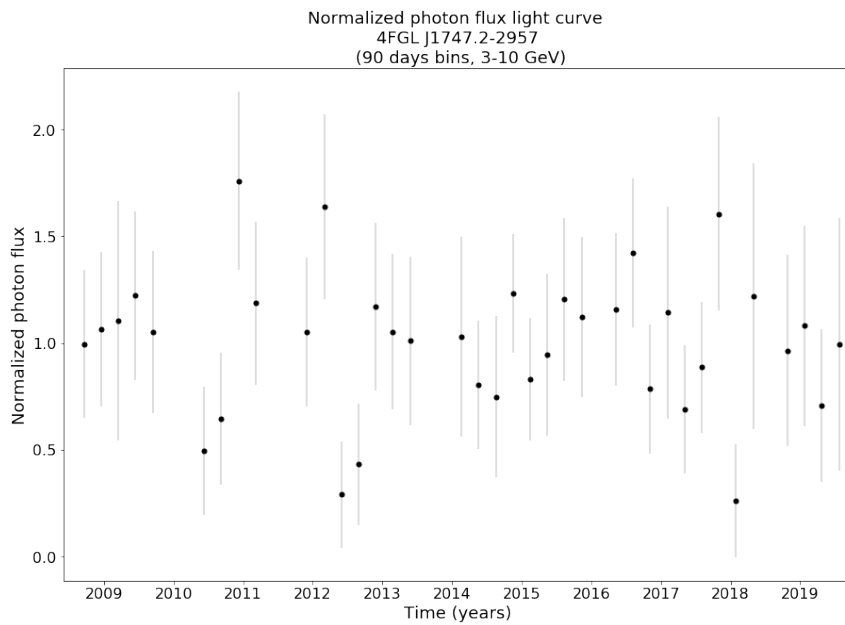


Figure J.16: 90 days average normalized photon flux LC of 4FGL J1747.2-2957 (pulsar PSR J1747-2958) in the 3–10 GeV energy range.

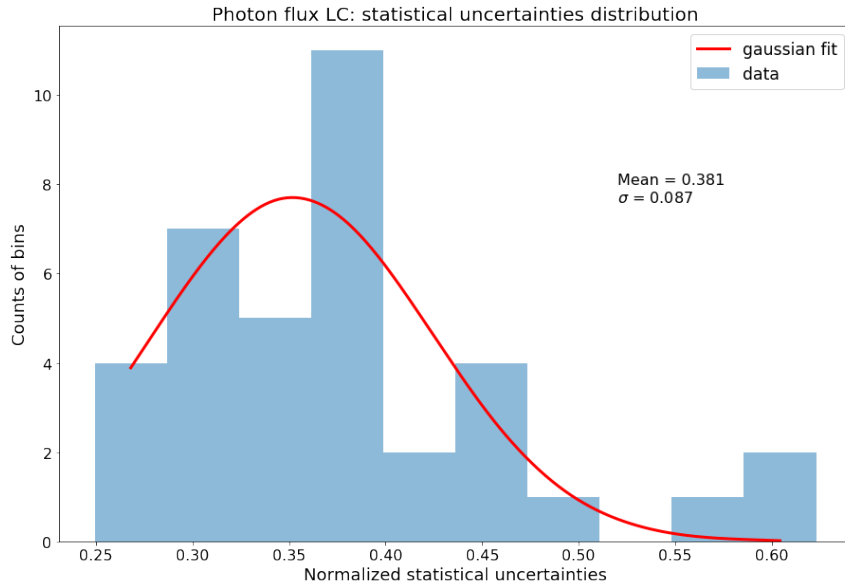


Figure J.17: Histogram of the statistical uncertainties of the 90 days average normalized photon flux LC of 4FGL J1747.2-2957 in the 3–10 GeV energy range. The red line is a normal distribution with the same mean and standard deviation of the statistical uncertainties (the values are shown in the Figure).

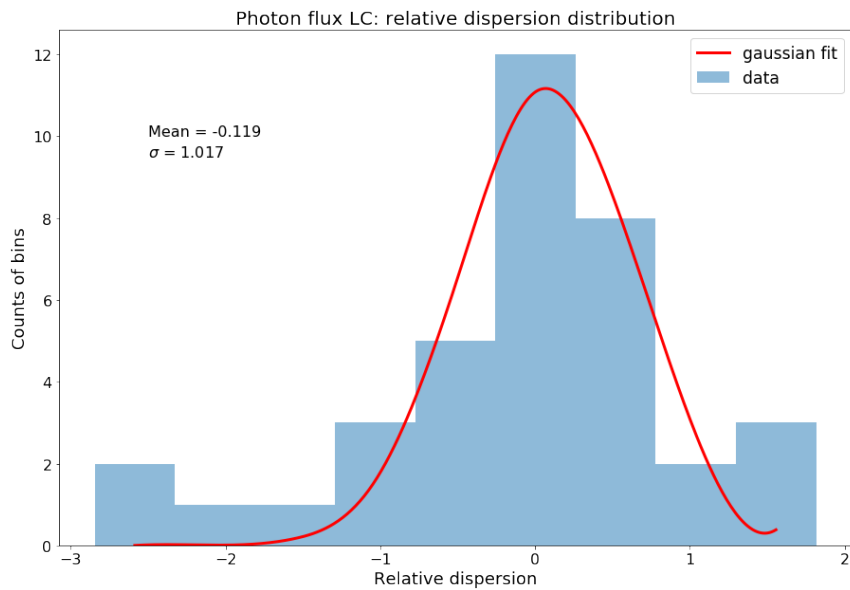


Figure J.18: Histogram of the relative dispersion distribution of the 90 days average normalized photon flux LC of 4FGL J1747.2-2957 in the 3–10 GeV energy range calculated following Equation 2.13. The mean and standard deviation of this distribution are also shown in the Figure.

Appendix K

The 45 days bins LC created based on the Universal Model (100 MeV–500 GeV)

Here we show the plots for the 45 days bins LC created based on the Universal Model (100 MeV–500 GeV energy range). They are similar to the plots shown in Section 3.3 for the 15 days bins LC in the same energy band.

The TS of the 45 days bins LC bins are shown in Appendix M.

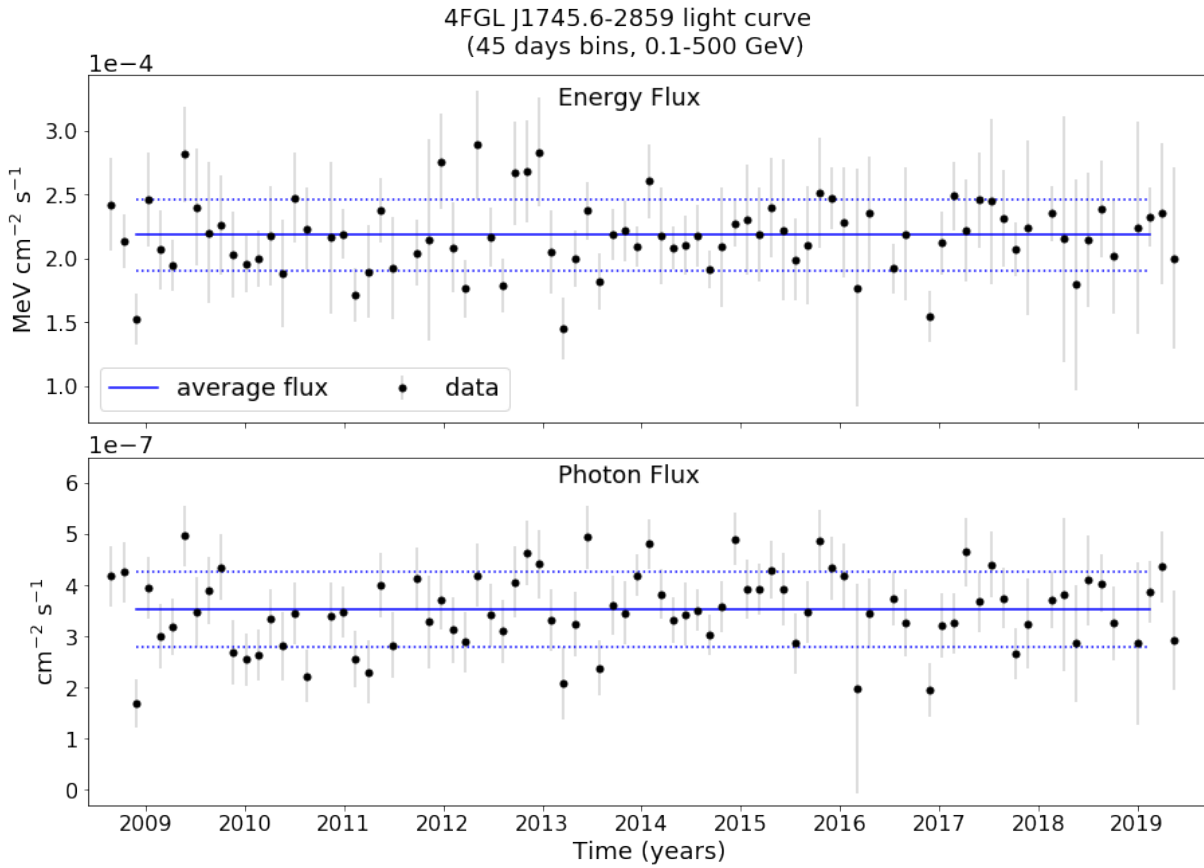


Figure K.1: 45 days LCs of 4FGL J1745.6–2859 in the 100 MeV–500 GeV energy band. The error bars correspond to the 68% confidence level uncertainty. In every bin the source was detected with $TS > 16$. The dotted blue lines correspond to the 1σ uncertainty of the average flux.

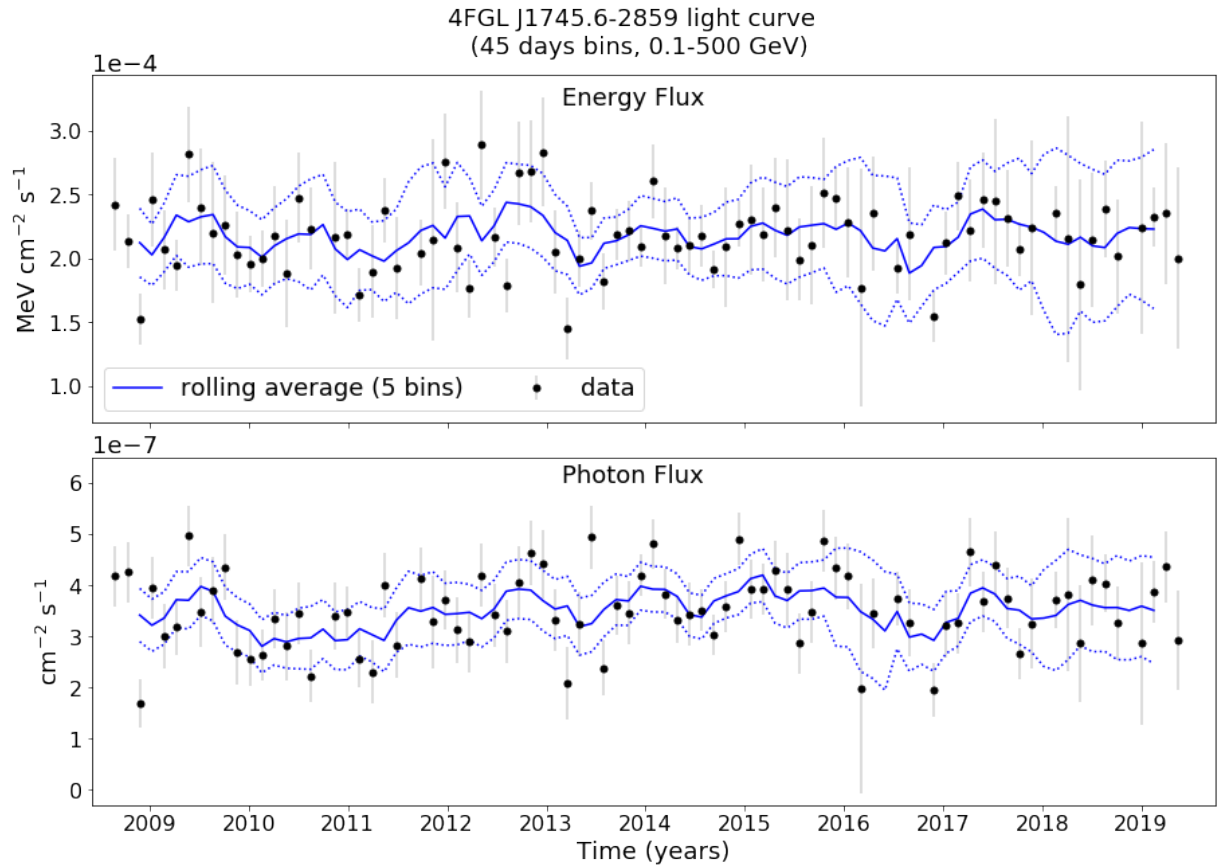


Figure K.2: 45 days LCs of 4FGL J1745.6–2859 in the 100 MeV–500 GeV energy band. The error bars correspond to the 68% confidence level uncertainty. The dotted lines correspond to the 2σ uncertainty of the rolling average flux.

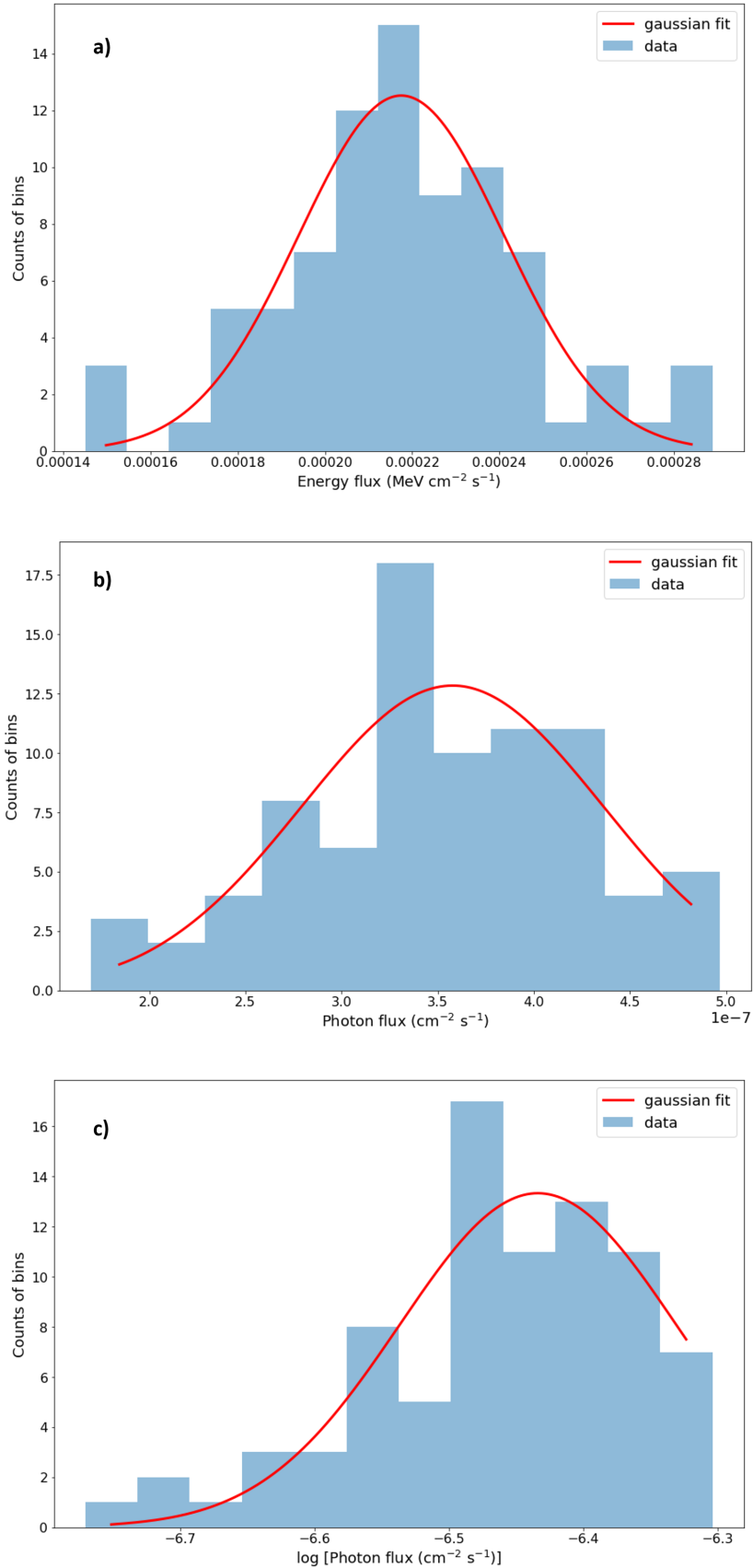


Figure K.3: The flux distribution for the 45 days bins LCs in the 0.1 MeV–500 GeV. We show the distributions for the energy flux, the photon flux and the logarithm of the photon flux in panels a), b) and c), respectively. The red curve corresponds to the Gaussian fits to the distribution (a log-normal fit in panel c)). A Gaussian fit is clearly preferable for the fluxes distribution (see Tables K.1 and K.2).

Table K.1 - Results of the Shapiro-Wilk and the D’Agostino’s K^2 normality tests for the 45 days LCs in the 0.1 MeV–500 GeV energy range. The flux distribution is compatible with a Gaussian fit.

Test	Energy flux		Photon flux		Log(Photon flux)	
	H_0 : normal distribution		H_0 : normal distribution		H_0 : log-normal distribution	
	p-value	result	p-value	result	p-value	result
Shapiro-Wilk	0.4615	fail to reject H_0	0.6432	fail to reject H_0	0.007	reject H_0
D’Agostino’s K^2	0.562	fail to reject H_0	0.684	fail to reject H_0	0.009	reject H_0

Table K.2 - Results of the Anderson-Darling normality test for the 45 days LCs in the 0.1 MeV–500 GeV energy range. The flux distribution is better described by a Gaussian fit.

Sig.	Energy flux			Photon flux			Log(Photon flux)		
	H_0 : normal distribution			H_0 : normal distribution			H_0 : log-normal distribution		
level	statistic	crit. value	result	statistic	crit. value	result	statistic	crit. value	result
15		0.551	fail to reject H_0		0.551	fail to reject H_0		0.551	reject H_0
10		0.628	fail to reject H_0		0.628	fail to reject H_0		0.628	reject H_0
5	0.4178	0.753	fail to reject H_0	0.1867	0.753	fail to reject H_0	0.834	0.753	reject H_0
2.5		0.878	fail to reject H_0		0.878	fail to reject H_0		0.878	fail to reject H_0
1		1.045	fail to reject H_0		1.045	fail to reject H_0		1.045	fail to reject H_0

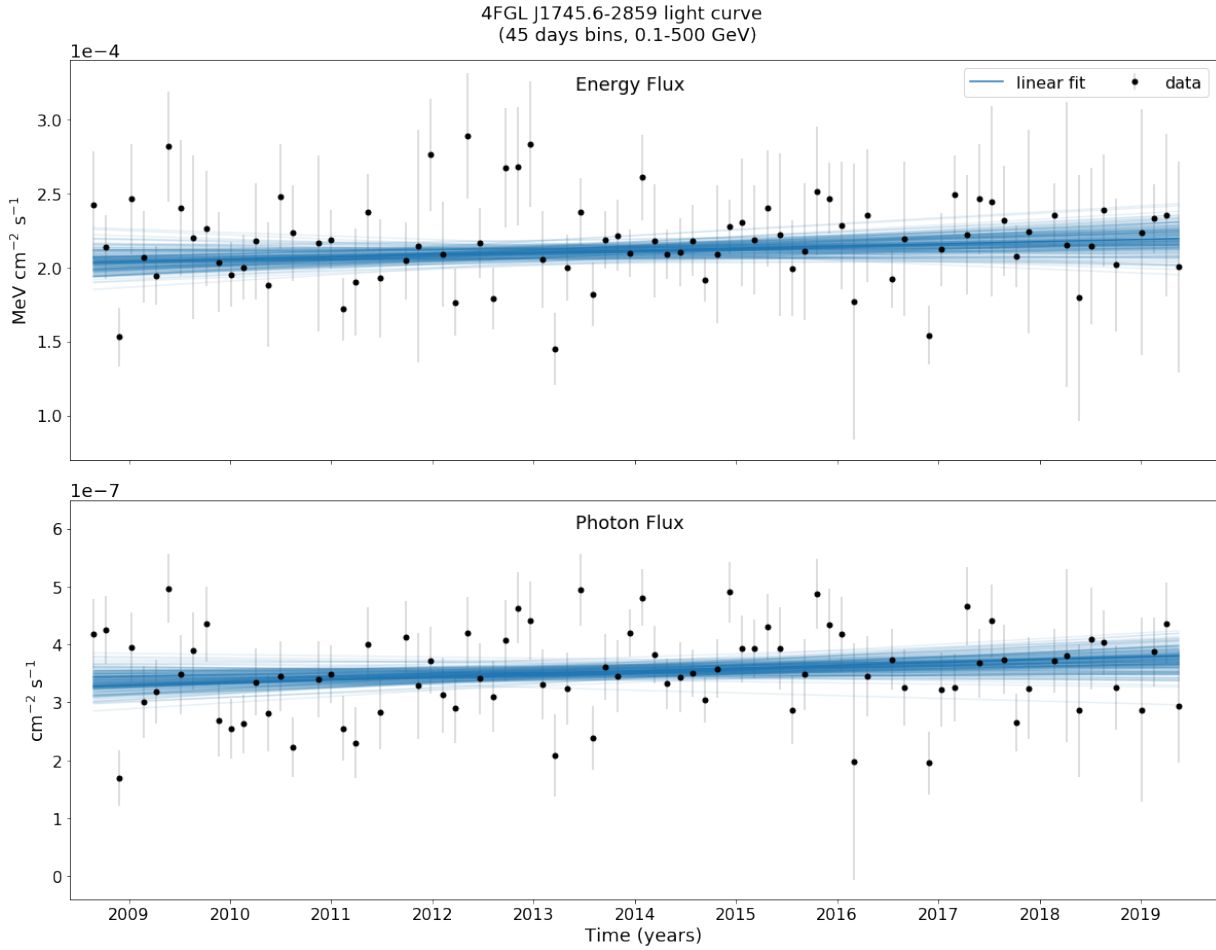


Figure K.4: These are the same 45 days LCs of 4FGL J1745.6–2859 in the 100 MeV–500 GeV energy band shown in Figure K.1 fitted with linear functions. We plotted in blue 200 randomized selected MCMC linear fits to the data. The results of the fit are in Table K.3.

Table K.3 - Results of a linear fit to the 100 MeV–500 GeV energy range 45 days bins LCs.

Parameter	Light curve	
	Energy flux	Photon flux
Angular coefficient	$(4.2 \pm 4.2) \times 10^{-14}$	$(12.9 \pm 9.0) \times 10^{-17}$
Linear coefficient	$(19.2 \pm 1.7) \times 10^{-5}$	$(30.2 \pm 3.7) \times 10^{-8}$

Appendix L

The 95% confidence level central point position as a function of energy

Figure L.1 shows the dependence of the source location on energy, together with the radio position of Sgr A* as measured by the Very Long Baseline Array (Petrov et al., 2011) and locations of other potential gamma-ray emitters in the GC. The solid and dashed circles represent the 68% and 95% confidence level positional uncertainties.

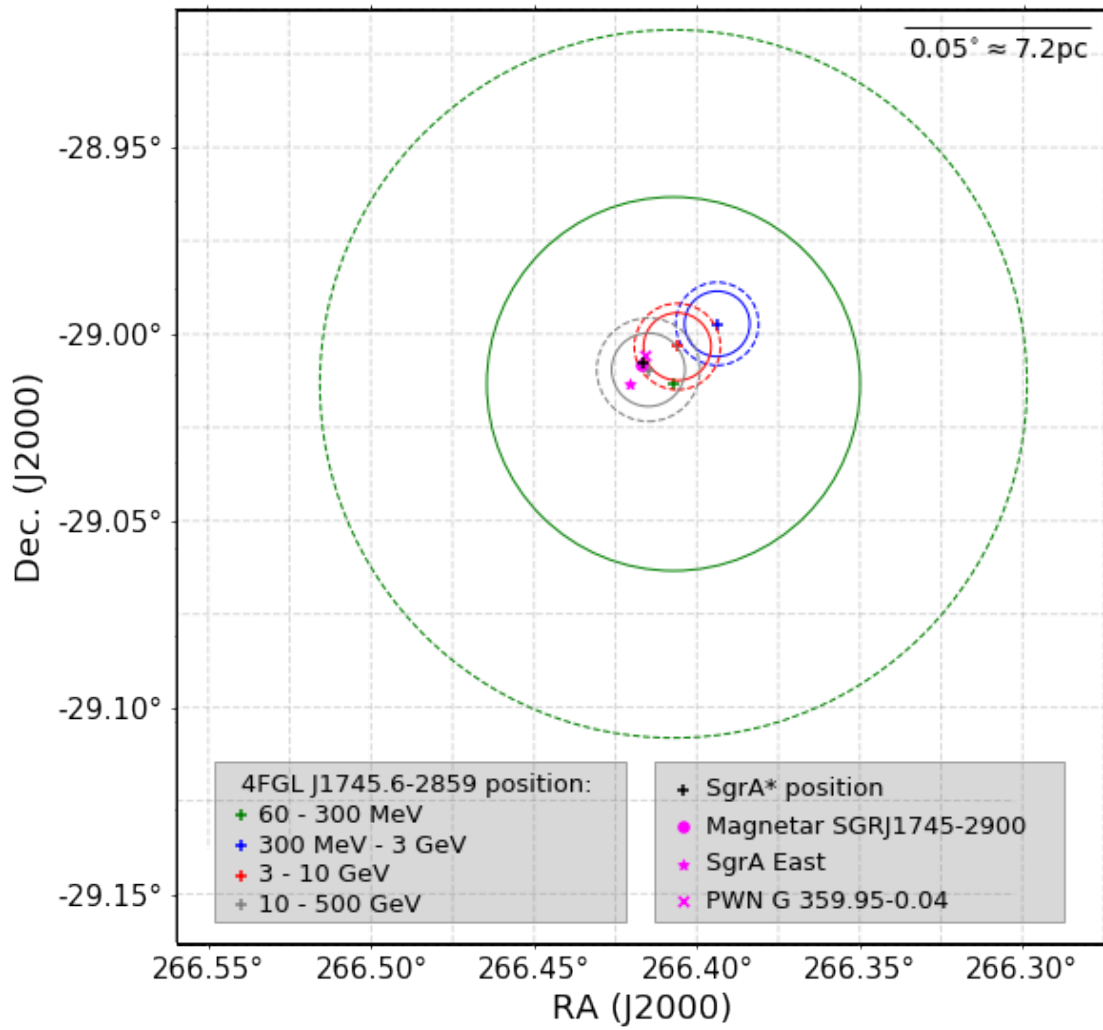


Figure L.1: The position of the central source as a function of the energy range used in the analysis: green (60–300 MeV), blue (300 MeV–3 GeV), red (3–10 GeV) and gray (10–500 GeV). The solid and dashed circles represent the 68% and 95% confidence level positional uncertainties. The radio position of Sgr A* is indicated by the black cross. The positions of other gamma-ray-emitters in the GC are also indicated.

The TS of the LCs

Here we present the TS of every bin of the LCs created in this work. For the bins with $TS < 16$, indicated by a red line in the Figures, we showed the 95% confidence level UL in the LCs.

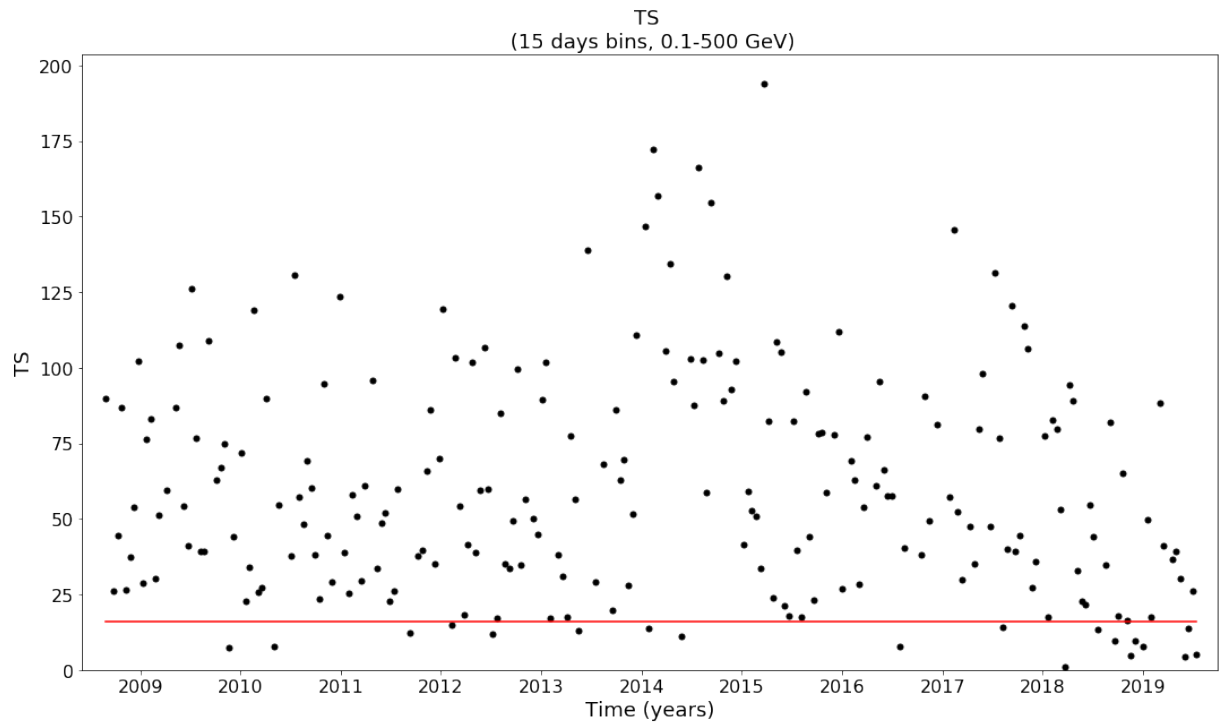


Figure M.1: The TS of the 15 days LC of 4FGL J1745.6–2859 in the 100 MeV–500 GeV energy band. A red line indicates the limit of $TS = 16$ under which we showed the 95% confidence level UL in the LCs in this work.

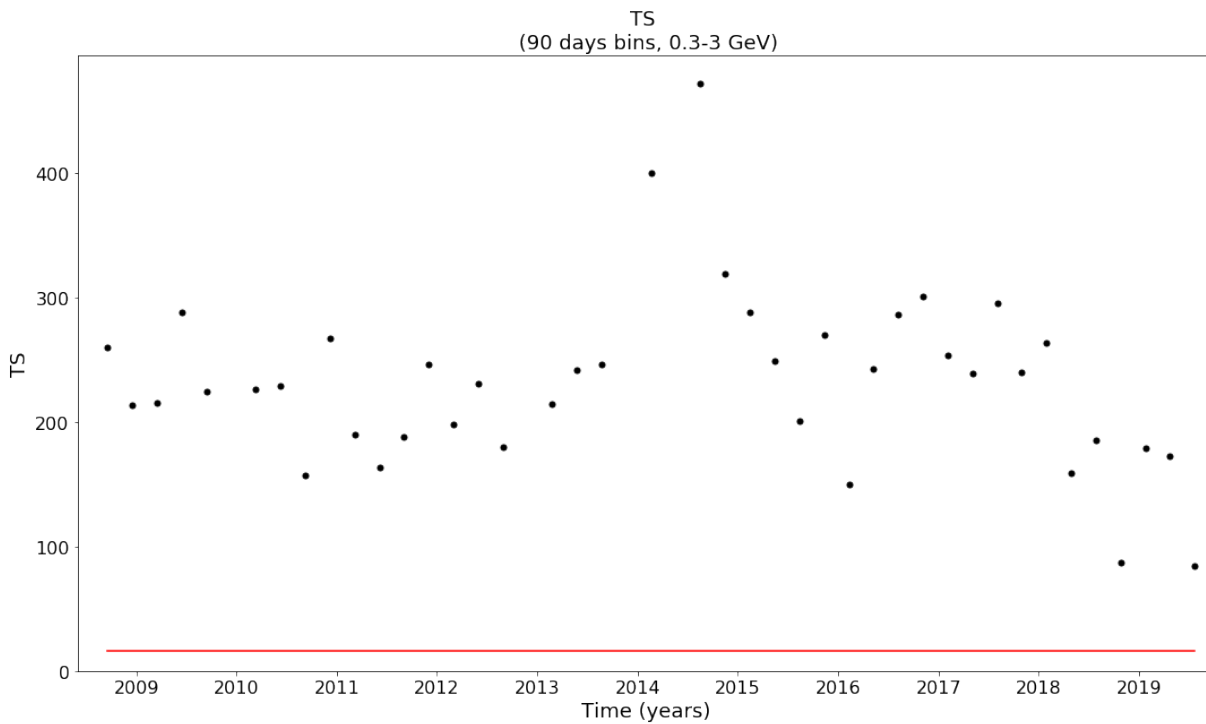


Figure M.2: The TS of the 90 days LC of 4FGL J1745.6–2859 in the 300 MeV–3 GeV energy band. The red line indicate the limit of $TS = 16$.

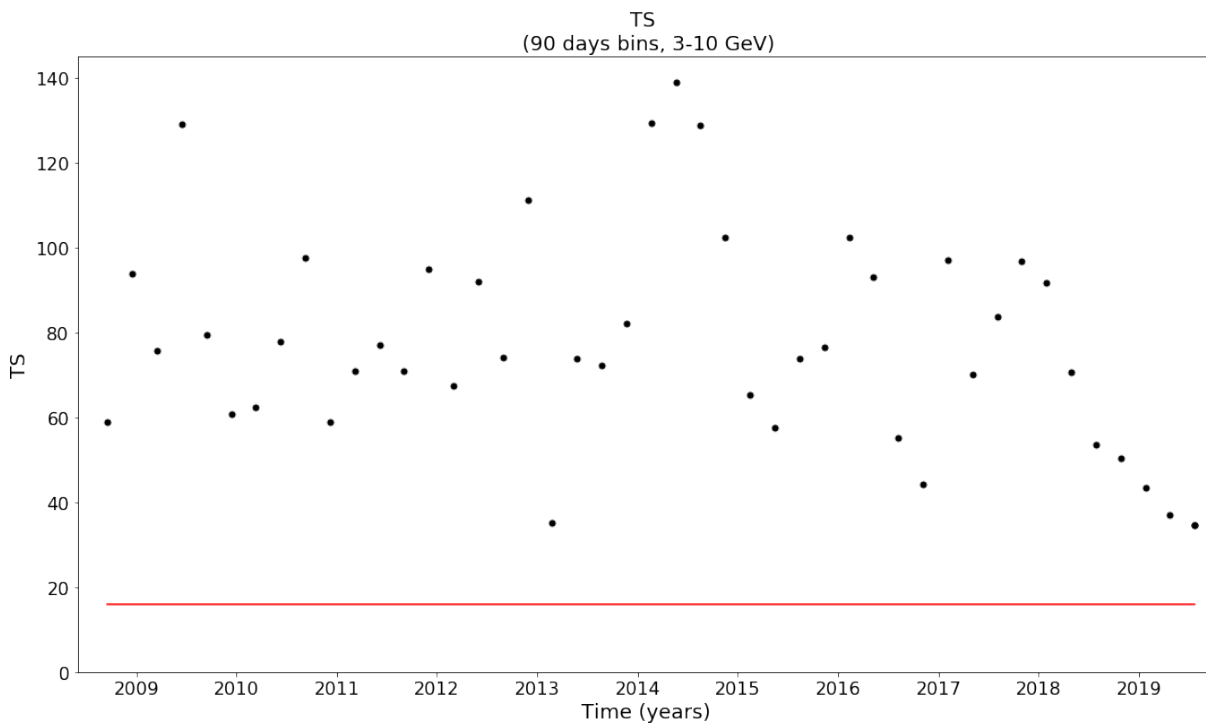


Figure M.3: The TS of the 90 days LC of 4FGL J1745.6–2859 in the 3–10 GeV energy band. The red line indicate the limit of $TS = 16$.

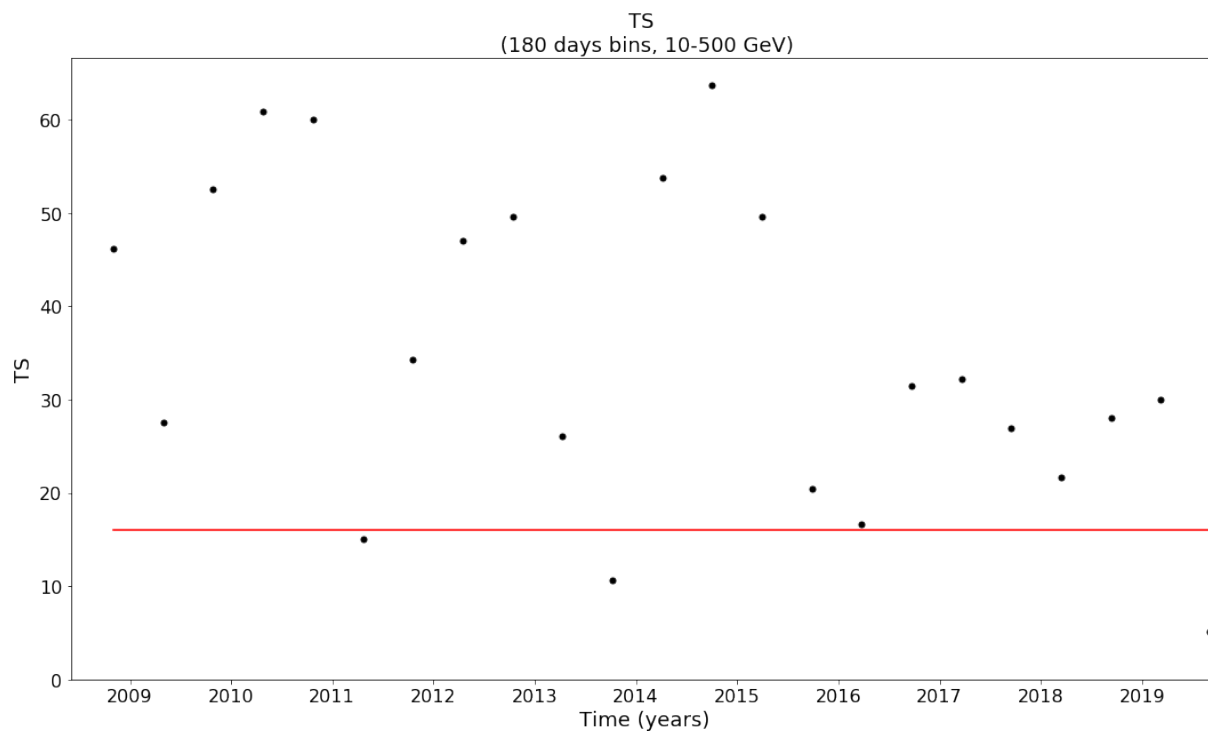


Figure M.4: The TS of the 180 days LC of 4FGL J1745.6–2859 in the 10–500 GeV energy band. The red line indicate the limit of $TS = 16$.

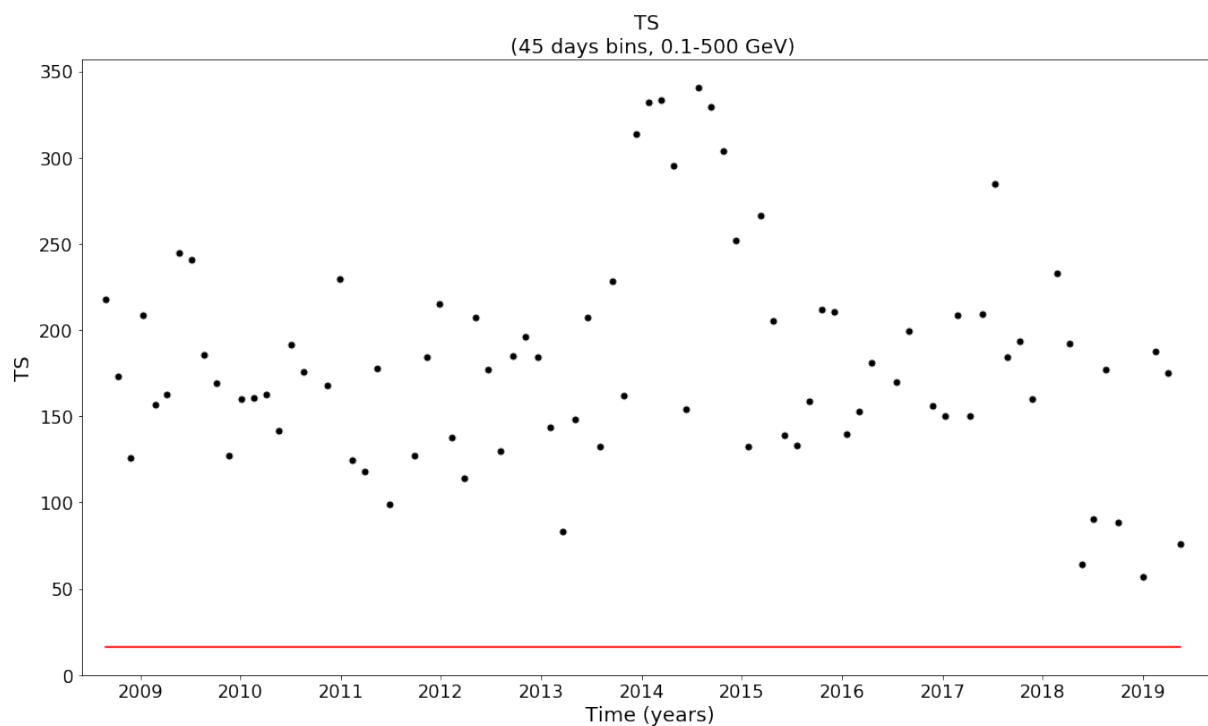


Figure M.5: The TS of the 45 days LC of 4FGL J1745.6–2859 in the 100 MeV–500 GeV energy band. The red line indicate the limit of $TS = 16$.